STRUCTURAL STUDIES OF NEW INORGANIC OXIDES AND POLYMER ELECTROLYTES

James Burgess Thomson

A Thesis Submitted for the Degree of PhD
at the
University of St Andrews

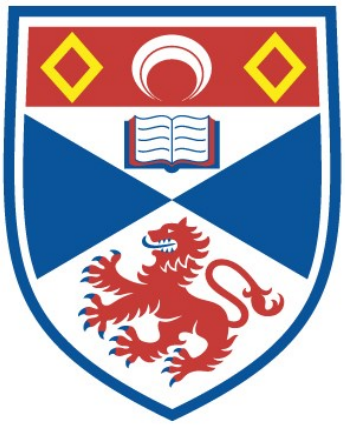

1997

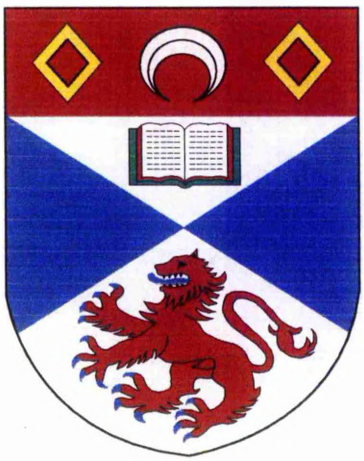

STRUCTURAL STUDIES OF NEW INORGANIC OXIDES AND POLYMER ELECTROLYTES

A thesis presented for the degree of

Doctor of Philosophy

in the Faculty of Science of the University of St. Andrews

by James Burgess Thomson, *B.Sc.*

Centre for Electrochemical

and Material Sciences

School of Chemistry

St. Andrews

August, 1996

DECLARATION

I, James Burgess Thomson, hereby certify that this thesis, which is approximately 58000 words in length, has been written by me, that it is a record of work carried out by me and that it has not been submitted in any previous application for a higher degree.

Signed: Date: 26 August 1996

I was admitted as a research student in October 1992 and as a candidate for the degree of Doctor of Philosophy on October 1993; the higher study for which this is a record was carried out in the University of St. Andrews between 1992 and 1995.

Signed: Date: 26 August 1996

CERTIFICATION

I hereby certify that the candidate has fulfilled the conditions of the Resolution and Regulations appropriate for the degree of Doctor of Philosophy in the University of St. Andrews and that the candidate is qualified to submit this thesis in application for that degree.

Signed: Date: 26 August 1996

P.G. Bruce

Director of Research

LIBRARY DECLARATION

In submitting this thesis to the University of St. Andrews I understand that I am giving permission for it to be made available for use in accordance with regulations of the University Library for the time being in force, subject to any copyright vested in the work not being affected thereby. I also understand that the title and abstract will be published, and that a copy of the work may be made and supplied to any bona fide library or research worker.

Signed: Date: 26 August 1996

For Mum and Dad

Abstract

A knowledge of structure is crucial to the understanding of inorganic solids and polymers. Neutron and X-ray powder diffraction are two powerful complementary techniques which can be used in the structural characterisation of a variety of crystalline materials. Chemical and electrochemical oxygen intercalation techniques involving both aqueous and non-aqueous systems, have been investigated for a number of crystalline inorganic oxides. The pyrochlore structure has been discovered to be a new class of host for the chemical intercalation of oxygen and the interstitial solid solution of $Ce_2Zr_2O_{7+x}$ based on this structure-type has been investigated. Intercalation in this system is found to involve an unusual mechanism of oxygen displacement.

The structures of other complex metal oxides have also been elucidated using a combination of X-ray and neutron powder diffraction, including those of '$Li_{29}Zr_9Nb_3O_{40}$' and '$Li_{29}Zr_{9.6}Ta_{2.4}O_{40}$'. The doping behaviour of magnesium into the technologically important material lithium niobate has also been studied using these techniques.

Polymer electrolytes are a class of ionically conducting solid phases formed by the dissolution of salts in ion co-ordinating macromolecules. The relationship between the crystalline and amorphous phase of the polymer-salt complex PEO_3:$LiCF_3SO_3$ has been examined by variable-temperature powder X-ray diffraction. This has shed new light on the relationship between the crystalline and amorphous structures of polymer electrolytes. Finally, the crystal structure of the polymer-salt complex PEO_4:RbSCN has been determined.

Table of Contents

Table of Contents

Table of Contents

Heading *Page No.*

Table of Contents

Table of Contents

Heading *Page No.*

Table of Contents

Table of Contents

Chapter 1
New Materials and Techniques in Solid State Chemistry

1.1 Introduction

The field of solid state chemistry has witnessed a marked progress in its development over the past 25 years. However, much chemical ingenuity is still required in the synthesis of solid materials, and this aspect of materials science is becoming increasingly recognised as a crucial component of the subject. This is because an important goal of solid state chemistry is the production of tailor-made materials with specific structures and properties. Hence, while a rational approach to the synthesis of solid materials has been developed[1], serendipitous elements still play an important part.

A variety of inorganic solids have been prepared in the past several years by the traditional ceramic method[2] which involves mixing and grinding powders of the constituent oxides, carbonates and other similar compounds, and heating them at high temperatures with intermediate grinding. A wide range of conditions, such as high temperatures and pressures, very low oxygen partial pressures and rapid quenching, have all been employed in materials synthesis. However, low temperature chemical routes and other methods involving mild reaction conditions are also of great interest. The present trend is to avoid the brute-force methods in order to achieve an improved control of the structure, stoichiometry and phase purity.

The soft chemistry routes[3], now known by the French idiom "*chemie douce*" are often desirable because they lead to novel products, many of which are metastable and so cannot be prepared by other means. They make use of simple reactions such as intercalation, hydrolysis, dehydration and reduction that can be carried out at low temperatures.

1.2 Intercalation

Intercalation reactions cover a broad range of chemical processes and constitute one branch of the *chemie douce* field.

Intercalation is the reversible insertion of mobile guest species into a rigid host lattice containing a contiguous network of empty lattice sites of appropriate sizes. This process is represented in equation 1.2a.

$$xG + \bullet_xH \rightleftarrows G_xH \qquad \text{(Eqn. 1.2a)}$$

where G is the guest species and • is a vacant site in the host, H.

When a new phase is created, the main factors which control the rate of solid-state reactions are the nucleation and growth of product phases (if one is produced), and the transport of reactants in the solid to the reaction site. Since the activation energy barriers for these processes are usually high, most reactions and transformations of this type proceed at low rates at room temperature.

However, some solid-state reactions are less kinetically restricted. Topotactic processes maintain a close structural relationship between the initial and final phase, so nucleation and growth of the product is highly facile. Also, reactions involving the filling of empty lattice positions without a change in structure, e.g. in metal oxides with lattice vacancies, may exhibit unusually high diffusion rates for species fitting into these sites, as seen in fast ion conductors[4]. Both these favourable kinetic conditions are found in intercalation reactions.

During the intercalation process the host may undergo changes in structural dimensions to accommodate the guest, but the integrity of the host lattice is preserved. The term *intercalation* was traditionally used for lamellar or layered host materials, and *insertion* in connection with other types of hosts, but they are now often used interchangeably in the literature.

In addition to the physical perturbation of the host lattice (e.g. from interlayer expansion), intercalation often induces changes in magnetic, electrical or optical properties in the host material. These effects arise because intercalation is frequently accompanied by redox processes, with the transfer of electrons between the guest and host. The potential for tuning these properties by employing a variety of guest-host combinations has lead to useful applications (e.g. the lithium "rocking chair" solid state battery - Figure 1.2b).

A wide variety of intercalation materials are known. The guests include both molecular species and ions. Insertion of ions requires the simultaneous accommodation of compensating charges by the host matrix, either delocalised in its band structure or localised by the reduction / oxidation of discrete atomic or molecular entities in the host. In both cases the electronic conductivity of the host is an important factor in determining the kinetics of the intercalation reaction. Partial charge transfer between the guest and host is often observed in molecular intercalates.

Figure 1.2a Schematic of (a) 3, (b) 2 and (c) 1-dimensional lattices.

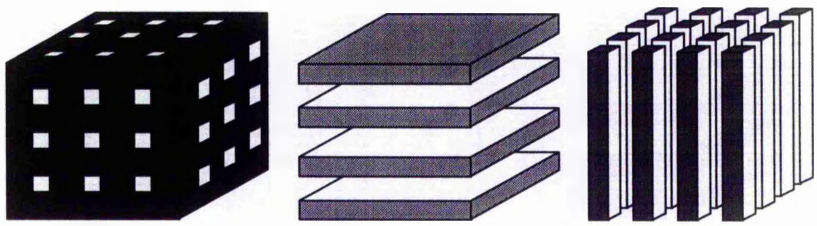

Host structures may exhibit differing dimensionality, from three dimensional framework structures with empty lattice positions forming channels or interconnected cavities, through two dimensional layer structures, where the insertion takes place in the van der Waals gaps between the layers, to one dimensional chain

structures or nearly amorphous materials where the inserted species occupy positions between the structural elements. A schematic of the three different types of lattice is shown in Figure 1.2a.

The high degree of dimensional stability that is required of the host lattice demands strong directional bonding. This is only obtained in compounds with appreciable covalency such as metal oxides or chalcogenides, or in carbon based materials such as graphite or conjugated polymers.

Intercalation reactions involving ionic intercalates can be readily controlled and studied by electrochemical techniques. In these cases the host material is used as one of the electrodes in an electrochemical cell. A suitable source or sink of the intercalate is used as the other electrode. For alkali metal intercalates, this electrode will typically, but not necessarily, be the free alkali metal. Under equilibrium conditions, the open circuit voltage of such a cell will be determined by the difference in free energy between the metal in the metallic state and in the intercalated state. Intercalation reactions have many scientific and technological applications[5], including in the development of new catalysts and sensors, fuel cells, and in electrode materials in secondary batteries.

One problem which arises in the design of simple rechargeable all solid state batteries is the adverse effect of changes in the morphology of the electrode-electrolyte interface as progressive charge-discharge cycles are performed. With metal-solid electrolyte interfaces, the growth of metallic dendrites during charge and the increasing loss of contact between the phases during discharge generally leads to the rapid deterioration and eventual failure of the cell. One answer is to use an intercalation compound as the electrode in place of the metal. Host materials can often incorporate large quantities of guest metal atoms without a phase change. For a successful battery material, the mixed conductor phase must have a wide range of homogeneity and a flat partial molar free energy versus composition curve, so that the discharge voltage may be relatively constant. A reversible secondary cell can be constructed using a solid electrolyte together with two different intercalation

materials acting as positive and negative electrodes. Figure 1.2b shows a schematic of such a 'rocking chair' rechargeable lithium battery.

Figure 1.2b Schematic of a 'rocking chair' rechargeable lithium battery.

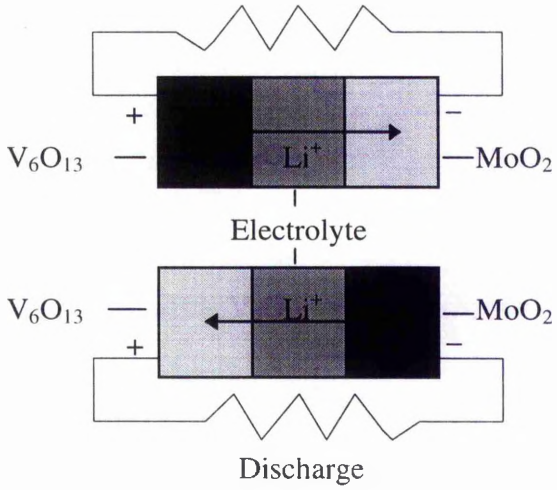

A high-temperature hydrogen-oxygen fuel cell using yttria doped zirconia as the electrolyte has been under development for a number of years. It is acknowledged that one of the difficulties with the technology is the high (900-1000°C) operating temperature. A lower operating temperature would require an electrolyte with a higher conductivity than the zirconia based system at 500-800°C. Also, an oxygen intercalation electrode at the cathode would permit the electrode reaction:

$$O_2 \rightarrow 2O. + 4e^- \rightarrow 2O^{2-} \qquad \text{(Eqn. 1.2b)}$$

to occur over the whole surface of the electrode and not just at the triple point where the electrolyte meets the gas and the electronic conductor. The possibility of the discovery of alternative electrolytes with a satisfactory performance at lower

temperatures is now being examined, making the development of oxygen intercalation compounds of considerable technological interest.

In most cases, oxide ion diffusion is slow at ambient temperature and consequently higher temperatures of 400-500°C are generally required to achieve reasonable rates. In a few special cases reactions occur at room temperature. This topic has acquired particular importance since the discovery of high temperature superconductivity in cuprates with perovskite related structures[6]. In the cuprates, copper oxidation state can vary from +1 to +3 and the Cu–O co-ordination environment from 2 to 6 as the oxidation state increases. Changes in the oxygen stoichiometry play a critical role in determining the electronic properties in this class of materials.

Oxygen intercalation was first discussed explicitly in relation to reactions of mixed valence copper oxides with perovskite related structures. Michel and Raveau[7] showed that for three systems ($La_3Ba_3CuO_{14+\delta}$, $La_{2-x}A_{1+x}Cu_2O_{6+\delta}$ and $La_{2-x}A_xCuO_{4-\delta}$ [A = Sr, Ca]) oxygen could be reversibly intercalated and deintercalated into the structures at 400°C by varying the oxygen partial pressure between 1 and 10^{-3} atm. The intercalation of the oxide ions occurs by filling vacant lattice sites without a significant rearrangement of the structure. In addition to the cuprates, oxides with perovskite related structures containing other transition metals or Group V metal cations show similar behaviour. The compounds $BaBiO_{3-x}$ ($0 \leq x \leq 0.5$) and La_2NiO_{4+x} ($0 < x < 0.18$) show quite wide ranges of nonstoichiometry. The La_2NiO_4 material and several oxides with perovskite related structures can also be intercalated with oxygen ions by an electrochemical method, which will be discussed further in Chapter 3.

A variety of oxygen intercalation techniques into a number of perovskite related complex metal oxides and a material of the pyrochlore structure type are examined in Chapters 4 and 5.

1.3 Structural Characterisation of Solids[8]

1.3.1 Introduction

The rational synthesis of materials requires a knowledge of crystal chemistry besides thermodynamics, phase equilibria and reaction kinetics. A thorough knowledge of the structure of solids as well as the nature of bonding is essential for an appreciation of solid state chemistry, since the properties of a solid usually stem from the structure. For example, in order to understand the mechanism of oxygen intercalation into oxide hosts, it is imperative that the structures of the materials under investigation are known. This normally requires the use of more than one analytical tool for structural determination, and in this work the complementary nature of X-ray and neutron powder diffraction is used to probe the structure of a variety of crystalline solids.

The characterisation of a new material must examine the -

(i) chemical composition and homogeneity of the specimen,

(ii) impurities which may affect the properties,

(iii) structure, revealing the degree of crystallinity and

(iv) nature and concentration of defects influencing the properties.

The scope of "characterisation" is so vast that it encompasses nearly all aspects of solid state chemistry. The various techniques available for structural characterisation may be considered in the following categories- optical methods, diffraction methods, electron microscopic methods, spectroscopic methods and the use of physical properties as characterisation tools. The various methods and their applications are summarised in Table 1.3.1a. The following discussion is by no means a comprehensive listing of all the characterisation techniques available to the solid state chemist, but only seeks to serve as a qualitative introduction to some of the main methods currently at the disposal of a research chemist today.

Table 1.3.1a Methods used in the structural characterisation of solids.

Structural Detail	**Experimental Techniques**
Morphology, phase identification, amorphous or crystalline nature, crystal system, space group, atomic positions. Ultra structure.	X-ray diffraction, optical microscopy, electron diffraction, electron microscopy, neutron diffraction, E.X.A.F.S. and X.A.N.E.S. High resolution electron microscopy.
Site symmetry.	Spectroscopic techniques (I.R., Raman, U.V.-visible, N.M.R[9]., E.S.R.).
Perfection of crystals	Microscopy and X-ray topography.
Thermal Amplitudes of vibration.	X-ray diffraction, neutron diffraction, Mössbauer spectroscopy.
Phase transitions.	D.T.A., D.S.C., light scattering, spectroscopic techniques, diffraction methods, thermal expansion.
Bonding and electronic structure.	Electron spectroscopies, electron density (X-ray diffraction), spin density (neutron diffraction).
Defects and ordering.	Thermogravimetry, T.E.M., neutron diffraction, E.S.R. and optical spectroscopy.
Magnetic ordering and spin configuration.	Magnetic susceptibility, neutron diffraction and Mössbauer spectroscopy.
Chemical environment of nuclei.	Spectroscopic techniques (H.R.N.M.R.of solids, Mössbauer spectroscopy, E.X.A.F.S., X.A.N.E.S. and electron spectroscopies.
Oxidation states of metals.	Redox titrations, X.P.S., E.E.L.S., A.E.S. and X-ray absorption spectroscopy.

Optical methods involve the examination of the substance under an optical (polarising) microscope, measurement of refractive indices and surface topography. These studies provide information on the morphology, crystal symmetry, physical defects, magnetic and electric domains.

Spectroscopic methods provide a variety of information on solids- the local symmetry, point defects, chemical environments of atoms, bonding and phase transitions.

However, a complete description of the structure of a solid requires the discovery of the spatial positions of the elements from which it is composed. If the solid is crystalline, the crystal system, space group, unit cell dimensions, atomic co-ordinates and the electron density around the atoms can be determined by diffraction techniques. However, the solid must contain a periodic arrangement of scattering matter if diffraction is to be observed i.e. it must be crystalline. Various diffraction techniques involving X-rays, neutrons and electrons have now been developed, and can be used to probe different parts of the atomic structure. X-rays interact with the electrons of an element, neutrons with the atomic nucleus and electrons with the charge on the nucleus and associated electrons. These interactions are represented in Figure 1.3.1a.

Figure 1.3.1a. A comparison of the scattering of X-rays, neutrons and electrons by an atom.

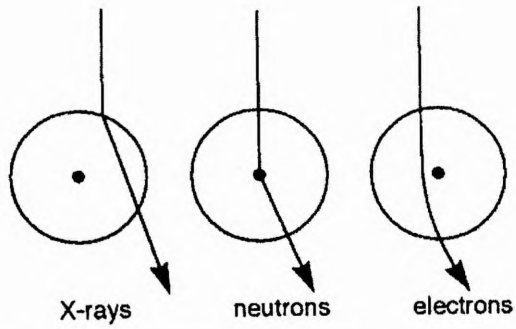

The diffraction condition is described by Bragg's Law, shown in equation 1.3.1a.

$$n\lambda = 2d\sin\theta \qquad \text{(Eqn. 1.3.1a)}$$

where n is an integer, λ is the wavelength of the radiation or particle wave, d the spacing between atomic planes in a crystal and θ the Bragg angle. The relation between the diffraction pattern and the structure of the crystal is understood in terms of the reciprocal lattice. Amongst the different diffraction techniques, X-ray diffraction has been the most commonly used for routine characterisation as well as for detailed structural elucidation, but solid state chemists now make considerable use of electron and neutron diffraction to obtain information not provided by X-ray diffraction.

1.3.2 X-ray Diffraction

The major interaction of electromagnetic radiation is with the electrons of a material (Figure 1.3.1a). X-rays with a wavelength of 0.4 - 2.5 Å are of particular use in crystallography because of their associated diffraction phenomena due to the similarity between the X-ray wavelength and distance between scattering planes.

There are three standard methods of X-ray diffraction:

(i) the Laue method involves a stationary single crystal and 'white' X-rays. This method can be used to determine the crystal symmetry and orientation, and less commonly the structure;

(ii) the rotating crystal method involves a single crystal rotated in a beam of monochromatic X-rays. This can be used to determine the single crystalline nature and unit cell parameters of the sample. The main difficulty is the overlapping of reflections due to different hkl values (or scattering planes). This can be overcome by the Weissenberg method by moving the film or detector parallel to the axis of rotation as the crystal rotates; and

(iii) the powder method involves a polycrystalline sample rotated in a beam of monochromatic X-rays. This can readily give basic crystal structure data and is commonly used for the 'finger print' identification of crystal structures and for the accurate determination of unit cell dimensions.

A knowledge of diffraction intensities is essential to obtain detailed crystal structure, because these intensities are related to the structure factor, which can be used to obtain the co-ordinates of a scattering atom. Computer controlled single crystal X-ray diffractometers have made structure elucidation a routine matter. The availability of synchrotron X-radiation of high intensity and continuously variable wavelength has made X-ray diffraction a still more powerful structural tool for the study of solids. An analytical technique of great utility to solid state chemists is the Rietveld treatment of powder X-ray diffraction profiles (See section 2.2.3). Automated structure packages for the determination of structures by this method are now commercially available.

X-ray diffraction can also give a variety of other information. X-ray powder diffraction can be widely used for phase identification, quantitative analysis of a mixture of phases, particle size analysis, characterisation of physical imperfections and *in situ* studies of reactions. In the case of amorphous solids, X-ray diffraction data provide radial distribution functions which give the number of atoms per unit volume at any distance from the reference atom and so co-ordination number information.

Variable temperature X-ray diffraction studies of crystalline substances are useful in the study of phase transitions, thermal expansion and thermal vibrational amplitudes of atoms in solids. Diffraction studies at high pressures can be employed to examine pressure induced phase transitions in a similar manner.

1.3.3 Electron Diffraction

The scattering of an electron beam is caused by the interaction of the electrons with the electrostatic field of the atoms created by the nucleus and electron cloud (Figure 1.3.1a). Electron beams differ from X-rays in two respects which render electron diffraction a valuable tool for structural studies of solids. The smaller wavelength of electron beams leads to smaller Bragg angles in electron diffraction, making it possible to record extensive sections of the reciprocal lattice directly with a small stationary crystal. The charge on an electron creates a much stronger interaction between electrons and atoms than X-rays (about 10^3 times stronger), making it possible to record electron diffraction patterns almost instantaneously. However, this strength of interaction limits sample thickness to 10^{-7} - 10^{-5} cm in transmission. Electron diffraction patterns are readily obtained with commercial electron microscopes and can be employed to investigate defect ordering, superstructures and fine particle samples. Electrons with energies in the range 10 - 200 eV have wavelengths of the same order as interatomic spacings in the crystals, but have very little penetrating power. Thus low energy electron diffraction (LEED) can be used to give patterns characteristic of the atomic arrangement of the surface layers.

1.3.4 Neutron Diffraction and related techniques

The neutron as well as the electron can be used in diffraction studies. Thermal neutrons with a velocity of approximately 4000 ms^{-1} have an associated wavelength of about 1.0 Å and can be used in neutron diffraction experiments. Whereas X-rays are scattered primarily by the electrons in atoms, neutrons are scattered mainly by the atomic nucleus (Figure 1.3.1a). Since the neutron scattering amplitude does not show a smooth dependence on the atomic number of the atoms, it is more useful in locating light atoms (especially hydrogen) in crystals. Additional scattering of neutrons can arise due to the magnetic moment of neutrons interacting with the

permanent magnetic moments of atoms or ions in a crystal. In the absence of an external magnetic field, the magnetic moments of atoms in a paramagnetic crystal are arranged at random, so that the magnetic scattering of such a crystal by neutrons is also random. This contributes a diffuse background to the diffraction pattern. In magnetically ordered materials, the magnetic moments are regularly aligned. The magnetic scattering of such a crystal by neutrons is therefore ordered, and the magnetic structure can be determined. As well as the two elastic scattering effects already discussed, neutrons can also undergo inelastic scattering by crystals. This involves an exchange of energy between the lattice and neutrons and can be used in the study of quantised vibrational modes i.e. phonons.

Neutron beams are much weaker in intensity than X-rays, and so neutron diffraction requires larger single crystals (10-100 mm^3 in volume as compared to the 0.1 mm^3 crystal volume used in X-ray diffraction work). However, useful structural data can be obtained more easily by the analysis of neutron diffraction profiles from polycrystalline materials.

Neutron diffraction can also be used to investigate amorphous solids such as glasses and liquids. It can also be used to provide valuable information on dynamics of processes occurring in the solid state. Quasielastic scattering can give information on molecular motion, hydrogen diffusion, tunnelling states and critical scattering, as well as about spin diffusion. An instrument with back-scattering geometry can be used to obtain a very high resolution and allows the separation of elastic and quasielastic components.

1.3.5 Electron Microscopy

The electron microscope is a versatile tool in the study of the ultrastructure of materials, allowing the identification of known or new phases while simultaneously yielding information on composition. It is usual for electron diffraction and imaging to be employed together in transmission electron microscopy (TEM), which can

produce images of isolated atoms. Since the typical wavelengths of electron beams are about 10^5 times smaller than those of visible radiation, an electron microscope is capable of imaging electronic structures, if wavelength is the only factor in determining the resolving power. In scanning instruments (scanning electron microscopy, SEM) which record signals due to back-scattered electrons or emitted secondary electrons, it is possible to detect extremely small quantities of materials and also map the topography of surfaces of a wide range of materials. These capabilities can be combined and enhanced in a scanning transmission electron microscope (STEM), where the transmission of the electrons through the sample together with the scanning and analytic facilities can be analysed. The information obtained about the specimen involves an analysis of the perturbations suffered by the electrons in their collisions with the atoms (and molecules) in the specimen.

Analytical electron microscopy is the most sophisticated tool available for microstructural analysis today and allows the construction of both the high-resolution structure and elemental composition of a specimen. When a high energy electron beam is incident on a specimen, elastically and inelastically scattered (transmitted) electrons, characteristically emitted X-rays, back scattered electrons and secondary (emitted) electrons are obtained. All these can be collected at the same time in the microscope from a small specimen area in order to carry out analysis of the structure and composition. Elastically scattered electrons can be used to give images and diffraction patterns, and electrons which have lost energy, and emitted X-rays, can give information on composition. Electron energy loss spectroscopy (EELS) can be used to obtain information on the oxidation states of metals and the electronic structures of oxides and other materials.

The most important aspect of electron microscopy in solid state chemistry lies in its ability to elucidate problems which are beyond the capability of X-ray or neutron crystallography. High-resolution electron microscopy (HREM) can show images of the local structure of crystals in remarkable detail, where ultramicrostructures of imperfections are readily observed. It is also a useful

technique for the identification of new phases, even if they only occur in one or two rows or layers as imperfections or as intergrowths in other phases.

1.3.6 Summary

In reality, a combination of techniques is normally necessary to understand a phenomenon or solve a structural problem in solid state chemistry. As the boundaries of solid state chemistry are continually progressing forward, new questions will inevitably arise which will require the improvement of these techniques, or the development of new and better ones, to provide the answers.

The complementary nature of powder X-ray and neutron diffraction has been exploited to probe the structures of a number of crystalline materials in Chapters 4, 5 and 6 of this work. Chapter 4 examines the structural changes in a compound with the pyrochlore structure type on oxygen intercalation. The structural modifications in certain oxygen deficient perovskites and related materials on oxygen intercalation are investigated in Chapter 5. Chapter 6 describes the elucidation of the structures of a number of complex ceramic oxides, while Chapter 7 uses powder X-ray diffraction to analyse two polymer-electrolyte structures.

1.4 Polymer Electrolytes

The polymer electrolytes are one class of materials which have required a combination of some of the most powerful characterisational techniques at the disposal of the solid state chemist in their analysis. They have received a great deal of attention in recent years because of their potential applications in all solid state electrochemical devices such as batteries and electrochromic windows.

The field of polymer electrolytes encompasses two major classes of materials, the polymer-salt complexes and polyelectrolytes. Polymer-salt complexes are ionically conductive solid phases formed by the dissolution of salts by ion-co-ordinating macromolecules. This class of materials was first discovered by Wright and co-workers[10] in 1973, when they reported that alkali-metal salts form crystalline complexes with poly(ethylene oxide) [$(\text{-CH}_2\text{CH}_2\text{O-})_n$, or PEO]. A few years later, Armand, Chabagno and Duclot[11, 12] recognised the potential of these materials in electrochemical devices. After more detailed electrical characterisation, the fundamentals of ion transport in polymers became the focus of much interest.

The study of ionic conduction has traditionally concentrated on liquid solutions of electrolytes in low molecular weight polar solvents. However, there have also been parallel investigations of molten salts and crystalline or vitreous solid electrolytes. More recently, attention has been focused on ion transport in more complex systems such as solvent-containing polyelectrolyte and biological membranes, and doped electronically conducting organic polymers. Unlike polymer-salt complexes, the polyelectrolytes comprise systems where either the cation or the anion is immobilised by chemically bonding one of the ionic charge carrying species to the polymer backbone. The polymer electrolytes are in principle very simple systems, which form an important bridge between the solvent-free ceramic or molten electrolytes and the conventional liquid electrolytes where the ions are solvated by low molecular weight polar molecules which can undergo long range displacement.

Although the polymer electrolytes often exhibit macroscopic mechanical properties which are typical of a solid, a mechanism of short range ionic motion is provided by local liquid-like relaxation processes at the atomic level[13].

In general, a polymer which is capable of strongly co-ordinating cations is necessary for electrolyte formation. Some typical examples are the polyethers [e.g. poly(ethylene oxide)[10], poly(propylene oxide)[12], the amorphous methoxy-linked poly(ethylene oxide)[14] etc.], polyimines[15] and polyesters[16]. Typically the salts which most readily enter into polymer-salt formation contain large singly charged anions. Some of the most studied salts are the lithium and sodium salts of I^-, ClO_4^-, $CF_3SO_3^-$ and AsF_6^-. The factors that influence polymer salt formation can be understood by analysing the relative strength of polymer-salt interaction against the lattice energy of the salt e.g. the highly delocalised charge of $Li[(CF_3SO_2)_2N]$ leads to a high solubility. The lattice energy of the salt must be compensated by the exothermic ion-solvent interactions (primarily cation-solvent) in order for the complexes to form. Many cations including mono-, di- and tripositive ions may be dissolved in co-ordinating polymers. In contrast to the monovalent cations, some di- and trivalent cations are mobile while others are not. This can lead to polymer-salt complexes which are purely anionic conductors. Cation mobility depends upon the lability of the cation-polymer interactions: if these are strong, cation transport is suppressed, in marked contrast to the low molecular weight liquid electrolytes where the solvent is transported with the ion.

Poly(ethylene oxide) has become the most extensively studied host polymer for polymer electrolytes. This polymer in its pure form is chemically and electrochemically stable since it contains only strong, unstrained C-O, C-C and C-H bonds. A wide variety of salts based on alkali-metal, alkaline-earth-metal, transition metal and lanthanide ions are soluble in the pure polymer, often in concentrations exceeding 2 mol dm^{-3}.

Polymer-salt complexes based on PEO are generally formed by one of two methods, thin films may be fabricated by solvent casting, where the solvent is slowly

removed from a homogeneous solution of the polymer and salt. A more rapid technique is to cryogrind appropriate mixtures of polymer and salt and then subject the resulting powder to modest heat treatment.

Polymer-salt systems may be amorphous, crystalline or amorphous-crystalline mixtures depending on the polymer, salt and preparative conditions. Polymer-salt complexes of PEO and some other polymer hosts can have a high degree of crystallinity and these crystalline phases represent well defined stoichiometric polymer-salt complexes. Depending on the composition and temperature these systems also contain the pure polymer or an amorphous phase. The multiphase character of these polymer electrolytes means that they are best described by a phase diagram. However, since the phase changes can be slow due to the slow diffusion of the entangled polymer chains, these diagrams are not as precise as for simple inorganic substances - the term pseudophase diagrams is more appropriate for polymer-salt systems. When crystallisation does occur, it normally takes place by the formation of spherulites, three dimensional structures of crystal fibrils embedded in amorphous material[17]. This intracrystalline phase exists as microdomains at the crystal boundaries and is not in thermodynamic equilibrium. The relative amount and composition of this phase are dependent on crystal-growth kinetics and hence on the method of preparation of the electrolyte. Caution must therefore be exercised when comparing the electrical and other physical properties of multiphase electrolytes formed in different ways or with different thermal histories. Nevertheless, pseudophase diagrams based on thermal, optical microscopic, X-ray and conductivity measurements permit a descriptive approach to understanding the conductivity, stability and mechanical properties of polymer-salt systems.

The crystalline PEO-salt complexes invariably exhibit inferior conductivity to the amorphous complexes above their glass transition temperatures, where segments of the polymer are in rapid motion. This indicates the importance of polymer segmental motion in ion transport. The onset of segmental motion occurs near the glass transition temperature and becomes more rapid as the temperature of the

sample is raised beyond this. The segmental motions are thought to promote ion motion by making and breaking the co-ordination sphere of the solvated ion and by providing free volume into which the ion may diffuse. The indication that polymer segmental motion is necessary for ion transport has focused most of the current research and development on amorphous materials with low glass transition temperatures. Solid polymer electrolytes are presently being considered as replacements for conventional low molecular weight liquid-based systems for practical electrochemical devices such as power sources, smart-windows and displays[18].

Figure 1.4a shows various configurations for extended area polymer electrolyte batteries. Although a conductivity of the order of 10^{-4} S cm^{-1} may be obtained for a number of polymer electrolytes, this is not high enough to be ideal. However, by configuring the electrodes to be very thin, large area elements, the internal resistance of the resultant cell may be brought within an acceptable range. Also, by fabricating the anode and cathode structures in a similar manner, the cells can be operated at relatively low values of current density, while still permitting the battery to operate at practical rates.

Figure 1.4a Various configurations for extended-area polymer electrolyte cells[18].

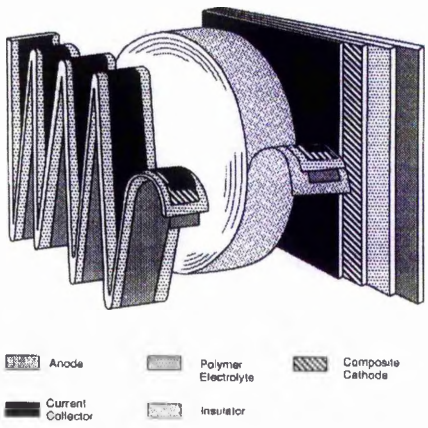

Typical cell dimensions are a 15 - 30 μm thick electrolyte, 25 - 50 μm thick Li electrode and 20-100 μm thick composite cathode.

The polymer electrolyte plays three important roles: it is a lithium ion carrier and can be formed into thin films to improve energy density; it acts as an electrode spacer, which eliminates the need to incorporate an inert porous separator; it is a binder which ensures a good electrical contact between the electrodes. There is therefore no requirement for high temperature operation to obtain liquid electrodes as in the Na - S battery. Also, the flexibility and mechanical strength of the battery means that electrode-electrolyte contact can be maintained at all times through charging and discharging. The replacement of the liquid electrolyte by a plastic material means that no corrosive solvents are present that may react with seals and containers. The absence of gas formation during operation and therefore of any significant vapour pressure, means that the battery can be packaged in low pressure containers. Cells can also be configured in almost any shape because of the flexibility of the materials involved, and because it is an all solid state device, the production process can be highly automated using existing plastic film manufacturing techniques.

Another potential use for polymer electrolytes is as a component in electrochromic devices such as smart windows or displays. Electrochromism may be broadly defined as the phenomenon which gives rise to a reversible colour change, brought about either by the electrochemical insertion and extraction of electrons or ions into inorganic materials e.g. WO_3. The colouration in tungsten oxide is induced by the electrochemical reaction shown in equation 1.4a:

$$xM^+ + WO_3 \rightleftarrows M_xWO_3 \text{ where } M^+ = Li^+, Na^+, H^+ \qquad \text{(Eqn. 1.4a)}$$

where by altering the applied voltage, the transmittance of the system can be varied. Unlike liquid crystal displays, electrochromic materials exhibit open circuit memory,

so that a reverse polarisation is required to restore the colourless state. A schematic diagram of an electrochromic window is shown in Figure 1.4b.

Figure 1.4b Schematic diagram of an electrochromic window[18].

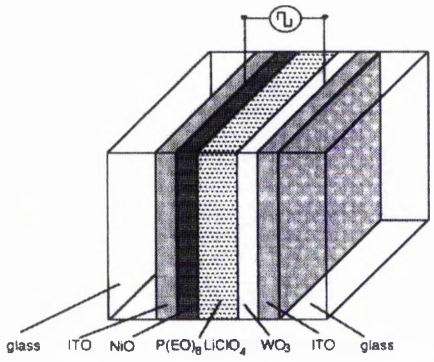

Unlike electrochromic displays which operate in reflectance mode, the entire window is in the optical path and therefore the counter electrode must be optically passive (i.e. colourless) whether in the oxidised or reduced state or electrochromic in a complementary sense to the working electrode. The former mode has been difficult to achieve, but the latter has several advantages. If the working and counter electrodes are complementary electrochromics then there is the potential for lower applied voltages and power consumption to bring about a specific optical density change.

As already discussed, it is the amorphous phases of the polymer electrolytes which exhibit the highest conductivities. However, despite the fact that the crystalline phases are not significantly conducting, they can be studied in far more detail by diffraction techniques than the amorphous phases. The strategy used in Chapter 7 of this work is to start with a knowledge of the crystalline structure and then combine this with spectroscopic studies to provide information on the amorphous phases.

1.5 References

1. R. Roy, *Solid State Ionics*, **32/33**, 3, 1989.

2. "Solid State Chemistry Techniques", Eds. A. K. Cheetham and P. Day, Oxford Science Publications, 24.

3. M. Foglarz, *Chemica Scripta*, **28**, 3-7, 1988.

4. G. C. Farrington and J. L. Briant, *Science*, **204**, 1371, 1979.

5. M. D. Ingram and C. A. Vincent, *Chemistry in Britain*, March, 235, 1984.

6. J. G. Bednorz and K. A. Z. Muller, *Physica*, **B64**, 189, 1986.

7. A. Wattiaux, J. C. Grenier, M. Pouchard and P. Hagenmuller, *J. Electrochem. Soc.*, **134**(7), 1714, 1987.

8. C. N. R. Rao and J. Gopalakrishnan, "New Directions in Solid State Chemistry", Cambridge Solid State Science Series, 1989, 70-106.

9. "Spectroscopic Methods", Eds. D. H. Williams and I. Fleming, McGraw Hill, 63, 1989.

10. D. E. Fenton, J. M. Parker and P. V. Wright, *Polymer*, **14**, 589, 1973.

11. M. B. Armand, J. M. Chabagno and M. Duclot, "Extended Abstracts Second International Conference On Solid Electrolytes", St Andrews, Scotland, 1978.

12. M. B. Armand, J. M. Chabagno and M. Duclot, "Fast Ion Transport in Solids", Eds. P. Vahista, J. N. Mundy and G. K. Shenoy, North-Holland, Amsterdam, 131.

13. P. G. Bruce and C. A. Vincent, *J. Chem. Soc. Faraday Trans.*, **89**(17), 3187, 1993.

14. J. R. Craven, R. H. Mobbs and C. Booth, *Makromol. Chem. Rapid Commun.*, **7**, 81, 1986.

15. C. K. Chiang, G. T. Davis, C. A. Harding and T. Takahashi, *Macromolecules*, **18**, 825, 1985.

16. M. C. Wintersgill, J. J. Fontella, J. P. Calame, S. G. Greenbaum and C. G. Andeen, *J. Electrochem. Soc.*, **121**, 2208, 1984.

17. R. Neat, M. Glasse, R. Linford and A. Hooper, *Solid State Ionics*, **18/19**, 1088, 1986.

18. F. M. Gray, "Solid Polymer Electrolytes", VCH Publishers, 1991, 22.

Chapter 2
Theoretical Considerations

2.1 Introduction

This Chapter aims to examine certain theoretical aspects of the analytical techniques employed in this work. The structural studies reported in the following Chapters involved the analysis of X-ray and neutron diffraction data. Although these techniques were introduced in Section 1.3, the next section on Diffraction Techniques seeks to introduce a more rigorous interpretation of the diffraction process. Subsequent sections examine some of the mathematical techniques used to extract the structural information from the diffraction data.

The calculation of bond valence numbers can yield useful information in the structural analysis of crystalline materials. These calculations can be used to determine the valence state of an element on a particular crystallographic site, and can produce an estimate of the site occupancy if the valence of the element is already known. The theoretical aspects of these empirical calculations are briefly discussed in Section 2.3, and applied in the structural elucidation of two complex ceramic oxides in Chapter 6.

Section 2.4 details the usefulness of cyclic voltammetry in the initial study of an electroactive species in an electrochemical system. This technique is used in Chapters 3 and 5 to characterise two methods of electrochemical oxygen intercalation in widely different systems, the first aqueous based and the second involving molten salts.

Thermal analysis involves the measurement of physical and chemical properties of materials as a function of temperature. Section 2.5 examines two important thermal analysis techniques - thermogravimetric analysis and differential scanning calorimetry. These techniques have been exploited in Chapter 4 to examine the thermal oxidation behaviour of a material with the pyrochlore structure type, and in Chapter 7 to determine the existence of any phase changes in a polymer-salt complex on heating.

2.2 Diffraction Techniques

2.2.1 X-ray Diffraction

X-rays constitute one portion of the electromagnetic spectrum with wavelengths in the range 0.1 to 100 Å, and can be found in the region between ultraviolet and γ-radiation. The interval of wavelengths of particular usefulness in crystallography is 0.4 to 2.5 Å, making X-ray diffraction an ideal structural probe for the atomic level. X-rays are produced when high energy charged particles (e.g. electrons) collide with matter. The loss of kinetic energy on impact is converted to electromagnetic radiation. Conventional laboratory X-ray diffraction experiments involve monochromatic X-rays produced by the bombardment of a metal target by a beam of electrons, produced by thermionic emission, that have been accelerated through an electric field. The incident electron beam is tuned to have sufficient energy to ionise electrons from the K (1s) shell of the target atoms. This process generates core hole vacancies that are immediately filled by electrons from the outer L (2p) or M (3p) shells releasing energy as X-radiation.

The energy of the X-ray released, and therefore its wavelength, depends upon the difference between the energy levels of the two shells of the electron transition. $K_{\alpha 1}$ and $K_{\alpha 2}$ radiation are produced from a L $\rightarrow$ K transition, while $K_{\beta 1}$ and $K_{\beta 2}$ radiation are produced from a M $\rightarrow$ K transition. The close doublets arise for each transition because it can occur from two electronic configurations which differ in energy. The K_{α} transition is more probable than the K_{β} and hence the more intense K_{α} radiation is used in diffraction experiments. The $K_{\alpha 1}$ peak is more intense than the $K_{\alpha 2}$ peak, and so the weaker peak is normally removed from the incident radiation. Moseley's Law gives the relationship between the wavelength of the K_{α} radiation and the atomic number of the target. As the atomic number of the target element increases, the wavelength of the emitted X-rays decreases, enabling X-rays of

of different wavelengths to be produced, e.g. $CuK_{\alpha 1}$ = 1.54051 Å and $MoK_{\alpha 1}$ = 0.70926 Å.

There are two interpretations of X-ray diffraction by a crystal[2]. The more mathematically rigorous model was created by Laue, but Bragg's model is simpler and will be discussed here. Bragg introduced the concept of crystals built of a set of planes which act as semi-transparent mirrors. The diffraction of X-rays by a crystal can then be described in terms of reflections from these lattice planes. A portion of the incident X-rays are reflected off a given plane with the angle of reflection equal to the angle of incidence, with the rest transmitted and reflected by other planes. The reflection of monochromatic X-rays with a wavelength λ from two adjacent lattice planes with a perpendicular interplanar spacing d and angle of incidence θ is shown in Figure 2.2.1a.

Figure 2.2.1a The Derivation of Bragg's Law.

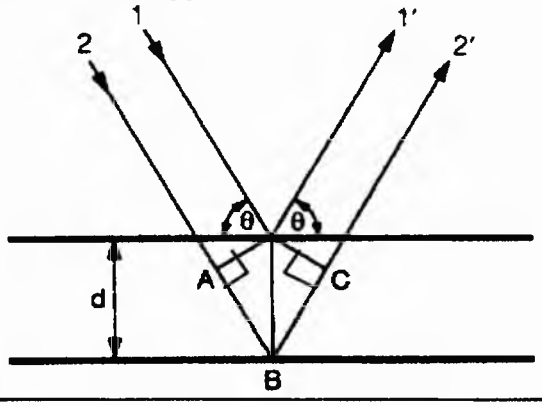

If the deviation of the beam is given by 2θ, and the path difference by 2dsinθ, then for constructive interference (i.e. n is an integer), the Bragg equation is obtained:

$$n\lambda = 2d\sin\theta \qquad \text{(Eqn. 2.2.1a)}$$

Equation 2.2.1a represents the condition that must be fulfilled if diffraction is to take place. At any other angle of incidence, the reflected beams are out of phase and destructive interference occurs. In reality, a crystal will contain many planes and if the incident angle is incorrect by a few tenths of a degree, cancellation of the reflected beams is usually complete. More than one solution for the Bragg Equation is possible, but it is customary to assume n = 1, and so for nth-order scattering a d value of (d/n) is used. In the diffraction experiment, the planes relevant to Bragg's Law are lattice planes which cut the unit cell axes of the crystal into fractional parts. These crystal system planes are uniquely defined by three Miller indices h, k, l.

In powder diffractometry, the sample is composed of a polycrystalline material which in the ideal case contains an infinite number of crystals in every possible orientation. Therefore, for each set of planes, some crystals will be orientated at the Bragg angle given by Equation 2.2.1a for each set of planes, and constructive interference will be observed. In a finely powdered sample, crystals are present in every possible angular position about the incident beam. The resultant diffracted beams therefore appear as cones of radiation (Figure 2.2.1b), rather than a diffraction maximum at a specific position in reciprocal space as in the single crystal case.

Figure 2.2.1b Scattering of X-rays from a polycrystalline sample.

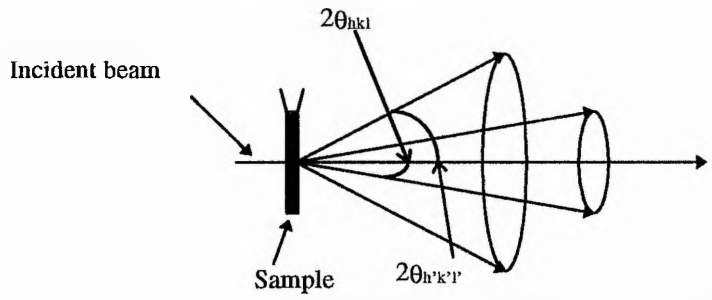

Although the diffraction pattern may be recorded as a series of concentric rings at different 2θ values on an X-ray film, a powder diffractometer may also be used. This method uses a detector to measure the intensity of scattered X-rays as a function of angle, defining each reflection in terms of 2θ and intensity. The simplest detector path is that of a circle centred on the sample in a plane that contains the X-ray beam.

The positions of the maxima in the powder diffractogram can be used to determine the unit cell parameters a, b, c, α, β and γ of the crystal system under consideration. The Bragg angle for a reflection hkl is related to the reciprocal lattice constants (a*, b*, c*, α*, β* and γ*) by the following equation:

$$\frac{1}{d^2} = \frac{4\sin^2\theta}{\lambda^2} = h^2a^{*2} + k^2b^{*2} + l^2c^{*2} + 2hka^*b^*\cos\gamma^* + 2hla^*c^*\cos\beta^* + 2klb^*c^*\cos\alpha^*$$

(Eqn. 2.2.1b)

The lattice parameters can therefore be obtained from this expression. Auto-indexing programs such as VISSER[3] are commonly used on single phase materials. Once the unit cell parameters have been obtained, possible space groups for the crystal can be determined by analysis of the reflection classes for systematic absences.

A number of corrections are necessary before indexed data can be used for atomic structure refinement or solution. The integrated intensity I_H of a reflection is related to the structure factor F_H by Equation 2.2.1c:

$$I_H = k_0 LPET|F_H|^2 \qquad \text{(Eqn. 2.2.1c)}$$

where vectorial index **H** has components (h, k, l) and represents the vector (h**a*** + k**b*** + l**c***) and where L is the Lorentz factor, P is the polarisation factor, E is the extinction coefficient, T is the transmission factor and k_0 a term which takes account of the intensity of the beam and certain universal constants and those for a given diffraction experiment.

The Lorentz factor depends on the diffraction technique used. This term arises because the times required for different reciprocal lattice points to cross the sphere of reflection varies with its position in reciprocal space and the velocity with which it sweeps through the sphere of reflection. This applies to both single crystal and to a greater extent, powder diffraction methods. The polarisation factor depends upon the state of polarisation of the incident beam and on the scattering angle of the diffracted beam. This term arises because the electric vectors parallel and perpendicular to the reflecting plane are scattered by different amounts. These Lorentz and polarisation factors are usually grouped into a single factor and have the overall effect of decreasing the intensity of reflections at intermediate angles when compared with those in the forward and backward directions.

The extinction coefficient is applied because imperfect crystals exhibit a reduced diffracting power either because the lattice is not perfectly regular or the lattice planes first encountered by the primary beam will reflect a large proportion of the primary intensity, causing deeper planes to receive less radiation and so reflect less than would otherwise be the case (secondary extinction). This effect tends to be negligible in well ground powders where multiple reflections occurring from each regular block in the lattice and the shielding of deeper planes is reduced.

The transmission of a sample can be accounted for by the introduction of an absorption coefficient[4]. The intensities of the diffracted rays are affected by absorption which takes place in the sample, and this depends upon the geometry of the diffraction method and the scattering angle θ. As the overall absorption coefficient increases rapidly with atomic number, this correction is normally only made if the phase examined contains heavy atoms.

However, the most significant effect is preferred orientation, which can arise when there is a stronger tendency for the crystallites in the specimen to lie in certain planes than in others, distorting the natural intensity ratios of the reflections. This effect produces systematic distortions of the reflection intensities which can be

modelled mathematically . A preferred orientation parameter can correct this, but this can only be applied to the refinement of a complete structural model.

Individual integrated intensities can be extracted from the X-ray pattern using pattern decomposition methods. The LeBail[5] profile fitting procedure employs a modified Rietveld algorithm (Section 2.2.3) to assign intensities to the powder diffraction profile using the lattice parameters and peak shape function as constraints. No attempt is made to assign correct values to overlapping reflections, rather they are assigned arbitrary values consistent with the observed profile. The pattern decomposition procedure is vital in structure analysis because the success of most structure determinations from powder diffraction data is largely dependent upon the extraction of reliable integrated intensity values. However, uncertainties in the intensity values exist for partially or fully overlapping reflections.

Once integrated intensity values are extracted from the diffractogram, it is necessary to obtain the atomic positions for a complete structural determination. In X-ray diffraction this requires the extraction of the distribution of electron density in the unit cell from the diffraction data. If the structure factors for a complete set of X-ray reflections are known, the electron density ρ at any point (x, y, z) defined by the vector $\boldsymbol{r}$ (xa + yb + zc) in the unit cell can be calculated from Equation 2.2.1d:

$$\rho(\boldsymbol{r}) = \frac{1}{V} \sum_{h,k,l=-\infty}^{+\infty} F_{h,k,l} \exp\left(-2\pi i(hx + ky + lz)\right) \qquad \text{(Eqn. 2.2.1d)}$$

Therefore knowledge of the amplitudes of the scattered waves (in modulus and phase) unequivocally defines $\rho(\boldsymbol{r})$. The structure factor $F_{h,k,l}$ is given by the following equation:

$$F_{h,k,l} = \sum_{j=1}^{N} f_j \exp\left(2\pi i(hx_j + ky_j + lz_j)\right) \qquad \text{(Eqn. 2.2.1e)}$$

where N is the number of atoms in the unit cell and f_j is the scattering power (or form factor) of the j^{th} atom. The structure factor in equation 2.2.1e can also be expressed as a complex quantity with a modulus of $|F_H|$ and phase φ_H:

$$F_H = |F_H|\exp(i\varphi_H) \qquad \text{(Eqn. 2.2.1f)}$$

It is not possible to apply equation 2.2.1f only on the basis of information obtained from X-ray diffraction. According to equation 2.2.1c only the moduli of the structure factor, $|F_H|$, can be obtained from the diffraction intensities because the corresponding phase information is lost. This limitation is known as the phase problem - how to identify the atomic positions starting from only the moduli $|F_H|$. A general solution to this problem has not been found. Therefore, in order to calculate the electron density, the missing phase information must be somehow derived from the data. One route to deriving this missing phase information using Direct Methods is examined in section 2.2.4.

2.2.2 Neutron Diffraction[1]

The neutron is a heavy particle with spin ½ and a magnetic moment of 1.9132 nuclear magnetons. It exhibits wave-like properties and can therefore exhibit diffraction phenomena.

Neutron diffraction experiments require high fluxes which can be provided by modern nuclear reactors. These produce fast neutrons whose energy is reduced by collisions in a moderator of heavy water or graphite. These retarded neutrons are called thermal neutrons with speeds obeying a Maxwell distribution - corresponding to a white spectrum. A monochromator, usually composed of single crystal Ge, Cu, Zn or Pb is used to select the required wavelength.

Neutrons can also be produced in a pulsed manner by a spallation source, at a repetition rate between 24 Hz and 50 Hz. At the ISIS[6] spallation source at the

Rutherford Appleton Laboratories, a linear accelerator is used to inject hydride ions into a synchrotron ring where they are accelerated before being stripped of their electrons to form a beam of high energy protons (≈1 GeV) in short pulses at the appropriate pulse frequency. This proton beam then strikes a target such as tantalum or uranium releasing several tens of neutrons per proton (≈25 neutrons for ^{238}U). The pulsed neutron flux is only present for a very short space of time, lasting around 0.4 μs, which makes heat removal easy allowing higher fluxes than those produced by reactors. The high energy neutrons produced are slowed down to thermal energies by appropriate moderators such as water, polyethylene, liquid hydrogen or liquid methane, with the choice being determined by the scattering experiment. During the thermalisation process neutrons undergo a large number of collisions which cause pulse broadening. The width of the pulse leaving the moderator is roughly proportional to the wavelength so that the fractional wavelength resolution is nearly constant.

High intensities at wavelengths of less than 1 Å are a significant characterisation of pulsed neutron sources. Figure 2.2.2a shows an image of the beam hall at the ISIS pulsed neutron source, the proton beam line can be seen running from the bottom-left corner of the picture to the spallation target in the centre, with the various neutron beam lines radiating out from this towards the experimental stations.

At spallation neutron sources, the pulsed nature of the neutron beam allows discrimination among neutrons of different wavelengths by measuring their time of arrival at the detector (time of flight), this is in contrast to diffraction techniques using monochromatic radiation where the intensities are measured by moving a detector to different scattering angles θ, chosen according to Bragg's Law (Eqn. 2.2.1a) where λ is fixed. At a spallation source, diffraction effects can therefore be measured at a fixed scattering angle θ_0:

$$\lambda = 2d\sin\theta_0 \qquad \text{(Eqn. 2.2.2a)}$$

Figure 2.2.2a An Image of the beam hall of the ISIS pulsed neutron facility[7].

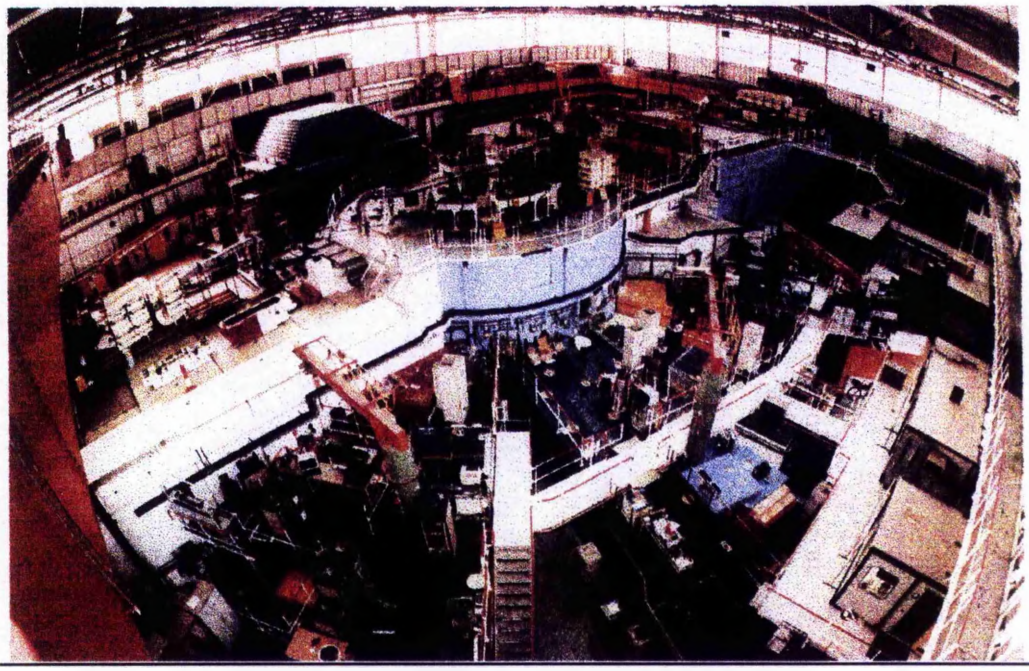

From de Broglie's relation:

$$m_n v = \frac{h}{\lambda} \qquad \text{(Eqn. 2.2.2b)}$$

where m_n and v are the neutron mass (in kg) and velocity (in ms^{-1}) respectively and h is the Planck constant (6.62618×10^{-34} Js), it follows that:

$$m_n v = m_n \frac{L}{t} = \frac{h}{\lambda} \qquad \text{(Eqn. 2.2.2c)}$$

where L is the distance travelled in m and t is the time taken (in s). It then follows that for neutron diffraction at a spallation source:

$$t = \frac{m_n}{h} L\lambda \ = 252.778 L\lambda \qquad \text{(Eqn. 2.2.2d)}$$

where t is in μs, L is the distance from the moderator to the sample to the detector in m and λ, the wavelength and d, the interplanar spacing are both in Å. Substituting the right hand side of equation 2.2.2a for λ:

$$t = 505.555Ld\sin\theta_0 \qquad \text{(Eqn. 2.2.2e)}$$

Thus time of flight depends linearly on both the flight path and the wavelength. From equation 2.2.2d the resolution, $\frac{\Delta d}{d}$ may be derived to be:

$$\frac{\Delta d}{d} = \left[\Delta\theta^2 \cot^2\theta + \frac{\Delta t^2}{t^2} + \frac{\Delta L^2}{L^2}\right]^{\frac{1}{2}} \qquad \text{(Eqn. 2.2.2f)}$$

It is clear from equation 2.2.2f that for a given Δθ, the contribution of the resolution from the angular uncertainties increases as the scattering angle decreases, becoming infinite at $2\theta = 0°$, while it is zero at $2\theta = 180°$. Figure 2.2.2b shows a schematic of the POLARIS instrument at the ISIS pulsed neutron source which was used in the collection of neutron powder diffraction data for the experiments discussed in Chapters 4, 5 and 6.

The backscattering detectors from which the data was analysed ("C-bank" comprising 38 ^{3}He detectors) are arranged in a straight line inclined to the scattered neutron beam and all intersecting approximately the same fraction of the diffraction cones to give a constant resolution and line shape across the bank. At large scattering angles the contribution of the $\Delta\theta\cot\theta$ term angular term is small and the C bank resolution is dominated by time uncertainties.

As mentioned in Section 1.3.4, the neutron-atom interaction comprises the interaction between the neutron and the nucleus and the interaction between the magnetic moment associated with the spin of the neutron and the magnetic moment of the atom. The neutron-nucleus interaction is governed by very short-range nuclear

forces (in the region of 10^{-13} cm). Since the nuclear radius is several orders of magnitude less than the wavelength associated with the incident neutrons (of the order of 10^{-15} cm), the nucleus will behave like a point and its point scattering factor, b_0, will be isotopic and therefore not dependent on $\sin(\theta/\lambda)$ as described in section 2.2.1 for X-rays. There is therefore no decrease in scattering power for neutrons with increasing $\sin(\theta/\lambda)$.

Figure 2.2.2b Schematic layout of the POLARIS diffractometer[6].

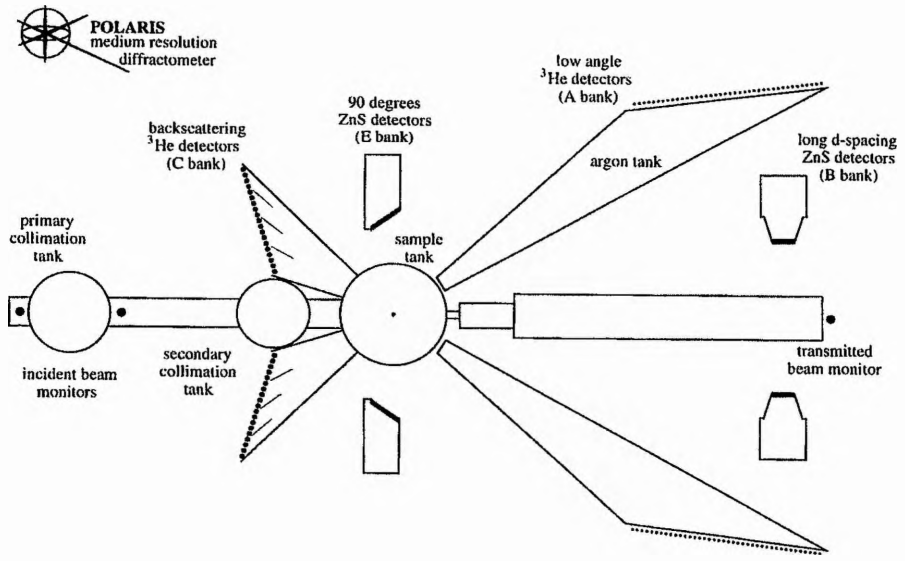

Thus reflections with high values of $\sin(\theta/\lambda)$ can be collected giving atomic positions and thermal parameters with higher accuracy than from X-rays. By convention, the scattering amplitude is assumed positive where there is a phase change of 180° between the incident and scattered waves - it has the dimension of length and is measured in cm^{-12}. When the neutron is very close to the nucleus, a metastable system (neutron + nucleus) is created which decays by a re-emission of the neutron. For appropriate energy a resonance effect can occur, giving a scattering factor of the form:

$$b = b_0 - \Delta b' \qquad \text{(Eqn. 2.2.2g)}$$

Since $\Delta b'$, the resonance contribution to the scattering factor, can be greater than b_0, it is possible to have negative scattering factors for some nuclei, for which the scattering is 180° out of phase with respect to the nuclei with b>0. A few nuclei also present an imaginary wavelength-dependent term $\Delta b''$, which can lead to anomalous scattering, but this effect was not encountered in this work.

The angular momentum of the nucleus is another factor which influences the capacity of scattering. If I is the angular momentum, then it can be combined with the neutron spin in a parallel or in an antiparallel fashion yielding the total spin of either $J = I + ½$ or $J = I - ½$, and corresponding scattering factors of either b_+ or b_-. According to quantum mechanics, there are $2J + 1$ orientations in space compatible with one spin of value J. The compound nucleus will then have $2(2I + 1)$ possible states. One fraction of these, $w_+ = \frac{(I+1)}{(2I+1)}$ corresponds to states of parallel spins while the other one, $w_- = \frac{I}{(2I+1)}$, corresponds to states of antiparallel spins. In conclusion, a single isotope with I>0 can be described as a random mixture of nuclei with atomic fractions w_+ and w_- and scattering amplitudes b_+ and b_-. The coherent scattered amplitude is therefore given by:

$$b = w_+b_+ + w_-b_- \qquad \text{(Eqn. 2.2.2h)}$$

Incoherent scattering will also occur with the square amplitude given by: $[(w_+b_+^2 + w_-b_-^2) - (w_+b_+ + w_-b_-)^2]$ which contributes to a uniform background with no diffraction effects. This is particularly important for hydrogen, where most of the scattering is incoherent background.

In general, one chemical element exists in a crystal structure in different isotopic forms which are randomly distributed over the sites occupied by the element. The scattering factor of the element will be a weighted average over the various spin

various spin states of every isotope and over the various isotopes. This disorder generates a pervasive coherent and incoherent background in the diffraction spectrum. If w_n is the relative abundance of the n^{th} isotope then the effective scattering factor will be:

$$b = \Sigma w_n b_n \qquad \text{(Eqn. 2.2.2i)}$$

and the total diffuse background scattered intensity will be $\sum_n w_n b_n^2 - b^2$.

Atoms which posses a magnetic moment because of the presence of unpaired electrons interact with the magnetic moment of the neutron giving additional neutron scattering. Interaction occurs in a finite domain around the nucleus and magnetic scattering will decline with $\sin(\theta/\lambda)$. In the case of identical atoms with spins parallel (ferromagnetic materials) and antiparallel (antiferromagnetic materials) the magnetic scattering amplitude of each atom is given by:

$$p = \frac{e^2 \gamma S f_{mag}}{m_e c^2} \qquad \text{(Eqn. 2.2.2j)}$$

where γ is the neutron magnetic moment in nuclear magnetons, e and m_e are the charge and mass of the electron, c is the velocity of light, S the electron spin quantum of the scattering atom and f_{mag} the atomic scattering form factor given by the Fourier transform of the distribution of electrons having unpaired spin and normalised so that $f_{mag} = 1$ for $\theta = 0°$. Equation 2.2.2j reduces to $\approx 0.54 S f_{mag}$ (10^{-12} cm), which is of the same order as nuclear scattering.

Nuclear and magnetic scattering are additive for unpolarised neutron beams:

$$|F|^2 = |F_{nucl}|^2 + \sin^2\alpha |F_{mag}|^2 \qquad \text{(Eqn. 2.2.2k)}$$

where F is the structure factor, F_{nucl} is the nuclear structure factor and F_{mag} the magnetic structure factor, where α is the angle between the unit vector in the

direction of the spin orientation in the sample and the lattice vector of ha* + kb* + lc*. For a sample containing a single magnetic domain $\sin^2\alpha$ is equal for all atoms. For a multidomain sample it is necessary to average over the various spin orientations. Measurements of ferromagnetic and antiferromagnetic structures in external fields can orientate the spins so $\sin^2\alpha = 0$ or 1. Measurements of $|F|^2$ can then be used to separate magnetic and nuclear scattering and allow the study of magnetic structures. In some cases the magnetic cell coincides with the 'chemical' cell so that the magnetic distribution of intensities is added to the nuclear contribution. In other cases the magnetic structure may have a cell which is a multiple of the 'chemical' cell causing additional purely magnetic reflections.

Monochromatic beams of polarised neutrons are easily obtained from unpolarised beams by the use of a single-crystal monochromator e.g. Co-Fe alloy. For a given polarisation, either constructive or destructive interference occurs between nuclear and magnetic scattering amplitudes. Thus this technique may detect weak magnetic scattering even if it is accompanied by strong nuclear scattering.

A further effect is that the neutron form factors are not a simple function of atomic number. Even isotopes of the same element may have very different scattering factors. This allows atoms with very close values of Z but very different values of b to be distinguished. Light atoms can make a substantial contribution to the neutron diffraction pattern. Thus, refinement using neutron diffraction can lead to higher precision in the location of light atoms (See Chapters 4 and 6).

2.2.3 The Rietveld Method[8]

The Rietveld method has vastly improved the ease of structure refinement from X-ray and neutron powder diffraction data since its creation in 1969. The powder diffraction pattern is first collected in a step scan mode so that intensity is measured for a given interval of time at two-theta, and then stepped to the next position. Once the powder pattern has been indexed, appropriate Miller indices are associated with observed

observed reflections and simultaneously accurate unit cell dimensions are calculated. A space group can then be determined from the examination of possible systematic absences.

If even an imperfect structural model is available then the intensity y_{io} observed at the i^{th} step may be compared with the corresponding intensity y_{ic} calculated from the model. The model is then refined by minimising by a least squares process the residual, S, given by:

$$S = \Sigma w_i |y_{io} - y_{ic}|^2 \qquad \text{(Eqn. 2.2.3a)}$$

where w_i is a weight derived from the standard deviations associated with the peak and background, y_{ib}.

The term y_{ic} is the sum of the contributions from neighbouring Bragg reflections and from the background intensity:

$$y_{ic} = y_{ib} + s\sum_{h,k,l} m_{h,k,l} L_{h,k,l} |F_{h,k,l}|^2 G(\Delta\theta_{ik}) \qquad \text{(Eqn. 2.2.3b)}$$

where s is the scale factor, $L_{h,k,l}$ is the Lorentz-polarisation factor for a reflection (h, k, l), $F_{h,k,l}$ is the structure factor , $m_{h,k,l}$ is the multiplicity factor and $G(\Delta\theta)_{ik}$ is the profile function containing a zero-point correction.

The refinement process includes the adjustment of a number of parameters: a scale factor for each phase; the lattice parameters; the atomic positional co-ordinates; the atomic site occupancies; the atom isotropic thermal parameters; the background function; the zero-point; the profile parameters; the preferred orientation correction and the absorption coefficients.

The determination of an accurate model for the profile function $G(\Delta\theta)_{ik}$ is one of the fundamental problems in Rietveld analysis. The shape of a diffraction peak depends on both instrumental features, e.g. the radiation source, beam characteristics

characteristics and detector system, and specimen effects e.g. absorption and broadening of the reflection profiles. There are therefore many choices of analytical peak shape functions available in peak shape refinement programs. The most widely used peak profile function in the treatment of X-ray diffraction data is the pseudo-Voigt function[9]. This involves the flexible variation of two common profiles - the broad Gaussian and narrow Lorentzian peak shapes - by the refinement of a mixing parameter η in which determines the degree of Gaussian (G) and Lorentzian (L) shapes to fit the observed profile. The pseudo-Voigt function is defined as a linear combination of Lorentzian and Gaussian shapes:

$$G(\Delta\theta)_{ik} = \eta L + (1-\eta)G \qquad \text{(Eqn. 2.2.3c)}$$

where $L = \frac{\eta C_1^{\frac{1}{2}}}{\pi H_k}\left(1+C_1 X_{ik}^2\right)^{-1}$ and $G = \frac{C_0^{\frac{1}{2}}}{\sqrt{\pi} H_k}\exp\left(-C_0 X_{ik}^2\right)$, with C_0=4ln2, C_1=4, $X_{ik} = \frac{\Delta\theta_{ik}}{H_k}$ and H_k is the full-width at half-maximum of the k^{th} Bragg reflection.

The background intensity, y_{ib}, is mainly due to diffuse scattering, incoherent scattering and electronic noise in the detector system. An accurate background can be obtained by linear interpolation between points in the powder diffraction pattern where there are no peaks, or by the refinement of the coefficients of a power series in 2θ:

$$y_{ib} = \sum_n b_n 2\theta_i^n \qquad \text{(Eqn. 2.2.3d)}$$

where the b_n terms are refinable parameters.

The success of the Rietveld refinement procedure requires a large degree of similarity between the initial structural model and the correct crystal structure. If the structural model is very different from the true structure then the refinement may fail by increasing parameter shifts. The introduction of 'soft' restraints can help to

stabilise the refinement by acting as supplementary observations. These are normally imposed on certain parameters in order to permit only realistic deviations of their values from chemically sensible ones. In chapter 7, soft constraints are used to set the interatomic distances and angles in the structural models used to values of related materials of known geometry. These values are then allowed to vary within set deviations during the refinement.

In order to chart the progress of the refinement a number of indicators are used, the two most common are the weighted profile index R_{wp} (Eqn. 2.2.3e) and the reduced χ^2 (Eqn. 2.2.3f). These terms are the most meaningful because they have the quantity S (Eqn. 2.2.3a) as their numerator.

$$R_{wp} = \sqrt{\frac{S}{\sum w_i Y_{ic}^2}} \qquad \text{(Eqn. 2.2.3e)}$$

$$\chi^2 = \frac{S}{(N-P)} \qquad \text{(Eqn. 2.2.3f)}$$

where N and P are the number of profile points and refined parameters respectively. The weighted profile value decreases as the fit improves and the reduced χ^2 should approach 1.

If a refinement has been successful, a chemically sensible result should be obtained where all the bond lengths and angles are within acceptable limits and the plotted profile fit between the observed and calculated intensities is good.

2.2.4 Direct Methods and Difference Fourier Analysis

The goal of a structural analysis by X-ray diffraction is to obtain the distribution of atomic electron density in the unit cell (from which the atomic positions may be derived) starting from the diffraction data. As discussed in section 2.2.1, it is not possible to reach this goal in a unique and automatic way, because only the

magnitudes, and not the phases of the structure factors may be obtained from experimental data. Therefore, in order to compute the electron density by means of equation 2.2.1d, the missing information must somehow be derived. The term direct methods is used in relation to those techniques which seek to derive the structure factor phases directly from the observed amplitudes through mathematical relationships.

A number of important results useful in the direct methods process are derivable from a statistical analysis of the observed intensities. Such a statistical analysis of observed structure factor moduli can give useful indications as to the presence or absence of those symmetry elements which do not give rise to systematic absences. It also allows an estimation of both the scale factor and the temperature factor and is a basic step in the calculation of unitary and normalised structure factors.

Equation 2.2.1e shows that the amplitude of the structure factor depends upon the scattering powers of the atoms in the structure. The X-rays that are scattered by an atom are the resultant of the waves scattered by each electron in an atom. The scattering power of an atom is therefore proportional to the number of electrons in the atom, or less rigorously, the atomic number Z. This means that in structure determinations from X-ray powder diffraction data, light atoms such as lithium are difficult to locate because of their low scattering power (See Chapter 6). The scattering power of each atom is also a function of $\sin(\theta/\lambda)$, a consequence of the finite size of the atom regarded as a scattering source. At $\sin(\theta/\lambda) = 0$, the scattering factor is equal to the total number of electrons in the atom. This quantity decreases with increasing 2θ, because X-rays scattered from one part of an atom are increasingly out of phase with those scattered from another part of the electron cloud. This is the main reason why there are only weak reflections at high angles in the X-ray powder diffractogram.

The decrease of $|F_H|$ with increasing 2θ can be overcome by using structure factors which correspond to idealised point atom structures and are hence

independent of scattering angle[10]. The unitary structure factor is given in equation 2.2.4a:

$$|U_H| = \frac{|F_H|}{\sum_{j=1}^{N} f_j} \qquad \text{(Eqn. 2.2.4a)}$$

This expression has the same phase as $|F_H|$ but an absolute value which ranges from 0 to 1. The equation takes the value 1 when all the atoms scatter in phase. The normalised structure factor is given in equation 2.2.4b.

$$|E_H| = \frac{|F_H|}{\sqrt{\varepsilon \sum_{j=1}^{N} f_j^2}} \qquad \text{(Eqn. 2.2.4b)}$$

where ε is an integer depending on the symmetry class of reflections under consideration. The distribution of $|E_H|$ values is independent of the size and content of the unit cell, but does depend on the presence or absence of a centre of symmetry.

The unitary and the normalised structure factor are useful quantities used in the direct methods based approaches of structure solution. These techniques have allowed the routine solution of structures from single crystal data. However the process is much more complex for powder diffraction data, where there may be a high degree of peak overlap, leading to problems in the assignment of intensities to the reflections which comprise the overlapping peaks.

In general the phase and amplitude of a wave are independent quantities, however it is possible to relate these two quantities in the case of X-ray diffraction if two important quantities of the electron density function are considered:

1) the electron density function should be positive at all values for a given set of amplitudes ($\rho(\boldsymbol{r}) \geq 0$).

2) the electron density function should be composed of discrete atoms.

The first mathematical relationships capable of giving phase information were obtained in the form of inequalities. These were then expanded to establish the basic concepts and the probabilistic foundations of direct methods.

Sayre, using the atomicity condition (2) was able to derive the relation shown in equation 2.2.4c by considering that for a structure formed by well resolved and almost equal atoms, the two functions $\rho(r)$ and $\rho^2(r)$ are quite similar and show maxima in the same positions.

$$F_{\mathbf{H}} = \frac{\theta_{\mathbf{H}}}{V} \sum_{\mathbf{K}} F_{\mathbf{K}} F_{\mathbf{H-K}} \qquad \text{(Eqn. 2.2.4c)}$$

where $\theta_{\mathbf{H}}$ is a scaling term derived from the atomic scattering factor. Equation 2.2.4c is valid for both centrosymmetric and non-centrosymmetric structures and implies that the structure factor $F_{\mathbf{H}}$ can be determined by the products of all the pairs of structure factors whose indices add to give **H**. Multiplying both sides of this equation by $F_{-\mathbf{H}}$, the following equation is obtained:

$$|F_{\mathbf{H}}|^2 = \frac{\theta_{\mathbf{H}}}{V} \sum_{\mathbf{K}} |F_{\mathbf{H}} F_{\mathbf{K}} F_{\mathbf{H-K}}| \exp\left[i(\varphi_{-\mathbf{H}} + \varphi_{\mathbf{K}} + \varphi_{\mathbf{H-K}})\right] \qquad \text{(Eqn. 2.2.4d)}$$

For large values of $|F_{\mathbf{H}}|$ the left-hand side of equation 2.2.4d will be large, real and positive. It is therefore likely that the largest terms in the sum on the right will also be real and positive. It follows that, if $|F_{\mathbf{H}}|$ and $|F_{\mathbf{K-H}}|$ also have large values:

$$\Phi_{\mathbf{HK}} = \phi_{\mathbf{H}} + \phi_{\mathbf{K}} + \phi_{\mathbf{H-K}} \qquad \text{(Eqn. 2.2.4e)}$$

which for centrosymmetric structures becomes:

$$S_{\mathbf{H}} S_{\mathbf{K}} S_{\mathbf{H-K}} \approx +1 \qquad \text{(Eqn. 2.2.4f)}$$

where S_H stands for the sign of reflection F_H of reflection **H**, and has a value of +1 or –1 corresponding to phases 0 and π respectively and the symbol ≈ means 'probably equal'. The relations shown by equations 2.2.4e and 2.2.4f are expressed in a probabilistic form and indicate the necessity of applying probability methods to estimate their reliability. The unitary, U_H, and normalised, E_H, structure factors discussed above can be used to strengthen and simplify the resulting equations.

The use of probability techniques like these to obtain relationships between phases and magnitudes has proved to be the most important approach for the practical use of direct methods.

Once a number of potential atomic co-ordinates for atoms have been obtained by direct methods, a convenient way of completing and refining a structural model is by the difference Fourier synthesis method. A Fourier series having as coefficients $|F_h^c|$, is shown in equation 2.2.4f (this corresponds to equation 2.2.1d).

$$\rho_c(\boldsymbol{r}) = \frac{1}{V}\sum_{\boldsymbol{h}} F_{\boldsymbol{h}}^c \exp(-2\pi i \boldsymbol{h}.\boldsymbol{r}) \qquad \text{(Eqn. 2.2.4f)}$$

where $\boldsymbol{h}.\boldsymbol{r} = hx + ky + lz$ ($\boldsymbol{r} = x\mathbf{a} + y\mathbf{b} + z\mathbf{c}$, $\boldsymbol{h} = h\mathbf{a}^* + k\mathbf{b}^* + l\mathbf{c}^*$ where **a**, **b**, **c** and **a***, **b***, **c*** represent the real and reciprocal lattices respectively). Equation 2.2.4f will show maxima at the positions of the atoms given in the model, whereas a series with coefficients $F_{\boldsymbol{h}}^o = |F_{\boldsymbol{h}}^o| \exp(i\varphi_{\boldsymbol{h}}^o)$:

$$\rho_o(\boldsymbol{r}) = \frac{1}{V}\sum_{\boldsymbol{h}} F_{\boldsymbol{h}}^o \exp(-2\pi i \boldsymbol{h}.\boldsymbol{r}) \qquad \text{(Eqn. 2.2.4g)}$$

represents the true structure. In order to determine the deviation of the initial model from the real structure, the difference series shown in equation 2.2.4h should be computed.

$$\Delta\rho(\boldsymbol{r}) = \rho_o(\boldsymbol{r}) - \rho_c(\boldsymbol{r}) = \frac{1}{V}\sum_{\boldsymbol{h}} \left(F_{\boldsymbol{h}}^o - F_{\boldsymbol{h}}^c\right) \exp(-2\pi i \boldsymbol{h}.\boldsymbol{r}) \qquad \text{(Eqn. 2.2.4h)}$$

Unfortunately, the values of φ_h^o are not known and it is assumed $\varphi_h^o \approx \varphi_h^c$, an approximation which will improve as the initial model gets better. Equation 2.2.4h then becomes:

$$\Delta\rho(\boldsymbol{r}) = \frac{1}{V}\sum_{\boldsymbol{h}}\left(\left|F_h^o\right| - \left|F_h^c\right|\right)\exp\left(-2\pi i\boldsymbol{h}.\boldsymbol{r} + i\varphi_h^c\right) \qquad \text{(Eqn. 2.2.4i)}$$

If in the model an atom is missing, then $\rho_c(\boldsymbol{r})$ will be zero at the corresponding position, while $\rho_o(\boldsymbol{r})$ will show a maximum. The difference synthesis will also show a peak at the same position, the opposite of this will also be true, so if an atom is incorrectly placed a minimum will be observed. The difference synthesis will be almost zero at the positions where the model is correct i.e. $\rho_o(\boldsymbol{r}) \approx \rho_c(\boldsymbol{r})$.

An important property of the difference syntheses is that they are almost unaffected by series truncation errors. The limited number of observations will mean that the Fourier maps will show ripples around each peak, the size of which increases with increasing peak height. As a consequence a light atom close to a heavy atom may be obscured by its ripples. Since the number of terms in the two Fourier series is the same, the truncation errors will also approximately be the same and will cancel out in the difference Fourier synthesis.

This procedure is limited by a large number of overlapping reflections (e.g. powder data) because the individual intensity values will be uncertain. However it is still possible to obtain a structure solution using this method if a good starting model is chosen.

2.3 Bond Valence Calculations[11]

2.3.1 Introduction

The concept of bond valence is widely applicable in solid state chemistry. It has developed from the concept of bond number first introduced by Pauling[12] in 1947. The concept derives its usefullnes because to a good degree of accuracy, the length of a bond is a unique function of bond valence. It can therefore provide a powerful method for the prediction and interpretation of bond lengths in crystals.

2.3.2 The Bond Valence Calculation

The valence, v_{ij} of a bond between two atoms i and j is defined so that the sum of all the valences from a given atom i with valence V_i obeys:

$$\sum_j v_{ij} = V_i \qquad \text{(Eqn. 2.3.2a)}$$

The most commonly adopted empirical expression for the variation of the length d_{ij} of a bond with valence is:

$$v_{ij} = \exp\left[\frac{\left(R_{ij} - d_{ij}\right)}{b}\right] \qquad \text{(Eqn. 2.3.2b)}$$

where b is commonly taken to be a 'universal' constant equal to 0.37 Å.

Equations 2.3.2a and 2.3.2b serve as a basis for determining the parameters R_{ij} for bonds between pairs of atoms in observed crystal structures. R_{ij} is normally referred to as the bond valence parameter. These parameters can be used in

crystallography to predict bond lengths for a given bond valence and the bond-valence sums at atoms can be used to check on the reliability of a determined structure. The bond-valence method of calculating a bond length is clearly superior to using the sums of radii in most instances. Approximate bond-valence parameters can also be useful in deciding if there is a significant bonding interaction between pairs of atoms, as well as in computer programs for determining co-ordination number[13].

Bond-valence parameters have now been developed for many chalcogenides and halides by the critical examination of over 1000 structures from a number of sources such as the journal *Acta Cryst.* and various handbooks containing crystal structures. However, crystal structures containing disorder or partial site occupancy, and those compounds with ambiguous valences were necessarily excluded.

For a structure where a central atom is bound to only atoms of the same kind, R_{ij} can be determined by rearranging equation 2.3.2b:

$$R_{ij} = b \ln \frac{V_i}{\sum_j \exp\left(\frac{-d_{ij}}{b}\right)} \qquad \text{(Eqn. 2.3.2c)}$$

Brese and O'Keeffe have evaluated this expression using a constant value of b = 0.37 Å. The accuracy of a calculated bond length is ±0.2 Å, although it may be higher for many oxides and fluorides. It was found that although atoms were initially distinguished on oxidation state, that for many bonds to oxygen the bond-valence parameter did not depend strongly on oxidation state. However, the bond-valence parameters for some atoms such as Cu, Ag and Au do depend significantly on oxidation state and so there is a R_{ij} value for each oxidation state. Data has now been collected on bonds from cations from the alkali-metals, alikali-earth metals, Transition metals, Lanthanides and Actinides for the anions of - H, F, Cl, Br, I, O, S, Se, Te, N, P and As (As was also considered as an anion).

The hypothesis that bond lengths can be expressed as a sum of radii (which may be specific to a given co-ordination number) implies that the difference between bond lengths for a given atom with a given co-ordination number will be a constant. This means that by rearranging equation 2.3.2b:

$$d_{ij} = R_{ij} - b\ln(v_{ij}) \qquad \text{(Eqn. 2.3.2d)}$$

The same hypothesis holds for bond-valence i.e. the difference between bond lengths from a given atom with a given bond valence is constant. This strong linear correlation of bond-valence parameters for bonds from the same cation to different anions suggests that bond-valence parameters which are not readily available could be obtained by linear interpolation. This means that the assumption that there is a linear relationship between R_{ij} and R_{ik} was found to be correct, so that:

$$R_{ij} = a_{jk} + b_{jk}R_{ik} \qquad \text{(Eqn. 2.3.2e)}$$

For example when j = N and k = O, a_{jk} = –0.027 and b_{jk} = 1.090, equation 2.3.2e allows the calculation of bond-valence parameters between an atom i and nitrogen from the bond-valence parameter of the atom i and oxygen. The result of this is that a set of equations relating bond-valence parameters for bonds from cations to pairs of the 12 anions allowing the prediction of bond-valence parameters which are not readily obtainable.

2.3.3 Conclusions

A number of tables containing bond-valence parameters have now been published in the literature[11, 13]. These can now be used effectively to relate bond valences and bond lengths for a large number of bonds. This model was used to calculate the bond valences discussed in sections 6.2 and 6.3.

2.4 Cyclic Voltammetry[14]

2.4.1 Introduction

Cyclic voltammetry is one of the most powerful techniques that can be used during the initial study of an electroactive species in an electrochemical system. Many experiments can be carried out within a short time period, and the output data are presented in a format which allows rapid, qualitative interpretation, giving information on the redox behaviour of the system including the potentials at which processes occur, the presence of coupled reactions and the existance of any adsorption processes. Other more quantitative results, such as kinetic information, may also be extracted from the data.

2.4.2 The Cyclic Voltammetry Experiment

In a cyclic voltammetry experiment, the potential of the working electrode (relative to the reference) is scanned linearly from one potential to another and the current response is monitored. After examining the potential range where one or more electrode reactions takes place, the scan is reversed and the redox behaviour of the intermediates or products formed in the forward scan can be investigated. This reverse scan determines if the product of the electron transfer is stable and if the reaction intermediate or final product is electroactive.

This cycle can be performed singly or repeatedly at a variety of scan rates (ν), to produce a triangular waveform function. The current is monitored as a function of potential to produce a cyclic voltammogram (CV). In conventional experiments scan rates range form mVs^{-1} up to Vs^{-1}. Rates up to several thousand Vs^{-1} have been used but such high values introduce considerable experimental difficulties. A schematic of the potential - time waveform used in this type of experiment is shown in Figure

2.4.2a. The potential is swept linearly between E_1 and E_2 at a known sweep rate, v. The sweep is then reversed (usually at the same scan rate) and on reaching the initial potential E_1 the sweep may be halted, reversed again, or continued further to a value E_3. The difference between first and subsequent voltammograms frequently provides useful mechanistic information, but kinetic data can only be accurately obtained from the first sweep.

Figure 2.4.2a The potential - time profile used in cyclic voltammetry.

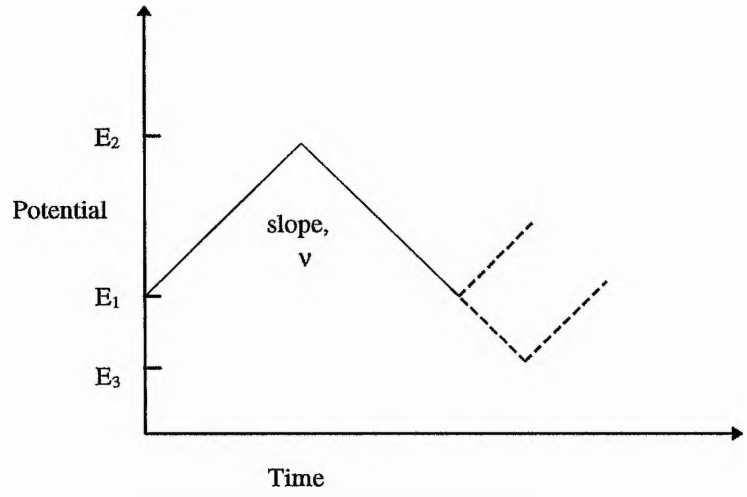

It is conventional to plot the CV as a current - potential response, however it could also be presented as a current - time response because the potential is varied as a linear function of time.

2.4.3 Reversible Reactions

A reversible CV is only observed if the kinetics of the electron transfer process are fast compared to the rate of mass transport.

For the oxidation process shown in equation 2.4.3a involving two species O and R, which are both stable in solution:

$$R \rightleftarrows O + ne^- \qquad \text{(Eqn. 2.4.3a)}$$

under steady-state conditions, the concentrations of species above a certain distance from the electrode are maintained uniform by natural convection. Within the region next to the electrode, known as the Nernst diffusion layer, the concentration gradients are essentially linear. The ratio of concentrations of O and R for a reversible reaction are given by the Nernst equation:

$$\left(\frac{c_O^\sigma}{c_R^\sigma}\right) = \exp\left[\frac{nF}{RT}\left(E - E_e^\circ\right)\right] \qquad \text{(Eqn. 2.4.3b)}$$

Where E_e° is the standard reduction potential and c_O^σ and c_R^σ are the concentrations of O and R at the electrode surface respectively. F is the Faraday constant, R the gas constant and T the temperature.

The cathodic peak in the CV results from the competition between the rate of mass transport of species to the electrode and the rate of the electron transfer reaction. It can be seen from equation 2.4.3b that as the potential is made more negative, the surface concentration of the reactant must be progressively decreased. The region close to the working electrode therefore becomes depleted in O as it is swept to more negative potentials and a concentration gradient increases. The net current density at the electrode can be obtained from Fick's First Law:

$$I = -nFD_O\left(\frac{\partial c_O(x)}{\partial x}\right)_{x=0} \qquad \text{(Eqn. 2.4.3c)}$$

where I is the current density, n is the number of electrons involved in the reduction, F is Faraday's constant, x is the distance from the electrode surface, c_O is the concentration of O and D_O is the diffusion coefficient of O. It can be seen from equation 2.4.3c that as the concentration gradient increases, the current also increases. Eventually the current will reach a plateau value when the concentration of O at the electrode approaches zero and the concentration profile cannot change any further. At this stage the concentration gradient will start to decrease due to the relaxation effect of diffusion, and therefore the current will also fall i.e the current becomes diffusion controlled ($I \propto t^{-0.5}$) and independent of the applied potential.

As the sweep is reversed, reduction continues until the potential becomes sufficiently positive to cause the oxidation of R. The magnitude of the anodic current will increase until the surface becomes depleted in R and the current becomes diffusion controlled, resulting in the anodic peak. Figure 2.4.3a shows a cyclic voltammogram for a reversible process.

Figure 2.4.3a Cyclic voltammogram for the reversible process $O + ne^- \rightleftarrows R$.
At t = 0, only O present in solution.

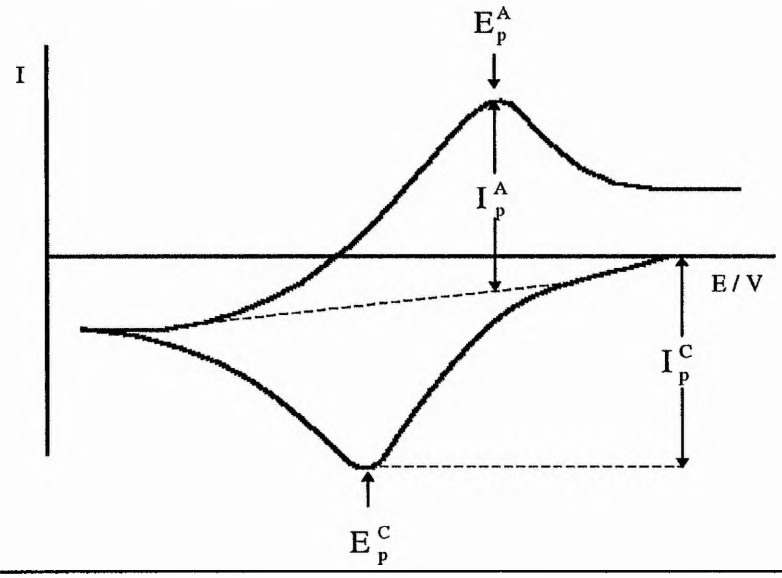

In order to determine mathematically the exact form of the CV it is necessary to solve Fick's Second Law for O and R, subject to the boundary conditions for the experiment. For planar diffusion the Randles-Sevcik equation results:

$$\left|I_p\right| = 0.4463nF\left(\frac{nF}{RT}\right)^{\frac{1}{2}} c_O^{\infty} D^{\frac{1}{2}} v^{\frac{1}{2}} \qquad \text{(Eqn. 2.4.3d)}$$

Where I_p is the peak current density, c_O^{∞} is the bulk concentration of O and v is the scan rate. It can be seen from the equation that a plot of I_p as a function of $v^{0.5}$ is linear and will pass through the origin for a reversible reaction and that the difference in the maxima of the anodic and cathodic peaks is $\Delta E_p = E_p^A - E_p^C = \frac{59}{n}$ mV.

2.4.4 Irreversible Reactions

An irreversible system occurs when the rate of the electron transfer at all potentials is insufficient to maintain the surface equilibrium at the electrode. The Nernst equation will therefore not hold and the shape of the CV will change when compared with a reversible reaction.

The exact form of the CV for a completely irreversible reaction may be obtained by solution of Fick's Second Law subject to the new boundary conditions. Delahey[15] obtained the following for peak current density:

$$\left|I_p\right| = 0.282\frac{\pi^{\frac{1}{2}} F^{\frac{3}{2}}}{(RT)^{\frac{1}{2}}} n(\alpha_c n_\alpha)^{\frac{1}{2}} c_O^{\infty} D_O^{\frac{1}{2}} v^{\frac{1}{2}} \qquad \text{(Eqn. 2.4.4a)}$$

where n_α is the number of electrons transferred up to and including the rate determining step, and α_C is the transfer coefficient for the cathodic process. The peak

current density is thus proportional to the concentration and to the square root of the sweep rate and the square root of the transfer coefficient.

There is no reverse peak in a totally irreversible system. However, the absence of such a peak in a CV does not necessarily imply an irreversible process but may be due to a fast chemical reaction following electron transfer. In the reversible case the value of the cathodic peak potential, E_p^c is independent of the sweep rate, while it is found to vary with the sweep rate for an irreversible reaction:

$$E_p^c = K - \frac{2.3RT}{2\alpha_c n_\alpha F}\log v \qquad \text{(Eqn. 2.4.4b)}$$

where $K = E_e^\circ - \frac{RT}{\alpha_c n_\alpha F}\left[0.78 - \frac{2.3}{2}\log\left(\frac{\alpha_c n_\alpha FD}{k^{o2}RT}\right)\right]$ and k^{o2} is the standard state rate constant for the oxidative electron transfer couple. From the equations above, it can be seen that as the sweep rate increases, the cathodic peak moves to more negative potentials. Similarly, the anodic peak will move to more positive potentials.

2.4.5 Quasi-reversible Reactions

It is common for a process that is reversible at slow sweep rates and irreversible at high sweep rates to pass through a region of quasi-reversibility at intermediate values.

This transition from reversibility occurs when the relative rate of electron transfer with respect to that of mass transport is insufficient to maintain a Nernstian equilibrium at the electrode interface. In this region both forward and backward reactions make a contribution to the observed current, and it has the following boundaries:

$$0.3v^{0.5} \geq k^\circ \geq 2\times10^{-5}\ \text{cms}^{-1} \qquad \text{(Eqn. 2.4.5a)}$$

A reversible-like CV may be obtained for the slowest sweep rates, while as the sweep rate is increased, the rate of mass transport will approach that of electron transfer and the peak separation increases.

The change from reversible to irreversible behaviour can be seen from a plot of I_p as a function of $\nu^{0.5}$ (Figure 2.4.5a).

Figure 2.4.5a Plot of dependence of I_p versus $\nu^{0.5}$.

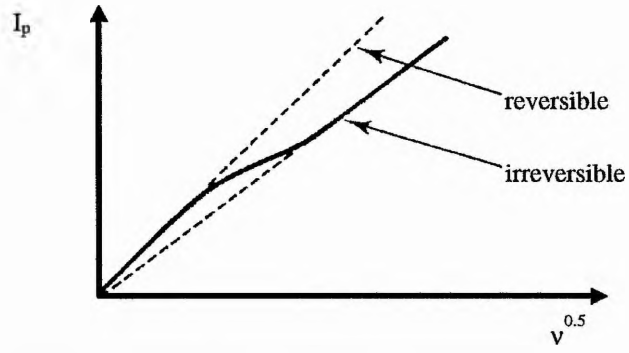

2.4.6 Conclusions

Cyclic voltammetry is the ideal technique for the study of an electroactive species. In chapter 5 this technique is applied to analyse the electrochemical intercalation of oxygen into various host structures using aqueous and molten-salt systems.

2.5 Thermal Analytical Techniques[16]

2.5.1 Introduction

Thermal analysis may be defined as the measurement of physical and chemical properties of materials as a function of temperature and encompasses a number of techniques such as thermogravimetric analysis (TGA), thermomechanical analysis (TMA or dilatometry), evolved gas analysis (EGA), differential scanning calorimetry (DSC) and differential thermal analysis (DTA). The production of new high-technology materials and the resulting requirement for a more precise characterisation of these substances have increased the demand for thermal analysis techniques. These have been used to determine the physical and chemical properties of polymers, electronic circuit boards and geological materials such as coals. In practice, the term thermal analysis is used to cover certain specific properties only such as enthalpy, heat capacity, mass and coefficient of thermal expansion. The uses of thermal analysis in solid state science are varied and include the study of solid state reactions, thermal decompositions and phase transitions and the determination of phase diagrams.

The two main thermal analysis techniques are thermogravimetric analysis, which automatically records the change in weight of a sample as a function of either temperature or time, and differential thermal analysis which measures the difference in temperature, ΔT, between a sample and an inert reference material as a function of temperature. A closely related technique is differential scanning calorimetry, which follows a quantitative measure of the enthalpy changes that occur in a sample as a function of either temperature or time. In modern equipment, it is possible to combine these techniques in the same instrument.

2.5.2 Thermogravimetric Analysis

Thermogravimetry is a technique for measuring the change in weight of a substance as a function of temperature or time. It provides a quantitative measurement of any weight changes associated with thermally induced transitions, or with time when operating under isothermal conditions. Thermogravimetric curves are characteristic of a given compound due to the unique sequence of physical transitions and chemical reactions that occur over definite temperature ranges. A thermally induced process may evolve a volatile product that results in a change in the weight of a sample. TGA data is therefore useful in characterising materials and investigating the thermodynamics and kinetics of the reactions and transitions that result from the application of heat to these materials.

In TGA the weight of the sample is continuously recorded as the temperature is increased. A sample, usually of a few milligrams in weight is placed in a crucible that is positioned in a furnace under a predetermined atmosphere on a beam attached to an automatic recording balance. The beam is maintained in the null position by the current flowing through the transducer coil of an electromagnetic balance. A pair of photosensitive diodes act as a position sensor to determine the movement of the beam. Any change in the weight of the sample causes a deflection of the beam, which is sensed by one of the photodiodes. The beam is then restored to the original position by a feedback current sent from the photodiodes to the coil of the balance. This current is proportional to the change in weight of the sample.

The results of a TGA experiment normally appear as a continuous chart record, an example of which is shown in Figure 2.5.2a. This figure shows a typical single step decomposition reaction. The sample has a constant weight W_i, until it begins to decompose at a temperature T_i. Under conditions of dynamic heating, decomposition will usually take place over a range of temperatures, T_i to T_f, and a second constant weight plateau is then observed above T_f, which corresponds to the

weight of residue W_f. The weights W_i, W_f and the difference in weight ΔW are fundamental properties of the sample and can be used for quantitative calculations.

Figure 2.5.2a Schematic thermogram for a single step composition reaction.

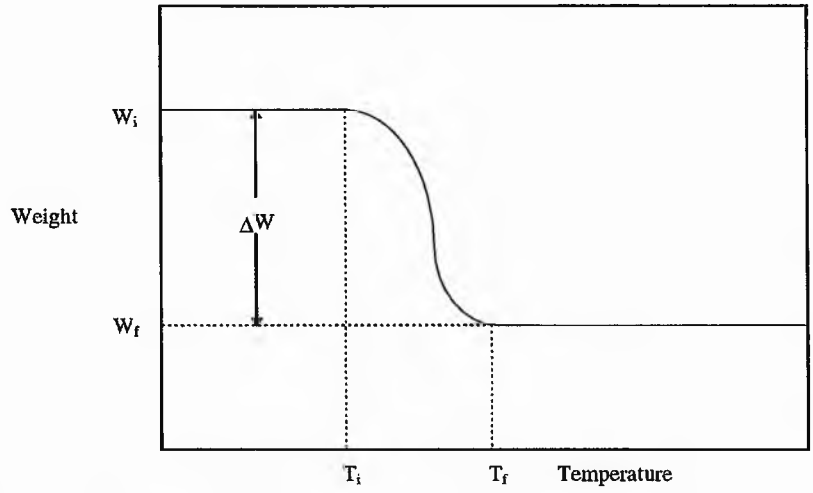

Unlike the weights, temperatures T_i and T_f depend on variables such as heating rate, which is typically in the range 1 to 20°C min^{-1}, the particle size of the solid and the atmosphere above the sample.

TGA has been used in the kinetic analysis of polymer stability, compositional analyses of multicomponent materials, atmospheric analyses and corrosion studies, moisture and volatiles determinations, and accelerated tests of ageing. This technique is used in Chapter 4 to examine the thermal oxidation behaviour of a pyrochlore.

2.5.3 Differential Scanning Calorimetry

Differential scanning calorimetry is a widely used experimental technique where the sample and reference are subjected to a precise temperature change. When a thermal transition occurs in the sample i.e. a chemical or physical change that results in the

emission or absorption of heat, thermal energy is added to either the sample or the reference in order to maintain both at the same temperature. The energy transferred is exactly equivalent in magnitude to the energy absorbed or evolved in the transition, and so this balancing energy yields a direct calorific measurement of the transition energy.

In some DSC apparatus, the sample and reference are maintained at the same temperature during the heating programme and the extra heat input to the sample (or to the reference if the sample undergoes an exothermic change) required in order to maintain this temperature balance is measured. In an alternative configuration, the difference in temperature between the sample and reference is measured, with the equipment being carefully designed to ensure a calorimetric response.

The differential scanning calorimeter used to obtain the heat flow - temperature plots discussed in Chapter 7 was of the former type discussed above. The calorimeter consists of two sample holders with individual heaters and thermocouples. One holder contains an empty sample pan and acts as a reference, while the other holds the sample in an identical pan. Both holders are heated and cooled over an appropriate temperature range at a predetermined rate, usually in the range 1 to 50°C min^{-1}. The temperature of the sample and reference holder is monitored and as the sample undergoes thermally-induced transitions, and compensation for the energy absorbed or evolved by the sample is provided by adding or subtracting an equivalent amount of energy to the heater. The continuous adjustment of heater power necessary to keep the sample holder at the same temperature as the reference provides a varying electrical signal equivalent to the thermal behaviour of the sample. This measurement is made directly in milliwatts providing an electrical energy measurement of the area under a peak in the DSC trace. The area under the peak can be converted to the change in enthalpy of the sample.

2.6 References

1. "Fundamentals of Crystallography", Ed. C Giacovazzo, Oxford Science Publications 1995, Ch 3, 141, Ch 5,319.

2. A. R. West, "Solid State Chemistry and its Applications", Oxford University Press, Ch5, 115.

3. J. W. Visser, *J. Appl. Crystallogr.*, **2**, 380, 1969.

4. "International Tables for X-ray Crystallography", Klawer Academic Publishers, 1995, Vol B, 355-357.

5. A. LeBail, H. Duroy and L. Fourquet, *Mater. Res. Bull.*, **23**, 447, 1988.

6. R. I. Smith and S. Hull, *Rutherford Appleton Laboratory Report*, REL-94-115, November 1994, 3.

7. Image courtesy of University Liason Secritariat, Rutherford Appleton Laboratory.

8. "The Rietveld Method", Ed. R. A. Young, Oxford University Press, 1993.

9. G. K. Wertheim, M. A. Butler, K. W. West and D. N. Buchanan, *Rev. Sci. Instrum.*, **45**, 1369, 1974.

10. G. H. Stout and L. H. Jensen, "X-ray Structure Determination", Wiley, 1989, 250-255.

11. N. E. Brese and M. O'Keeffe, *Acta Crystallogr.*, B**47**, 192, 1991.

12. L. Pauling, *J. Am. Chem. Soc.*, **69**, 542, 1947.

13. D. Altermatt and I. D. Brown, *Acta Crystallogr.*, A**43**, 125, 1987.

14. "Instrumental Methods in Electrochemistry", Southampton Electrochemistry Group, Ellis Horwood Series in Physical Chemistry, Ch6.

15. P. J. Delahey, *J. Am. Chem. Soc.*, **75**, 1191, 1953

16. 2. A. R. West, "Solid State Chemistry and its Applications", Oxford University Press, Ch4, 102.

Chapter 3
The Synthesis of Oxygen Intercalates

3.1 Introduction

The interaction of oxygen with an oxide, such as the insertion of the O^{2-} species into the ionic network of a non-stoichiometric oxide, is usually described in terms of a heterogeneous equilibrium.

Certain binary oxides of the form MO_{2-x} (M = Pr, Ce)[1] contain available oxygen vacancies, the formation of which can be described by the equilibrium shown in equation 3.1a.

$$O_o + 2M_M \leftrightharpoons V_O^{\cdot\cdot} + 2M_M^* + 0.5\ O_2(g) \qquad \text{(Eqn. 3.1a)}$$

where O_o is an oxide ion on the anion sublattice, M_M is a metal ion on the cation sublattice, $V_O^{\cdot\cdot}$ is a vacancy on the oxide sublattice and M_M^* is the reduced metal on the cation sublattice. Oxygen vacancies of this type are generally ordered, as is evident in the PrO_x system (x = 1.714, 1.778, 1.800, 1.818 and 1.833)[1].

The occupancy of interstitial sites in overstoichiometric oxides, such as UO_{2+x} may be expressed by the equilibrium shown in equation 3.1.b.

$$0.5\ O_2\ (g) \leftrightharpoons O_i^{\cdot\cdot} + 2\ h^{\bullet} \qquad \text{(Eqn. 3.1b)}$$

where $O_i^{\cdot\cdot}$ is an oxide ion in an interstitial site and $h^{\bullet}$ is a positive hole. In the uranium-oxide system, the interstitial oxygen atoms are not randomly distributed[1, 2], but form various types of complexes depending on the value of x.

Recent work by a number of groups have shown that the insertion of oxygen into ternary oxide systems with the Brownmillerite[3] or K_2NiF_4[3-14] structures is possible at room temperature. Such an oxidation reaction leads to mixed valence oxides containing high oxidation states.

In thermodynamic terms these reactions can be formally described as heterogeneous equilibria such as those discussed previously. However, room temperature reactions like these belong to the field of "chimie douce". Such processes may not lead systematically to the thermodynamically most stable phase as assumed for heterogeneous equilibria, which are generally investigated at high temperature. This implies that kinetics plays an important role in the formation of metastable phases provided that their free energy is lower than that of the starting materials. In order to interpret and rationalise such results, the concepts and models used in the field of intercalation are the most appropriate.

Intercalation compounds may be classified according to the nature of the intercalated species or that of the host material. Intercalated species can be cations, anions or neutral species. The intercalation of charged species usually involves a redox process between guest species and the host network: the insertion of an A^- anion, for example, results from the ionisation of the electronegative guest element A, which oxidises the host matrix Z, into Z^+.

Diffusion in the solid phase is normally the limiting step for kinetics, with size effects predominating. The closer the fit between the host channel size and the guest size, the easier the diffusion. The size of cations being generally smaller than anions means that many solids can have channels large enough to accommodate them. On this basis, cationic intercalation may be considered to be more easily achieved than anionic.

Cationic and molecular intercalations are well known and have been investigated for a long time. However, anionic intercalation, implying the oxidation of the host matrix has been thoroughly studied only in the case of graphite salts containing anions such as HSO_4^-, NO_3^-, and MF_6^- (M = As, W, Re, Os, Ir, Pt,..)[15].

Anionic intercalation involving an exchange reaction has also been reported for oxyhydroxides of transition elements such as NiOOH[16]. The room temperature intercalation of oxygen species- atomic, molecular or anionic- by electrochemical[3-12] and chemical[13, 14] routes has only recently been reported.

3.2 Electrochemical Oxygen Intercalation Techniques

3.2.1 Aqueous Electrochemical Oxygen Intercalation - an Established Method.

3.2.1.1 Introduction

Pouchard[3] has reported an aqueous based electrochemical method for oxygen intercalation. This method is reviewed here to set in context a new technique developed by us based on molten salt electrolytes.

The electrochemical oxidation of a number of ternary oxides of transition metals was first reported by Pouchard and co-workers in 1992[3]. It was shown that the oxidation leads to mixed valence oxides containing formal oxidation states such as Fe(IV), Ni(III) and Cu(III).

The electrochemical process in aqueous solution was shown to oxidise the Brownmillerite-type ferrite $Sr_2Fe_2O_5$ to the perovskite $SrFeO_3$, and two La_2MO_4 (M = Ni, Cu) oxides to $La_2MO_{4+\delta}$. Analysis by powder X-ray diffraction, chemical methods and Mössbauer spectroscopy showed that the intercalated compounds containing intercalated oxide ions. The fact that the intercalated species are the same as the host anions distinguishes these materials from the majority of other intercalation compounds, in which the guest species are usually chemically different from the host ions. The oxidation process that Pouchard has discovered appears to be a powerful method for preparing oxides containing transition-metals in high oxidation states.

3.2.1.2 Experimental

The electrochemical measurement and intercalation experiments were performed at room temperature under Ar in a two compartment cell containing 1M KOH solution with a three electrode device. A schematic representation of the cell is shown in Figure 3.2.1a.

Figure 3.2.1a A schematic representation of the electrochemical cell used in the oxygen intercalation reaction.

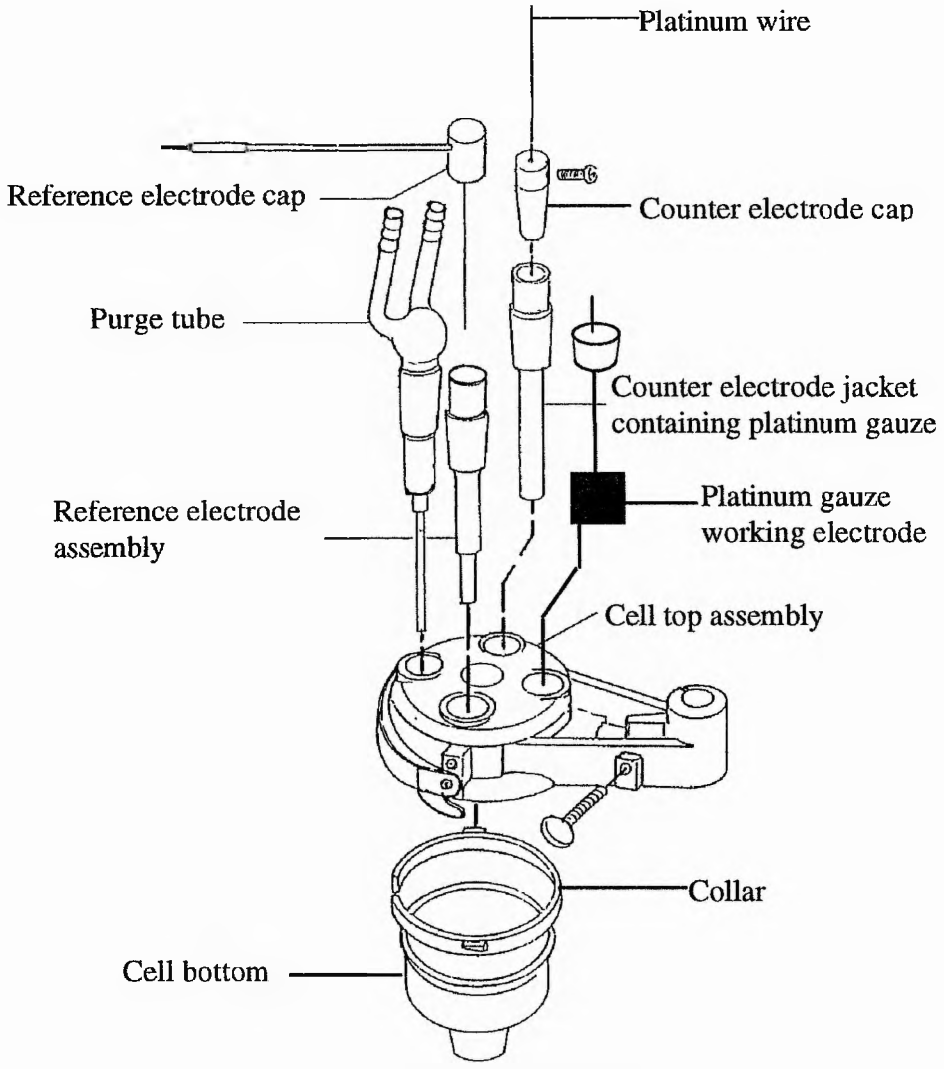

The reference electrode was a standard calomel electrode (E.G. & G.) [Hg_2Cl_2 / Hg, E = +0.2412 V / versus S.H.E.). All potentials quoted in this work refer to this electrode. The counter electrode was a platinum gauze of large surface area. The working electrode consisted of a 1×1 cm square of platinum gauze onto which the material to be examined was pressed using a 13 mm die at a pressure of 5 $toncm^{-2}$. After the host was attached to the gauze a length of platinum wire was added by spark welding. All the wires and gauze were cleaned in concentrated HCl between analyses and then thoroughly washed with distilled water before being flame dried.

The electrolyte was made by dissolving KOH (Aldrich, 99.999 %) [28.055 g] in 500 ml of distilled water, which had been degassed by bubbling Ar through it for 30 min. Approximately 200 ml of this solution was used in the cell during each experiment.

The cyclic voltammograms were obtained using a P.P.R.1 waveform generator, Amel S.S.3 potentiostat and Linseis L.Y. 18100 plotter. Scan ranges from 100 mVs^{-1} to 0.1 mVs^{-1} were examined from 0.0 → 1.2 → –1.3 → 0.0 V.

The cell polarisations were achieved using a Ministat Precision potentiostat. The insertion host was polarised for 3 days at a potential equivalent to the start of the oxidation plateau observed on the cyclic voltammogram. The oxidation was confirmed by powder X-ray diffraction. Structural analyses will be discussed in detail in Chapter 5.

3.2.1.3 Discussion

A cyclic voltammetric analysis of the type of cell described in section 3.2.1.2, without a host material attached to the working electrode produced the "blank" CV shown in Figure 3.2.1b. The potential was swept from 0.0 → 1.2 → –1.3 → 0.0 V at a scan rate of 10 mVs^{-1}.

Figure 3.2.1b Blank CV of the aqueous electrochemical cell, sweep rate 10 mVs^{-1}.

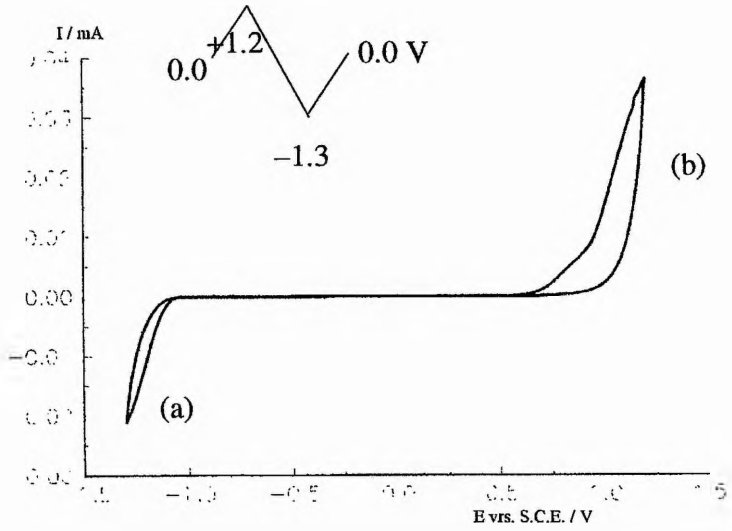

The limiting range of the CV corresponds to the decomposition of the alkaline electrolyte solution. The cathodic peak shown at (a) corresponds to hydrogen evolution and the half reaction shown in equation 3.2.1a.

$$2\ H_2O + 2\ e^- \rightarrow H_2\ (g) + 2\ OH^- \qquad \text{(Eqn. 3.2.1a)}$$

while the anodic peak shown at (b) corresponds to oxygen evolution shown in equation 3.2.1b.

$$4\ OH^- \rightarrow O_2\ (g) + 2\ H_2O + 4\ e^- \qquad \text{(Eqn. 3.2.1b)}$$

When a suitable intercalation host is pressed onto the working electrode, a C.V similar to the one showed in Figure 3.2.1c is obtained. The oxidation plateau (designated O_1) is found to arise between 350 and 700 mV, depending on the nature of the 3d metal, M. This corresponds to the overall reaction shown in equation 3.2.1c.

$$A_xMO_y + 2\delta\ OH^- \rightarrow A_xMO_{y+\delta} + \delta\ H_2O + 2\delta\ e^- \qquad \text{(Eqn. 3.2.1c)}$$

where a metal ion on the surface of the host M_{sfc}^{n+}, is oxidised to $M_{sfc}^{(n+1)+}$. The applied potential for the electrochemical oxidation was chosen as that corresponding to the end of the oxidation plateau.

A reduction peak is also evident in Figure 3.2.1c, and corresponds to the reduction of the metal ions on the surface of the host from $M_{sfc}^{(n+1)+}$ to M_{sfc}^{n+}.

Figure 3.2.1c An idealised CV obtained from the 3d transition metal oxides.

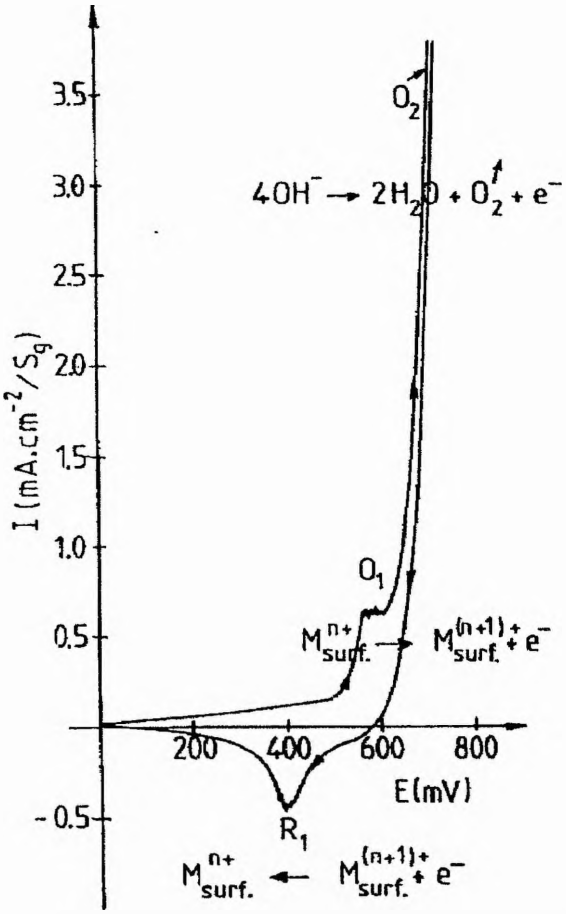

The oxidation reaction can be reversed, as is expected for an intercalation reaction. The complete transformation of the Brownmillerite to perovskite structure demonstrates the intercalation of "foreign" species into the parent network. If the electrical neutrality of the $Sr_2Fe_2O_5$ to $SrFeO_3$ phase change is considered, the intercalated species cannot be OH^-. This was corroborated by an absence of an OH band in the I.R. spectrum, and the lack of protons in N.M.R. experiments. The possibility that the intercalated species were O_2^- or O_2^{2-} was investigated by X.P.S., but the experimental data did not confirm the existence of these species. Pouchard therefore concluded that the inserted species were formally O^{2-} ions.

In the Brownmillerite material, the intercalated oxide ions occupy vacant sites in the anion sublattice, whereas in the La_2MO_4 phases all the normal anion sites are completely full, and so overstoichiometric oxide ions must be located in interstitial sites.

The mechanism of electrochemical oxidation can be split into two main steps:

(i) a surface oxidation involving an electroactive species and dependent upon the nature of the electrolyte.

(ii) a bulk oxidation involving the diffusion of charged or neutral species which eventually can be the same as the electroactive species occurring during the surface oxidation.

In the electrochemical oxidation reaction, the potential was set at a value lying in the range of the plateau, O_1. The theoretical activity of oxygen at the surface is very large at such potentials, possibly reaching several orders of magnitude.

The oxidation mechanism is not presently known. However, the mechanism of oxygen evolution at the surface of similar materials has been studied, and Pouchard and coworkers have proposed a mechanism for $La_{1-x}Sr_xFeO_{3-y}$ materials.

In an alkaline solution, the oxygen evolution reaction shown previously in equation 3.2.1b can occur in various ways. A 5 step mechanism can be written as-

$$M_{sfc} + OH^- \rightleftharpoons M_{sfc}...(OH^-)_{ads} \quad \text{(Eqn. 3.2.1d)}$$

$$M_{sfc}...(OH^-)_{ads} \rightleftharpoons M_{sfc}...(OH)_{ads} + e^- \quad \text{(Eqn. 3.2.1e)}$$

$$M_{sfc}...(OH)_{ads} + OH^- \rightleftharpoons M_{sfc}...(O^-)_{ads} + H_2O \quad \text{(Eqn. 3.2.1f)}$$

$$M_{sfc}...(O^-)_{ads} \rightleftharpoons M_{sfc}...(O)_{ads} + e^- \quad \text{(Eqn. 3.2.1g)}$$

$$2\ M_{sfc}...(O)_{ads} \rightarrow 2\ M_{sfc} + O_2\uparrow \quad \text{(Eqn. 3.2.1h)}$$

where M is an active site on the surface of the material satisfying Langmuir's adsorption conditions which are usually assumed for ferrites[17], and $(\ )_{ads}$ is a surface adsorbed species. It can be seen that a further one electron exchange after the equilibrium shown in equation 3.2.1f would lead to the formation of an adsorbed oxide ion which could then diffuse into the bulk of the structure.

Goodenough[18] has proposed an alternative mechanism for this process based on the assumptions that the metal atoms of the oxide retain their full coordination throughout the reaction by binding oxygen from the water of the electrolyte and exchanging the protons of the bound water to come into equilibrium with the pH of the electrolyte. The charge on the surface oxide must also remain constant.

The oxygen evolution reaction on an oxide is found where the surface (sfc) equilibrium-

$$M_{sfc}^{(n+1)+}...O^{2-} \rightleftharpoons M_{sfc}^{n+}...O^- \quad \text{(Eqn. 3.2.1i)}$$

is not biased too strongly to the left. If M is a transition metal ion for which equation 3.2.1j is satisfied-

$$M_{sfc}^{n+}...(OH)^- + OH^- \rightarrow M_{sfc}^{(n+1)+}...O^{2-} + H_2O + e^- \qquad \text{(Eqn. 3.2.1j)}$$

From equation 3.2.1i, equation 3.2.1j is followed by-

$$M_{sfc}^{n+}...O^- + OH^- \rightarrow M_{sfc}^{n+}...OOH^- + e^- \qquad \text{(Eqn. 3.2.1k)}$$

where equilibrium 3.2.1i has made the surface oxygen an active site for attack by an OH^- group from the solution. This equilibrium also makes possible the next two steps-

$$M_{sfc}^{n+}...OOH^- + OH^- \rightarrow M_{sfc}^{(n+1)+}...(O_2)^{2-} + H_2O + e^- \qquad \text{(Eqn. 3.2.1l)}$$

$$M_{sfc}^{(n+1)+}...(O_2)^{2-} \rightarrow M_{sfc}^{(n+1)+}...O^{2-} + 0.5O_2\uparrow \qquad \text{(Eqn. 3.2.1m)}$$

which returns to the surface equilibrium 3.2.1i. The insertion of interstitial oxygen into the bulk can occur between the steps shown in equations 3.2.1l and 3.2.1m. This phenomenon may then be predicted to occur where equilibrium 3.2.1i is found and at potentials where the oxygen evolution reaction is just being initiated or is in competition with others.

If equation 3.2.1l is the rate determining step of the oxygen evolution reaction, then the competitive oxidation reaction is-

$$2M_{bulk}^{n+}...M_{sfc}^{n+}...OOH^- \rightarrow 2M_{bulk}^{(n+1)+}...O_i^{2-}...M_{sfc}^{n+}...OH^- \qquad \text{(Eqn. 3.2.1n)}$$

which returns the surface to its condition in equation 3.2.1j. Where O_i represents interstitial oxygen. In order to compete with equations 3.2.1l and 3.2.1m it is

necessary to insert interstitial oxygen having good mobility at room temperature. This condition appears to be satisfied in the pyrochlore, K_2NiF_4 structures and in the oxygen deficient perovskites.

It is also possible that the equilibrium shown in equation 3.2.1i plays an important role in the oxygen diffusion mechanism. An electron transfer from O_i^{2-} to $M_{bulk}^{(n+1)+}$ would create a mobile O_i^- species, and the transferred electron could be returned after a diffusion jump so that it may be carried with the mobile ion.

3.2.2 Molten Salt Electrochemical Oxygen Intercalation - a New Method.

3.2.2.1 Introduction

Molten nitrates have been widely studied as suitable solvents for the analysis of electrochemical reactions. This is because they have low melting points and a good thermal stability[19].

Investigations of fused nitrates have revealed oxidation-reduction processes which are uncommon in conventional solvents[20]. The nitrate ion in an alkali nitrate melt is found to exhibit the characteristics of a powerful reactive oxidant, in contrast to the behaviour of NO_3^- in aqueous solution, where it is a thermodynamically weak and non-reactive oxidant. For example, it is capable of converting Mn(II) to Mn(IV)[21] and Cr(III) to Cr(VI)[22].

3.2.2.2 Experimental

The cell used in the molten salt electrochemical oxygen intercalation was constructed of silica glass to contain 200g of electrolyte and is shown in Figure 3.2.2a.

Figure 3.2.2a A schematic representation of the molten salt electrochemical cell used in the oxygen intercalation reaction.

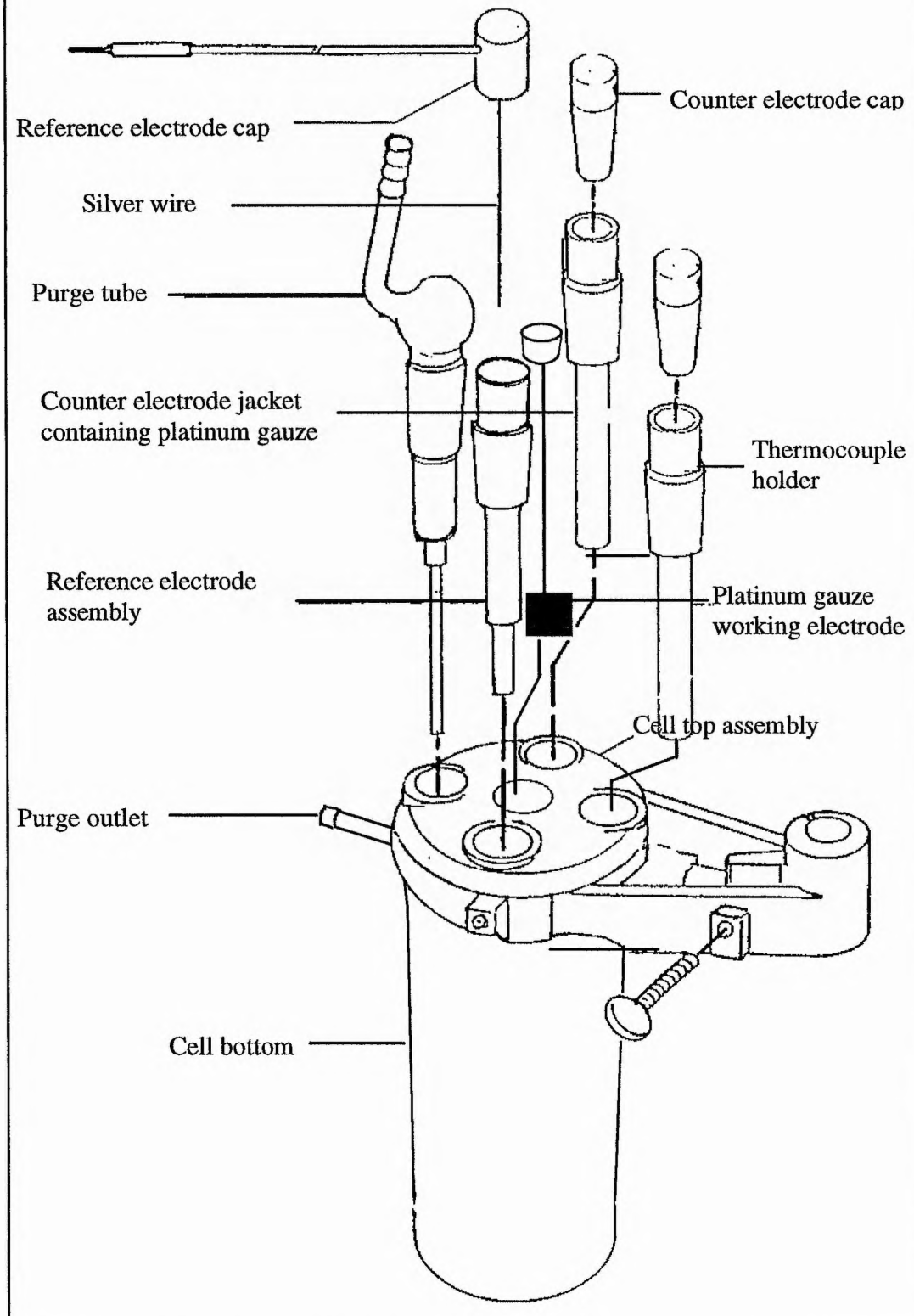

The cap was connected to the main chamber by a ground glass seal and contained five quick-fit joints for three tubes containing the thermocouple, reference electrode and gas bubbler. The two remaining joints were used to connect the counter and working electrodes using sure seal stoppers. The electrolyte used in the cell consisted of a eutectic mixture of KNO_3 (Aldrich 99 %) [118.5017 g] and $NaNO_3$ (Aldrich 99 %) [81.4983 g] (a 55:45% mole ratio KNO_3:$NaNO_3$). The reference electrode used was separated from the rest of the cell by a medium glass frit. It was composed of 1.5 g of a 0.07 molal $AgNO_3$ (Aldrich 99.9 %) [0.1784 g] in the KNO_3 / $NaNO_3$ eutectic [15 g], and the Ag/Ag^+ couple completed by dipping a 25 cm piece of wound silver wire (Aldrich 99.999 %) into the mixture of nitrates.

A small quantity of the intercalation host was pressed onto a 1.0x1.0 cm piece of platinum gauze using a 1.3 cm die and a pressure of 5 tons cm^{-2}. This was then spark welded to a 2cm piece of Pt wire and this nickel welded to a 25 cm piece stainless steel wire to complete the working electrode. The counter electrode consisted of a 3 cm piece of wound Pt wire nickel welded to a 25 cm piece of stainless steel wire. The cell was heated to 225°C using a silicone oil bath (surrounded by an insulating jacket) by a standard stirrer/hotplate. A teflon stirring bar was placed in the cell to mix the nitrates once a melt had been achieved. The cell was degassed for 1 h using a dried Ar supply before each experiment.

The cyclic voltammograms were obtained using a P.P.R.1 waveform generator, Amel S.S.3 potentiostat and Linseis L.Y. 18100 plotter. Scan ranges from 100 mVs^{-1} to 0.1 mVs^{-1} were examined from $0.0 \rightarrow -1.4 \rightarrow 1.2 \rightarrow 0.0$ V. An Amel potentiostat was used to polarise the cell, and the temperature monitored using a digital thermometer connected to the thermocouple. The insertion host was polarised for 8 h at a potential equivalent to the end of the oxidation plateau observed on the cyclic voltammogram. After the appropiate time, the working electrode was removed from the cell, washed with distilled water to remove the electrolyte and then dried at 60°C. The product was then removed from the gauze and ground. The oxidation was

confirmed by powder X-ray diffraction, and the structural analyses will be discussed in detail in Chapter 5.

3.2.2.3 Discussion

The oxidative properties of the nitrate ion in fused salts can be interpreted in two ways:

An extension of the Lux-Flood acid-base concepts[23] postulates that the nitrate ion is a Lux-Flood base which 'dissociates':

$$NO_3^- \rightleftharpoons NO_2^+ + O^{2-} \qquad \text{(Eqn. 3.2.2a)}$$

Oxidations occurring in nitrate melts would then reflect the half reaction:

$$NO_2^+ + e^- \rightarrow NO_2 \qquad \text{(Eqn. 3.2.2b)}$$

However, other researchers[24] have questioned the previous rationalisations of the redox properties of the melts, suggesting that the oxide ion only exists in very small concentration levels in fused nitrates due to oxidation by nitrate to an equilibrium mixture of peroxide (O_2^{2-}) and superoxide (O_2^-), as shown in Table 3.2.2a. In this interpretation, the oxidation processes in fused nitrates involve superoxide and/or peroxide as the actual oxidising agents.

One of the main equilibria involved in the removal of the oxide ion is its reaction with water. Table 3.2.2b summarises the opposing views. Proponents of the Lux-Flood hypothesis have calculated the equilibrium constant for the reaction shown by a potentiometric method using an oxygen gas electrode.

Table 3.2.2a Equilibrium Constants for Reactions in Nitrate Melts.

Reaction	Equilibrium Constant / molality units
$O^{2-} + NO_3^- \leftrightharpoons O_2^{2-} + NO_2^-$	3
$O_2^{2-} + 2\,NO_3^- \leftrightharpoons 2\,O_2^- + 2\,NO_2^-$	6.7×10^{-11}
$2\,O_2^- \leftrightharpoons O_2 + O_2^{2-}$	3.5×10^{-6}
$3\,O_2^{2-} \leftrightharpoons 2\,O_2^- + 2\,O^{2-}$	10^{-11}

This value is at least five orders of magnitude lower than that calculated by the direct measurement of the partial pressure of water vapour equilibriated with nitrate melts.

Table 3.2.2b Equilibrium Constant for the Oxide /Water Reaction in Molten Nitrates.

$$O^{2-} + H_2O \leftrightharpoons 2\,OH^- \qquad \text{(Eqn. 3.2.2c)}$$

Analytical Method	Equilibrium Constant	Temperature
Partial pressure of water vapour[25]	$K_{10} >>> 10^3$	250°C
Oxygen gas sensor[26]	$K = 3.2\times10^{-2}$	300°C

To study this oxide ion controversy, Ingram and co-workers[19] examined the role of KO_2, Na_2O_2, CaO and NaOH as solutes in the melt. Only in the case of NaOH is dissolution of the substrate unambiguously observed.

Whether oxide exists in significant concentrations or not, it is certain that some form of anionic oxygen species is present, and this will be a suitable participant in the electrochemical oxidation process.

Much work has been centred on the $NaNO_3$-KNO_3 melts of eutectic composition (45:55 mole ratio) because of the interesting chemical behaviour observed (Table 3.2.2c).

Table 3.2.2c Electrochemical Reactions in the $NaNO_3$-KNO_3 Melt[19].

CV	Electrode Reaction	E/V versus 0.07m Ag(I)/Ag	Comment
(b)	$NO_3^- \rightarrow NO_2 + 0.5\ O_2 + e^-$	+1.2	Anodic limit
(f)	$NO_2^- \rightarrow NO_2 + e^-$	+0.5	
	$O^{2-} \rightleftarrows 0.5\ O_2 + 2e^-$	+/–0.1	
	$2OH^- \rightarrow H_2O + 0.5\ O_2 + 2e^-$	–0.1	Irreversible
(e)	$O_2^- \rightleftarrows O_2 + e^-$	–0.74	
(d)	$NO_3^- + H_2O + 2\ e^- \rightarrow NO_2^- + 2\ OH^-$	–0.9	Irreversible
	$2\ O^{2-} \rightleftarrows O_2^{2-} + 2\ e^-$	–1.3	Reverse of (c)
	$O_2^- + e^- \rightleftarrows O_2^{2-}$	–1.32	
(c)	$NO_3^- + 2\ e^- \rightleftarrows NO_2^- + O^{2-}$	–1.65	Cathod. wave
(a)	$M^{n+} + n\ e^- \rightarrow$ Products	–3.0	Cathod. limit

A cyclic voltammetric analysis of the type of cell described in section 3.2.2.2, without a host material attached to the working electrode produced the "blank" CV shown in Figure 3.2.2b. The potential was swept from 0.0 → –1.725 → +1.425 → 0.0 V at a scan rate of 100 mVs^{-1}. The scan was in the cathodic direction to remove any water electrochemically from the system by the reaction shown in (d). After the first sweep, the water peak can be seen to deminish.

Figure 3.2.2b Blank CV of the molten salt electrochemical cell, sweep rate 100 mVs^{-1}.

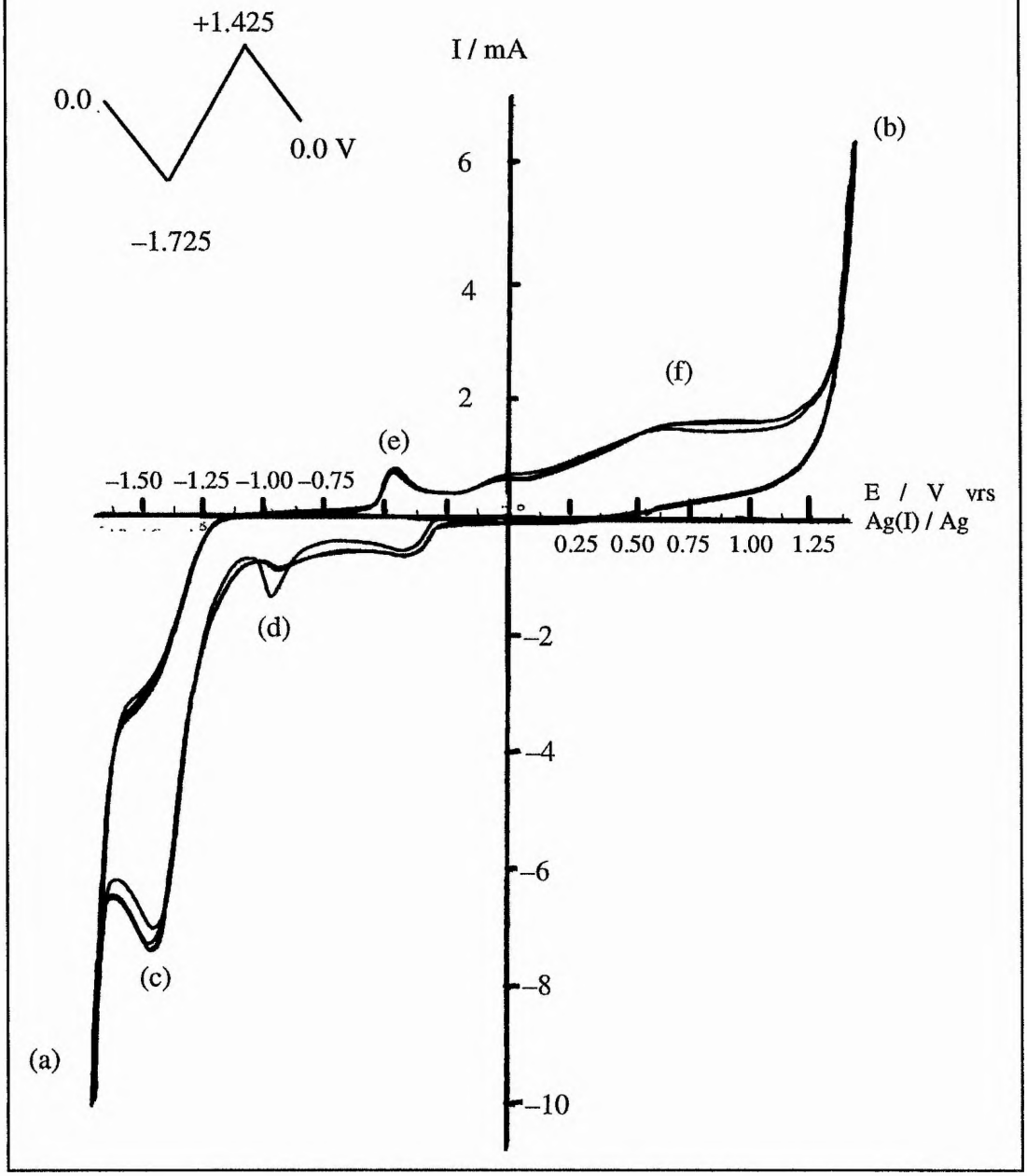

The limiting range of the CV corresponds to the decomposition of the electrolyte. The rising cathodic peak shown at (c) corresponds to the the half reaction shown in equation 3.2.2d.

$$NO_3^- + 2\,e^- \rightleftharpoons NO_2^- + O^{2-} \qquad \text{(Eqn. 3.2.2d)}$$

while the anodic peak shown at (b) corresponds to the decomposition shown in equation 3.2.2e.

$$NO_3^- \rightarrow NO_2 + 0.5\,O_2 + e^- \qquad \text{(Eqn. 3.2.2e)}$$

When a suitable intercalation host is pressed onto the working electrode, a CV containing an oxidation plateau (designated O_1) and a reduction plateau (designated R_1) for the M^{n+} species is obtained in a similar manner to the aqueous system.

Electrochemical oxidation should occur close to the anodic limit at 1.2V shown in equation 3.2.2e above.

Conversely, the equilibrium between the different oxygen species in the system will provide a sink for the oxide ions produced by the electrochemical reduction of a material. Reduction should be possible in the cathodic region of –1.5V.

3.3 Chemical Oxygen Intercalation.

3.3.1 The Hypobromite System - an Established Method.

3.3.1.1 Introduction

Schöllhorn[13] has introduced an aqueous based solution method of oxygen intercalation which has been used in this study. Rudolf and Schöllhorn[13], while investigating the mechanism of the anodic electrochemical oxygen intercalation reaction examined in the previous section, discovered a simple, convenient and efficient chemical oxidation process for the conversion of the K_2NiF_4-type La_2CuO_4 at room temperature to a superconductor with T_c = 44 K. This oxidation reaction was found to be reversible, with a return to the semiconducting state being produced by a chemical reduction.

Systematic screening studies revealed that aqueous solutions of the alkali hypochlorites and hypobromites are able to react with La_2CuO_4 in a topotactic process under retention of the host lattice. The average oxidation state of copper during the reaction was determined by iodometric titration. The Cu^{3+} content calculated by this method was found to be 0.000(5) for the starting material and 0.145(5) for the oxidised product.

The kinetics of the reaction were examined by following the change in the c lattice parameter (determined by powder X-ray diffraction) with time in the oxidising solution. An S-shaped conversion curve was obtained, indicative of surface kinetic hindrance of the electron / ion transfer process in the starting region of the solid state reaction. The reaction was found to come to an end after 15 h, after which no further change was found in the lattice parameters or copper average oxidation state.

The X-ray diffractograms were found to show a slight increase of the line width of the product when compared to the starting phase, which is normal for a solid

solid state reaction at ambient pressure as a consequence of a finite increase in defect concentration[27].

Rial and coworkers[14] have used this method to oxidise a number of samples in the K_2NiF_4-type $La_{2-x}Sr_xCuO_4$ (x = 0.05, 0.09, 0.12, 0.125. 0.13, 0.14) solid solution. The overstoichiometric oxygen was characterised by T.G.A. and neutron diffraction. A maximum oxygen content of 4.135(4) was obtained for the x = 0.05 sample.

These types of syntheses have lead to the concept of chemical reactions which can mimic electrode reactions in *chemie douce* preparations.

3.3.1.2 Experimental

The chemical oxidising agent was prepared from a 5 M solution of NaOH by dissolving NaOH (Aldrich 99.9 %) [39.9967 g] in 200 ml of distilled water. This solution was then cooled to 0°C using an ice / saline bath, at which time the Br_2 (Aldrich, 98 %) [5.0 ml]was added dropwise to produce a 0.5 M NaOBr solution (also containing 4.0 M NaOH and 0.5 M NaBr (aq)) via the equilibrium shown in equation 3.3.1a.

$$Br_2 + 2\ OH^- \rightleftharpoons OBr^- + H_2O + Br^- \qquad K_{eq} = 2\times10^8\ mol^2l^{-2} \quad \text{(Eqn. 3.3.1a)}$$

Once all the Br_2 was added, the solution was allowed to warm slowly to room temperature. The disproportionation of BrO^- is moderate at room temperature, therefore there may be the presence of a small amount of BrO_3^- in the solution.

Any dissolved oxygen was removed from the solution by bubbling Ar gas through it for 30 min. The chemical oxidations were carried out on 2.5 g samples of the intercalation hosts. A suspension of the host material was stirred vigorously with 5 molar equivalents of the 0.5 NaOBr solution. After a prescribed time, the host was

and then washed with acetone (Aldrich, laboratory grade). The samples were then dried and stored in a vacuum desiccator.

3.3.1.3 Discussion

The chemical oxidation reaction described is experimentally straightforward and reproducible, leading to a final product that can be clearly characterised in terms of crystal structure and oxygen content.

The standard electrode potential and half reaction for the reduction of the hypobromite species is shown in equation 3.3.1b.

$$BrO^- + H_2O + 2\,e^- \rightarrow Br^- + 2\,OH^- \qquad E^{\ominus} = +0.76\ V \quad \text{(Eqn. 3.3.1b)}$$

Schöllhorn found that the oxidised superconducting $La_2MO_{4+\delta}$ phase could be chemically reduced at room temperature by a wide series of reagents with varying reduction potentials from –1.87 to +0.08 V (NH_2OH, N_2H_5OH, $S_2O_4^{2-}$, SO_3^{2-}, H_2O_2 and $S_2O_3^{2-}$).

It was also suggested that the process leading to a Cu^{2+} / Cu^{3+} mixed valence state could be explained by two different electron / ion transfer models:

(i) the intercalation of oxygen into the La_2CuO_4 lattice and the formation of $La_2MO_{4+\delta}$.

(ii) an oxidative electron / proton transfer process as a consequence of La defects in the pristine material, compensated for by OH groups.

The neutron data by Rial from the $La_{2-x}Sr_xCuO_{4+\delta}$ system suggests that the former mechanism may occur, as the analysis found the presence of interstitial oxygen within the lattice, and no evidence was found for the existence of protons within the structure.

3.3.2 The Periodate System - a New Method

3.3.2.1 Introduction

In 1928, Malaprade discovered that periodic acid and its salts could be used in the efficient cleavage of the carbon-carbon bond of 1,2-diols to produce carbonyl compounds. These glycol cleavage reactions are usually very rapid, clean, quantitative and specific. The reactions are also usually stoichiometric, with one mole of oxidant being consumed for each carbon-carbon bond cleaved.

Sodium metaperiodate, $NaIO_4$ is a two electron chemoselective oxidant in organic chemistry which can oxidise alcohols to carbonyl compounds[28] and sulphides to sulphoxides[29]. This can only be used in water or aqueous organic solvents due to its solubility properties, but metaperiodate oxidations can be carried out in non-aqueous media using the soluble quaternary ammonium salts.

The redox potential for the periodate-iodate couple varies from +0.7 V in aqueous basic media to +1.6 V in aqueous acidic media. This makes the periodate species a potential oxidant to facilitate the room temperature intercalation of oxygen into materials, in a similar manner to the aqueous hypobromite species. In addition, since the quaternary ammonium periodates are soluble in non-aqueous organic solvents, the possibility of the chemical intercalation of oxygen at room temperature in non-aqueous media can also be probed. This would allow the investigation of systems such as $YBa_2Cu_3O_{7-x}$ ($0 \leq x \leq 1$), which is not stable in water.

3.3.2.2 Experimental

The $NaIO_4$ (Aldrich 99.9 %) [0.2332 g] was dissolved in 25 ml distilled water to form a 0.04 M solution.

A finely ground sample (0.0005 mole) [0.5 equivalents] of the intercalation host was then added to the solution containing the oxidising agent and the suspension stirred vigorously for a prescribed time. The intercalation host was then separated from the solution using a medium filter, washed with water and then acetone, and stored in a desiccator under vacuum.

The non-aqueous oxidising experiment was carried out in a similar manner, except that tetrabutyl ammonium periodate, $((CH_3)_3C)_4NIO_4$ (Aldrich 99.9 %) [0.4724 g] was dissolved in 25 ml dioxane (Aldrich, 98 %) to form a 0.04 M solution. Again, 0.0005 moles of the intercalation host was stirred vigorously in the solution containing the oxidising agent for a specific time, after which it was filtered from the solution, and washed with acetone before being dried in a vacuum desiccator.

3.3.2.3 Discussion

In order to obtain the appropriate electroactive oxidising species in aqueous media, a number of equilibria must be considered for the metaperiodate ion, IO_4^- in solution[30]-

$$IO_4^- + 2\,H_2O \rightleftharpoons H_4IO_6^- \qquad K_{eq} = 2.5\times10^{-2}\ mol^{-2}\ dm^{-2} \qquad \text{(Eqn. 3.3.2a)}$$

$$H_4IO_6^- \rightleftharpoons H^+ + H_3IO_6^{2-} \qquad K_{eq} = 2.0\times10^{-7}\ mol\ dm \qquad \text{(Eqn. 3.3.2b)}$$

$$H_4IO_6^- + H^+ \rightleftharpoons H_5IO_6 \qquad K_{eq} = 2.0\times10^{3}\ mol^{-1}\ dm^{-1} \qquad \text{(Eqn. 3.3.2c)}$$

$$H_3IO_6^{2-} \rightleftharpoons H^+ + H_2IO_6^{3-} \qquad K_{eq} = 1.0\times10^{-15} \text{ mol dm} \qquad \text{(Eqn. 3.3.2d)}$$

In acidic solution, the metaperiodate anion can be considered to be fully protonated. This means that the associated standard electrode potential and half reaction is for the reduction of the paraperiodic acid to iodate. This is shown in equation 3.3.2e.

$$H_5IO_6 + H^+ + 2\,e^- \rightarrow IO_3^- + 3\,H_2O \qquad E^\ominus \cong +1.6 \text{ V} \qquad \text{(Eqn. 3.3.2e)}$$

In alkaline solution, from the ionisation constants shown above, it is the $H_3IO_6^{2-}$ anion which is the electroactive species. The associated periodate-iodate reduction couple is shown in equation 3.3.2f.

$$H_3IO_6^{2-} + 2\,e^- \rightarrow IO_3^- + 3\,OH^- \qquad E^\ominus \cong +0.7 \text{ V} \qquad \text{(Eqn. 3.3.2f)}$$

This means that even in neutral or slightly alkaline solution, the periodate-iodate couple will oxidise iodide to iodine. This system therefore has the potential to be used as a room temperature chemical oxidising agent for various intercalation hosts.

3.4 Host Types

3.4.1 Introduction

The oxygen intercalation techniques exploited to produce the variety of oxidised hosts require a starting material which exhibits a combination of ionic and electronic conductivity, coupled with lattice vacancies to accommodate the inserted oxide ions. The concept that a significantly oxygen deficient metallic oxide lattice could be produced without the vacancies being eliminated by crystallographic shear was first proposed and studied over 30 years ago[31].

The perovskite structure has been observed to exist over the composition range ABO_{3-x}; $0 \leq x \leq 0.5$, for many transition metal and some main group cations. The first perovskite compounds recognised to have ordered oxide ion vacancies were based on the mineral Brownmillerite[32], Ca_2AlFeO_5, and its analogue $Ca_2Fe_2O_5$. Other superstructures based on the perovskite structure and oxide ion vacancies are known for manganese[33], iron[34], cobalt[35], nickel[36], and copper[37].

The discovery of high temperature superconductivity in several perovskite-related copper oxides e.g. $YBa_2Cu_3O_{7-y}$[38], which exhibit variable oxygen stoichiometry, has initiated renewed interest in the structures of oxygen deficient perovskites and similar compounds.

3.4.2 Material Requirements

The electrochemical oxidation technique described by Pouchard[3] requires oxygen intercalation hosts to have a number of features:

i) The material must show some electronic conduction to facilitate charge compensation for the intercalated oxygen.

ii) It must contain suitably sized vacancies to allow oxygen intercalation, either in the oxide sublattice, or in interstitial sites.

iii) It must also be a reasonable oxide ion conductor, to allow the diffusion of the intercalated oxygen species from the electrode surface into the bulk.

iv) It must contain an oxidisable species to compensate charge for the intercalation

e.g. a transition metal cation with a variable oxidation state-

$$2Fe^{3+} \rightarrow 2Fe^{4+} + 2e^-$$

$$V_O^0 + O^{2-} \rightarrow O_O^{2-}$$

The oxygen deficient perovskites and materials with the K_2NiF_4 structure were initially targeted because of their structural simplicity.

3.4.3 The Perovskite Structure

The perovskite structure is one of the best known structures in oxide chemistry. It has a general formula ABO_3, where A is usually an alkaline earth or one of the larger lanthanides, and B is usually a transition metal or one of the smaller lanthanides.

It is possible to have more than one element occupying the A or B sites in a compound e.g. $BaLaNiRuO_6$, where the A and B sites are occupied by random distributions of Ba / La and Ni / Ru respectively. These compounds can be represented by the general formula $AA'BB'O_6$.

In an ideal cubic perovskite (Figure 3.4.3a), the B cations are octahedrally coordinated to 6 oxygens. The larger A site cations are 12 coordinated by oxygen. This array can be constructed from corner sharing BO_6 units, while the equivalent perovskites with hexagonal symmetry have the BO_6 units linked by both corner and face sharing.

The electronic and magnetic properties of the perovskites vary widely e.g. $SrFeO_3$ is a metallic antiferromagnet, $SrCoO_3$ is a metallic ferromagnet, $LaFeO_3$ is an insulating antiferromagnet and $LaNiO_3$ is a metallic Pauli paramagnet[39].

Figure 3.4.3a The ideal cubic perovskite.

O shown as red and A atoms as yellow spheres. The BO_6 octahedra are shown in purple.

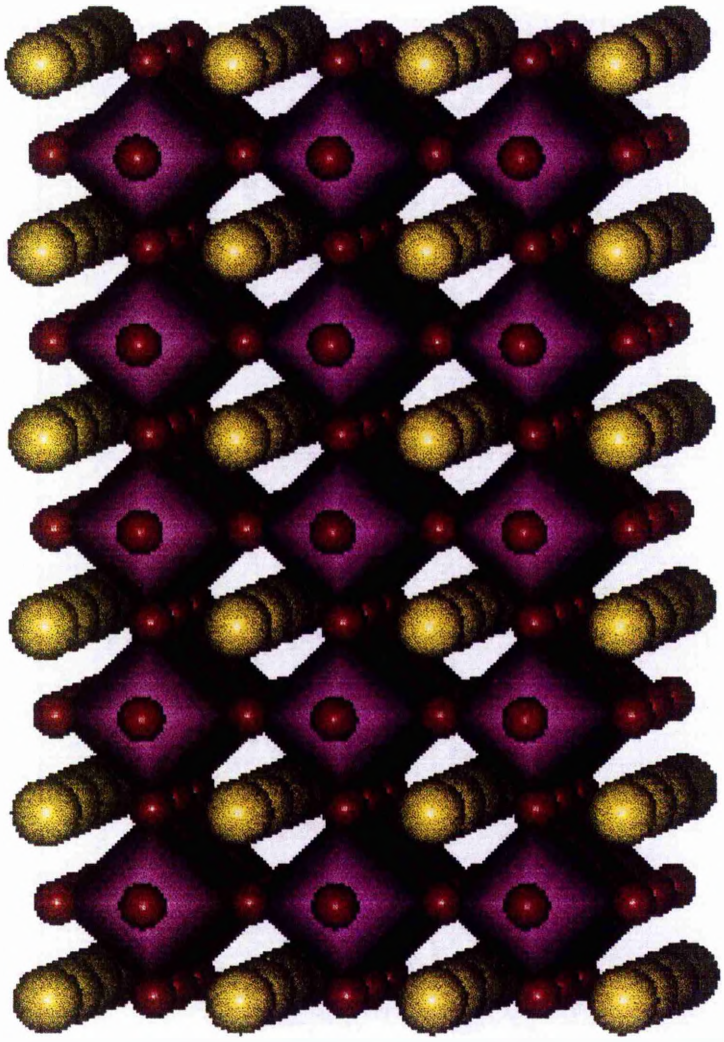

The transition metals in perovskites can all take more than one oxidation state. This leads to the possibility of non-stoichiometry in the oxide sublattice- ABO_{3-y}, e.g. in the Sr-Co-O system the oxygen content can vary from $SrCoO_3$ (Co^{4+}) to $SrCoO_{2.5}$ (Co^{3+}). The variation in the number of d electrons on the transition metal cation can have a marked effect on the electronic properties of the system, e.g. the change from metallic ferromagnetism in $SrCoO_3$ to insulating antiferromagnetism in $SrCoO_{2.5}$. This variation is governed by the oxygen content, which itself is controlled by the method of preparation, i.e. the electronic properties of perovskites are controlled by chemistry.

3.4.4 The Oxygen Deficient Perovskites

There are a large number of oxygen deficient perovskites, encompassing a number of vacancy patterns. Many new compounds have been reported since 1986, when high temperature superconductivity was found in oxygen deficient perovskite related compounds.

The coordination, electronic structure and metal-oxygen bond lengths of the A and B cations are the primary factors that control the manner in which the layers stack and the differences in these parameters leads to the array of vacancy patterns.

The oxygen deficient perovskite structure can be described as a $BO_{6/2-x/2}$ framework where some of the A and B cations are less than 12 and 6 coordinate respectively. The two general formulae used to describe these compounds are $A_mB_mO_{3m-x}$ which emphasises structural similarities and is convenient for the description of materials with ordered vacancies (x is an integer and therefore m is an integral multiple of the number of perovskite blocks in the unit cell), and $A_nB_nO_{3n-1}$. This second notation is useful to emphasise the degree of oxygen deficiency among the compounds. In general they exist for n=1 to ∞ i.e. ABO_2 to ABO_3. Compounds with ordered oxygen vacancies are known for n=5, 4, 3, 2, 1.5, 1.33 and 1.0.

Oxygen atoms are generally removed from $[100]_c$ or $[110]_c$ rows or $(001)_c$ planes (i.e. both $[100]_c$ and $[010]_c$). Removal from $[100]_c$ rows results in the formation of MO_5 square pyramids or MO_4 square planes. Removal from $[110]_c$ rows results in the formation of MO_4 tetrahedra, and removal from $(001)_c$ planes results in MO_5 square pyramids (Figure 3.4.4a)

Figure 3.4.4a The Common Oxygen Defect Patterns Found in Oxygen Deficient Perovskites.

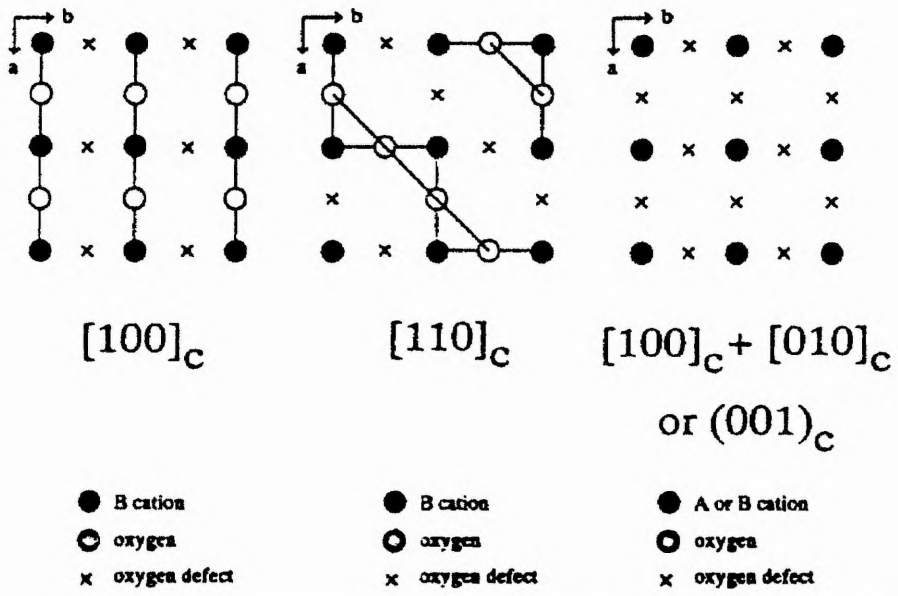

There are six vacancy patterns known for $A_mB_mO_{3m-x}$, m=2 oxygen deficient perovskites which have the formula $A_2B_2O_5$. The most common structure is Brownmillerite, Ca_2AlFeO_5[40]. This form is also exhibited in $LaSrCuGaO_5$[41] (Figure 3.4.4b), and $Sr_2Fe_2O_5$[42] (Figure 3.4.4c).

Figure 3.4.4b Various oxygen deficient $A_2B_2O_5$ compounds and their relationship to perovskite.

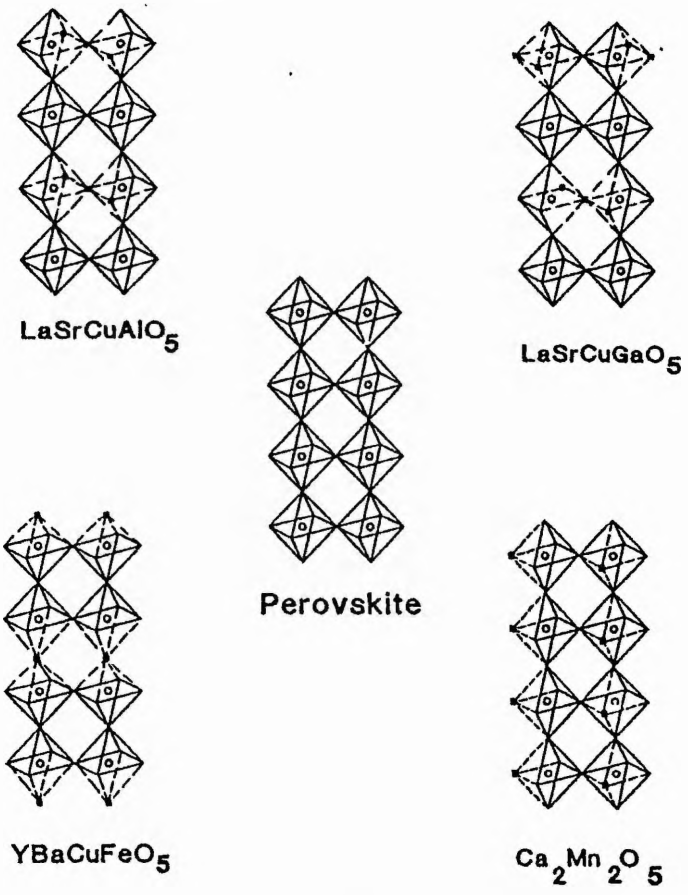

$Sr_2Fe_2O_5$ is orthorhombic and has oxygen atoms removed from alternate [001] i.e. $[110]_c$ rows, in every other (100) $BO_{4/2}$ plane. The rows of vacancies are staggered as viewed down [100]. The Fe coordination polyhedra are OTOT'O parallel to the a axis, where O is octahedral and T is tetrahedral (T' means it is in a different orientation from T).

This was targeted as an ideal candidate for the electrochemical oxidation reaction by Pouchard. An expression for the oxidation of the Brownmillerite is shown in equation 3.4.4a.

$$Sr_2Fe_2O_5 + (\delta/2)\ O_2 \rightleftharpoons Sr_2Fe_2O_{5+\delta} \quad (0 \leq \delta \leq 1) \qquad \text{(Eqn. 3.4.4a)}$$

Figure 3.4.4c The Brownmillerite Structure, $A_2B_2O_5$.

The O is shown as red and A atoms as yellow spheres. The BO_6 octahedra are shown in purple and the BO_4 tetrahedra in dark blue.

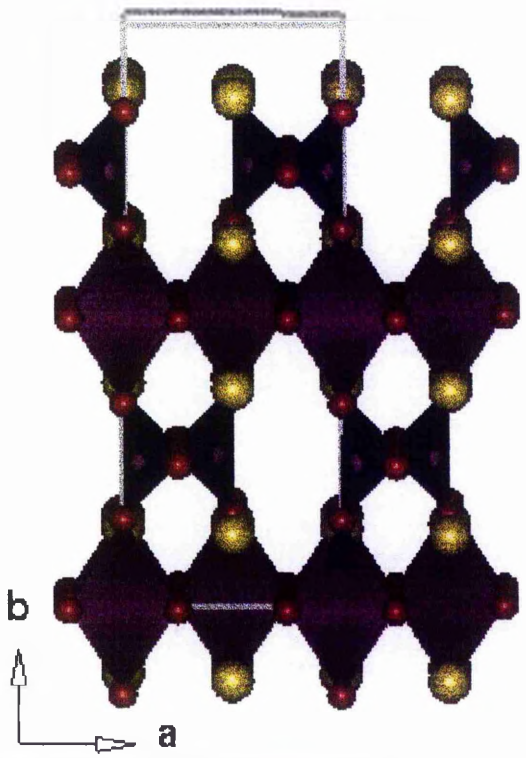

The compounds $Ca_2Mn_2O_5$[43] (Figure 3.4.4b) and $La_2Ni_2O_5$[36] (both n=2), have oxygen atoms removed from [001] and [100] rows respectively.

$La_2Ni_2O_5$ is tetragonal and has oxygen atoms removed from every [100] row in every other (001) $BO_{4/2}$ plane. The nickel coordination polyhedra are OPOPO parallel to the c axis (P is square planar). Since it is known that $LaNiO_3$ has the hexagonal perovskite structure[44], $La_2Ni_2O_5$ would be a suitable target for a test of electrochemical reduction on a hexagonal perovskite.

For $A_mB_mO_{3m-x}$, m=3, the oxygen deficient compounds have overall oxygen contents in the range from 6 to 9 for $A_3B_3O_{9-x}$.

Two vacancy types are found in $A_3B_3O_8$. $Ca_2LaFe_3O_8$[45]-type compounds such as $Sr_2LaFe_3O_8$ (Figure 3.4.4d) have an OOT OOT stacking arrangement along c, while the $YBa_2Fe_3O_8$ type have oxygen atoms completely removed from every third $(001)_c$ $AO_{4/4}$ plane, stacking OSS OSS along c (where S is square pyramidal). This can be compared with $YBaCuFeO_5$ (Figure 3.4.4b) where all of the oxygen atoms are removed from every other $(001)_c$ $AO_{4/4}$ plane.

Figure 3.4.4d The $Sr_2LaFe_3O_8$ structure.

The O shown as red and the Sr / La as yellow spheres. The FeO_6 octahedra are shown in purple and the FeO_4 tetrahedra are shown in dark blue.

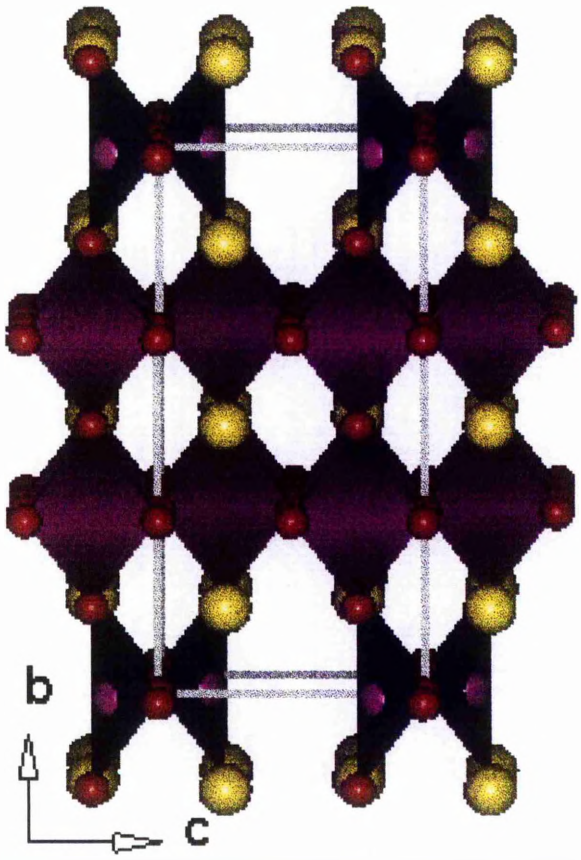

$YBa_2Cu_3O_7$[46] is one of the end members of the 1:2:3 Y-Ba-Cu-O system. It is orthorhombic and has oxygen atoms removed from every third (001) $AO_{4/4}$ plane, and every [100] row in every third (001) $BO_{4/4}$plane (Figure 3.4.4e). The copper coordination polyhedra are SPS SPS parallel to the c axis (where S is square pyramidal and P is square planar).

Figure 3.4.4e The $YBa_2Cu_3O_7$ structure.

The O is shown as red, the Y as small and the Ba as large purple spheres. The CuO_5 square pyramids are shown in light green and the CuO_4 square planes in dark green.

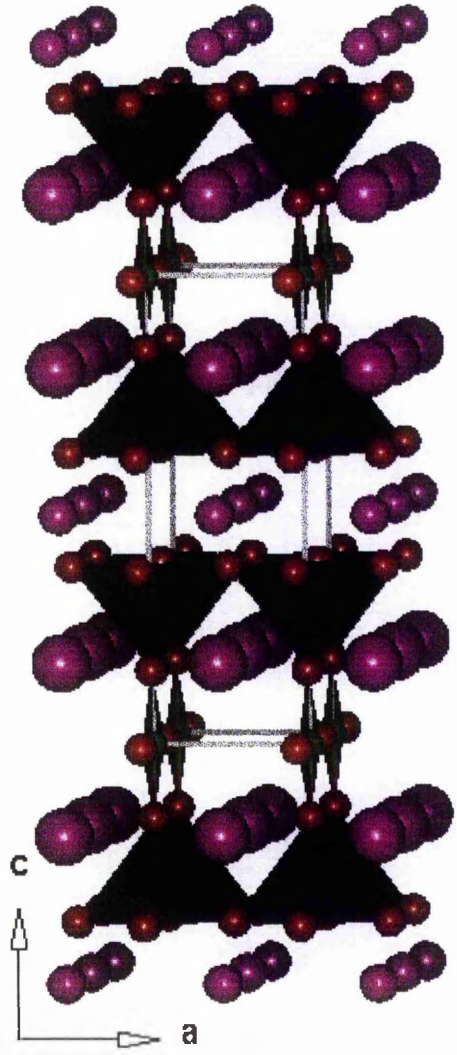

This material was targeted for oxygen intercalation because it may be possible to intercalate oxygen into every third (001) $BO_{4/4}$ plane to form an OPOOPO array parallel to the c axis or into every [100] row in every third (001) $BO_{4/4}$ plane to give a SOS SOS polyhedra array. If all the vacancies are filled then a perovskite would be obtained.

3.4.5 The K_2NiF_4-type Structure

The K_2NiF_4-type structure was initially described by Balz and Plieth[47], as a sequence of layers of tetragonally distorted NiF_6 octahedra, with the K^+ ions being located in 9-coordinate sites between the layers.

In K_2NiF_4 itself, the separation between the layers is almost twice the interplanar distance between two Ni^{2+} nearest neighbours. This causes a strong tendency for a distortion of the octahedral sites along the c axis leading to a stabilisation of a specific electronic configuration for cations occupying these sites, and relatively weak interplanar interactions between the magnetic ions so that 2D behaviour is expected.

Many compounds belong to this structural type (also called the T-phase), most being halides or oxides. The oxides of this class or closely related structures are known to exhibit a significant range of oxygen non-stoichiometry[48]. The nature of the deviations from the ideal stoichiometry remains unresolved, but recent characterisation of single crystals of the lanthanide nickelates $La_2NiO_{4+\delta}$ has revealed a large degree of non-stoichiometry, which cannot be attributed to the presence of intergrowth phases or deviations in the metal atom ratio[49].

The oxygen non-stoichiometry could be associated with the presence of vacancies in stoichiometric proportions on the metal atom sublattice (i.e. $(A_2B)_{1-x}O_4$), or with the presence of interstitial oxygen in the lattice. Ganguly[50] proved that sufficient space exists in the lattice to permit excess oxygen to be incorporated as

peroxide. Rao and co-workers[51] suggested that the most likely species is O_2^{2-}, as defects in the NiO basal planes. Recent work by Pouchard showed that the nonstoichiometry may be from interstitial oxygen forming O_3^{5-} species with its two nearest neighbours in the oxide lattice.

La_2CuO_4 has the T-phase K_2NiF_4-type structure[52] (Figure 3.4.5a), and was targeted for electrochemical oxidation by Pouchard and co-workers[12].

Figure 3.4.5a The T-phase and S-phase Structures of K_2NiF_4.

The Sr are shown as yellow and O as red spheres. The left hand side structure is that of the T-phase such as La_2CuO_4, with the CuO_6 octahedra shown in purple. The right hand side structure is that of the oxygen deficient S-phase such as Sr_2CuO_3, with the CuO_4 square planes shown in green.

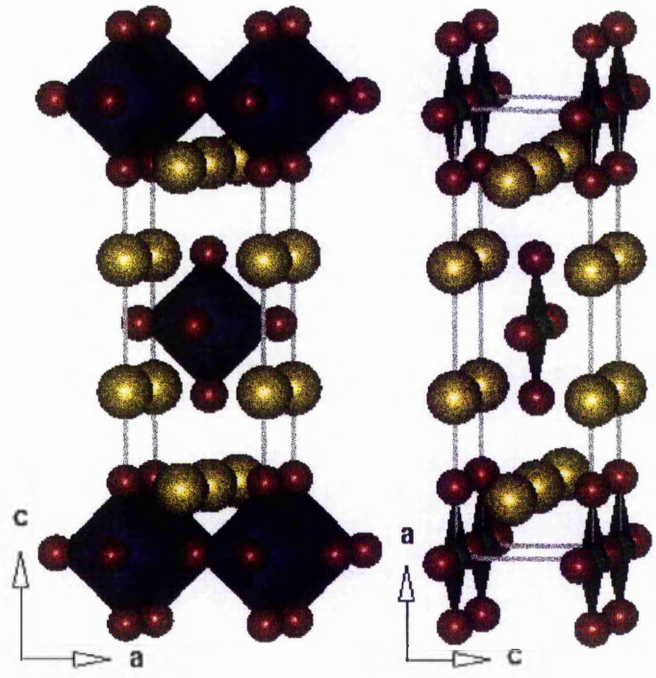

Sr_2CuO_3[53] has an oxygen deficient K_2NiF_4-type structure (S-phase, Figure 3.4.5.1) and contains isolated CuO_3 chains running along the a axis of its orthorhombic structure. The 25% oxygen vacancy in the anion sublattice make it a promising candidate for oxygen intercalation.

3.4.6 The Pyrochlore Structure

The pyrochlore structure-type is associated with the general formula $A_2B_2X_7$. The A and B cations form an ordered cubic close packed array within which the X anions occupy tetrahedral sites. The structure, with space group $Fd\bar{3}m$, is related to that of fluorite but with 1/8 of the anions missing. Many important compounds adopt the pyrochlore structure, these include catalysts and oxygen ion conductors such as $Gd_2Zr_2O_7$[54]. In the latter case, the ability of pyrochlore oxides to exhibit relatively high oxide ion conductivities, due to intrinsic Frenkel disorder, present even at their stoichiometric composition, is interesting. Such behaviour sets them apart from the majority of oxide ion conductors in which high ionic conductivity can only be achieved by the formation of a solid solution, e.g. the doped fluorite $Zr_{1-x}Ca_xO_{2-x}$.

The larger A cations occupy the 16c sites and the smaller B cations occupy the 16d sites, forming parallel strings of atoms along the <110> directions (Figure 3.4.6a). The six anions per formula unit occupy the 48f sites while the additional oxygen is found in the 8a site (Figure 3.4.6b). The 48f anions are displaced from their fluorite positions towards the neighbouring empty 8b sites. This produces a distorted cubic coordination for the A cation of $AO(48f)_6O(8a)_2$, while the B cation is in a distorted octahedral environment of $BO(48f)_6$.

Many pyrochlore oxides may be prepared as vacancy solid solutions, e.g. $(Gd_{2-x}Ca_x)Zr_xO_{7-x/2}$[55]. However, there are, as yet, no examples of interstitial solid solutions based on the pyrochlore structure.

Figure 3.4.6a Cation Coordination Polyhedra in the Pyrochlore Structure.

a) The A_2O_8 array of distorted, corner connected $A(16c)O(48f)_6O(8a)_2$ cubes are shown in green. b) The B_2O_6 array of distorted, corner connected $B(16d)O(48f)_6$ octahedra are shown in purple. c) Both cation coordination polyhedra are shown together.

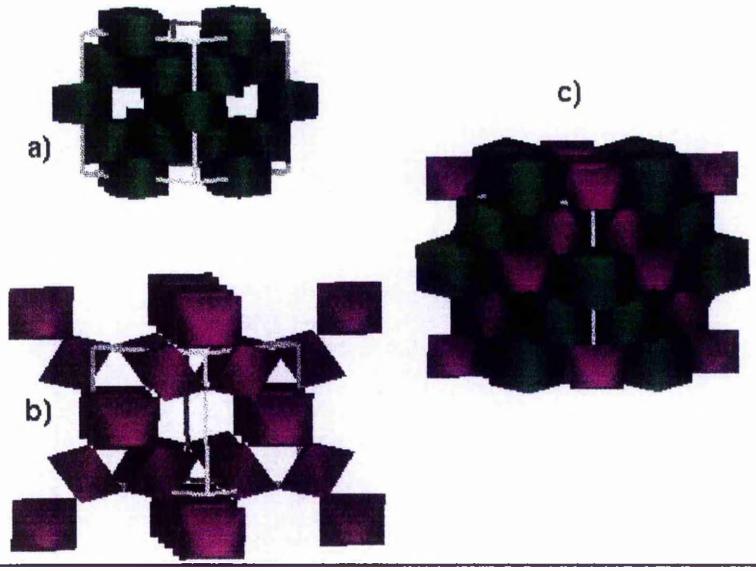

Figure 3.4.6b Anion Coordination Polyhedra in the Pyrochlore Structure.

$O(8a)Ce_4$ tetrahedra shown in red, $O(8b)ZrO_4$ tetrahedra shown in blue.

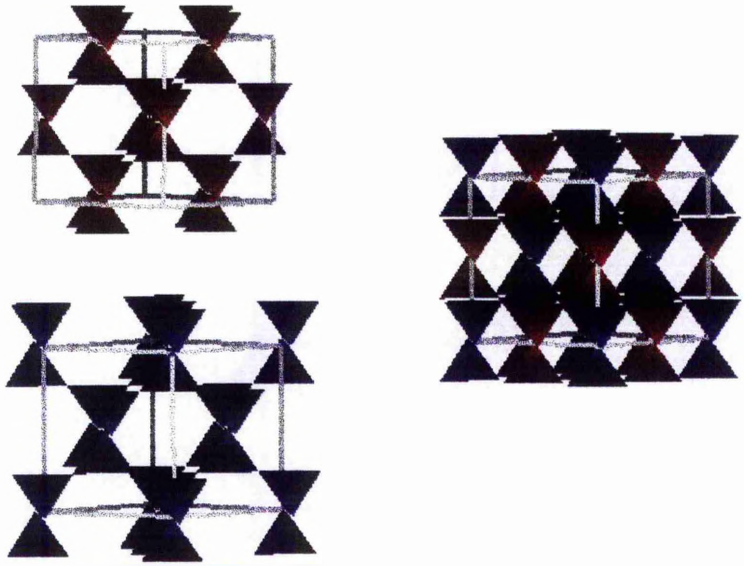

A pyrochlore containing a cation which could exhibit a variable oxidation state would be an idea candidate for oxygen intercalation. The formation of the solid solution series $Ce_2Zr_2O_{7+x}$ could be achieved starting from the stoichiometric $Ce_2Zr_2O_7$, where the cerium and zirconium are in the nominally 3+ and 4+ oxidation states respectively. Since cerium is commonly found in both the 3+ and 4+ oxidation state in nature, the pyrochlore structure may be flexible enough to accommodate the intercalated oxygen.

3.5 References

1. O. T. Sorensen, "Non Stoichiometric Oxides", Materials Science Series, Academic Press, New York, 1, 1981.

2. B. T. M. Willis, *J. Phys. (Paris)*, **25**, 431, 1964; *Acta Cryst. A*, **88**, 88, 1978.

3. J. C. Grenier, A. Wattiaux, J. P. Doumerc, P. Dordor, L. Fournes, J. P. Chaminade, and M. Pouchard, *J. Solid State Chem.*, **96**, 20, 1992.

4. A. Wattiaux, J-C. Park, J-C. Grenier and M. Pouchard, *C. R. Acad. Sci. Paris, Ser. II*, **310**, 1047, 1990.

5. J-C. Grenier, A. Wattiaux, N. Lagueyte, J-C. Park, E. Marquestaut, J. Etourneau and M. Pouchard, *Physica C*, **173**, 139, 1991.

6. F. C. Chou, D. C. Johnston, S-W. Cheong and P. C. Canfield, *Physica C*, **216**, 66, 1993.

7. P. G. Radaelli, J. D. Jorgensen, A. J. Schultz, B. A. Hunter, J. L. Wagner, F. C. Chou and D. C. Johnston, *Phys. Rev. B*, **48**(1), 499, 1993.

8. R. D. Sanchez, R. M. Torresi, C. Rettori, S. Oseroff and Z. Fisk, *Electrochimica Acta*, **40**(2), 209, 1995.

9. F. C. Chou, J. H. Cho and D. C. Johnston, *Physica C*, **197**, 303, 1992.

10. A. Demourgues, A. Wattiaux, J-C. Grenier, M. Pouchard, J. L. Soubeyroux, J. M. Dance and P. Hagenmuller, *J. Solid State Chem.*, **105**, 458, 1993.

11. A. Demourgues, F. Weill, B. Darriet, A. Wattiaux, J-C. Grenier, P. Gravereau and M. Pouchard, *J. Solid State Chem.*, **106**, 317, 1993.

12. A. Demourgues, F. Weill, B. Darriet, A. Wattiaux, J-C. Grenier, P. Gravereau and M. Pouchard, *J. Solid State Chem.*, **106**, 330, 1993.

13. P. Rudolf and R. Schöllhorn, *J. Chem. Soc., Chem. Commun.*, 1158, 1992.

14. C. Rial, U. Amdor, E. Moran, N. H. Andersen and M. A. Alario-Franco, private communication.

15. N. Bartlett and B. W. McQuillan, in "Intercalation Chemistry", Materials Science Series, Academic Press, New York, 19, 1982.

16. C. Delmas, in "Proceedings of the M. R. S. Meeting of Boston", 1990.

17. I. Langmuir, *J. Am. Chem. Soc.*, **40**, 1361, 1918.

18. J. B. Goodenough, R. Manoharan and M. Paranthaman, *J. Am. Chem. Soc.*, **112**, 2076, 1990.

19. M. B. Ingram and G. G. Lewis, *J. Electroanal. Chem.*, **55**(3), 399, 1974.

20. J. Jordan, *J. Electroanal. Chem.*, **29**, 107, 1971.

21. R. M. Bennett and O. G. Holmes, *Can. J. Chem.*, **41**, 108, 1963.

22. J. Jordan, K. A. Romberger and M. W. Young, *Angew. Chem.*, **75**, 1031, 1963.

23. Acid-Base Reactions in Fused Salts, Eds. R. K. Murmann, R. T. M. Fraser and J. Baumann, "Mechanisms of Inorganic Reactions", *Advan. Chem. Ser.*, **49**, 220, 1965.

24. P. G. Zambonin, *J. Electroanal. Chem.*, **45**, 451, 1973.

25. P. G. Zambonin and J. Jordan, *Anal. Lett.*, **1**, 1, 1967.

26. M. Fredericks, R. B. Temple and G. W. Thickett, *J. Electroanal. Chem.*, **38**, App. 5, 1972.

27. "The Rietveld Method", Ed. R. A. Young, Oxford Science Publications, Oxford University Press, 135, 1993.

28. D. Villemin and M. Ricard, *Nouv. J. Chim.*, **6**, 605, 1982.

29. W. T. Liu and Y. C. Tong, *J. Org. Chem.*, **43**, 2717, 1978.

30. W. M. Latimer "Oxidation Potentials". 2nd edition, Prentice-Hall Inc., New Jersey, 66, 1952.

31. G. H. Jonker, *Physica*, **20**, 1118, 1954.

M. Kestigan, J. G. Dickenson, and R. Ward, *J. Am. Chem. Soc.*, **79**, 5598, 1960.

S. Anderson, and A. D. Wadsley, *Nature*, **187**, 499, 1960.

32. W. C. Hansen, L. T. Brownmiller, and R. H. Bogue, *J. Am. Chem. Soc.*, **50**, 396, 1928.

33. K. R. Poeppelmeier, M. E. Leonowicz, J. C. Scanlon, J. M. Longo, and W. B. Yelon, *J. Solid State Chem.*, **45**, 71, 1982.

34. J. C. Grenier, M. Pouchard, and P. Hagenmuller, *Struct. Bonding*, **47**, 1, 1981.

35. K. Vidyasagar, J. Gopalakrishnan, and C. N. R. Rao, *Inorg. Chem.*, **23**, 1206, 1984.

36. K. Vidyasagar, A. Reller, J. Gopalakrishnan, and C. N. R. Rao, *J. Chem. Soc. Chem. Comm.*, 7, 1985.

37. C. Michel and B. Raveau, *Rev. Chem. Miner.*, **21**, 407, 1984.

38. J. G. Bednorz and K. A. Z. Muller, *Physica*, **B64**, 189, 1986.

39. P. D. Battle, National Institute of Standards and Technology Special Publication 804, "Chemistry of Electronic and Ceramic Materials, Proceedings of the International Conference", 53, 1990.

40. A. A. Colville and S. Geller, *Acta Crystallogr. Sect. B*, **27**, 2311, 1971.

41. J. T. Vaughey, J. B. Wiley and K. R. Poeppelmeier, *Z. Anorg. Allg. Chem.*, **598/9**, 327, 1991.

42. P. Hagenmuller, M. Pouchard and J-C. Grenier, *Solid State Ionics*, **43**, 7, 1990.

43. K. R. Poeppelmeier, M. E. Leonowicz and J. M. Longo, *J. Solid State Chem.*, **44**, 89, 1982.

44. A. Wold, B. Post and E. Banks, *J. Am. Chem. Soc.*, **79**, 4911, 1957.

45. P. D. Battle, T. C. Gibb and P. Lightfoot, *J. Solid State Chem.*, **84**, 237, 1990.

46. M. A. Beno, D. W. Soderholm, D. W. Capone, J. D. Jorgensen, K. I. Schuller, C. U. Serge, K. Zhang and J. Grace, *J. D. Appl. Phys. Lett.*, **51**, 57, 1987.

47. D. Balz and K. Pleith, *Z. Elektrochem.*, **59**, 545, 1955.

48. P. Ganguly and S. Ramasesha, *Magn. Lett.*, **1**, 131, 1980.

N. Nguyen, J. Choisnet, M. Hervieu and B. Raveau, *J. Solid State Chem.*, **39**, 120, 1981.

P. Odier, M. Leblanc and J. Choisnet, *Mater. Res. Bull.*, **21**, 787, 1986.

49. D. J. Buttrey, H. R. Harrison, J. M. Honig and R. R. Schartman, *J. Solid State Chem.*, **54**, 407, 1984.

50. P. Ganguly, "Advances in Solid State Chemistry", Ed. C. N. R. Rao, Indian National Science Academy, New Delhi, 135.

51. D. J. Buttrey, J. M. Honig and C. N. R. Rao, *J. Solid State Chem.*, **64**, 287, 1986.

52. F. C. Chou, J. H. Cho and D.C. Johnston, *Physica C*, **197**, 303, 1992.

53. C. L. Teske and H. Muller-Buschbaum, *Z. Anorg. Allg. Chem.*, **371**, 325, 1969.

54. J. B. Goodenough, "High Temperature Electrochemistry, 14th Riso Symposium", Denmark 1993, 43.

H. L. Tuller, S. Kramer and M. A. Spears, "High Temperature Electrochemistry, 14th Riso Symposium", Denmark 1993, 151.

55. T. Fournier, J. Y. Noys, J. Muller and J. C. Joubert, *Solid State Ionics*, **15**, 71, 1985.

Chapter 4

The Synthesis and Structural Chemistry of the $Ce_2Zr_2O_{7+x}$ System

4.1 Introduction

The pyrochlore structure type was discussed in Chapter 3.4, where various potential hosts for oxygen intercalation were examined. In this chapter the effects of the insertion of oxygen into the structure are examined by X-ray and neutron powder diffraction techniques. The pyrochlore structure may be derived from the defect fluorite by a doubling of the lattice parameter, and the removal of 1/8 of the oxide ions. The general formula may be represented as $A_2B_2O_6X$, where X is normally also an oxide ion but with a different site symmetry from the remaining six formula oxygens.

A large number of complex oxides with the formula $A_2B_2O_7$ crystallise with the pyrochlore structure (Space Group $Fd\bar{3}m$, Z = 8). The structure is stable when the ionic radii of the ratio of the A:B cations is in the range 1.46-1.80. The A cations can have a valence of 2+ or 3+ and the B of 5+ or 4+ respectively[1]. Many of the pyrochlore structures reported in the literature are of the type $A_2^{3+}B_2^{4+}O_7$, this is due to the existence of a large number of A^{3+} and B^{4+} cations with suitable ionic radii for the formation of this structure compared with the availability of suitable A^{2+} and B^{5+} cations.

The stoichiometric pyrochlore contains four crystallographically inequivalent ions. The A and B cations occupy the 16c and 16d respectively, forming parallel strings of atoms along the crystallographic [110] directions. The six oxygens per formula unit occupy the 48f sites, while the additional oxygen is found on a tetrahedral 8a site. As can be seen in Figure 4.1a, the tetrahedrally coordinated 48f oxygens are displaced from their fluorite positions towards the empty 8b sites. While oxygen vacancies occur at random throughout the anion sublattice in vacancy solid solutions based on fluorite (e.g. YSZ), they are ordered onto particular sites (8b) in the pyrochlore structure. These positions are therefore more correctly regarded as empty interstitial oxygen sites rather than oxygen vacancies.

The larger A cations are coordinated by eight oxygens and are located within distorted cubes that contain six equally spaced anions (the 48f O) at a slightly shorter distance from the central cation than the two equally spaced 8a oxygens (X). The smaller B cations are coordinated by six to oxygens on the 48f sites and are located within trigonal antiprisms with all the six anions at equal distances from the central cations.

Figure 4.1a The near [110] projection of one unit cell of the pyrochlore $Ce_2Zr_2O_7$. The ionic radii are based on $Ce_2Zr_2O_7$, with Ce shown as green, Zr as purple and O as red spheres.

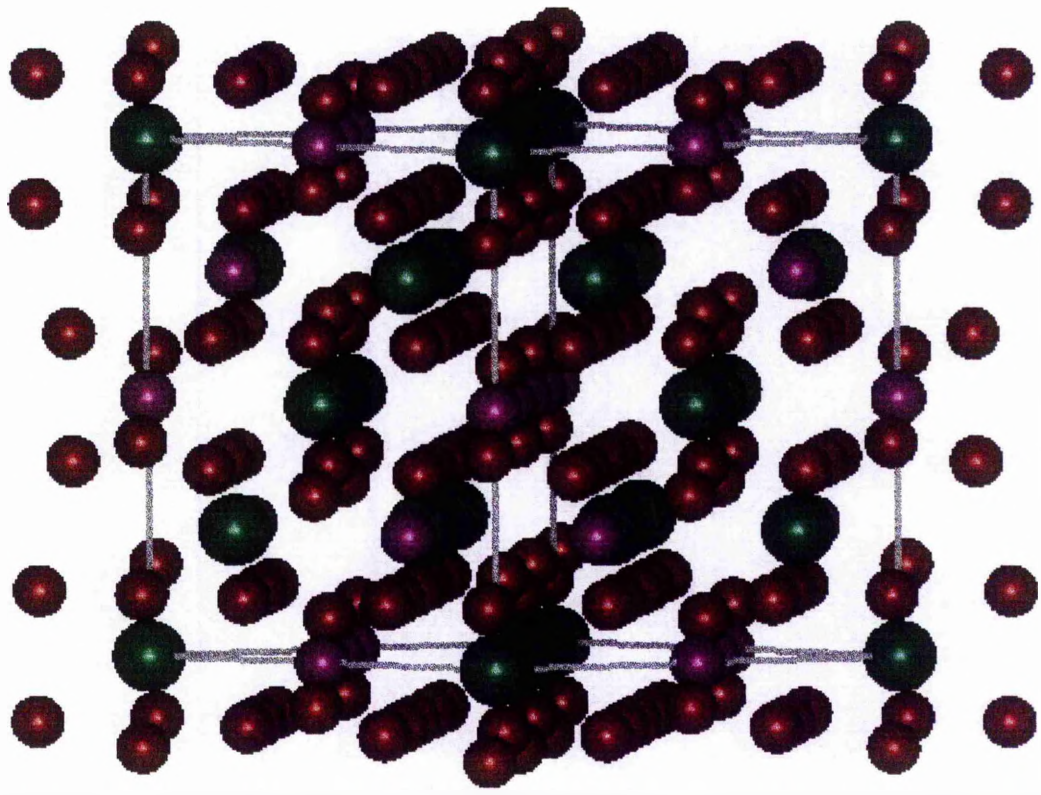

Duwez and Odell[2] made the first tentative examination of the phase diagram of the ceria-zirconia system. However, it was while studying the ion distribution in the

the solid-melt system of $BaCl_2$-$CeCl_3$-$BaZrO_3$, that Casey *et al*[3] isolated an unoxidised residue to which they assigned an approximate composition of $Ce_2O_3.2ZrO_2$, on the basis of the phase diagram postulated by Duwez and Odell. The X-ray data from this material suggested that it was a face-centred cubic phase with a lattice parameter of 10.699 Å. This powder pattern was found to resemble that of $Cd_2Ta_2O_7$[4], which has the pyrochlore structure, but the refinement of the structure was impossible due to peak broadening.

Since the isolation of $Ce_2Zr_2O_7$ in 1955, only its combustion synthesis and properties have been examined[5].

In each of the reported studies, only the stoichiometric pyrochlore was observed. However, the $Ce_2Zr_2O_7$ phase is an ideal candidate for oxygen intercalation, due to the existance of the empty 8b oxygen interstitial sites in the structure, and the potential for variability in the oxidation state of the 16c-site cerium from 3+ to 4+.

The stoichiometric pyrochlore, $Ce_2Zr_2O_7$ was synthesised by a modified sol-gel route and the subsequent intercalation of oxygen achieved by a chemical method at room temperature and by heating in oxygen. Certain structural aspects of the $Ce_2Zr_2O_{7+x}$ system were then investigated by a combination of X-ray and neutron powder diffraction techniques.

4.2 Experimental Details

A high temperature synthesis of $Ce_2Zr_2O_7$ involving sintering pellets of Ce_2O_3 and ZrO_2 under N_2 at 1377°C has been reported[6]. In other studies[3, 5], the stoichiometric pyrochlore was synthesised by a relatively low temperature route using either a novel combustion process employing the rapid heating of aqueous solutions of cerium (III) nitrate, zirconium (IV) nitrate and carbohydrazide/urea in the required molar ratio, or the fusion of the correct molar ratio of $BaCl_2$, $CeCl_3$ and $BaZrO_3$ under vacuum at 1000°C, and then the subsequent removal of $BaCl_2$ by leaching with water to yield the desired product.

Since both syntheses were rather complicated, a third route was devised. $Zr(OC_2H_5)_4$ (Aldrich 98 %) [9.4478 g] and $Ce(NO_3)_3.6H_2O$ (Aldrich 99.9 %) [15.1122 g] were added to 250 ml of distilled water, placed in an ultrasonic bath for two hours and then stirred vigorously for 48 hr. Approximately 200 ml of water was then removed on a rotary evaporator and the remaining solution freeze dried (i.e. the solution was frozen in liquid nitrogen and then allowed to warm to room temperature under vacuum to remove the remaining water). The resultant powder was placed in an alumina crucible with a lid and heated to 500°C at 1°/min in a tube furnace in an atmosphere of 95 % Ar / 5 % H_2 (BOC, pureshield) to allow a controlled decomposition of the ethoxide and nitrate. The sample was then heated to 1200°C at 10°/min and this temperature maintained for 24 h. After cooling to room temperature, the product was then removed from the furnace and ground using an agate mortar and pestle. The powder was then fired at 1200°C for a further 48 h in an alumina boat in a 95 % Ar / 5 % H_2 atmosphere and then cooled to room temperature to give the stoichiometric pyrochlore.

The decomposition of the nitrate in this synthesis produced an extremely vigorous reaction which required that a lid be used with the crucible to prevent loss of material into the furnace tube. The synthesis was subsequently improved by

substituting dry cerium (III) oxalate ($Ce_2(C_2O_4)_3$, Aldrich, 99 %) [9.4714 g] for the cerium (III) nitrate, producing an initial decomposition reaction which was much less severe. The experimental details were similar to those shown above, except that the initial heating rate was 2°/min to 250°C, where the temperature was maintained for 30 min to allow a complete decomposition of the organic component of the starting materials. The temperature was then raised to 1300°C, where it was held for 18 h, and then cooled to room temperature at 10°/min. As in the previous experiment, the furnace atmosphere was a 95 % Ar / 5 % H_2 mixture. The increased reaction temperature of 1300°C was used in the improved synthesis after the examination of the T.G.A trace of the $Ce_2Zr_2O_7$ (see Section 4.3.2.2). All samples produced were found to contain a small amount of ZrO_2 impurity, caused by the loss of a small amount of volatile cerium.

During preliminary investigations of the pyrochlore it was observed that the lattice parameter and oxygen content changed slowly with exposure to air. As a result care was taken to avoid prolonged exposure of the pyrochlore to air. In each case, the product phase was stored in a M Braun argon filled glove box (O_2 < 2 ppm, H_2O < 0.2 ppm).

The oxidised species, $Ce_2Zr_2O_{7+x}$, were synthesised in 1.5g batches (0.0026 mole) using the chemical oxygen intercalation reaction discussed in Section 3.3.1. The stoichiometric pyrochlore was added to a 5-fold molar excess of the hypobromite solution (26.1 ml of 0.5M NaOBr aq.) for a specified time, ranging from one to seventy two hours, to give the range of oxygen contents examined. The solution was stirred vigorously to ensure a homogeneous exposure of the crystallites to the solution. The reactions were carried out under argon and in deoxygenated water to avoid oxidation of the starting material from any source other than the NaOBr (aq). The quantity of oxygen in water can vary significantly and could lead to uncontrolled oxidation of the host. The oxidised phases were then removed from the solution using a sintered glass filter, washed with distilled water, acetone and then dried in a vacuum desiccator.

A group of four samples were also obtained from an aging study performed at the ISIS neutron facility. This involved exposing a sample of the stoichiometric pyrochlore to air for a specified time.

The thermally oxidised sample discussed in section 4.3.2.2 was produced by placing 1.5g of the stoichiometric pyrochlore in an alumina crucible. This was then located in a furnace which was heated to 500°C at a rate of 10°/min, in an atmosphere of flowing oxygen. This temperature was maintained for 18 h, after which the sample was cooled to room temerature at the same rate. After reaction, all the samples were then stored in an argon filled glove box.

Data suitable for structure determination were recorded at room temperature in transmission mode on a Stoe STADI/P high-resolution powder diffractometer, using Cu-$K_{\alpha 1}$ radiation. Data were collected over the range $5° < 2\theta < 85°$ in steps of 0.02°, the entire experiment lasting *ca*, 10 h.

Time-of-flight powder neutron diffraction data were collected on the POLARIS diffractometer at ISIS, Rutherford Appleton Laboratory. Approximately 2 g of finely ground material was placed in an 6 mm diameter vanadium sample can. Data were collected in the time-of-flight range 0.2 to 19.6 ms at 298 K, from the backscattering detectors ("C bank" 38 ^{3}He detectors). Only the data between 2.0 and 19.5 ms were used in the refinement. The neutron scattering lengths[7] used were Zr = 0.7160, Ce = 0.4840 and O = 0.5803×10^{-12} cm.

4.3 Structural Determination

The various samples prepared as described above were subjected to initial structural examination using powder X-ray diffraction. In all cases the powder patterns studied could be indexed based on the pyrochlore structure. Refinement of the lattice parameter indicated a continuous variation with the reaction time used in the chemical intercalation. Such a variation is indicative of a continuous range of solid solution.

The initial structural model for refinement was based on stoichiometric $Ce_2Zr_2O_7$, with the pyrochlore structure. This was used as a starting point for the refinements and a similar procedure was adopted for refining the structures of all the compositions. Initially the Ce and Zr ions were placed on the 16 c and 16d sites, and their occupancies were allowed to vary and exchange between the two sites in order to investigate anti-site disorder between the A and B sites, a common feature of many pyrochlore oxides. The refinement also explored the possibility of vacancies on the oxygen 48f and 8a sites. Two interstitial sites are available to oxide ions in the pyrochlore structure, the tetrahedral 8b site and the octahedral 32e site. The occupancies of these sites were also examined.

The scattering of X-rays by oxygen is weak compared with heavy atoms such as Ce and Zr. It is therefore not possible to establish the structures of $Ce_2Zr_2O_{7+x}$, and in particular the oxygen distribution, by X-ray methods. In contrast, the relative neutron scattering lengths of Ce, Zr and O (0.4840×10^{-12} cm, 0.7160×10^{-12} cm and 0.5803×10^{-12} cm respectively) make possible the refinement of the entire structure using neutron diffraction

All Rietveld refinement of the powder neutron diffraction data was carried out using the CCSL[8] suite of programs.

4.3.1 The Unintercalated Pyrochlore

Considering first the material synthesised at high temperature but not exposed to the chemical intercalation, a good fit was discovered to a near stoichiometric pyrochlore.

Table 4.3.1a Structural model for $Ce_2Zr_2O_7$.

Atom	**Site**	**x**	**y**	**z**
Ce	16c	0	0	0
Zr	16d	0.5	0.5	0.5
O1	48f	x = 0.39	0.125	0.125
O2	8a	0.125	0.125	0.125
O3	8b	0.375	0.375	0.375
O4	32e	x = y = z = 0.25		

The model shown above proved to give a good fit to the experimental data. Initial examination showed that a small amount of tetragonal ZrO_2 was present in the sample, and this was therefore included in a multiple phase refinement. A peak at 1.93 Å could not be indexed as belonging to either phase. It would seem that this peak belongs to a simple cubic structure related to CeO_2, and it was excluded from the data during refinement. This impurity was only present in one batch of the stoichiometric pyrochlore, and was not apparent in the initial powder X-ray diffraction pattern.

The crystallographic data and profile fit produced from the refinement are shown in Table 4.3.1b and Figure 4.3.1a.

Table 4.3.1b Crystallographic data from the neutron refinement of $Ce_2Zr_2O_{7.016}$.

$Ce_2Zr_2O_{7.016}$		a = 10.74748(3) Å		O1 x = 0.41701(9)		R_{wp} = 3.87		307 reflections	
Atom	**Site**	**B_{iso} /Å^2**	**B_{11} /Å^2**	**B_{22} /Å^2**	**B_{33} /Å^2**	**B_{23} /Å^2**	**B_{13} /Å^2**	**B_{12} /Å^2**	**Occup.**
Ce	16c	-	0.47(2)	0.47(2)	0.47(2)	0.04(3)	0.04(3)	0.04(3)	1
Zr	16d	-	0.290(14)	0.290(14)	0.290(14)	0.04(2)	0.04(2)	0.04(2)	1
O1	48f	-	0.94(3)	0.40(2)	0.40(2)	–0.25(3)	-	-	1
O2	8a	0.34(4)	-	-	-	-	-	-	0.930(15)
O3	8b	0.34(4)	-	-	-	-	-	-	0.086(7)

ZrO_2 impurity: Space group $P4_2/nmc$, 188 reflections; a = b = 3.60145(9), c = 5.2015(2) Å;

Zr x = 0.75, y = z = 0.25, B_{iso} = 0.42(4) Å^2; O x = y = 0.25, z = 0.4551(6), B_{iso} = 0.73(4) Å^2;

T.O.F. 3.0-19.5 ms, 3476 observations, χ^2 = 11.6402.

Figure 4.3.1a Profile fit from the neutron refinement of $Ce_2Zr_2O_{7.016}$.

Experimental data shown as dots, profile fit as a continuous line, and difference / e.s.d. is shown at the bottom. Upper tick marks are associated with the main phase, lower from ZrO_2.

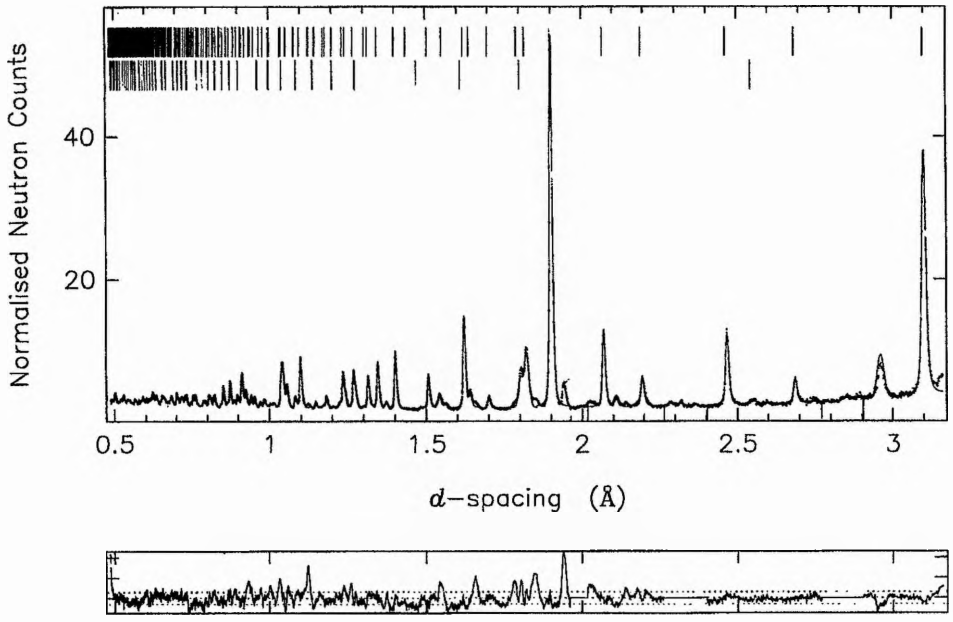

As expected in the pyrochlore structure, O1, the oxygen in the 48f tetrahedral site was fully occupied within experimental error (O1 occupancy 1.022(8)). However, O2, the 8a oxygen site which is normally fully occupied in pyrochlores refined to an occupancy of 0.930(15). Further analysis revealed that this 7% site vacancy is compensated by an almost identical occupancy of 0.086(9) in the normally empty 8b site at (0.375, 0.375, 0.375). The 32e octahedral oxygen site, O4, at (0.232(6), 0.232(6), 0.232(6)), was found to be completely vacant within experimental error, with an occupancy of -0.008(4). These results produce a stoichiometry for the phase of $Ce_2Zr_2O_{7.016(24)}$, i.e. it is stoichiometric within one e.s.d.

The existence of oxide ions on the 8a site in ideal pyrochlore is related to satisfying the coordination requirements of the cations. Figure 4.3.1c shows how the cations are coordinated to the 8a and 8b sites. The larger A cations preferring 8 coordinate sites whereas the B site ions prefer 6. Disorder of 8a to 8b oxygen sites is often related to anti-site disorder of the cations i.e. disorder between the A and B site cations[9]. However, both cation site occupancies were full within experimental error, suggesting that there is no *measurable* anti-site disorder (Ce occupancy 0.980(12), Zr occupancy 0.978(11)). The second type of disorder important in pyrochlores concerns a Frenkel-like disorder on the anion sublattice. In this case, oxygen ions leave the normally occupied 48f sites and enter the 8b interstitial sites, thereby forming oxygen vacancy-interstitial pairs[9]. Again, this hypothesis is unlikely since the O1, 48f site was found to be fully occupied.

These results imply that there is an intrinsic disorder of the oxygen in the anion sublattice, between the 8a and 8b sites, even at the stoichiometric composition of $Ce_2Zr_2O_7$. Since the 8a or 8b sites are not interconnected, the transport between these sites must occur by some vacancy motion within the 48f sublattice, or via the 32e tetrahedral site.

Figure 4.3.1c Cation Local Coordination in $Ce_2Zr_2O_7$.

Ce (16c) are shown as green, Zr (16d) purple, O1 (48f) red, O2 (8a) blue and O3 (8b) yellow spheres.

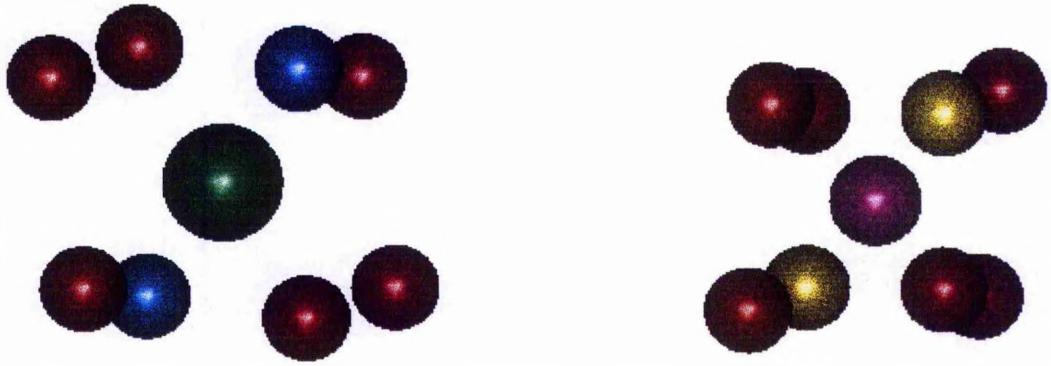

The location of Ce in the 16c site with the resultant filling of the 8a site suggests that the cerium is indeed the larger A cation, requiring an eight coordinate site. It can be concluded that the cerium oxidation state is unchanged from that in the starting material i.e. +3, which has an ionic radius of 1.143 Å in an 8 coordinate site. Similarly, from the low occupancy of the 8b site it may also be concluded that the nominal oxidation state of the B cation, zirconium, in the 16d site +4, which has an ionic radius of 0.72 Å in a 6 coordinate site (Table 4.3.1c).

Table 4.3.1c Effective ionic radii for various coordination numbers[10].

Element	**6 Coordinate / Å**	**7 Coordinate / Å**	**8 Coordinate / Å**
Ce^{3+}	1.01	1.07	1.143
Ce^{4+}	0.87	-	0.97
Zr^{4+}	0.72	0.78	0.84

4.3.2 Non-stoichiometric $Ce_2Zr_2O_{7+x}$

4.3.2.1 Room Temperature Oxidations of $Ce_2Zr_2O_7$

The elucidation of the structure of the stoichiometric pyrochlore, $Ce_2Zr_2O_7$, provides the foundation for a more complete analysis of the $Ce_2Zr_2O_{7+x}$ system, $0 \leq x \leq 1$. The flexibility inherent in the pyrochlore structure due to the presence of the vacant 8b interstitial site produces a theoretical oxidation limit of $Ce_2Zr_2O_8$, if the 8b site were to become completely filled, forming a cation ordered fluorite structure. This would correspond to an increase in the Ce oxidation state from +3 to +4.

Fifteen samples were prepared by room temperature oxygen intercalation and analysed by powder neutron diffraction, up to a maximum oxidation limit of $Ce_2Zr_2O_{7.36(3)}$ (as determined from the refinement). The crystallographic data are shown in Tables 4.3.2a-4.3.2o, with the corresponding profile fits in Figures 4.3.2a-4.3.2o. The atomic coordinates are given in Table 4.3.1a. A number of the samples were found to contain a small amount of ZrO_2 impurity, and this phase was included in a multipattern refinement.

For each sample the cerium and zirconium site occupancies were refined to determine the existence of any anti-site defects. None was found with full occupancy being obtained for each site within two e.s.d.'s (Table 4.3.2p).

In order to check for Frenkel defects on the anion sublattice, the temperature factors of the four oxygen sites were constrained to be equivalent and the occupancies allowed to refine freely. The O1, 48f oxygen site was fully occupied within 2 e.s.d.'s in each sample, indicating that there is no displacement from this site. Any occupancy of the O3 (8b) site is therefore from the oxidation of the sample rather than an intrinsic displacement from the 48f site. The O2 and O3 (8a and 8b) site occupancies were found to vary depending upon the total oxygen content and are examined in detail in the next section. The last interstitial site to be investigated is the 32e at approximately (0.25, 0.25, 0.25). It was found to be vacant in all cases.

Table 4.3.2p Site occupancies for selected $Ce_2Zr_2O_{7+x}$ stoichiometries.

Variable	$Ce_2Zr_2O_{7.016}$	$Ce_2Zr_2O_{7.190}$	$Ce_2Zr_2O_{7.297}$
Ce (16c) Occup.	0.980(12)	0.97(2)	1.014(11)
Zr (16d) Occup.	0.978(11)	0.98(2)	0.997(10)
O1 (48f) Occup.	1.012(7)	1.013(8)	1.002(7)
O2 (8a) Occup.	0.930(15)	0.83(2)	0.99(2)
O3 (8b) Occup.	0.086(7)	0.36(16)	0.307(11)
O4 (32e) Occup.	–0.007(3)	–0.005(4)	–0.016(4)
O4 x = y = z	0.266(6)	0.257(4)	0.220(4)
R_{wp}	3.87	4.17	2.97
Total O content	7.02(2)	7.19(4)	7.30(3)

Examination of Fourier maps gave no indication of the presence of any other interstitial species. These findings show that only the Ce, Zr, and O1-O3 sites need to be considered in the refinement of the oxidised samples, producing the definitive structural model for the $Ce_2Zr_2O_{7+x}$ system shown in Table 4.3.2q. In the final refinements for each composition the occupancy of the Ce and Zr ions were fixed at unity on the 16c and 16d sites respectively, as was the occupancy of the 48f site.

Table 4.3.2q Final structural model for $Ce_2Zr_2O_{7+x}$.

Atom	Site	x	y	z
Ce	16c	0	0	0
Zr	16d	0.5	0.5	0.5
O1	48f	$x \approx 0.41$	0.125	0.125
O2	8a	0.125	0.125	0.125
O3	8b	0.375	0.375	0.375

Table 4.3.2a Crystallographic data from the neutron refinement of $Ce_2Zr_2O_{7.054}$

$Ce_2Zr_2O_{7.054}$		a = 10.74014(4) Å		O1 x = 0.41602(11)		R_{wp} = 4.20		304 reflections	
Atom	**Site**	**B_{iso} /Å^2**	**B_{11} /Å^2**	**B_{22} /Å^2**	**B_{33} /Å^2**	**B_{23} /Å^2**	**B_{13} /Å^2**	**B_{12} /Å^2**	**Occup.**
Ce	16c	-	0.47(3)	0.47(3)	0.47(3)	–0.03(3)	–0.03(3)	–0.03(3)	1
Zr	16d	-	0.32(2)	0.32(2)	0.32(2)	0.06(2)	0.06(2)	0.06(2)	1
O1	48f	-	1.14(3)	0.42(2)	0.42(2)	–0.30(3)	-	-	1
O2	8a	0.42(5)	-	-	-	-	-	-	0.92(2)
O3	8b	0.42(5)	-	-	-	-	-	-	0.134(11)

ZrO_2 impurity: Space group $P4_2/nmc$, 188 reflections; a = b = 3.60269(9), c = 5.2022(2) Å;

Zr x = 0.75, y = z = 0.25, B_{iso} = 0.41(4) Å^2; O x = y = 0.25, z = 0.4551(6), B_{iso} = 0.79(5) Å^2.

T.O.F. 3.0-19.5 ms, 3588 observations, χ^2 = 13.1640.

Figure 4.3.2a Profile fit from the neutron refinement of $Ce_2Zr_2O_{7.054}$.

Experimental data shown as dots, profile fit as a continuous line, and difference / e.s.d. is shown at the bottom. Upper tick marks are associated with the main phase, lower from ZrO_2.

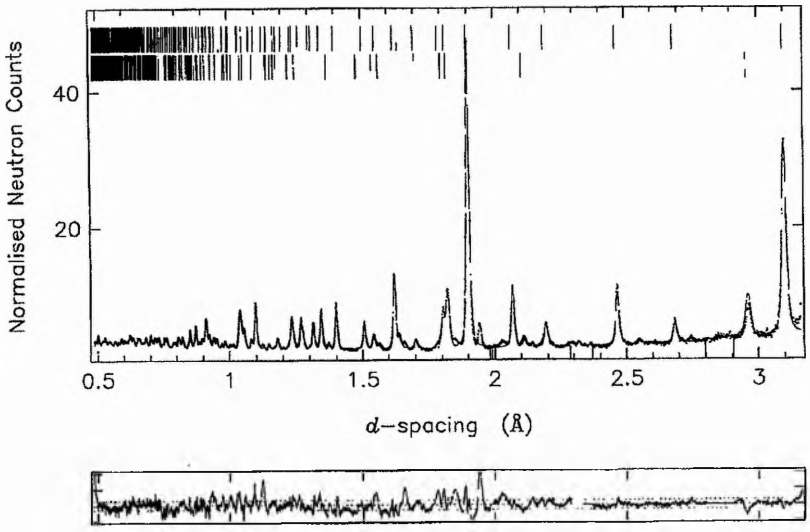

Table 4.3.2b Crystallographic data from the neutron refinement of $Ce_2Zr_2O_{7.040}$.

$Ce_2Zr_2O_{7.040}$		a = 10.73075(5) Å		O1 x = 0.41523(12)		R_{wp} = 4.53		304 reflections	
Atom	**Site**	**B_{iso} /Å^2**	**B_{11} /Å^2**	**B_{22} /Å^2**	**B_{33} /Å^2**	**B_{23} /Å^2**	**B_{13} /Å^2**	**B_{12} /Å^2**	**Occup.**
Ce	16c	-	0.44(3)	0.44(3)	0.44(3)	–0.05(4)	–0.05(4)	–0.05(4)	1
Zr	16d	-	0.34(2)	0.34(2)	0.34(2)	0.08(2)	0.08(2)	0.08(2)	1
O1	48f	-	1.29(3)	0.40(2)	0.40(2)	–0.33(4)	-	-	1
O2	8a	0.32(6)	-	-	-	-	-	-	0.87(2)
O3	8b	0.32(6)	-	-	-	-	-	-	0.170(12)

ZrO_2 impurity: Space group $P4_2$ / *nmc*, 188 reflections; a = b = 3.60209(9), c = 5.2021(2) Å;

Zr x = 0.75, y = z = 0.25, B_{iso} = 0.41(4) Å^2; O x = y = 0.25, z = 0.4556(6), B_{iso} = 0.80(6) Å^2.

T.O.F. 3.0-19.5 ms, 3606 observations, χ^2 = 15.9375.

Figure 4.3.2b Profile fit from the neutron refinement of $Ce_2Zr_2O_{7.040}$.

Experimental data shown as dots, profile fit as a continuous line, and difference / e.s.d. is shown at the bottom. Upper tick marks are associated with the main phase, lower from ZrO_2.

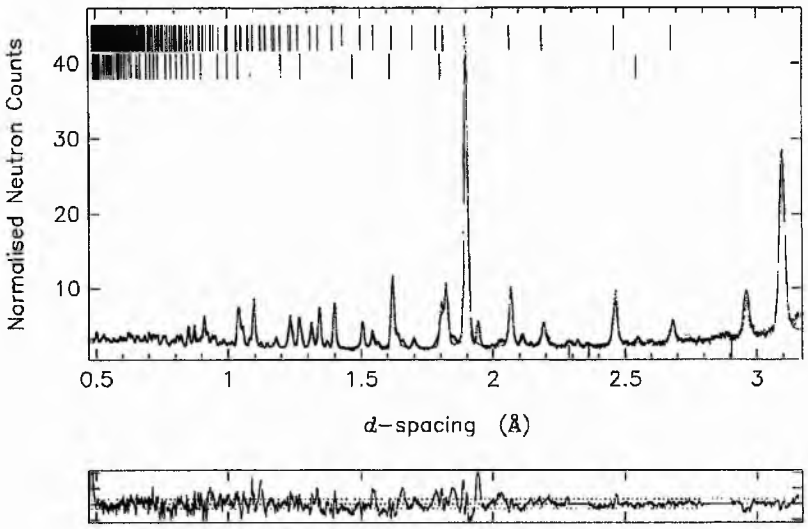

Table 4.3.2c Crystallographic data from the neutron refinement of $Ce_2Zr_2O_{7.093}$.

$Ce_2Zr_2O_{7.093}$		a = 10.71432(6) Å		O1 x = 0.41426(13)		R_{wp} = 4.42, 3.0-19.5 ms		304 reflections	
Atom	**Site**	B_{iso} /Å^2	B_{11} /Å^2	B_{22} /Å^2	B_{33} /Å^2	B_{23} /Å^2	B_{13} /Å^2	B_{12} /Å^2	**Occup.**
Ce	16c	-	0.40(3)	0.40(3)	0.40(3)	–0.06(4)	–0.06(4)	–0.06(4)	1
Zr	16d	-	0.35(2)	0.35(2)	0.35(2)	0.11(3)	0.11(3)	0.11(3)	1
O1	48f	-	1.40(4)	0.37(2)	0.37(2)	–0.39(4)	-	-	1
O2	8a	0.28(6)	-	-	-	-	-	-	0.87(2)
O3	8b	0.28(6)	-	-	-	-	-	-	0.223(13)

ZrO_2 impurity: Space group $P4_2/nmc$, 187 reflections; a = b = 3.59995(10), c = 5.2008(3) Å;

Zr x = 0.75, y = z = 0.25, B_{iso} = 0.38(4) Å^2; O x = y = 0.25, z = 0.4562(7), B_{iso} = 0.82(6) Å^2.

T.O.F. 3.0-19.5 ms, 3575 observations, χ^2 = 14.8921.

Figure 4.3.2c Profile fit from the neutron refinement of $Ce_2Zr_2O_{7.093}$.

Experimental data shown as dots, profile fit as a continuous line, and difference / e.s.d. is shown at the bottom. Upper tick marks are associated with the main phase, lower from ZrO_2.

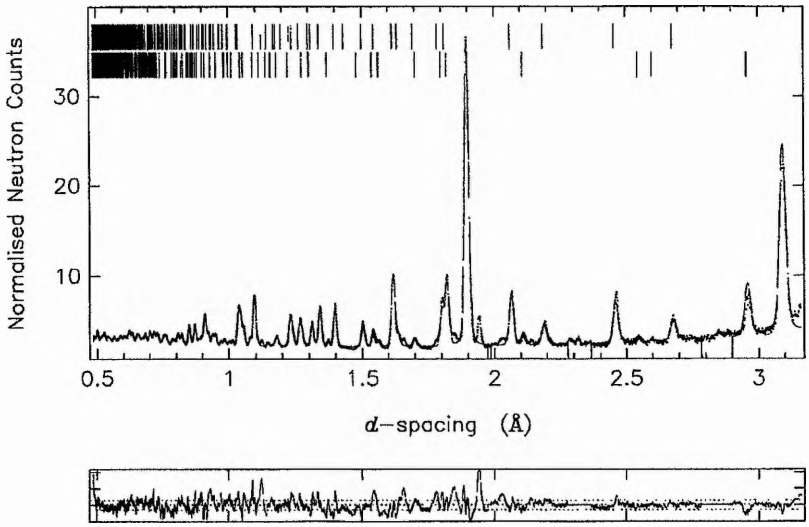

Table 4.3.2d Crystallographic data from the neutron refinement of $Ce_2Zr_2O_{7.108}$.

$Ce_2Zr_2O_{7.108}$		a = 10.70609(5) Å		O1 x = 0.41312(13)		R_{wp} = 4.39		304 reflections	
Atom	**Site**	**B_{iso} /Å²**	**B_{11} /Å²**	**B_{22} /Å²**	**B_{33} /Å²**	**B_{23} /Å²**	**B_{13} /Å²**	**B_{12} /Å²**	**Occup.**
Ce	16c	-	0.42(4)	0.42(4)	0.42(4)	-0.08(4)	-0.08(4)	-0.08(4)	1
Zr	16d	-	0.38(3)	0.38(3)	0.38(3)	0.15(3)	0.15(3)	0.15(3)	1
O1	48f	-	1.60(5)	0.36(3)	0.36(3)	-0.38(4)	-	-	1
O2	8a	0.29(6)	-	-	-	-	-	-	0.85(2)
O3	8b	0.29(6)	-	-	-	-	-	-	0.258(13)

ZrO_2 impurity: Space group $P4_2/nmc$, 188 reflections; a = b = 3.60080(8), c = 5.2027(2) Å;

Zr x = 0.75, y = z = 0.25, B_{iso} = 0.37(5) Å²; O x = y = 0.25, z = 0.4566(7), B_{iso} = 0.80(6) Å².

T.O.F. 3.0-19.5 ms, 3566 observations, χ^2 = 20.8459.

Figure 4.3.2d Profile fit from the neutron refinement of $Ce_2Zr_2O_{7.108}$.

Experimental data shown as dots, profile fit as a continuous line, and difference / e.s.d. is shown at the bottom. Upper set of tick marks are associated with the main phase, lower from ZrO_2.

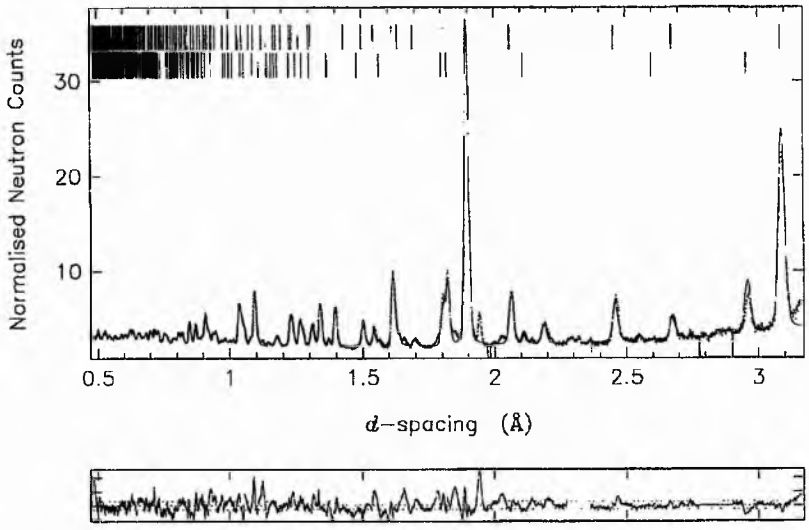

Table 4.3.2e Crystallographic data from the neutron refinement of $Ce_2Zr_2O_{7.190}$.

$Ce_2Zr_2O_{7.190}$		a = 10.67786(8) Å		O1 x = 0.4099(2)		R_{wp} = 4.16		300 reflections	
Atom	**Site**	**B_{iso} /Å^2**	**B_{11} /Å^2**	**B_{22} /Å^2**	**B_{33} /Å^2**	**B_{23} /Å^2**	**B_{13} /Å^2**	**B_{12} /Å^2**	**Occup.**
Ce	16c	-	0.46(4)	0.46(4)	0.46(4)	-0.10(4)	-0.10(4)	-0.10(4)	1
Zr	16d	-	0.47(3)	0.47(3)	0.47(3)	0.25(4)	0.25(4)	0.25(4)	1
O1	48f	-	2.10(6)	0.36(3)	0.36(3)	-0.43(5)	-	-	1
O2	8a	0.37(7)	-	-	-	-	-	-	0.83(2)
O3	8b	0.37(7)	-	-	-	-	-	-	0.36(2)

ZrO_2 impurity: Space group $P4_2$ / *nmc*, 188 reflections; a = b = 3.60079(15), c = 5.2048(4) Å;

Zr x = 0.75, y = z = 0.25, B_{iso} = 0.33(5) Å^2; O x = y = 0.25, z = 0.4589(8), B_{iso} = 0.83(6) Å^2.

T.O.F. 3.0-19.5 ms, 3659 observations, χ^2 = 7.7565.

Figure 4.3.2e Profile fit from the neutron refinement of $Ce_2Zr_2O_{7.190}$.

Experimental data shown as dots, profile fit as a continuous line, and difference / e.s.d. is shown at the bottom. Upper set of tick marks are associated with the main phase, lower from ZrO_2.

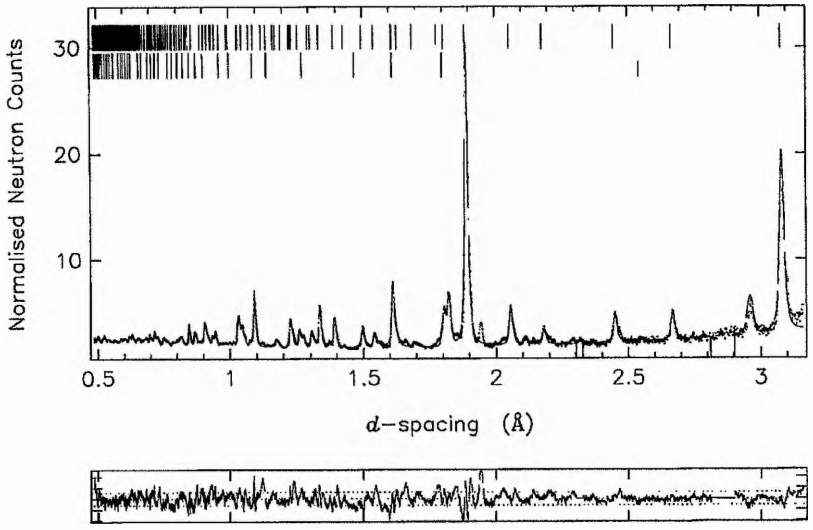

Table 4.3.2f Crystallographic data from the neutron refinement of $Ce_2Zr_2O_{7.261}$.

$Ce_2Zr_2O_{7.261}$		a = 10.67114(4) Å		O1 x = 0.41022(7)		R_{wp} = 3.11		941 reflections	
Atom	**Site**	**B_{iso}/Å^2**	**B_{11}**	**B_{22}**	**B_{33}**	**B_{23}**	**B_{13}**	**B_{12}**	**Occup.**
Ce	16c	-	0.287(14)	0.287(14)	0.287(14)	–0.07(2)	–0.07(2)	–0.07(2)	1
Zr	16d	-	0.564(13)	0.564(13)	0.564(13)	0.211(15)	0.211(15)	0.211(15)	1
O1	48f	-	1.96(3)	0.522(13)	0.522(13)	–0.41(2)	-	-	1
O2	8a	0.58(3)	-	-	-	-	-	-	0.951(10)
O3	8b	0.58(3)	-	-	-	-	-	-	0.310(7)

T.O.F. 2.0-19.5 ms, 4555 observations, $\chi^2 = 4.6120$.

Figure 4.3.2f Profile fit from the neutron refinement of $Ce_2Zr_2O_{7.261}$.

Experimental data shown as dots, profile fit as a continuous line, and difference / e.s.d. is shown at the bottom.Tick marks represent allowed reflections.

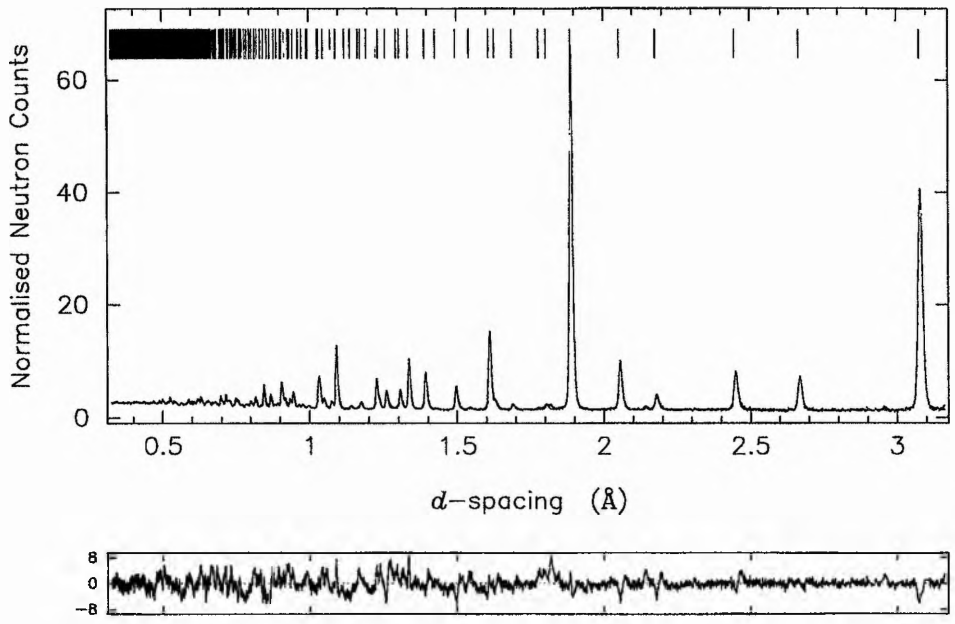

Table 4.3.2g Crystallographic data from the neutron refinement of $Ce_2Zr_2O_{7.254}$.

$Ce_2Zr_2O_{7.254}$		a = 10.66477(5) Å		O1 x = 0.40894(8)		R_{wp} = 3.29		941 reflections	
Atom	**Site**	**B_{iso}/Å^2**	**B_{11}**	**B_{22}**	**B_{33}**	**B_{23}**	**B_{13}**	**B_{12}**	**Occup.**
Ce	16c	-	0.33(2)	0.33(2)	0.33(2)	–0.08(2)	–0.08(2)	–0.08(2)	1
Zr	16d	-	0.563(15)	0.563(15)	0.563(15)	0.26(2)	0.26(2)	0.26(2)	1
O1	48f	-	2.14(3)	0.499(14)	0.499(14)	–0.40(2)	-	-	1
O2	8a	0.52(3)	-	-	-	-	-	-	0.904(11)
O3	8b	0.52(3)	-	-	-	-	-	-	0.350(8)

T.O.F. 2.0-19.5 ms, 4555 observations, χ^2 = 4.4639.

Figure 4.3.2g Profile fit from the neutron refinement of $Ce_2Zr_2O_{7.254}$.

Experimental data shown as dots, profile fit as a continuous line, and difference / e.s.d. is shown at the bottom. Tick marks represent allowed reflections.

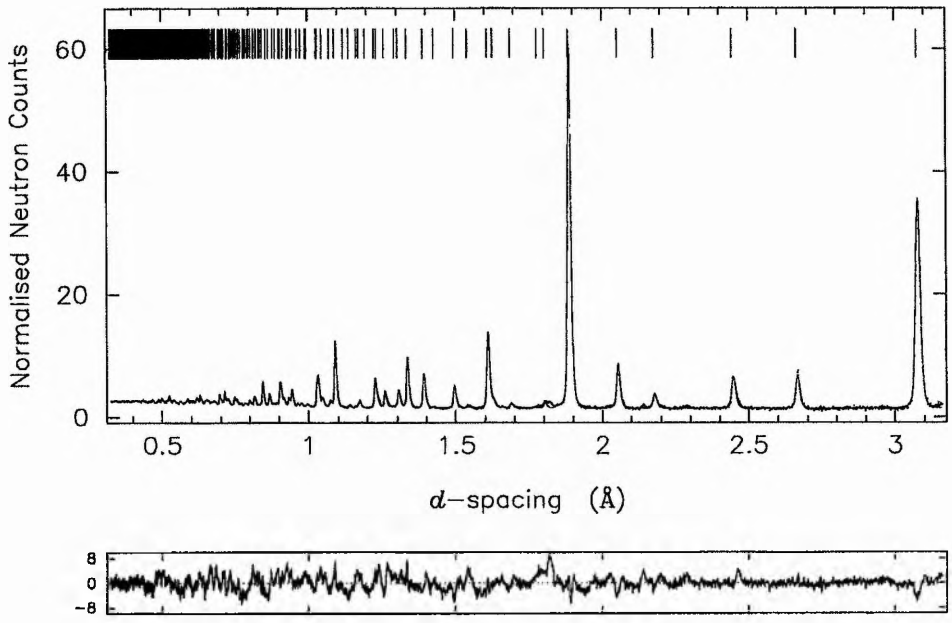

Table 4.3.2h Crystallographic data from the neutron refinement of $Ce_2Zr_2O_{7.257}$.

$Ce_2Zr_2O_{7.257}$		a = 10.66227(8) Å		O1 x = 0.40825(9)		R_{wp} = 2.73		939 reflections	
Atom	**Site**	**B_{iso} /Å²**	**B_{11} /Å²**	**B_{22} /Å²**	**B_{33} /Å²**	**B_{23} /Å²**	**B_{13} /Å²**	**B_{12} /Å²**	**Occup.**
Ce	16c	-	0.33(2)	0.33(2)	0.33(2)	–0.07(2)	–0.07(2)	–0.07(2)	1
Zr	16d	-	0.54(2)	0.54(2)	0.54(2)	0.26(2)	0.26(2)	0.26(2)	1
O1	48f	-	2.18(4)	0.47(2)	0.47(2)	–0.36(3)	-	-	1
O2	8a	0.51(4)	-	-	-	-	-	-	0.894(13)
O3	8b	0.51(4)	-	-	-	-	-	-	0.363(10)

T.O.F. 2.0-19.5 ms, 4555 observations, χ^2 = 1.8273.

Figure 4.3.2h Profile fit from the neutron refinement of $Ce_2Zr_2O_{7.257}$.

Experimental data shown as dots, profile fit as a continuous line, and difference / e.s.d. is shown at the bottom. Tick marks represent allowed reflections.

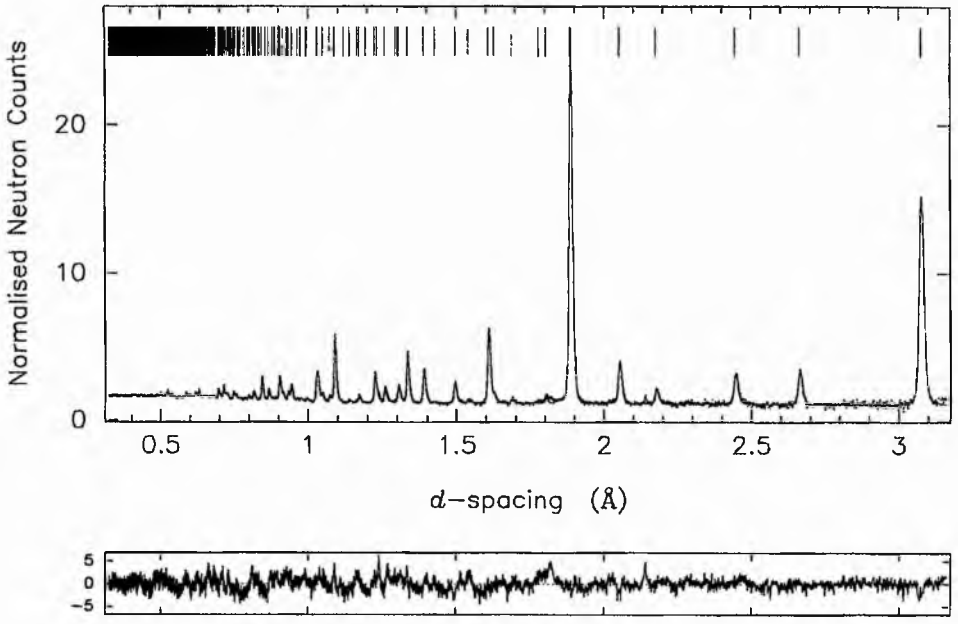

Table 4.3.2i Crystallographic data from the neutron refinement of $Ce_2Zr_2O_{7.291}$.

$Ce_2Zr_2O_{7.291}$		a = 10.66097(3) Å		O1 x = 0.40873(6)		R_{wp} = 2.99		939 reflections	
Atom	**Site**	**B_{iso} /Å^2**	**B_{11} /Å^2**	**B_{22} /Å^2**	**B_{33} /Å^2**	**B_{23} /Å^2**	**B_{13} /Å^2**	**B_{12} /Å^2**	**Occup.**
Ce	16c	-	0.328(13)	0.328(13)	0.328(13)	–0.09(2)	–0.09(2)	–0.09(2)	1
Zr	16d	-	0.609(13)	0.609(13)	0.609(13)	0.286(14)	0.286(14)	0.286(14)	1
O1	48f	-	2.17(3)	0.517(12)	0.517(12)	–0.37(2)	-	-	1
O2	8a	0.65(3)	-	-	-	-	-	-	0.958(9)
O3	8b	0.65(3)	-	-	-	-	-	-	0.333(7)

T.O.F. 2.0-19.5 ms, 4555 observations, χ^2 = 6.3883.

Figure 4.3.2i Profile fit from the neutron refinement of $Ce_2Zr_2O_{7.291}$.

Experimental data shown as dots, profile fit as a continuous line, and difference / e.s.d. is shown at the bottom. Tick marks represent allowed reflections.

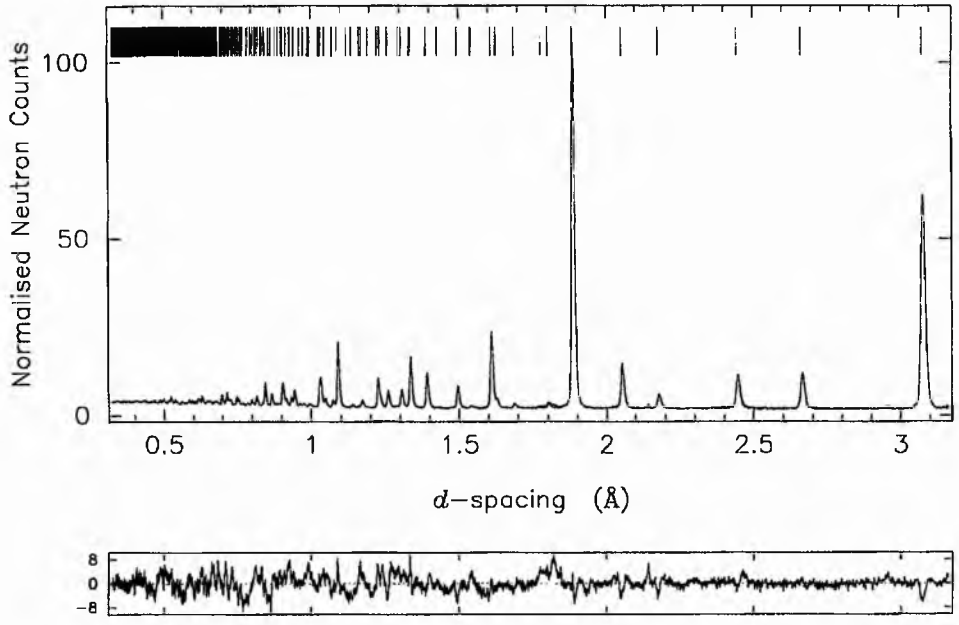

Table 4.3.2j Crystallographic data from the neutron refinement of $Ce_2Zr_2O_{7.298}$.

$Ce_2Zr_2O_{7.298}$		a = 10.65941(4) Å		O1 x = 0.40851(7)		R_{wp} = 1.80		939 reflections	
Atom	**Site**	**B_{iso} /Å^2**	**B_{11} /Å^2**	**B_{22} /Å^2**	**B_{33} /Å^2**	**B_{23} /Å^2**	**B_{13} /Å^2**	**B_{12} /Å^2**	**Occup.**
Ce	16c	-	0.33(2)	0.33(2)	0.33(2)	–0.03(2)	–0.03(2)	–0.03(2)	1
Zr	16d	-	0.573(15)	0.573(15)	0.573(15)	0.24(2)	0.24(2)	0.24(2)	1
O1	48f	-	2.16(3)	0.520(14)	0.520(14)	–0.34(2)	-	-	1
O2	8a	0.65(3)	-	-	-	-	-	-	0.961(10)
O3	8b	0.65(3)	-	-	-	-	-	-	0.337(8)

T.O.F. 2.0-19.5 ms, 4555 observations, χ^2 = 3.0218.

Figure 4.3.2j Profile fit from the neutron refinement of $Ce_2Zr_2O_{7.298}$.

Experimental data shown as dots, profile fit as a continuous line, and difference / e.s.d. is shown at the bottom. Tick marks represent allowed reflections.

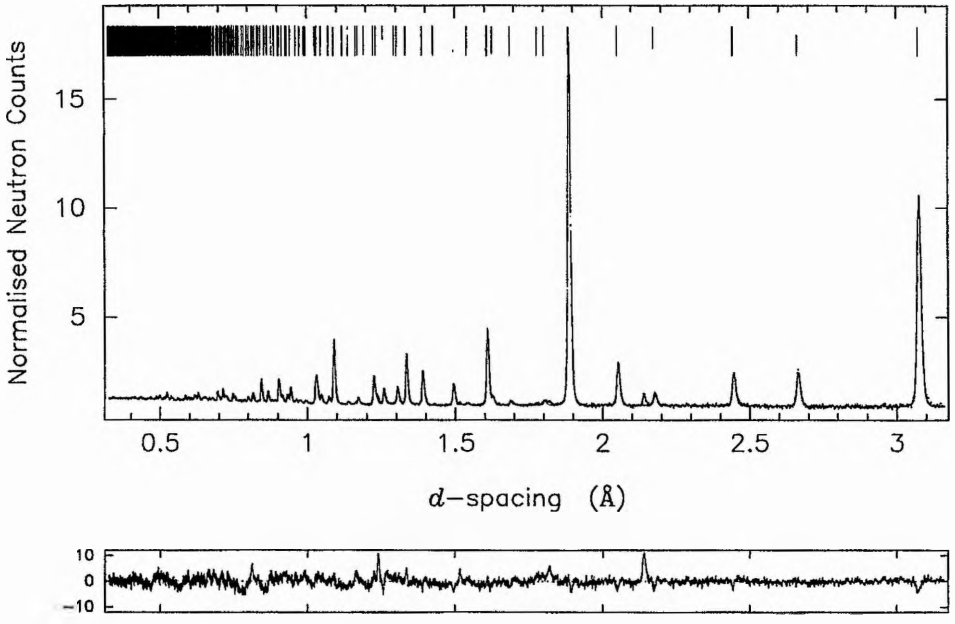

Table 4.3.2k Crystallographic data from the neutron refinement of $Ce_2Zr_2O_{7.279}$.

$Ce_2Zr_2O_{7.279}$		a = 10.65570(5) Å		O1 x = 0.40827(9)		R_{wp} = 2.64		300 reflections	
Atom	**Site**	**B_{iso} /Å^2**	**B_{11} /Å^2**	**B_{22} /Å^2**	**B_{33} /Å^2**	**B_{23} /Å^2**	**B_{13} /Å^2**	**B_{12} /Å^2**	**Occup.**
Ce	16c	-	0.34(2)	0.34(2)	0.34(2)	–0.06(2)	–0.06(2)	–0.06(2)	1
Zr	16d	-	0.69(2)	0.69(2)	0.69(2)	0.33(2)	0.33(2)	0.33(2)	1
O1	48f	-	2.31(4)	0.56(2)	0.56(2)	–0.42(3)	-	-	1
O2	8a	0.70(4)	-	-	-	-	-	-	0.971(15)
O3	8b	0.70(4)	-	-	-	-	-	-	0.308(10)

ZrO_2 impurity: Space group $P2_1$ / c; a = 5.15286(15), b = 5.2037(5), c = 5.31880(14) Å; β = 99.09°; Zr x = 0.2847, y = 0.0350, z = 0.2157, B_{iso} = 0.47 Å^2; O1 x = 0.0565, y = 0.3237, z = 0.3377, B_{iso} = 0.63 Å^2; O2 x = 0.4509, y = 0.7519, z = 0.4821, B_{iso} = 0.06 Å^2. T.O.F. 3.0-19.5 ms, 3667 observations, χ^2 = 3.3532.

Figure 4.3.2k Profile fit from the neutron refinement of $Ce_2Zr_2O_{7.279}$.

Experimental data shown as dots, profile fit as a continuous line, and difference / e.s.d. is shown at the bottom. Upper set of tick marks associated with the main phase, lower from ZrO_2.

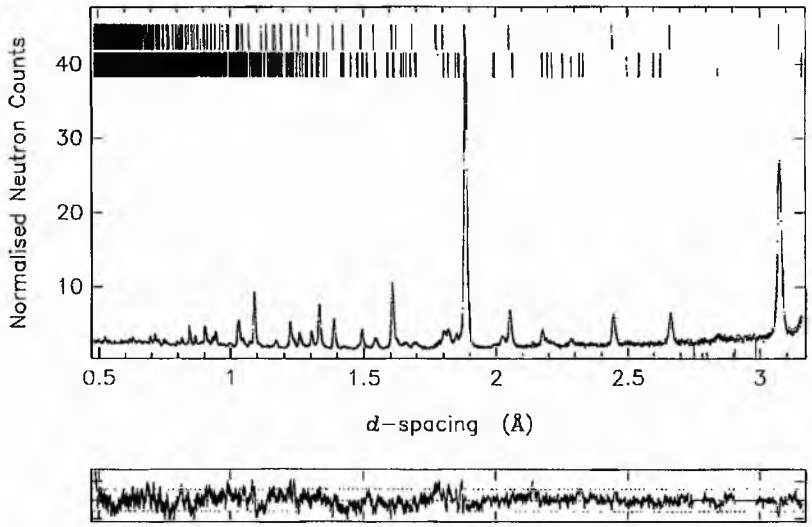

Table 4.3.2l Crystallographic data from the neutron refinement of $Ce_2Zr_2O_{7.297}$.

$Ce_2Zr_2O_{7.297}$		a = 10.65371(4) Å		O1 x = 0.40820(10)		R_{WD} = 2.98		299 reflections	
Atom	**Site**	**B_{iso} /Å^2**	**B_{11} /Å^2**	**B_{22} /Å^2**	**B_{33} /Å^2**	**B_{23} /Å^2**	**B_{13} /Å^2**	**B_{12} /Å^2**	**Occup.**
Ce	16c	-	0.45(3)	0.45(3)	0.45(3)	–0.08(3)	–0.08(3)	–0.08(3)	1
Zr	16d	-	0.73(2)	0.73(2)	0.73(2)	0.34(3)	0.34(3)	0.34(3)	1
O1	48f	-	2.49(5)	0.60(2)	0.60(2)	–0.39(3)	-	-	1
O2	8a	0.69(5)	-	-	-	-	-	-	0.99(2)
O3	8b	0.60(5)	-	-	-	-	-	-	0.307(11)

ZrO_2 impurity: Space group $P2_1$ / c; a = 5.15039(14), b = 5.2053(4), c = 5.31724(13) Å; β = 99.09°; Zr x = 0.2851, y = 0.0350, z = 0.2165, B_{iso} = 0.63 Å^2; O1 x = 0.0536, y = 0.3239, z = 0.3392, B_{iso} = 0.80 Å^2; O2 x = 0.4529, y = 0.7507, z = 0.4824, B_{iso} = 0.21 Å^2. T.O.F. 3.0-19.5 ms, 3672 observations, χ^2 = 6.1234.

Figure 4.3.2l Profile fit from the neutron refinement of $Ce_2Zr_2O_{7.297}$.

Experimental data shown as dots, profile fit as a continuous line, and difference / e.s.d. is shown at the bottom. Upper set of tick marks associated with the main phase, lower from ZrO_2.

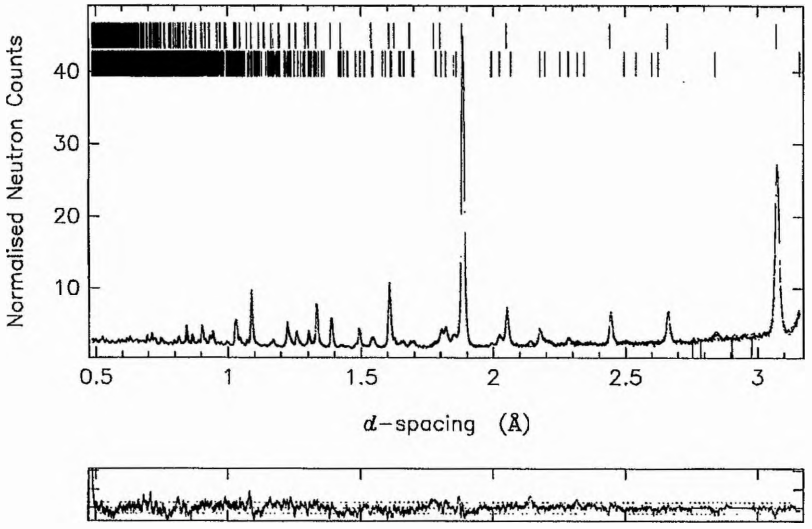

Table 4.3.2m Crystallographic data from the neutron refinement of $Ce_2Zr_2O_{7.298'}$.

$Ce_2Zr_2O_{7.298'}$		a = 10.65149(3) Å		O1 x = 0.40838(7)		R_{wp} = 3.09		939 reflections	
Atom	**Site**	**B_{iso} /Å^2**	**B_{11} /Å^2**	**B_{22} /Å^2**	**B_{33} /Å^2**	**B_{23} /Å^2**	**B_{13} /Å^2**	**B_{12} /Å^2**	**Occup.**
Ce	16c	-	0.315(14)	0.315(14)	0.315(14)	–0.09(2)	–0.09(2)	–0.09(2)	1
Zr	16d	-	0.596(13)	0.596(13)	0.596(13)	0.298(15)	0.298(15)	0.298(15)	1
O1	48f	-	2.20(3)	0.510(12)	0.510(12)	–0.38(2)	-	-	1
O2	8a	0.68(3)	-	-	-	-	-	-	0.956(10)
O3	8b	0.68(3)	-	-	-	-	-	-	0.342(7)

T.O.F. 2.0-19.5 ms, 4555 observations, χ^2 = 4.7768.

Figure 4.3.2m Profile fit from the neutron refinement of $Ce_2Zr_2O_{7.298'}$.

Experimental data shown as dots, profile fit as a continuous line, and difference / e.s.d. is shown at the bottom. Tick marks represent allowed reflections.

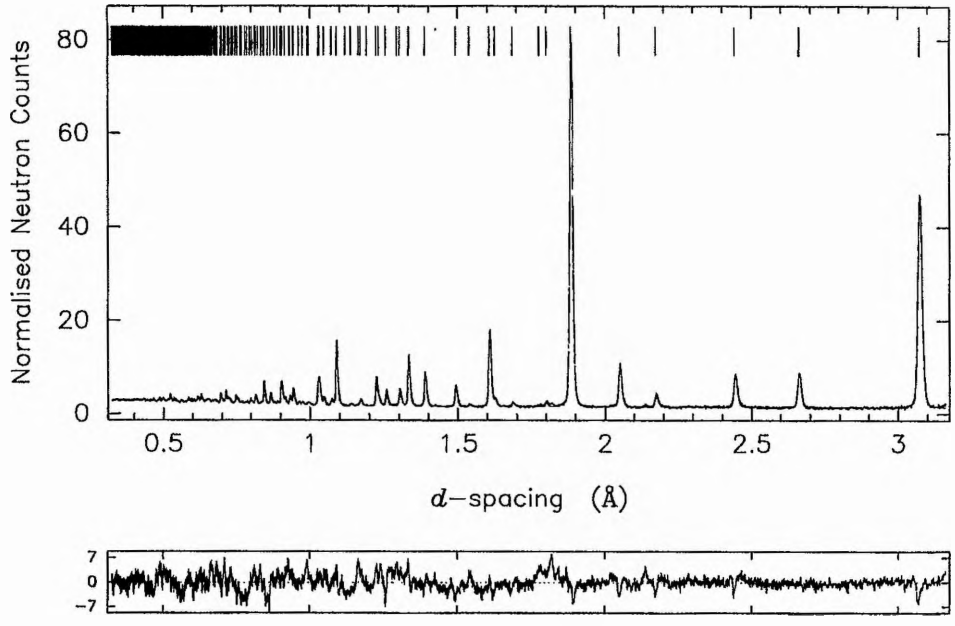

Table 4.3.2n Crystallographic data from the neutron refinement of $Ce_2Zr_2O_{7.287}$.

$Ce_2Zr_2O_{7.287}$		a = 10.64595(3) Å		O1 x = 0.40816(7)		R_{wp} = 2.96		939 reflections	
Atom	**Site**	**B_{iso} /Å^2**	**B_{11} /Å^2**	**B_{22} /Å^2**	**B_{33} /Å^2**	**B_{23} /Å^2**	**B_{13} /Å^2**	**B_{12} /Å^2**	**Occup.**
Ce	16c	-	0.295(14)	0.295(14)	0.295(14)	–0.09(2)	–0.09(2)	–0.09(2)	1
Zr	16d	-	0.585(14)	0.585(14)	0.585(14)	0.32(2)	0.32(2)	0.32(2)	1
O1	48f	-	2.20(3)	0.471(12)	0.471(12)	–0.37(2)	-	-	1
O2	8a	0.63(3)	-	-	-	-	-	-	0.957(10)
O3	8b	0.63(3)	-	-	-	-	-	-	0.330(7)

T.O.F. 2.0-19.5 ms, 4555 observations, χ^2 = 4.5285.

Figure 4.3.2n Profile fit from the neutron refinement of $Ce_2Zr_2O_{7.287}$.

Experimental data shown as dots, profile fit as a continuous line, and difference / e.s.d. is shown at the bottom. Tick marks represent allowed reflections.

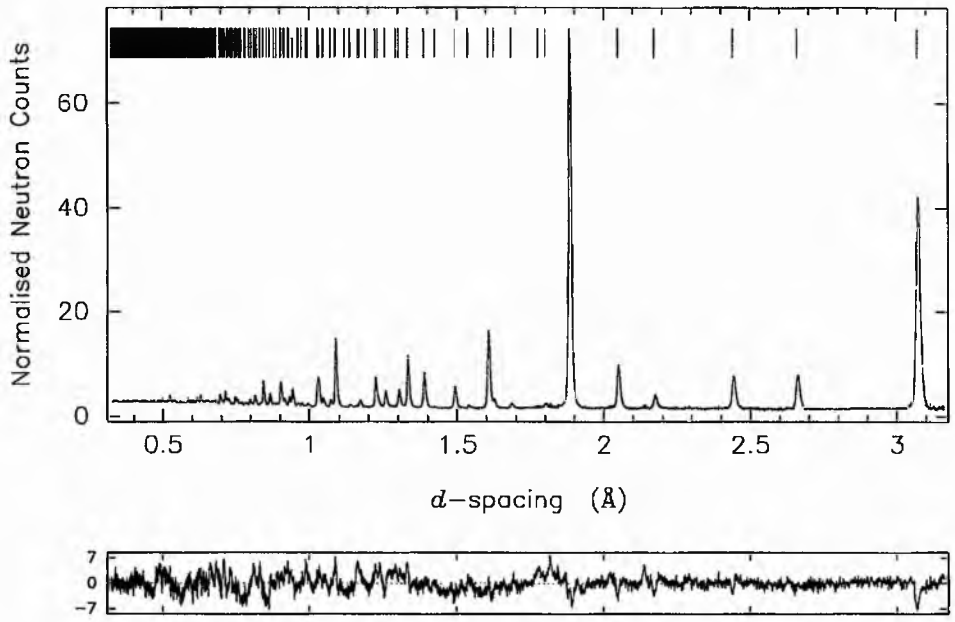

Table 4.3.2o Crystallographic data from the neutron refinement of $Ce_2Zr_2O_{7.357}$.

$Ce_2Zr_2O_{7.357}$		a = 10.64401(7) Å		O1 x = 0.40586(11)		R_{wp} = 2.94		299 reflections	
Atom	**Site**	**B_{iso} /Å^2**	**B_{11} /Å^2**	**B_{22} /Å^2**	**B_{33} /Å^2**	**B_{23} /Å^2**	**B_{13} /Å^2**	**B_{12} /Å^2**	**Occup.**
Ce	16c	-	0.42(3)	0.42(3)	0.42(3)	–0.08(3)	–0.08(3)	–0.08(3)	1
Zr	16d	-	0.68(2)	0.68(2)	0.68(2)	0.32(3)	0.32(3)	0.32(3)	1
O1	48f	-	2.54(5)	0.52(2)	0.52(2)	–0.28(3)	-	-	1
O2	8a	0.92(5)	-	-	-	-	-	-	1.01(2)
O3	8b	0.92(5)	-	-	-	-	-	-	0.357(12)

ZrO_2 impurity: Space group $P4_2$ / *nmc*, 188 reflections; a = b = 3.5977(7), c = 5.185(2) Å;

Zr x = 0.75, y = z = 0.25, B_{iso} = 0.41(5) Å^2; O x = y = 0.25, z = 0.4634(8), B_{iso} = 0.78(6) Å^2.

T.O.F. 3.0-19.5 ms, 3467 observations, χ^2 = 2.2522.

Figure 4.3.2o Profile fit from the neutron refinement of $Ce_2Zr_2O_{7.357}$.

Experimental data shown as dots, profile fit as a continuous line, and difference / e.s.d. is shown at the bottom. Upper set of tick marks are associated with main phase, lower from ZrO_2.

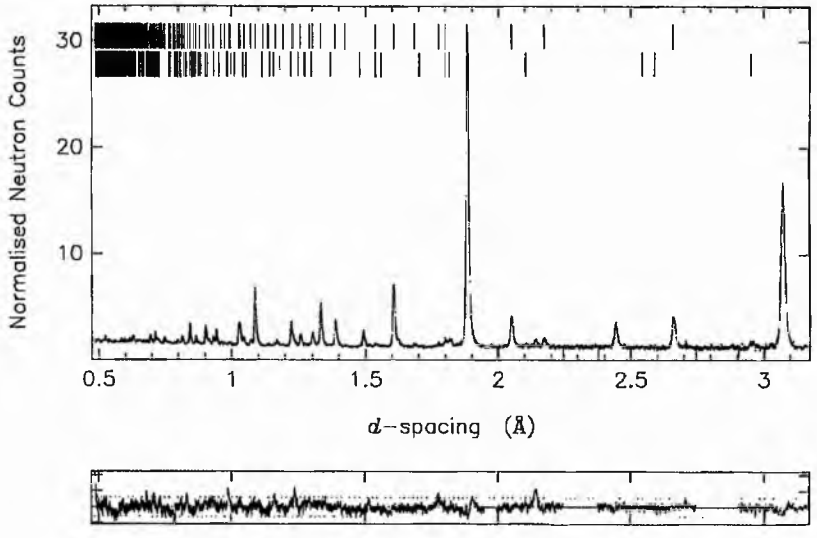

4.3.2.2 Thermal Oxidation of $Ce_2Zr_2O_7$

The previous section has examined the results of a topotactic chemical oxygen insertion reaction at room temperature.

The thermal behaviour of a sample of $Ce_2Zr_2O_7$ was investigated using thermogravimetric analysis. Figure 4.3.2p shows the thermogravimetric analysis trace of a sample of $Ce_2Zr_2O_7$ in the range 25 - 1300°C in air. It can be seen that the sample exhibits an increase in mass above 150°C due to oxygen uptake. However, above 1200°C there is a gradual loss in sample weight as the sample loses oxygen. This is the reason why the improved synthesis of $Ce_2Zr_2O_7$ was carried out at 1300°C, in order to prevent oxygen uptake and produce a material which was found to be stoichiometric by powder neutron diffraction.

Figure 4.3.2p Thermogravimetric Analysis trace of $Ce_2Zr_2O_7$ in the range 25 - 1300°C at a heating/cooling rate of 10°Cmin^{-1} in air.

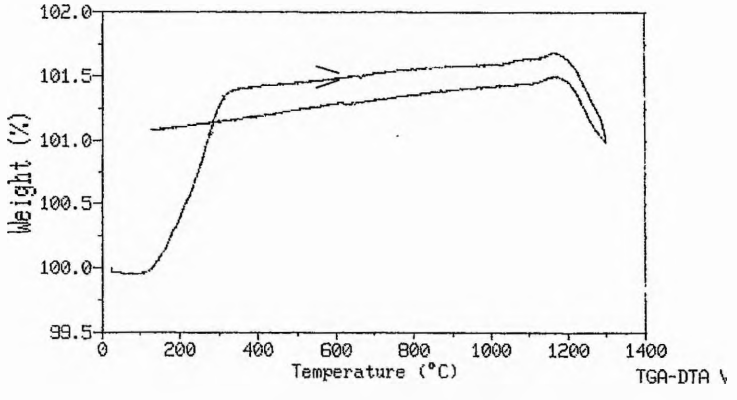

The thermal oxidation of a $Ce_2O_3.2ZrO_2$ mixture at temperatures in excess of 1500°C in air is known to result in the formation of a mixture of tetragonal zirconia, a cubic phase rich in ceria, and the pyrochlore phase[10]. In order to investigate the effects of the thermal oxidation of the pyrochlore at temperatures below this phase segregation

threshold, a sample of $Ce_2Zr_2O_7$ was heated at 500°C in flowing oxygen. The powder X-ray diffraction pattern of the product phase showed the fingerprint of the pyrochlore structure, with a greatly reduced lattice parameter of a = 10.5488(2) Å, and no impurities.

However, analysis of the powder neutron diffraction data of this thermally oxidised material revealed a number of additional weak reflections in the range 2.1-2.6 Å, which could not be assigned in the space group $Fd\bar{3}m$. This observation implies that the new structure is similar, but not identical to pyrochlore. The weak additional reflections could be indexed on the cubic unit cell obtained from X-ray diffraction, a = 10.5488(2) Å, but in the lower symmetry space group $Pm\bar{3}m$, or by doubling this cell length the pattern could be indexed in $Fm\bar{3}m$ or $Fd\bar{3}m$. However, all of the options necessitated removing the cation sublattice ordering in any of these possibilities.

The two maximal non-isomorphic subgroups of the space group $Fd\bar{3}m$ are $I4_1/amd$ and $R\bar{3}m$, with no transformation in the size of the unit cell. The tetragonal space group does not preserve the Ce and Zr ordering, however, the rhombohedral space group $R\bar{3}m$ does allow the conservation of the cation sublattice.

The model used in the solution of the pyrochlore structure can therefore be translated into the rhombohedral space group. This new model is described in Table 4.3.2r. It can be used to generate all the original atomic positions in the new space group, but allows an increased flexibility in the site positions because of the lower symmetry.

An initial analysis showed that this model provided a good fit to the data. All the cation sites were found to be fully occupied to within 2 e.s.d.'s. Analysis of the O site occupancies showed that O5 - O10, the 48f oxygen sites in the pyrochlore space group, were fully occupied to within 2 e.s.d.'s. The occupancies of these sites were therefore fixed at 1.0 for the remainder of the refinement.

Table 4.3.2r Atomic parameters of the thermally oxidised $Ce_2Zr_2O_{7+x}$ sample. Space Group $R\bar{3}m$.

Atom	**Site**	**x**	**y**	**z**	**$Fd\bar{3}m$ site**
Ce1	1a	0	0	0	Ce, 16c
Ce2	3e	0	0.5	0.5	Ce, 16c
Ce3	6h	0.25	0.25	0	Ce, 16c
Ce4	6g	0.25	–0.25	0.5	Ce, 16c
Zr1	1b	0.5	0.5	0.5	Zr, 16d
Zr2	3d	0.5	0	0	Zr, 16d
Zr3	6f	0.25	–0.25	0	Zr, 16d
Zr4	6h	0.25	0.25	0.5	Zr, 16d
O1	2c	0.125	0.125	0.125	O2, 8a
O2	6h	0.375	0.375	0.125	O2, 8a
O3	2c	0.375	0.375	0.375	O3, 8b
O4	6h	0.875	0.875	0.375	O3, 8b
O5	6g	x	0.125	0.125	O1, 48f
O6	12i	0.75 – x	0.125	0.625	O1, 48f
O7	12i	0.5 – x	0.875	0.375	O1, 48f
O8	6g	0.25 – x	0.375	0.375	O1, 48f
O9	6g	0.5 – x	0.625	0.625	O1, 48f
O10	6g	0.75 + x	0.125	0.125	O1, 48f

The O1 -O4 site occupancies (those oxygen sites generated from the 8a and 8b sites in the pyrochlore space group) were found to be 1.00(5), 0.77(4), 0.81(9) and 0.74(3) respectively, giving a total stoichiometry for the phase of $Ce_2Zr_2O_{7.59(7)}$. However, a comparison of the total oxygen content versus lattice parameter trend for the chemically oxidised samples (Figure 4.5.1, Section 4.5) suggests that a sample

with a lattice parameter of 10.54 Å would have a much higher oxygen content. As a result the octahedral interstitial sites within the structure were therefore investigated in an attempt to locate additional oxygen. The 32e interstitial site at (1/4, 1/4, 1/4) in the pyrochlore space group translates into the sites shown in Table 4.3.2s.

Table 4.3.2s Model for the octahedral intersitial site positions of the thermally oxidised $Ce_2Zr_2O_{7+x}$ sample. Space Group $R\bar{3}m$.

Atom	Site	x	y	z	Neighbours
O11	12i	0	0.50	0.75	Ce2,Ce3,Ce4,Zr2,Zr3,Zr4
O12	6h	0	0	0.25	Ce1,2×Ce3,Zr2,2×Zr3
O13	6h	0.50	0.50	0.25	Ce2,2×Ce4,Zr1,2×Zr4
O14	6h	0.25	0.25	0.75	Ce3,2×Ce4,2×Zr3,Zr4
O15	2c	0.25	0.25	0.25	3×Ce3,3×Zr4

The results of the Rietveld refinement of these sites and the corresponding occupancies are shown in Table 4.3.2t. All of the octahedral interstitial sites except the O11 (12i) site are unoccupied within two e.s.d.'s. The O11 site was therefore included in the final refinement. The extensive generation of Fourier maps encompassing the entire asymmetric unit did not reveal the existance of any further scattering intensity.

The final atomic coordinates from the refinement for the thermally oxidised sample are shown in Table 4.3.2u, selected bond lengths in Table 4.3.2v and the profile fit in Figure 4.3.2q. This rhombohedral structure is qualitatively very similar to that of the parent pyrochlore, but with a higher oxygen content than could be achieved by chemical oxidation. It is evident from the atomic coordinates that there is

It may be concluded therefore that the oxygen in the O11 site does not coordinate Zr^{4+}, this task is confined to oxygen in the O3 and O4 sites i.e. those equivalent to 8b in $Fd\bar{3}m$, and the other oxygen sites equivalent to 48f in $Fd\bar{3}m$. The sum of the O3 and O4 occupancies is 0.53, producing a coordination number around the Zr^{4+} of 7.06. The preferred coordination number for Zr^{4+} is observed to be 7 in many other structures e.g. the ZrO_2 structure at room temperature.

Figure 4.3.2q Profile fit for the thermally oxidised $Ce_2Zr_2O_{7+x}$ sample.
Experimental data shown as dots, profile fit as a continuous line and difference / e.s.d. at the bottom.

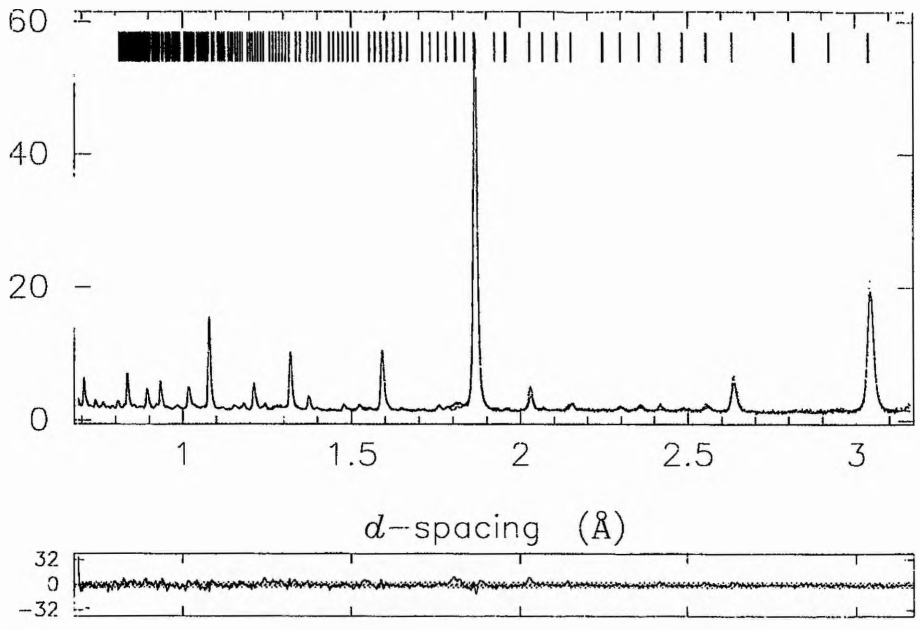

The cerium coordination environments are more complex since the individual oxide ions occupy both tetrahedral and octahedral sites.

All the cerium sites are surrounded by 8 tetrahedral sites designated O1-O10 and corresponding to 8a, 8b and 48f sites as described in Table 4.3.2r. However, the partially occupied octahedral oxide ion site O11 also coordinates Ce2, Ce3 and Ce4.

There are four O11 interstitial sites around the Ce2 and Ce3 positions, only two around the Ce4 site and none around the Ce1 (Table 4.3.2w). Figure 4.3.2r shows the structure of the thermally oxidised pyrochlore with the octahedral interstitial site represented in yellow. The coordination numbers were calculated based upon the refined occupancies of the oxide sites and are shown in Table 4.3.2w. The average Ce coordination number is 8.4.

Table 4.3.2w Average coordination numbers for the cation sites in the thermally oxidised $Ce_2Zr_2O_{7+x}$.

Atom	**O sites coordinating the cations**	**Coordination No.**	**Av. C.N.**
Zr1	2×O3 + (6×O9)	6.76	
Zr2	2×O4 + (2×O5 + 4×O7)	7.16	
Zr3	2×O4 + (2×O6 + 2×O7 + 2×O10)	7.16	
Zr4	O3 + O4 + (O5 + 2×O6 + 2×O8 + O9)	6.96	7.06
Ce1	2×O1 + (6×O10)	8.00	
Ce2	2×O2 + (4×O6 + 2×O8) + 4×O11	9.20	
Ce3	O1 + O2 + (2×O5 + 2×O7 + O8 + O10) + 4×O11	9.48	
Ce4	2×O2 + (2×O6 + 2×O7 + 2×O9) + 2×O11	8.32	8.40

The rhombohedral distortion of the cubic pyrochlore structure must occur to allow the subtle reorganisation of the anion sublattice under heating to enable oxide to be accommodated within the octahedral interstitial site. It can be seen from the rhombohedral angle, $\alpha = 90.05°$ that this is a relatively small deviation from cubic symmetry. It may be speculated as to why the additional interstitial oxygen is located exclusively on only one of the available octahedral sites i.e. the 12i site. This ordering

may result from the fact that all other octahedral sites coordinate a maximum of two distinct cerium and zirconium sites each (Table 4.3.2s) whereas the O11 site coordinates to Ce2-Ce4 and Zr2-Zr4 i.e. 30 of the 32 cation sites within the unit cell.

The final stoichiometry for the thermally oxidised pyrochlore is $Ce_2Zr_2O_{7.97(12)}$. This corresponds to a 97 % conversion of Ce^{3+} to Ce^{4+} to form $Ce^{3+}_{0.06}Ce^{4+}_{1.94}Zr_2O_{7.97}$.

Figure 4.3.2r Crystal structure of the thermally oxidised $Ce_2Zr_2O_{7+x}$. Ce shown as green, Zr as purple, O as red, O3 as blue and O11 as yellow spheres.

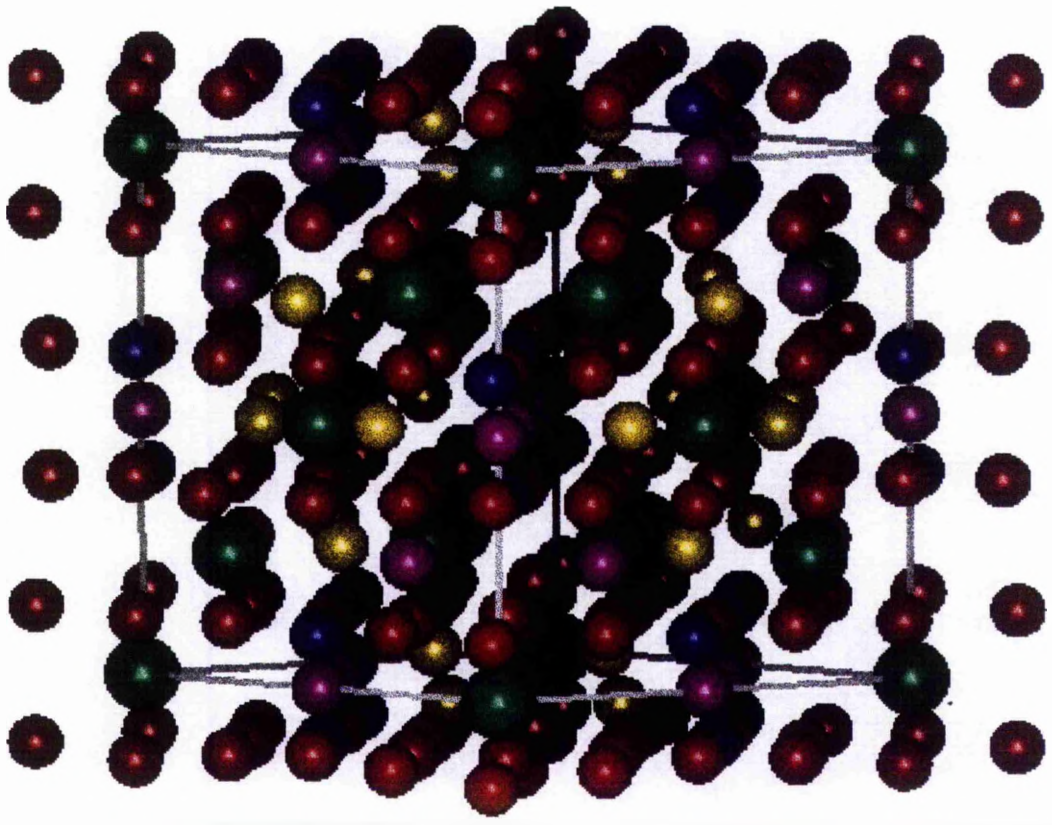

4.4 The Kinetics of Oxygen Intercalation

It is interesting to examine the kinetics of the oxygen intercalation process. The kinetics of oxidation from O_2 in the gas phase can be compared with oxidation by the aqueous hypobromite solution. This is most easily accomplished by a comparison of the growth of the oxygen content with time in air and in the hypobromite solution.

Intercalation of oxygen into $Ce_2Zr_2O_7$ must involve the following steps:

1. Adsorption of O_2 onto the particle surface.
2. Cleavage of the dioxygen bond.
3. Reduction of $O^{\bullet}$ to O^{2-}.
4. Transport of O^{2-} and the charge compensating holes into the solid.

Step 4 may simply involve diffusion controlled transport in the case of a continuous range of solid solution. On the other hand, if a two phase process is involved then nucleation and growth of the second phase must occur. It appears that in the case of $Ce_2Zr_2O_{7+x}$ oxygen insertion involves the former.

The rate of change of the concentration of a specified species is one measure of the instantaneous rate of a reaction. In this case, the rate can be charted by the oxygen concentration in the sample. The concentration of oxygen in the sample corresponds to the total oxygen content per mole of pyrochlore. If diffusion controlled transport was the overall rate determining step then the rate of change of the oxygen content with time would be given by equation 4.4a:

$$\frac{dc}{dt} = At^{-\frac{1}{2}} \qquad \text{(Eqn. 4.4a)}$$

where c is the oxygen content, t is the time and A is a constant. If equation 4.4a accurately discribes this process, then a plot of the oxygen content versus $t^{0.5}$ would

be linear. This is not observed in the case of oxidation in air. An examination of Figure 4.4a, which plots the variation of oxygen content with aging time of exposure to air, reveals that there is a linear relationship between total oxygen content and time, indicating that the reaction is not diffusion, but surface controlled.

Figure 4.4a The rates of oxidation of the $Ce_2Zr_2O_7$ in air and hypobromite.

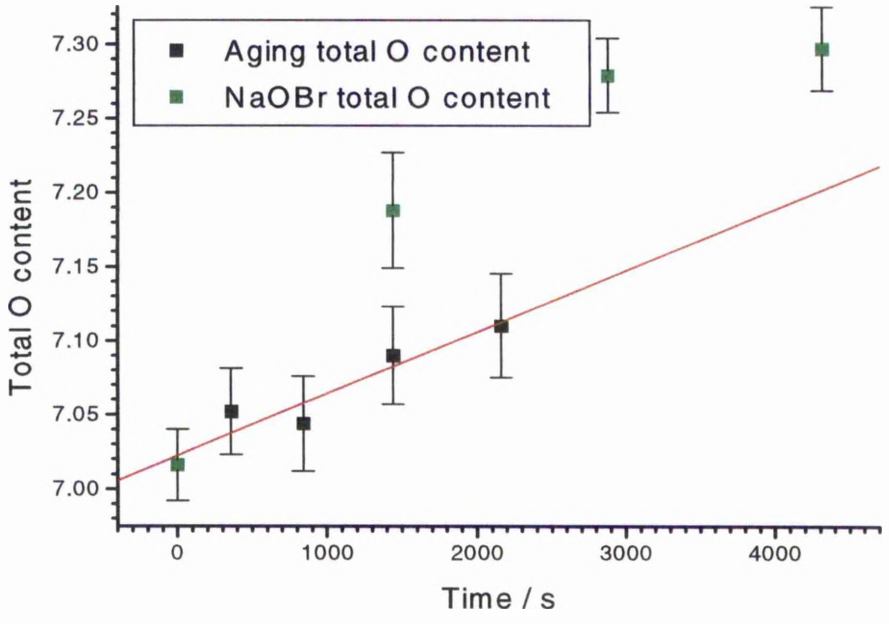

A linear regression of the oxygen content against the aging time gives equation 4.4b, and a goodness of fit to the data, R^2, of 0.95.

$$\text{Total Oxygen Content} = 0.000042(8) \times \text{Aging Time} + 7.022(9) \qquad \text{(Eqn. 4.4b)}$$

This reaction is therefore zero-order with a rate of oxidation of 0.000042(8) moles O per second per mole of pyrochlore, i.e. with a rate constant (or surface exchange coefficient) of 0.000042(8) s^{-1} at 25°C.

Although uncommon, zero order reactions do exist in certain heterogeneous processes[11]. In reactions involving a single gas saturated on a surface, where the reaction is unretarded by the products, and absorption is high, considerable amounts of gas may be removed by chemical change without the amount in the adsorbed layer suffering appreciable diminution. This means that as a gas reacts and leaves the surface it is immediately replaced from the gas phase. Thus there is a constant rate of reaction in spite of diminishing concentration in the gas phase, and the reaction appears to be 'zero order'. An example of a nearly zero order gas reaction is to be found in the catalytic decomposition of ammonia on the surface of tungsten[12]. Assuming that the diffusion of oxide and holes within the pyrochlore is high, and that the reacted species is removed quickly, then zero order kinetics are anticipated and observed.

It is interesting to compare the growth of oxygen content with time in the hypobromite solution and in air. It can be seen that the levels of oxidation produced by the chemical technique are significantly higher than those from the aging experiments for a similar time period, within experimental error (Figure 4.4a). In the case of hypobromite, diffusion control would be expected if a plot of the oxygen content versus $t^{0.5}$ was found to be linear (Figure 4.4b). This is observed to be the case. A linear regression of the oxygen content against the square root of the oxidation time in the hypobromite gives equation 4.4c, and a goodness of fit to the data, R^2, of 0.99.

$$\text{Total Oxygen Content} = 0.0045(4) \times \text{Oxidation Time}^{0.5} + 7.02(2) \qquad \text{(Eqn. 4.4c)}$$

The rate constant is therefore 0.0045(4) $s^{-0.5}$ for this diffusion controlled process. This indicates that the surface reaction is no longer rate limiting in the case of

oxidation by hypobromite, and suggests that the surface process is different between oxidation in air and by hypobromite.

Figure 4.4b A plot of $Ce_2Zr_2O_{7+x}$ oxygen content versus $t^{0.5}$ in hypobromite.

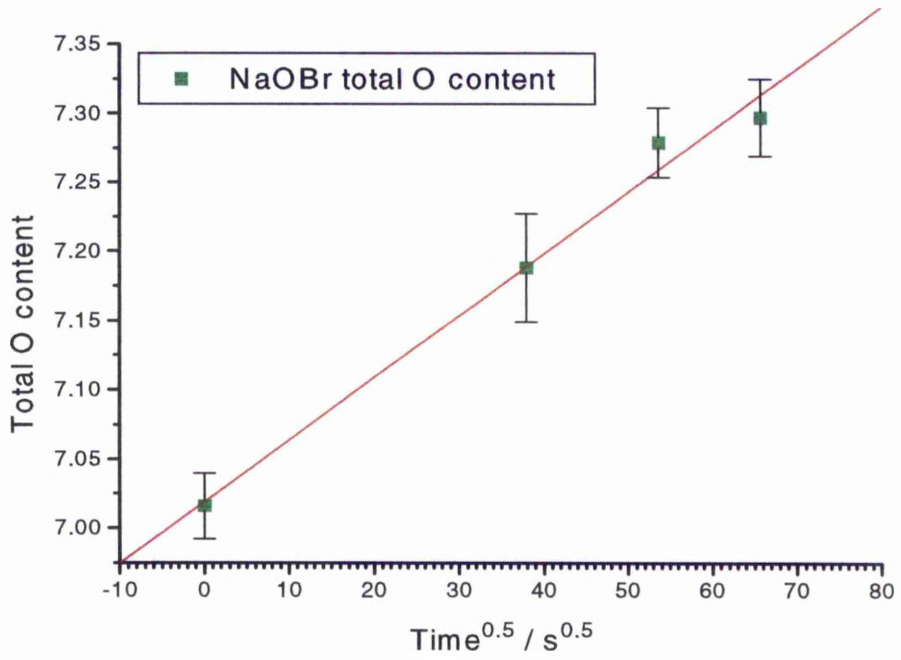

A total oxygen content of 7.30(3) is produced by the hypobromite after 72 h exposure, whereas a linear extrapolation from the aging study would suggest that it would require a period of approximately 111 h in air for a similar oxidation level to be achieved. Associated with this oxygen content is an oxidation of 0.6 Ce^{3+} ions to Ce^{4+} i.e. the explicit formula for the $Ce_2Zr_2O_{7.297}$ compound is $(Ce^{3+}_{1.4}Ce^{4+}_{0.6})Zr_2O_{7.3}$.

4.5 Structural changes on Intercalation

The structural information obtained from the powder neutron diffraction data from the samples produced by room temperature oxygen intercalation is summarised in Table 4.5a.

Table 4.5a Important crystallographic information for samples in the $Ce_2Zr_2O_{7+x}$ system, $0 \leq x \leq 0.36$.

Lattice param. a / Å	Occup. O1	Occup. O2	Occup. O3	Total O content	O1 x coordinate	R_{WP}
10.74748(3)	1	0.930(15)	0.086(9)	7.02(2)	0.41701(9)	3.87
10.74014(4)	1	0.92(2)	0.134(11)	7.05(3)	0.41602(11)	4.20
10.73075(5)	1	0.87(2)	0.170(12)	7.04(3)	0.41523(12)	4.53
10.71432(6)	1	0.87(2)	0.223(13)	7.09(3)	0.41426(13)	4.42
10.70609(5)	1	0.85(2)	0.258(14)	7.10(4)	0.41312(13)	4.39
10.67786(8)	1	0.83(2)	0.36(2)	7.19(4)	0.4099(2)	4.16
10.67114(4)	1	0.951(7)	0.310(7)	7.261(14)	0.41022(7)	3.11
10.66477(5)	1	0.904(11)	0.350(8)	7.25(2)	0.40894(8)	3.29
10.66227(8)	1	0.894(13)	0.363(9)	7.26(2)	0.40825(9)	2.73
10.66097(3)	1	0.958(9)	0.333(7)	7.29(2)	0.40873(6)	2.99
10.65941(4)	1	0.961(11)	0.337(8)	7.30(2)	0.40851(7)	1.8
10.65570(5)	1	0.971(15)	0.308(10)	7.28(3)	0.40827(9)	2.64
10.65371(4)	1	0.99(2)	0.307(11)	7.30(3)	0.40820(10)	2.97
10.65149(3)	1	0.956(10)	0.342(7)	7.30(2)	0.40838(7)	3.09
10.64595(3)	1	0.957(10)	0.330(7)	7.29(2)	0.40816(7)	2.96
10.64401(7)	1	1.01(2)	0.357(12)	7.36(3)	0.40586(11)	2.94

The 48f oxygen site remains full throughout the solid solution range. The variation of the oxygen occupancies of the 8a and 8b sites with total oxygen content (determined by the addition of these occupacies with that of the full 48f site) is shown in Figure 4.5a.

Figure 4.5a The variation of the 8a (O2) and 8b (O3) site occupancies with the total oxygen content in the $Ce_2Zr_2O_{7+x}$ system, $0 \leq x \leq 0.36$.

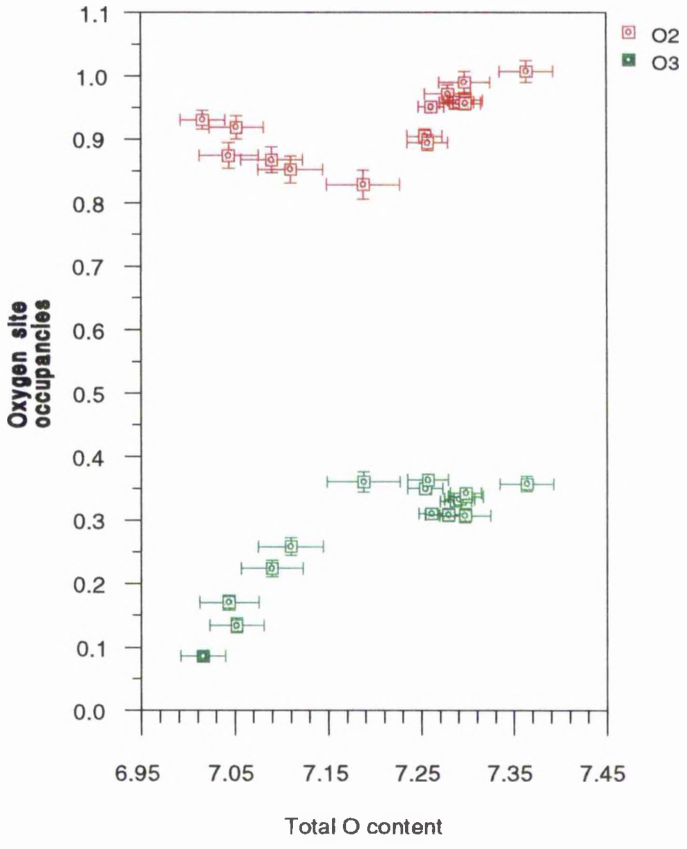

These data reveal a most interesting effect. Contrary to initial expectation the intercalated oxygen does not reside on the 8b sites with the original oxygen sub-array remaining intact, instead, as the guest oxygen content increases, the occupancy of the

8b site increases to a greater extent. This additional oxygen arises from the displacement of oxide ions from the 8a site. This continues up to a total oxygen content of 7.2. Above this composition the occupancy of the 8a site rises again as that of the 8b site appears to saturate. These observations suggest that the mechanism of interstitial solid solution formation for this pyrochlore oxide is not simple and involves the disruption of the oxygen sub-array in the host compound, but only on the 8a sites.

Two 8b sites surround each Zr^{4+} ion, therefore the filling of these sites increases the Zr^{4+} coordination number above 6. The Zr^{4+} ion will only tolerate this increased coordination up to a limit of 6.7 (corresponding to the maximum 8b occupancy of 0.35), after which the occupancy of the 8a site around the cerium ion begins to increase until the maximum oxygen coordination of 8 is recovered. This correlates well with the fact that it is known that Zr prefers a coordination number of 7 in an oxide environment, as is evident from the observation that ZrO_2 only adopts the cubic fluorite structure at high temperatures, more modest temperatures permit a distortion of the structure to yield 7 coordinate zirconium.

Each oxide ion in an 8b site in the pyrochore structure will coordinate 4 zirconium ions simultaneously. In contrast, occupancy of an oxide ion in a 32e position would coordinate only 3 zirconium ions and hence the preferred coordination number of 7 oxygens around each Zr^{4+} is more closely achieved for the same number of oxygens occupying the 8b position. Furthermore, the Zr-O(32e) distance is 2.662 Å compared with 2.305 Å for Zr-O(8b). The latter more closely approaches the preferred Zr-O bond length. This may explain the preference of the intercalated oxygen for the 8b sites.

Table 4.5b shows selected bond lengths for the $Ce_2Zr_2O_{7+x}$ compounds. As the oxygen content increases, the average cerium oxidation state will increase from 3+ to nearer 4+, producing a contraction in the Ce-O(48f) bond length, and a corresponding increase in the Zr-O(48f) bond length.

Table 4.5b Selected bond distances in the $Ce_2Zr_2O_{7+x}$ system, $0 \leq x \leq 0.36$.

Sample	O Cont.	Ce–O48f / Å	Zr–O48f / Å	Ce–O8a, Zr–O8b / Å
$Ce_2Zr_2O_{7.016}$	7.02(2)	2.6137(10)	2.0989(10)	2.3269(1)
$Ce_2Zr_2O_{7.054}$	7.05(3)	2.6046(12)	2.1020(12)	2.3253(1)
$Ce_2Zr_2O_{7.040}$	7.04(3)	2.5966(13)	2.1038(13)	2.3233(1)
$Ce_2Zr_2O_{7.093}$	7.09(3)	2.5855(14)	2.1051(14)	2.3197(1)
$Ce_2Zr_2O_{7.108}$	7.11(4)	2.5752(14)	2.1088(14)	2.3179(1)
$Ce_2Zr_2O_{7.190}$	7.19(4)	2.5454(17)	2.1185(17)	2.3118(1)
$Ce_2Zr_2O_{7.261}$	7.261(14)	2.5459(7)	2.1158(7)	2.3104(1)
$Ce_2Zr_2O_{7.254}$	7.25(2)	2.5352(9)	2.1207(9)	2.3090(1)
$Ce_2Zr_2O_{7.257}$	7.26(2)	2.5297(10)	2.1236(10)	2.3084(1)
$Ce_2Zr_2O_{7.291}$	7.29(2)	2.5329(6)	2.1210(6)	2.3082(1)
$Ce_2Zr_2O_{7.298}$	7.30(2)	2.5309(7)	2.1217(7)	2.3078(1)
$Ce_2Zr_2O_{7.279}$	7.28(3)	2.5283(10)	2.1222(10)	2.3070(1)
$Ce_2Zr_2O_{7.297}$	7.30(3)	2.5274(11)	2.1221(11)	2.3066(1)
$Ce_2Zr_2O_{7.298'}$	7.30(2)	2.5281(7)	2.1208(7)	2.3061(1)
$Ce_2Zr_2O_{7.287}$	7.29(2)	2.5252(7)	2.1208(7)	2.3049(1)
$Ce_2Zr_2O_{7.357}$	7.36(3)	2.5085(12)	2.1318(12)	2.3045(1)

The variation of the 8a and 8b site occupancy is consistent with analysis of the stability field of the pyrochlore structure. Analysis of many pyrochlore oxides shows that $A_2^{3+}B_2^{4+}O_7$ compounds adopt this structure type provided the ratio of the ionic radii, RR, obeys equation 4.5a[1].

$$1.46 \leq RR \leq 1.80 \qquad RR = \frac{r_{La}^{3+}}{r_B^{4+}} \qquad \text{(Eqn. 4.5a)}$$

The ratio for the stoichiometric pyrochlore, $\frac{Ce^{3+}}{Zr^{4+}}$ is equal to 1.588, and well within the stability field. However, the intercalation of an oxide ion results in the oxidation of two Ce^{3+} ions to Ce^{4+}. Upon oxidation, the cerium ion becomes smaller, with its ionic radius decreasing from 1.143 to 0.97 Å and Zr^{4+} which is now in a 7 coordinate environment possesses a longer ionic radius of 0.78 Å. This changes the Ce^{4+}:Zr^{4+} ratio to a value of 1.244, outwith the stability field. As a result of the change in ionic radii different oxygen coordinations around the ions are no longer tolerable, and hence oxide ions will be displaced from the 8a to the 8b sites. Therefore, as the radii of the ions on the 16c and 16d sites converge, the oxide ion distribution more closely approaches that of the fluorite structure.

Figure 4.5b The variation of the lattice parameter with the total oxygen content in the $Ce_2Zr_2O_{7+x}$ system, $0 \leq x \leq 0.36$.

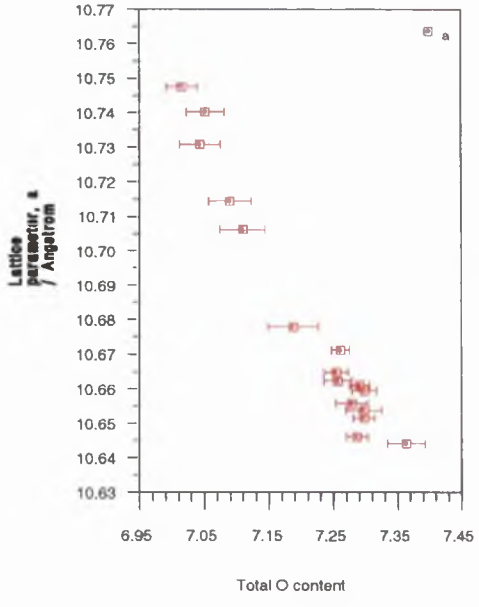

Further confirmation concerning the non-ideal nature of the solid solution is obtained by examining Figure 4.5b which shows the variation of lattice parameter with total oxygen content. It can be seen that as the degree of oxygen intercalation increases the lattice parameter continuously contracts, but this contraction does not appear to be linear, and instead exhibits a negative deviation from Vegard's law. This reduction of lattice parameter, and so in unit cell volume, with increasing oxygen content illustrates that the conversion of the Ce^{3+} to the smaller Ce^{4+} ion more than compensates for any expansion of the lattice due to the additional intercalated oxygen (From Table 4.3.1c the ionic radii for the 8 coordinate environments are Ce^{3+}, 1.143 Å; Ce^{4+}, 0.97 Å).

In a stoichiometric pyrochlore, the 48f site is displaced away from the fluorite position at (3/8, 1/8, 1/8) towards the empty 8b site. This can be understood by examining Figure 4.5c.

Figure 4.5c The O1 (48f, light blue), O2 (8a, red) and O3 (8b, dark blue) tetrahedral site coordination around the octahedral 32e site at (1/4, 1/4, 1/4).

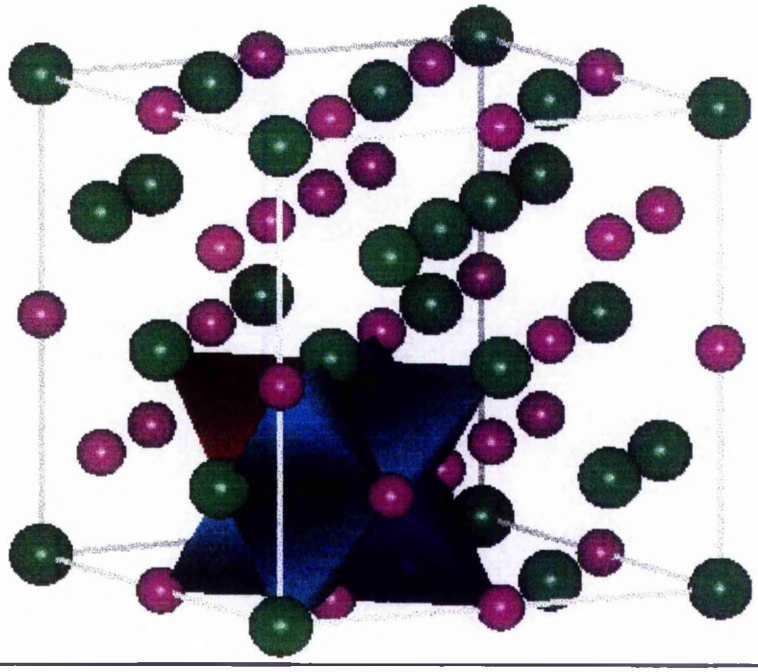

Six 48f tetrahedral sites share faces with the empty 32e octahedral site at approximately (1/4, 1/4, 1/4) forming a ring. The remaining two opposing faces of this octahedral site are shared with the 8a and 8b sites. If the 8b site is vacant, then relaxation of the ring of oxygens in the 48f sites away from the occupied 8a site is anticipated and observed.

However, in the $Ce_2Zr_2O_{7+x}$, as oxidation occurs the 8b site begins to fill, and the 48f oxygen is steadily displaced back to the fluorite position, i.e. to a point equidistant between the 8a and 8b sites. This behaviour is exhibited in the plot of the 48f x coordinate against the total oxygen content shown in figure 4.5d.

Figure 4.5d The relationship between the 48f x coordinate and the total oxygen content in the $Ce_2Zr_2O_{7+x}$ system, $0 \leq x \leq 0.36$.

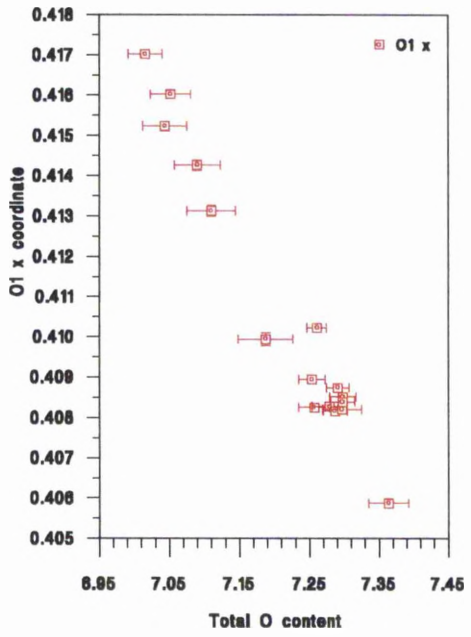

The repulsion of the 48f site back towards the fluorite position is also mirrored in the plot of the anisotropic temperature factor, B_{11}, for the oxygen on this site versus total oxygen content shown in Figure 4.5e. It is evident from the data that the anistropic temperature factor in the B_{11} direction is large, and increases with oxygen intercalation.

Figure 4.5e The relationship between the 48f B_{11} anisotropic temperature factor and the total oxygen content in the $Ce_2Zr_2O_{7+x}$ system, $0 \leq x \leq 0.36$.

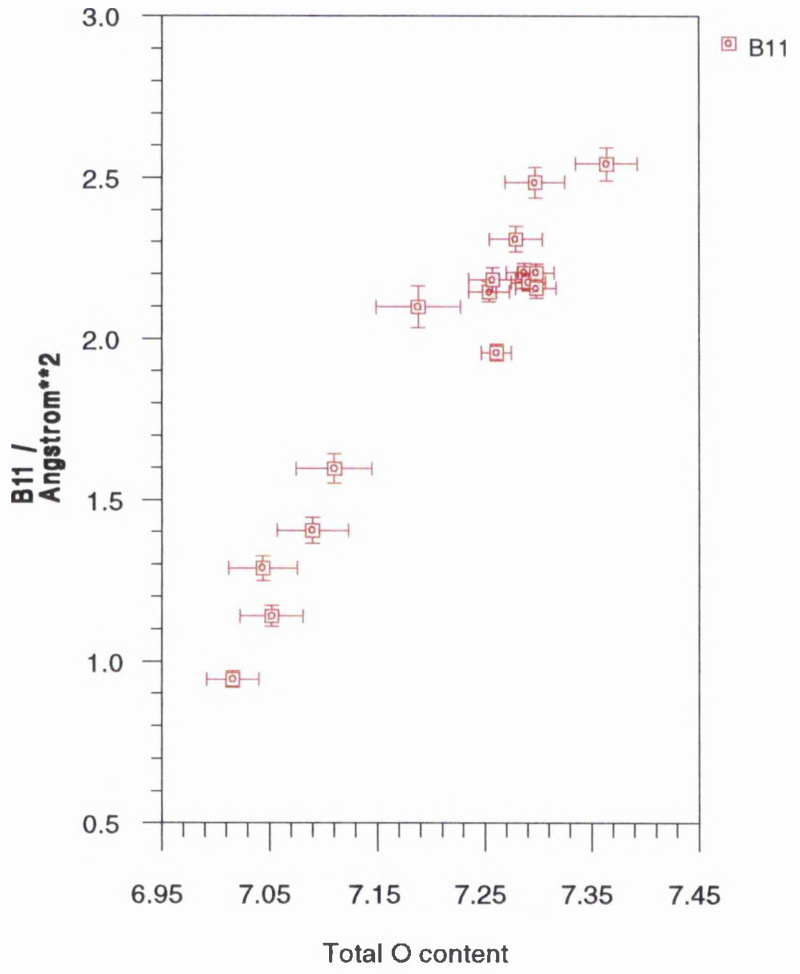

A large B_{11} factor implies that there is either a high degree of thermal vibration or a considerable variation in the position of the oxygen at that site. This means that the disorder along the x direction is either dynamic or static. One limitation of the diffraction technique is that it can only give an average structure for the crystalline material examined.

It is probable that on the nm scale oxygen intercalation will be heterogeneous. There will be localised areas where the oxygen has been inserted into the 8b sites, repelling oxygen on the 48f sites back towards the fluorite position. Similarly, there will be regions where there is no intercalated oxygen, and where as a result the 48f oxygen will be in its original position. However, conclusions concerning the local structure would require investigation by other techniques such as diffuse scattering or oxygen NMR.

4.6 The Mechanism of Intercalation

A key topic for any intercalation process is the mechanism by which oxygen is intercalated into the structure. For ion transport certain requirements must be satisfied. First the ions must partially occupy a set of equivalent or near equivalent sites and second the sites must be interconnected by pathways normally involving the face sharing of sites. Both the 8a and the 8b sites fulfill the first criterion but they share only edges with each other. However, transport between 8a and 8b is possible through the octahedral site at (1/4, 1/4, 1/4). Although this site was found to be vacant, it shares faces with both the 8a and 8b sites, allowing movement between these two sites. A part of the continuous network of 8a - 32e - 8b sites running throughout the structure is shown in Figure 4.6a.

Figure 4.6a The connectivity between the octahedral 32e site at (1/4, 1/4, 1/4) shown in yellow, and the O2 (red) and O3 (dark blue) tetrahedral sites.

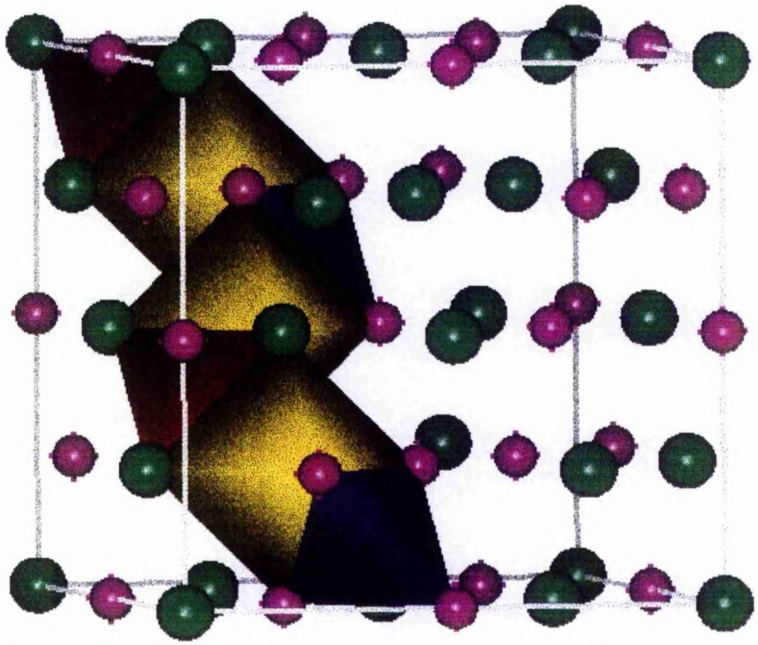

It is conceivable that an oxide ion could leave its 8a (or 8b) site, and enter the 32e site. It could then jump back to its original site, or into the 8b (or 8a) site if it is vacant. If the 32e position provided an accessible, but higher energy site, the occupancy of this site may be too small to measure by powder neutron diffraction.

An alternative mechanism involving cooperative motion is also possible. In this case an oxide ion from either the 8a or 8b site moves into a 32e position, where it displaces an oxide ion from one of the neighbouring 48f positions into a second 32e site (each 48f site shares all of its four faces with 32e sites). The resulting empty 48f site would subsequently be occupied by the oxide ion which originated from the 8a or 8b site (Figure 4.6b). Motion of oxide ions in this pathway would constitute an interstitialcy mechanism since it involves the displacement of ions which fully occupy a set of sites and therefore do not give rise to diffusion in themselves but are merely part of a cooperative conduction mechanism.

Figure 4.6b Schematic illustration of a possible cooperative conduction mechanism in $Ce_2Zr_2O_{7+x}$.

Stage	8a or 8b site	32e site	48f site	32e' site
1	O→		O'	
2		O	O'→	
3		O→		O'
4			O	O'

In conclusion, the $Ce_2Zr_2O_{7+x}$ system exhibits a variety of intriguing structural chemistry, due to the flexibility of the pyrochlore structure caused by the existence of accessible interstitial sites. The only other documented evidence of a pyrochlore structure with oxide occupying the 8b interstitial site is the pyrochlore-type region of

the $(1-x)ZrO_2$-$xGdO_{1.5}$ phase diagram. At x = 0.43 a phase of composition $Gd_{1.72}Zr_{2.28}O_{7.14}$ is formed. The structure of this material was investigated by Moeriga *et al*[13], who examined the cation order over the 16c (A) and 16d (B) sites. A partial disordering of the Gd and Zr over theses sites (Gd occupancy: 16c 0.673(5), 16d 0.187), presumably caused by the nonstoichiometry, results in partial oxide occupancies of 0.65(5) in the 8a, and 0.49 in the 8b sites. The partial occupancy of the 8a site reflects almost exactly the Gd occupancy of the neighbouring 16c site. This is to be expected as the larger Gd^{3+} ion (ionic radius 1.053 Å , 8 coordinate[9]), would be most stable in an 8 coordinate environment, and so the 8a site occupancy will alter to facilitate this. The smaller Zr^{4+} is more stable in a 6 coordinate environment and so the 0.327 occupancy of Zr on the 16c site is accompanied by an almost identical 0.35(5) vacancy in the 8a site.

It is interesting to note that it is the 8b site which is responsible for the charge compensation necessitated by the excess Zr in the structure. The Gd occupancy of the 16d site is 0.187. Following the above reasoning, the 8b occupancy would be expected to be approximately 0.19 as well. The observed occupancy of the 8b site in $Gd_{1.72}Zr_{2.28}O_{7.14}$ is 0.49, the difference being the 0.3 (i.e. 0.49-0.19) moles of oxide necessary for charge balancing. As in the $Ce_2Zr_2O_{7+x}$ system, it is the 8b site which accommodates the excess oxygen required to balance the cationic charge.

4.7 References

1. M. A. Subramanian, G. Aravamudan and G. V. Subba Rao, *Prog. Solid State Chem.*, **15**, 55, 1983.

A. W. Sleight, *Mat. Res. Bull.*, **9**, 1177, 1974.

2. P. Duwez and F. Odell, *J. Am. Chem. Soc.*, **33**(9), 274, 1950.

3. J. J. Casey, L. Katz and W. C. Orr, *J. Am. Chem. Soc.*, **77**, 2187, 1955.

4. A. Bystrom, *Arkiv. Kemi. Min. Geol.*, **18A**, 21, 1945.

5. N. A. Dhas and K. C. Patil, *J. Mater. Chem.*, **3**(12), 1289, 1993.

6. R. A. Chapman, D. B. Meadowcrofts and A. J. Walkden, *J. Phys. D*, **3**, 307, 1970.

7.V. F. Sears, "Neutron Scattering Lengths and Cross Sections", AECL Research, Chalk River Laboratories, Chalk River, Ontario, Canada, November, 2, 1991.

8. J. C. Matthewman, P. Thompson and P.J. Brown, *J. Appl. Crystallogr.*, **15**, 167, 1982.

P. J. Brown and J. C. Matthewman, Rutherford Appleton Laboratory Report 1987, Ral-87-010.

9. R. D. Shannon, *Acta Crystallogr.*, **A32**, 751, 1976.

10. M. Asquiedge, *Rev. int. hautes Temp. et Refract.*, **6**, 35, 1969.

11. C. N. Hinshelwood, "The Kinetics of Chemical Change", Clarendon Press, Oxford, 187, 1942.

12. C. N. Hinshelwood and W. Burke, *J. Chem. Soc.*, **127**, 1116, 1925.

13. T. Moriga, S. Emura, A. Yoshiasa, S. Kikkawa, F. Kanamaru and K. Koto, *Solid State Ionics*, **40/41**, 357, 1990.

Chapter 5
Oxygen Intercalation Studies

5.1 Introduction

A number of possible oxygen intercalation techniques were introduced in Chapter 3. These range from electrochemical based systems using an aqueous solution or a eutectic mixture of molten salts, to chemical based systems using aqueous and organic solvents.

In order to examine the potential of each technique to produce oxygen intercalation, a variety of host materials, whose structures were also discussed in Chapter 3, were screened using each system. The host materials with oxygen deficient perovskite, K_2NiF_4 type and pyrochlore structures were analysed by powder X-ray or neutron diffraction before and after the intercalation experiment to detect any changes in the lattice parameters or oxygen site occupancies. The greatest flexibility in oxygen stoichiometry was exhibited by $Ce_2Zr_2O_{7+x}$, a compound with the pyrochlore structure type. A detailed study of the variation of the structure of this material with oxygen content is discussed in Chapter 4.

The electrochemical oxygen intercalation techniques are examined in section 5.2. Section 5.2.1 discusses the aqueous method used by Pouchard and co-workers, while section 5.2.2 reports a new molten salt based method.

The chemical oxygen intercalation techniques are investigated in section 5.3. Section 5.3.1 reports the examination of oxygen insertion into hosts other than $Ce_2Zr_2O_{7+x}$ by the hypobromite method used in Chapter 4, while section 5.3.2 examines periodate based methods.

5.2 Electrochemical Oxygen Intercalation

5.2.1 Aqueous Electrochemical Oxygen Intercalation

5.2.1.1 Introduction

The aqueous electrochemical oxygen intercalation technique pioneered by Pouchard and co-workers is discussed in Chapter 3.2. Since its discovery this system has been used to oxidise: $Sr_2M_2O_5$ (M = Fe, Co) materials with the Brownmillerite structure to the perovskite, $SrMO_3$ (M = Fe, Co)[1]; and the T-phase K_2NiF_4 type La_2MO_4 to La_2MO_{4+x} (M = Cu, x = 0.07[2], 0.08[3, 4], 0.09[1], 0.12[5]; M = Ni, x = 0.26[1], 0.25[6]) and $La_{2-y}Sr_yCuO_4$ to $La_{2-y}Sr_yCuO_{4+x}$ ($0 < y \leq 33$, $0 < x \leq 13$)[4].

The Brownmillerite type ferrite $Sr_2Fe_2O_5$ was first examined in this work. The system was then used to attempt the oxidations of the perovskite related $YBa_2Cu_3O_{6.20}$, T-phase K_2NiF_4 type $YSr_5Ni_3O_{11}$ and the S-phase K_2NiF_4 type Sr_2CuO_3.

5.2.1.2 Experimental Details

The intercalation hosts were made by standard solid state synthetic techniques.

The $Sr_2Fe_2O_5$ was made by intimately grinding the correct stoichiometric mixture of $SrCO_3$ (Aldrich 99.9 %) [8.0468 g] and Fe_2O_3 (Aldrich 99.99 %) [4.3521 g]. The reactants were then placed in a platinum crucible and heated to 700°C in a muffle furnace at 20°/min, and this temperature maintained for 12 h to allow complete decomposition of the carbonate. The sample was cooled to room temperature at 5°/min, reground and heated to 1200°C at 20°/min for a further 12 h. It was then air quenched to yield the partially oxidised Brownmillerite. The fully reduced form was produced by heating the sample to 1000°C at 200°/min under an

Ar atmosphere (BOC, pureshield). This temperature was maintained for 18 h and the sample was cooled to room temperature at 5°/min. The sample was reground and this heating cycle repeated twice to yield the desired phase.

The $YBa_2Cu_3O_{6.20}$ was prepared by grinding together the correct stoichiometric mixture of Y_2O_3 (Aldrich 99.99 %) [1.7154 g], $BaCO_3$ (Johnson Matthey, puratronic) [5.9964 g] and CuO (Aldrich 99.99%) [3.6254 g]. The ground mixture was pressed into pellets 2-3 mm thick and 12 mm in diameter using a stainless steel dye under a pressure of 5 ton cm^{-2}. The pellets were then placed in an alumina crucible on a bed of powder of the same nominal composition in order to prevent reaction of the pellets with the crucible walls, and then annealed at 940°C in air for 2 days. At the end of this period the samples were cooled to 350°C at 1°/min. The pellets were then ground and repelleted, placed in a platinum crucible and annealed for 12 h in the uniform zone of a vertical tube furnace under flowing nitrogen (BOC, Pureshield). The sample was then quenched to room temperature by dropping onto copper shot to yield a final stoichiometry, as obtained from powder neutron diffraction (see section 5.3.1.3), of $YBa_2Cu_3O_{6.20}$.

The $YSr_5Ni_3O_{11}$ material was supplied by Dr J. P. Attfield, University of Cambridge.

The Sr_2CuO_3 was synthesised by grinding the correct stoichiometric mixture of $SrCO_3$ (Aldrich 99.9 %) [5.1478 g] and CuO (Aldrich 99.99%) [1.3868 g], placing the mixture in a gold boat and heating at 850°C for 5 days with frequent regrinding. The sample was then air quenched to room temperature to yield the desired phase.

The electrochemical experiment was carried out as described in section 3.2.1.2. In each case the intercalation host was pressed onto a platinum gauze working electrode and polarised at +0.6V versus a standard calomel electrode for 3 days. The working electrode was washed with distilled water to remove the electrolyte and then dried at 60°C. The product was then removed from the gauze, ground and analysed by powder X-ray diffraction.

Data suitable for structural refinement were recorded at room temperature in transmission mode on a Stoe STADI/P high-resolution powder diffractometer, using Cu-$K_{\alpha 1}$ radiation. Data were collected over the range $5° < 2\theta < 85°$ in steps of 0.02°, the entire experiment lasting *ca*, 8 h.

5.2.1.3 Results and Discussion

The structure of the Brownmillerite host, $Sr_2Fe_2O_5$, was obtained by Rietveld refinement of powder X-ray diffraction data using Sr_2CoFeO_5 as a model[7]. The refined atomic parameters are shown in Table 5.2.1a.

Table 5.2.1a Final refined atomic parameters for $Sr_2Fe_2O_5$ from X-ray data. Space group I *cmm*, 3748 observations, R_{wp}=0.0221, a=5.6696(2), b=15.5902(6), c=5.5299(2) Å.

Atom	Site	x	y	z	U_{iso}/ Å^2	Occupancy
Fe(1)	4a	0	0	0	0.018(2)	
Fe(2)	4e	0.5738(12)	0.25	0.5	0.018(2)	
Sr	8h	0.5165(7)	0.60964(15)	0	0.010(1)	
O(1)	8g	0.25	0.9805(9)	0.25	0.007(3)	
O(2)	8h	0.0801(19)	0.1418(8)	0	0.007(3)	
O(3)	8i	0.674(5)	0.25	0.156(6)	0.007(3)	0.5

Analysis by cyclic voltammetry showed an oxidation peak on the shoulder of the anodic limit, at +0.45 V versus the standard calomel reference electrode (SCE) at a scan rate of ν = 100 mVs^{-1}. $Sr_2Fe_2O_5$ was electrochemically intercalated with oxygen to yield the perovskite $SrFeO_3$, by polarising the working electrode at +0.6 V versus a SCE for 3 days. The X-ray diffraction pattern of the intercalated host was refined using the ideal cubic perovskite as a model to produce the result is shown in Table 5.2.1b.

Table 5.2.1b Final refined atomic parameters for $SrFeO_3$ by X-ray diffraction. Space group P $m\bar{3}m$, 3999 observations, R_{wp}=0.0274, a = b = c = 3.8660(2) Å.

Atom	Site	x	y	z	U_{iso} / Å^2
Sr	1a	0	0	0	0.0093(13)
Fe	1b	0.5	0.5	0.5	0.0104(12)
O	3d	0	0.5	0	0.025(2)

The Brownmillerite and perovskite structures are discussed in sections 3.4.4 and 3.4.3 respectively. The transformation from the $Sr_2Fe_2O_5$ structure to $SrFeO_3$ occurs when the oxygen vacancies in alternate [001] rows of the Brownmillerite material become occupied by intercalated oxygen. This changes the iron-oxygen co-ordination environment from -6(octahedral)-4(tetrahedral)-6(octahedral)-4(tetrahedral')- along the a axis of the unit cell to 6(octahedral), with a corresponding change in the iron oxidation state from (III) to (IV).

Having confirmed the applicability of this intercalation technique to a material of the Brownmillerite structure, other hosts not known to exhibit oxygen intercalation by this method were investigated. $YBa_2Cu_3O_{6.20}$ is an oxygen deficient perovskite related cuprate material that can be thermally oxidised to $YBa_2Cu_3O_7$ (see section 3.4.4). An alternative synthetic route to the more oxidised members of the 1:2:3 Y-Ba-Cu-O system would be of great use in the investigation of superconductivity in cuprate systems. However, the $YBa_2Cu_3O_{6.20}$ host was found to be unstable in the alkaline electrolyte solution, as were the K_2NiF_4 related Sr_2CuO_3 and $YSr_5Ni_3O_{11}$, both of which decomposed to produce $SrCO_3$. Decomposition of water sensitive cuprate materials could therefore be avoided by the use of a non-aqueous based electrochemical oxygen intercalation system.

5.2.2 Molten Salt Electrochemical Oxygen Intercalation

5.2.2.1 Introduction

The electrochemical intercalation of oxygen using a non-aqueous molten salt system is one way of avoiding the decomposition of water sensitive cuprate host materials. This intercalation technique is described in section 3.2.2, and was used to examine two host structures, $Sr_2Fe_2O_5$ and $YBa_2Cu_3O_{6.20}$.

5.2.2.2 Experimental Details

The Brownmillerite ferrite and $YBa_2Cu_3O_{6.20}$ hosts were synthesised as described in section 5.2.1.2.

The electrochemical experiment was carried out as described in section 3.2.2.2, with the intercalation host being pressed onto a platinum gauze working electrode. The cell was degassed for 1 hr using a dried Ar (BOC, pureshield) supply before being polarised at +1.2V (versus the Ag^+ / Ag reference electrode) for 8 h. After the appropriate time, the working electrode was removed from the cell, washed with distilled water or acetone to remove the electrolyte and then dried at 60°C. The product was then removed from the gauze, ground and the powder X-ray diffraction fingerprints of the product phases obtained.

5.2.2.3 Results and Discussion

A cyclic voltammogram of the $Sr_2Fe_2O_5$ pressed onto the working electrode of the cell showed a clear irreversible oxidation peak at +1.15V (versus the 0.07m Ag(I)/Ag reference electrode at ν = 1 mVs^{-1}, Figure 5.2.2a). Polarisation of this cell at +1.2V for 8 h at 230°C produced the fully oxidised $SrFeO_3$, with only a small amount of starting material remaining. The X-ray powder diffraction pattern of the

Brownmillerite starting material is shown in Figure 5.2.2b (a). The atomic co-ordinates obtained from the Rietveld refinement of this phase are shown in Table 5.2.1a. Figure 5.2.2b (b) shows the powder X-ray diffractogram of the perovskite product of the intercalation; this can be seen to have the same powder diffraction pattern as the $SrFeO_3$ produced by the aqueous electrochemical method, the structure of which was confirmed by Rietveld refinement (Table 5.2.1b).

In order to check that the oxidation of the host material was not a result of thermal oxidation caused by the 225°C operating temperature of the cell, $Sr_2Fe_2O_5$ was analysed by thermogravimetric analysis. The sample was heated from room temperature to 900°C in air, and with weight gain caused by oxidation initiating at 300°C, suggesting that the oxidation of the Brownmillerite was a direct result of electrochemical oxygen intercalation rather than thermal oxidation.

Figure 5.2.2a Cyclic voltammogram of $Sr_2Fe_2O_5$ in the molten salt electrochemical cell, sweep rate $1mVs^{-1}$.

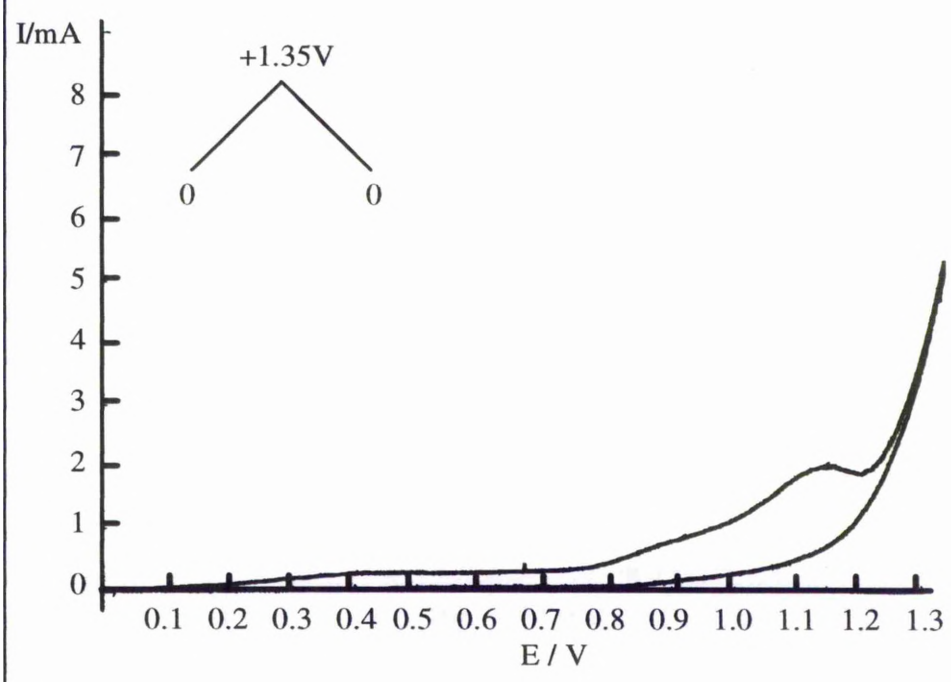

A similar procedure to the preparation of $SrFeO_3$ was used with $YBa2Cu_3O_{6.20}$, however this material was found to dissolve immediately in the electrolyte. The (Na, K)NO_3 eutectic melt has been reported to be a solvent for a wide variety of oxides[8], limiting the applicability of this technique.

Figure 5.2.2.3b Powder X-ray diffraction patterns of a) $Sr_2Fe_2O_5$, b) $SrFeO_3$ produced by the electrochemical molten salt method and c) $SrFeO_3$ produced by the aqueous electrochemical method (Section 5.2.1.3).

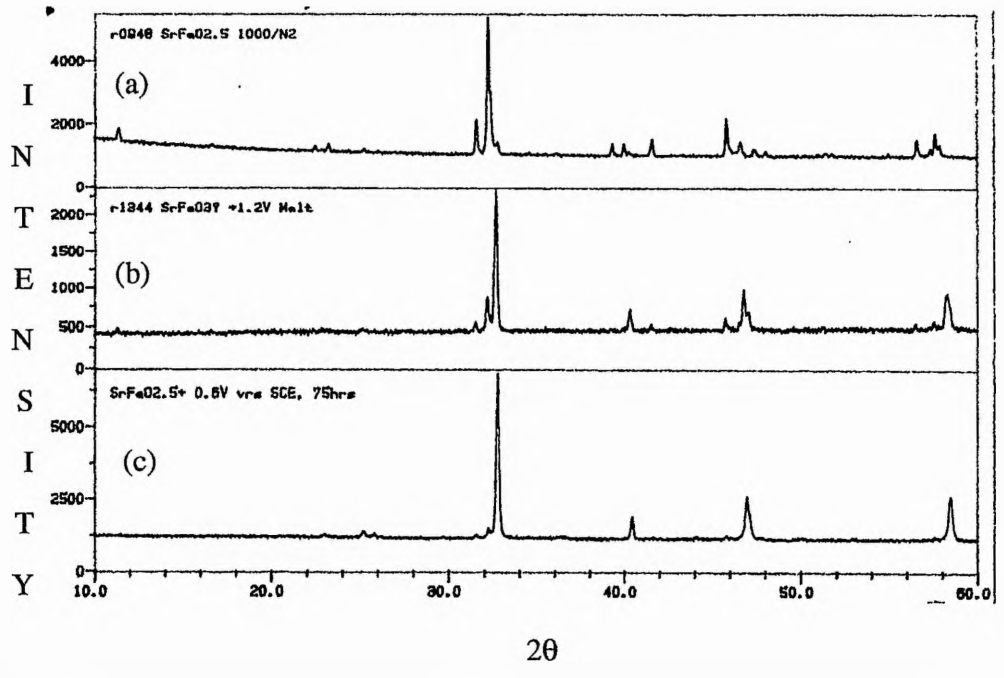

The limitations encountered due to the poor stability of the cuprates in both the aqueous and molten salt based electrochemical systems initiated the search for alternative methods of room temperature oxygen intercalation. A more suitable technique may be found using chemical oxidising agents, which are discussed in the next section.

5.3 Chemical Oxygen Intercalation

5.3.1 The Hypobromite System

5.3.1.1 Introduction

Rudolf and Schöllhorn were the first to discover the potential of aqueous sodium hypobromite solution as a chemical oxygen intercalating agent when they succeeded in oxidising the T-phase K_2NiF_4 type La_2CuO_4 to $La_2CuO_{4.14(5)}$[9]. Oxygen has also been intercalated into the $La_{2-y}Sr_yCuO_4$ system ($0 < x < 0.15$) using this technique[10] to produce a maximum oxygen content of 4.135(4) ($x = 0.05$).

The simplicity of this method has enabled the investigation of oxygen insertion into a number of host structures from the oxygen deficient perovskites, K_2NiF_4 and pyrochlore structure types.

5.3.1.2 Experimental Details

The syntheses of $Sr_2Fe_2O_5$, Sr_2CuO_3 and $YBa_2Cu_3O_{6.20}$ were described in section 5.2.1.2.

The $Sr_2Co_2O_5$ material was synthesised by grinding the correct stoichiometric ratio of $SrCO_3$ (Aldrich 99.9 %) [7.9158 g] and Co_3O_4 (Aldrich 99.995%) [4.3026 g]. The mixture was then placed in a platinum crucible and heated to 700°C in a muffle furnace for 12 h to allow complete decomposition of the carbonate. The sample was then heated to 1060°C for a further 12 h and quenched in air to yield a partially reduced material. After further grinding, the sample was heated at 850°C for 24 h under flowing nitrogen (BOC, pureshield) and cooled to room temperature at 1°/min to yield the desired phase.

The Sr_2CoFeO_5 material was synthesised by grinding the correct stoichiometric ratio of $SrCO_3$ (Aldrich 99.9 %) [7.9812 g], Co_3O_4 (Aldrich 99.995%) [2.1619 g] and Fe_2O_3 (Aldrich 99.99 %) [2.1577 g]. The mixture was then placed in a platinum crucible and subjected the same heating and reducing conditions as the $Sr_2Co_2O_5$ sample.

The La_2CuO_4 sample was synthesised by grinding together a stoichiometric mixture of La_2O_3 (Aldrich 99 %) [8.0376 g] and CuO (Aldrich 99.99 %) [1.9642 g]. The mixture was then sintered in a platinum boat in air for 36 h at 1050°C with intermediate regrinding. This sample was then air quenched to room temperature to yield the desired product.

The La_2NiO_4 sample was synthesised by grinding a stoichiometric mixture of La_2O_3 (Aldrich 99 %) [8.1351 g] and NiO (Aldrich 99.99 %) [1.8649 g]. It was then sintered in a platinum boat in air for 12 h at 1050°C with intermediate regrinding. This temperature was then raised to 1200°C and the sample air quenched to room temperature to yield the partially reduced product. The material was then reground and heated at 1300°C under flowing Ar (BOC, pureshield) for 12 h and then furnace cooled to room temperature to yield the desired product.

The chemical oxygen intercalation using aqueous sodium hypobromite was carried out as described in section 3.3.1.2. A 1.5 g sample of the intercalation host was added to a 5-fold molar excess of the hypobromite solution (0.5M NaOBr aq.) for a specified time, ranging from one to twenty-four hours. The solution was stirred vigorously to ensure a homogeneous exposure of the crystallites to the solution. The reactions were carried out under argon and in deoxygenated water to avoid oxidation of the starting material from any source other than the NaOBr (aq). The oxidised phases were then removed from the solution using a sintered glass filter, washed with distilled water, acetone and then dried in a vacuum desiccator.

Data suitable for lattice refinement were recorded as described in section 5.2.1.2. except data were collected over the range $5° < 2\theta < 85°$ in steps of 0.02° with the entire experiment lasting *ca*, 1 h.

Time-of-flight powder neutron diffraction data were collected on the POLARIS diffractometer at ISIS, Rutherford Appleton Laboratory. Approximately 1.5 g of finely ground material was placed in a 6 mm diameter vanadium sample can in the neutron beam. Data were collected in the time-of-flight range 0.3 to 19.6 ms at 298 K, from the backscattering detectors ("C bank" 38 ^{3}He detectors). Only the data between 3.5 and 19.5 ms were used in the refinement. The results are discussed in the next section, and the final atomic parameters of the refinements are given in Appendix II. Neutron scattering factors used in the refinements were Sr = 0.702, Co = 0.278, Fe = 0.954, La = 0.824, Cu = 0.7718, Ni = 1.03, Y = 0.775, Ba = 0.507 and O = 0.5803×10^{-12} cm.

5.3.1.3 Results and Discussion

The hypobromite method was used to determine if room temperature oxygen intercalation was possible in a variety of host structures. The results of these experiments are shown in Table 5.3.1a. As already discussed, the only insertion hosts reported for the hypobromite system are the cuprates with the T-phase K_2NiF_4 structure. The La_2CuO_4 was stirred in the hypobromite solution for 20 h. It has been noted by Jorgensen and co-workers[11] that the oxidised cuprate segregates into two phases, both with orthorhombic structures, one with the original host structure, and the other an oxygen rich phase with a very similar structure to the parent material but containing oxygen in interstitial sites. Although the oxygen content upon intercalation obtained from refinement of powder neutron diffraction data (see Appendix 2) is not significantly different from that in the starting material, the is a marked increase in the lattice parameters and cell volume ($c_{initial}$ = 13.1459(6), c_{final} = 13.2144(2) Å; $V_{initial}$ = 379.892(6), V_{final} = 381.85(2) Å^3) suggesting that intercalation has occurred. La_2NiO_4 also has the T-phase K_2NiF_4 structure, and was reacted in the hypobromite solution for 20 h. In this case analysis of the powder neutron diffraction data showed that no phase segregation was observed.

Table 5.3.1a Intercalation products in a variety of host structures.

Host	Oxygen Intercalation ?	Product
Brownmillerite-type		
$Sr_2Fe_2O_5$	✓	$SrFeO_3$[a]
$Sr_2Co_2O_5$	✓	$SrCoO_3$[a]
Sr_2CoFeO_5	✓	$SrCo_{0.5}Fe_{0.5}O_3$[a]
K_2NiF_4-type		
La_2CuO_4	✓	$La_2CuO_{4.03(6)}$[a]
La_2NiO_4	✓	$La_2NiO_{4.14(7)}$[a.]
$YSr_5Ni_3O_{11}$	X	Decomposition
Sr_2CuO_3	X	Decomposition
Other Hosts		
$Ce_2Zr_2O_7$	✓	$Ce_2Zr_2O_{7+x}$[a,Chapter 4]
$YBa_2Cu_3O_{6.20}$	X	Decomposition

[a] confirmation by neutron powder diffraction. Refinements shown in Appendix II.

In the case of the nickelate, the oxidised material, $La_2NiO_{4.14(7)}$, was a single phase with a similar structure to the oxidised $La_2CuO_{4.03}$, but with more interstitial oxygen. Given the identical experimental conditions, the reaction kinetics must be faster for the Ni analogue.

Three materials with the Brownmillerite structure type were also examined, $Sr_2Fe_2O_5$, $Sr_2Co_2O_5$ and Sr_2CoFeO_5. Samples of each material were reacted with the hypobromite solution for 1, 6, 12 and 20 h and then analysed by powder neutron diffraction (see Appendix 2). In the case of $Sr_2Co_2O_5$ and Sr_2CoFeO_5, complete oxidation to the corresponding perovskites, $SrCoO_3$ and $SrCo_{0.5}Fe_{0.5}O_3$ was observed after 1h. Analysis of the neutron powder diffraction pattern of the $Sr_2Fe_2O_5$ host stirred for 20 h in the oxidising media, still showed the presence of a small amount of

Brownmillerite starting material with the perovskite, suggesting that the kinetics of the oxygen insertion reaction are slower for the Fe analogue.

The results of the intercalation of oxygen into $Ce_2Zr_2O_7$ were discussed in Chapter 4.

The $YSr_5Ni_3O_{11}$, Sr_2CuO_3 and $YBa_2Cu_3O_{6.20}$ materials were found to be unstable in the oxidising solution. This limitation of the hypobromite system initiated a search for a chemical oxygen intercalating agent capable of operating in a non-aqueous media.

5.3.2 The Periodate System

5.3.2.1 Introduction

The periodate system was discussed as a potential room temperature chemical intercalating agent for oxygen in section 3.3.2. The two main classes of known room temperature oxygen intercalation hosts, the T-phase K_2NiF_4 and Brownmillerite materials, were used to examine the usefulness of periodate in aqueous and non-aqueous media as an oxygen intercalating agent.

5.3.2.2 Experimental

The syntheses of $Sr_2Fe_2O_5$, Sr_2CuO_3 and $YBa_2Cu_3O_{6.20}$ were described in section 5.2.1.2, and the synthesis of $Sr_2Co_2O_5$ was detailed in section 5.3.1.2.

The host species were treated in 1.5g batches using the chemical oxygen intercalation reaction discussed in Section 3.3.3. The host (0.0005 mole) was added to a 2-fold molar excess of the periodate solution (either $NaIO_4$ in 25 ml distilled water or $((CH_3)_3C)_4NIO_4$ in 25 ml dioxane) for a specified time. The solution was stirred vigorously to ensure a homogeneous exposure of the crystallites to the solution. The reactions were carried out under argon and in deoxygenated solvent to

avoid oxidation of the starting material from any source other than the IO_4^-. The resulting phases were then removed from the solution using a sintered glass filter, washed with distilled water and acetone (or dioxane in the non-aqueous system) and then dried in a vacuum desiccator.

X-ray powder diffraction data suitable for lattice refinement and time-of-flight powder neutron diffraction data were collected as described in section 5.3.1.2. The final atomic parameters of the refinements are given in Appendix 2. Neutron scattering factors used in the refinements were Cu = 0.7718, Y = 0.775, Ba = 0.507 and O = 0.5803×10^{-12} cm.

5.3.2.3 Results and Discussion

The $Sr_2Fe_2O_5$ and $Sr_2Co_2O_5$ host materials with the Brownmillerite structure type were stirred in an aqueous solution of $NaIO_4$ for 48 h. The powder X-ray diffraction fingerprints of the phases removed from the solution of intercalating agent were found to be identical to those of the starting materials, proving that the intercalation of oxygen had not occurred.

The La_2CuO_4 was also stirred in an aqueous solution of the intercalating agent for 48 h. The lattice refinement of the initial and final phases obtained from powder X-ray diffraction data showed that there was no significant increase in the lattice parameters or unit cell volume, indicating the absence of intercalated oxygen.

The $Sr_2Fe_2O_5$ and $YBa_2Cu_3O_{6.20}$ materials were also treated with a solution of tetrabutylammonium metaperiodate in dioxane. The powder X-ray diffraction fingerprint of the Brownmillerite host after treatment was identical to the starting phase, and Rietveld refinement of the powder neutron diffraction data obtained from the $YBa_2Cu_3O_{7-x}$ samples showed no significant change in the oxygen content upon treatment. These results suggest that the metaperiodate ion is not a suitable agent for the room temperature intercalation of oxygen.

5.4 References

1. J-C. Grenier, A. Wattiaux, J-P Doumerc, P. Dordor, L. Fournes, J-P. Chaminade and M. Pouchard, *J. Solid State Chem.*, **96**, 20,1992.

2. J-C. Grenier, A. Wattiaux, N. Lagueyte, J. C. Park, E. Marquestaut, J. Etourneau and M. Pouchard, *Physica C*, **173**, 139, 1991.

3. F. C. Chou, D. C. Johnston, S-W. Cheong and P. C. Canfield, *Physica C*, **216**, 66, 1993.

4. F. C. Chou, J. H. Cho and D. C. Johnston, *Physica C*, **197**, 303, 1992.

5. P. G. Radaelli, J. D. Jorgensen, A. J. Schultz, B. A. Hunter, J. L. Wagner, F. C. Chou and D. C. Johnston, *Phys. Rev.* B, **48**(1), 499, 1993.

6. A. Demourggues, A. Wattiaux, J. C. Grenier, M. Pouchard, J. L. Soubeyroux, J. M. Dance and P. Hagenmuller, *J. Solid State Chem.*, **105**, 458, 1993.

7. P. D. Battle, T. C. Gibb and P. Lightfoot, *J. Solid State Chem.*, **76**, 334-339, 1988.

8. G. Zambonin, *J. Electroanal. Chem.*, **24**, 365, 1970.

9. P. Rudolf and R. Schöllhorn, J. Chem. Soc., Chem. Commun., 1158, 1992.

10. Private correspondance, C. Rial, U. Amador, E. Moran, N. H. Andersen and M. A. Alario-Franco.

11. J. D. Jorgensen, B. Dabrowski, S. Pei, D. G. Hinks, L. Soderholm, B. Morosin, J. E. Schirber, E. L. Venturini and D. S. Ginley, Phys. Rev. B, 38(16), 11337, 1988.

Chapter 6

The Synthesis and Structure of Ceramic Oxides

6.1 Introduction

In this chapter the structural elucidation of four oxides are examined. Two of these are complex mixed metal oxides which exhibit a high degree of non-stoichiometry and are derived from doping transition metals into the Li_2O-ZrO_2 system. One of the structural studies is an examination of the doping behaviour of MgO into "$LiNbO_3$", an important optoelectronic material, while the final section contains an analysis of the nuclear structure of an anion ordered oxygen deficient perovskite by powder neutron diffraction.

6.2 *Ab Initio* Determination of the Crystal Structure of $Li_{29}Zr_9Nb_3O_{40}$

6.2.1 Introduction

The Li_2O-ZrO_2 system has been well characterised by a number of workers in recent years. Some compounds in this system have been investigated because of their properties as solid electrolytes[1, 2], whereas others have found applications as linings for fusion reactors[3].

The slow solid state reaction of refractory ZrO_2 and volatile Li_2O at elevated temperatures can lead to lithia loss, especially in materials with a high lithium content. Consequently, lithium zirconates can be difficult to prepare as single phases. However, despite these problems, a variety of compositions have been identified and their crystal structures characterised, examples of which are Li_2ZrO_3[4] and Li_8ZrO_6[5].

The structure of a metastable form of the $Li_6Zr_2O_7$ phase has recently been solved by Bruce et al[6]. It crystallises in the monoclinic space group *C2/c* with a = 10.4428(1), b = 5.9877(1), c = 10.2014(1)Å and V = 627.67(1)Å^3. The structure is based on a distorted ccp oxide ion array in which 1/8 of the oxygens are missing. Zr and Li adopt an ordered rock salt distribution in the lattice, with Zr in a six-coordinate octahedral geometry, and the Li ions in five-coordinate square pyramidal sites. The square pyramidal sites arise from the vacancy in the anion sublattice and correspond to five apices of an octahedral site in a full ccp array.

In an attempt to form phases of nominal composition $Li_6Zr_{2-x}Nb_xO_{7+x/2}$, the doping of the $Li_6Zr_2O_7$ system with Nb_2O_5 was examined. Samples produced in this solid solution range were expected to exhibit a high oxide ion conductivity induced by partially filling the vacant oxygen sites in the parent material. However, a completely new phase was discovered, at a composition of x = 0.5, the stoichiometry of which is approximately $Li_{29}Zr_9Nb_3O_{40}$.

6.2.2 Experimental Details

The ZrO_2 (Aldrich 99.9 %) [5.4214 g], Nb_2O_5 (Aldrich 99 %) [1.9492 g] and Li_2CO_3 (Aldrich 99.9 %) [7.1522 g] were ground in a 6:1:13.2 stoichiometric ratio (a 10 % molar excess of Li_2CO_3 was used). The mixture was placed in a gold boat and heated for 12 h at 600°C to decompose the lithium carbonate. The sample was then removed from the furnace and quenched to room temperature in air, reground and pelletised using a 13 mm die at a pressure of 4 ton cm^{-2}. The pellets were then fired at 880°C for 24 h in a gold boat and air quenched to room temperature to give the desired product.

Data suitable for structure determination were recorded at room temperature in transmission mode on a Stoe STADI/P high-resolution powder diffractometer, using Cu-$K_{\alpha 1}$ radiation. Data were collected over the range $5° < 2\theta < 110°$ in steps of 0.02°, the entire experiment lasting *ca*, 15 hr. Microanalysis for Li content was carried out on a Unicam PU9400X atomic absorption spectrophotometer.

Time-of-flight powder neutron diffraction data were collected on the POLARIS diffractometer at ISIS, Rutherford Appleton Laboratory. Approximately 10 g of finely ground material was placed in an 11 mm diameter vanadium sample can in the neutron beam. Data were collected in the time-of-flight range 0.200 to 19.600 ms at 298 K, from the backscattering detectors ("C bank" 38 ^{3}He detectors). Only the data between 3.5 and 19.5 ms were used in the refinement. The neutron scattering lengths used were Li = –0.190, Zr = 0.716, Nb = 0.7054 and O = 0.5803×10^{-12} cm.

6.2.3 Structure Determination

The first twenty observed lines of the X-ray powder pattern were indexed on an orthorhombic unit cell, a = 9.168, b = 21.278 and c = 4.156 Å using the program Visser[7] (figure of merit, M_{20} = 49.5). All the peaks in the powder pattern could be attributed to this unit cell, indicating the presence of a single phase material. Systematic absences were consistent with a body-centred cell (h + k, h + l, k + l all =

2n), with no further absence conditions. The centrosymmetric space group *Immm* was assumed for subsequent data analysis.

The pattern decomposition option[8] of the GSAS[9] package was used to extract integrated intensities from the powder pattern. This method employs a modified Rietveld algorithm to assign intensities to the powder diffraction profile using the lattice parameter and peak shape function (4 variables fitting a pseudo-Voigt peak shape) as constraints. No attempt is made to assign correct values to overlapping reflections, and they are instead assigned arbitrary values consistent with the observed profile.

A total of 223 reflections were used as input to the direct methods program SHELXS[10], from which the positions of three heavy atoms were determined (Table 6.2.3a).

Table 6.2.3a Probable atomic positions produced by SHELXS for $Li_{29}Zr_9Nb_3O_{40}$.

Atom	Peak	x	y	z	U_{iso} / Å^2
1	649	0.0000	0.2126	0.0000	0.05
2	489	0.3118	0.5000	0.0000	0.05
3	477	0.0000	0.3615	0.0000	0.05
4	230	0.3454	0.3388	0.0000	0.05
5	142	0.5000	0.2211	0.0000	0.05
6	137	0.2522	0.0624	0.0000	0.05
7	127	0.5000	0.0322	0.0000	0.05
8	124	0.5000	0.3950	0.0000	0.05

The three highest peaks from the direct methods output were chosen as the Zr / Nb sites. The positions of all the oxygen atoms and several lithium atoms were

determined from difference Fourier maps during subsequent Rietveld analysis of the whole diffraction profile, using the GSAS suite of programs. The close-packed nature of the structure became apparent at this point, and this aided in the final details of the refinement.

The final Rietveld refinement involved 43 parameters using 425 contributing reflections and 5993 data points in the range $5° < 2\theta < 110°$. The Zr:Nb occupancy was fixed at 3:1 according to the synthesis, with equal occupancy of all three sites. Temperature factors for Li were not refined and those for O were constrained to be equivalent. The final agreement factors were $R_{wp} = 14.3$ %, $\chi^2 = 2.17$.

6.2.4 Results and Discussion

The refined atomic parameters and selected bond lengths are given in Tables 6.2.4a and 6.2.4b respectively, and the final difference profile is shown in Figure 6.2.4a. Close packed layers of oxygen atoms define available octahedral metal sites at z = 0 and z = 1/2 (Figure 6.2.4b). The Rietveld refinement revealed that all the oxygen sites are fully occupied, except the O(8) site, the occupancy of which refined to 0.06(3). Since this value differs from zero by only two e.s.d.'s, it is probable that this site is completely vacant.

The Zr and Nb oxides are essentially involatile at the temperatures used in the synthesis (both ZrO_2 and Nb_2O_5 are very inert materials with melting points of 2710°C and 1872°C respectively). Since there is no evidence of a second phase, it may be concluded that the Zr and Nb content of the compound is fixed by the composition used in the synthesis. It is also unlikely given the preparation conditions that the oxidation states of the two transtion metals will have varied from those present in the oxides used in the synthesis, as both compounds are thermally stable from room temperature to 900°C.

Table 6.2.4a Final refined atomic parameters for $Li_{29}Zr_9Nb_3O_{40}$ from X-ray data. Space group *Immm*, a = 9.1759(2), b = 21.3113(5) and c = 4.1664(1) Å.

Atom	Site	x	y	z	U_{iso} / Å^2	Occupancy
Zr/Nb(1)	4g	0	0.2105(2)	0	0.0089(7)	0.75/0.25
Zr/Nb(2)	4f	0.3238(3)	0.5	0	0.0194(9)	0.75/0.25
Zr/Nb(3)	4g	0	0.3618(2)	0	0.0104(9)	0.75/0.25
O(1)	8n	0.163(2)	0.4275(6)	0	0.018(1)	
O(2)	4e	0.181(2)	0	0	0.018(1)	
O(3)	8n	0.147(1)	0.2840(7)	0	0.018(1)	
O(4)	8n	0.153(1)	0.1505(7)	0	0.018(1)	
O(5)	4h	0.5	0.2872(14)	0	0.018(1)	
O(6)	4h	0.5	0.1343(11)	0	0.018(1)	
O(7)	4h	0.5	0.4327(8)	0	0.018(1)	
O(8)	2b	0.5	0	0	0.018(1)	0.06(3)
Li(1)	8n	0.324(3)	0.215(3)	0	0.025	
Li(2)	4g	0	0.080(3)	0	0.025	
Li(3)	8n	0.313(4)	0.646(2)	0	0.025	
Li(4)	8n	0.328(5)	0.083(2)	0	0.025	
Li(5)	2d	0	0.5	0	0.025	0.5

An examination of the profile fit for the X-ray data shows that three peaks in the pattern are poorly fitted. These occur at 2θ = 41.845, 43.463 and 61.852°, corresponding to the (370), (002) and (372) reflections respectively. A variety of preferred orientation corrections were investigated, but none was found to improve the fit. However, it is still possible that there is some form of preferred orientation problem as there are no unindexed peaks indicative of an impurity phase.

Table 6.2.4b Selected bond distances and bond valences from X-ray data.

Bond	**Length / Å**	**Valence**	**Σ b.v. per atom type**
Zr(1)-O(3)×2	2.07(1)	1.407	
Zr(1)-O(4)×2	1.90(2)	2.2166	
Zr(1)-O(5)×2	2.08(1)	1.345	4.969
Zr(2)-O(1)×2	2.14(2)	1.1666	
Zr(2)-O(2)×2	2.083(1)	1.3454	
Zr(2)-O(7)×2	2.16(1)	1.091	3.603
Zr(3)-O(1)×2	2.05(2)	1.4786	
Zr(3)-O(3)×2	2.14(1)	1.1636	
Zr(3)-O(6)×2	2.084(1)	1.3412	3.983
Li(1)-O(3) ×2	2.100(4)	0.3602	
Li(1)-O(3)	2.18(3)	0.1410	
Li(1)-O(4)	2.09(4)	0.1872	
Li(1)-O(5)	2.23(5)	0.1266	
Li(1)-O(6)	2.37(5)	0.0894	0.904
Li(2)-O(2)×2	2.39(4)	0.1690	
Li(2)-O(4)×2	2.05(4)	0.4056	
Li(2)-O(7)×2	2.10(1)	0.3598	0.934
Li(3)-O(1)	2.09(5)	0.1876	
Li(3)-O(3)	2.14(4)	0.1653	
Li(3)-O(4)×2	2.11(1)	0.3522	
Li(3)-O(5)	2.22(5)	0.1270	
Li(3)-O(7)	2.39(5)	0.0802	0.912
Li(4)-O(1)×2	2.096(5)	0.3636	
Li(4)-O(2)	2.23(4)	0.1288	
Li(4)-O(4)	2.15(4)	0.1550	
Li(4)-O(6)	1.92(4)	0.2932	0.941
Li(5)-O(1)×4	2.15(2)	0.6292	0.639

Figure 6.2.4a Profile fit for $Li_{29}Zr_9Nb_3O_{40}$ from X-ray data.

Experimental data shown as crosses, profile fit as a continuous line and the difference between observed data and calculated fit at the bottom.

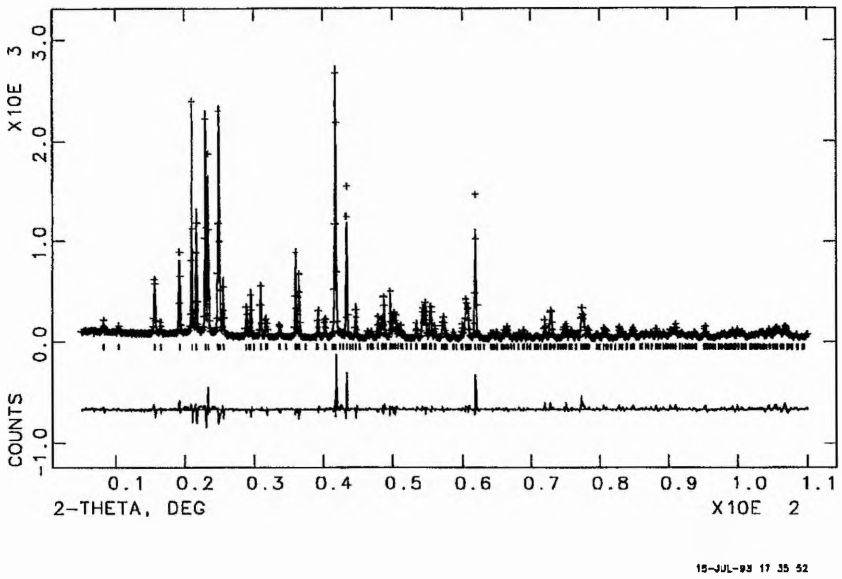

The Zr, Nb and O atoms are satisfactorily determined from the X-ray data (relative scattering factors for X-rays at $2\theta = 0°$ 40:41:8). This is not the case for Li, where the relative scattering factor for X-rays at $2\theta = 0°$ is 3. In view of this and the volatility of Li_2O at the temperatures used for the synthesis of the new phase, the Li content was initially rationalised on the basis that the Zr:Nb ratio was 3:1 from the composition of the starting materials (with no change in their oxidation states from their precursors), and that the O(8) site occupancy is zero within experimental error. This leads to a final composition of the new phase of $Li_{29}Zr_9Nb_3O_{40}$. This composition is supported by atomic absorption analysis of the sample, which gave a composition of 10.5 % Li, compared to the value of 10.4 % expected on the basis of the proposed formula.

There are 21 oxygen sites and 21 octahedral sites per layer, perpendicular to the c axis (Figure 6.2.4b), thus requiring one lithium site to be partially occupied. It is

not possible to state conclusively the location of these vacancies directly from this refinement, and so the occupancy of the Li(5) site was fixed at 0.5 on the basis of bond strength-valence calculations[11] which, as shown in Table 6.2.4b, clearly suggest full occupancy of the Li(1)-Li(4) sites but only partial occupancy (i.e. a valence sum of only 0.64 units) of the Li(5) site.

Neutron diffraction data were required to elucidate fully this problem because they allow a more accurate examination of the Li and O site occupancies, due to their increased relative scattering power compared to the higher X-ray scatterers such as Zr and Nb (neutron scattering are Li = –0.190, Zr = 0.716, Nb = 0.7054 and O = 0.5803×10^{-12} cm).

On initial examination of the neutron data from a new large-scale sample, the presence of a second phase was observed. This could not be accounted for by any of the binary oxides of the metals present (i.e. Li_2O, ZrO_2 or Nb_2O_5). However, a search of the JCPDS[12] database for ternary Li-Zr-O phases produced a number of possibilities: Li_2ZrO_3, $Li_6Zr_2O_7$ and Li_8ZrO_6. The highest intensity impurity peak was at 2.4 Å, and this could be accounted for by Li_8ZrO_6 (PDF No. 28 867). This material has hexagonal symmetry with a = 5.483 and c = 15.45 Å. The structure has never been fully characterised, but it was suggested by Trömel and Hauck to be isomorphous to Li_8SnO_6[5].

A two phase Rietveld refinement of the powder neutron diffraction data was carried out using the CCSL[13, 14] suite of programs. The atomic coordinates obtained from the X-ray data were used as a starting model for the main phase, while the initial atomic parameters for the impurity Li_8ZrO_6 were taken from those of the isostructural Li_8SnO_6.

Figure 6.2.4b View of $Li_{29}Zr_9Nb_3O_{40}$ along c axis, showing the layer at z = 0 only. The square planes of the Zr / Nb octahedra on the ab plane are highlighted in purple. Apical O atoms above and below the layer are not shown. Zr / Nb purple, O red, O(8) site yellow, Li light blue, Li(5) site dark blue spheres.

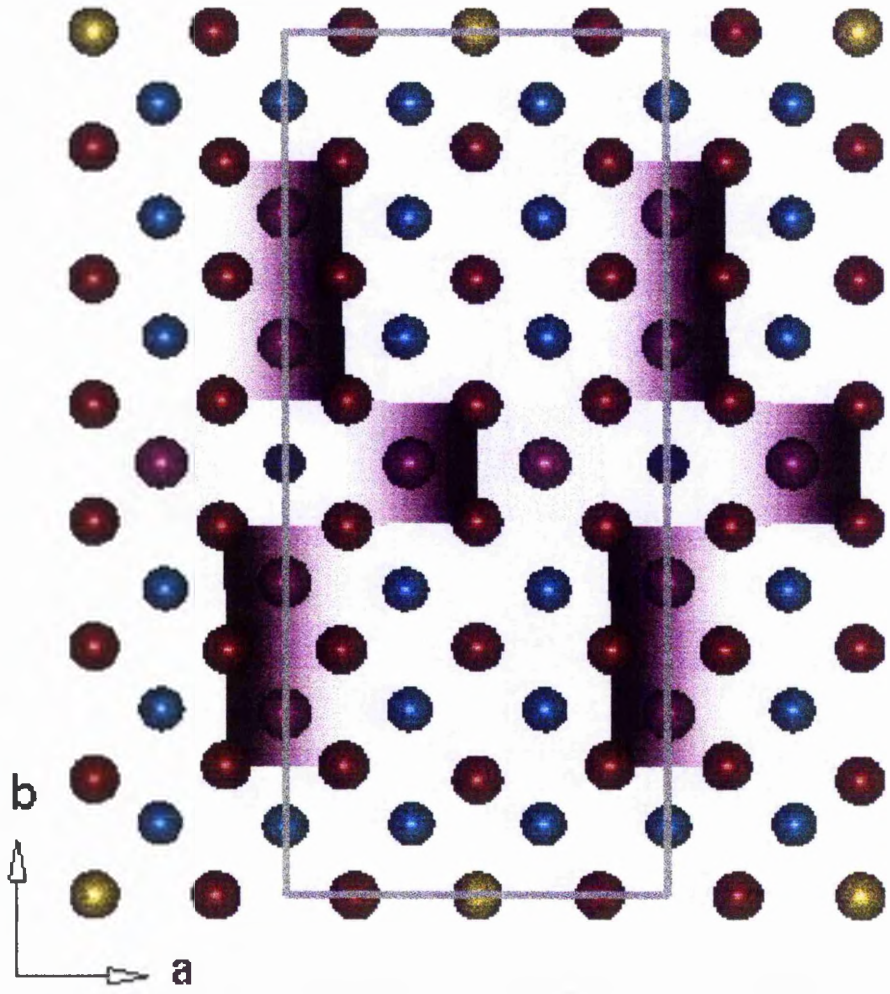

The final refinement involved 83 parameters using 1870 contributing reflections (1359 for $Li_{29}Zr_9Nb_3O_{40}$ and 511 for Li_8ZrO_6) and 3436 observations in the range 3.5-19.5 ms. The Zr:Nb occupancy was fixed at 3:1 according to the synthesis, with equal occupancy of all three sites and the isotropic temperature factor for O(8) was fixed at 0.5 because of its small occupancy. The final agreement factors were $R_{wp} = 2.12$ %, $\chi^2 = 5.3073$.

The refined atomic parameters and selected bond lengths for the neutron refinement of the impurity phase Li_8ZrO_6 are given in Tables 6.2.4d and 6.2.4e respectively, and the profile fit is shown in Figure 6.2.4c.

Table 6.2.4d Final refined atomic parameters for Li_8ZrO_6 from neutron data. Space group $R\bar{3}$, a = b = 5.4615(3) and c = 15.376(8) Å.

Atom	Site	x	y	z	B_{iso} / Å^2	Occupancy
Zr(1)	3a	0	0	0	0.94(12)	1.0
O(1)	18f	0.6760(9)	0.6443(8)	0.4134(3)	0.75(5)	1.0
Li(1)	18f	0.638(2)	0.636(3)	0.8773(5)	1.30(13)	1.0
Li(2)	6c	0	0	0.348(2)	3.0(5)	1.0

Table 6.2.4e Selected bond distances for Li_8ZrO_6.

Bond	Length / Å	Bond	Length / Å
Zr(1)-O(1)×6	2.077(8)	Li(1)-O(1)	1.91(2)
Li(2)-O(1)×3	2.16(3)	Li(1)-O(1)	1.93(2)
Li(2)-O(1)×2	2.37(3)	Li(1)-O(1)	2.01(2)
Li(2)-O(1)	3.77(3)	Li(1)-O(1)	2.01(2)

The structure of Li_8ZrO_6 consists of close packed oxygen atoms. The tetrahedral sites in a close packed structure are conventionally split equally into two types, T^+ and T^-. Tetrahedral sites of one type do not share faces with those of the other type.

Figure 6.2.4c Rietveld refinement of $Li_{29}Zr_9Nb_3O_{40}$ from neutron data.
Experimental data shown as dots, profile fit as a continuous line, and difference / e.s.d. plotted at the bottom. Upper set of tick marks are from the main phase, lower from Li_8ZrO_6.

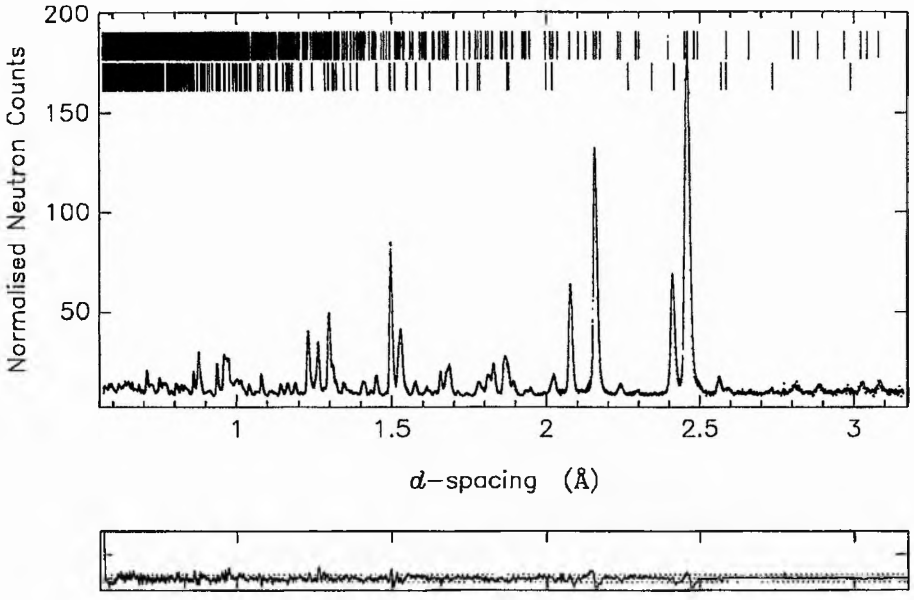

In this structure 1/2 of the tetrahedral sites filled with Li(1) in an ordered arrangement so that they do not share faces with other occupied tetrahedral sites leading to the filling of only the T^+ sites. The Zr(1) and Li(2) fill 1/2 of the octahedral sites in an ordered manner, 2/3 with Li(2) and 1/3 with Zr(1). It can be explained most easily by examining the stacking of the metal-oxygen coordination polyhedra down the c axis (Figure 6.2.4d).

The Zr is coordinated to six oxygens in an octahedral environment. These octahedra are tilted so that two parallel faces lie on the ab plane, and are independent of one another. These Zr sites are bridged, via corner sharing, by six $Li(2)O_6$ octahedra, in a similar orientation, which share vertices with three ZrO_6 octahedra.

Figure 6.2.4d View of Li_8ZrO_6 along the b axis. Li blue, O red and Zr purple spheres. ZrO_6 octahedra are highlighted in purple (LHS), LiO_4 tetrahedra in blue (RHS).

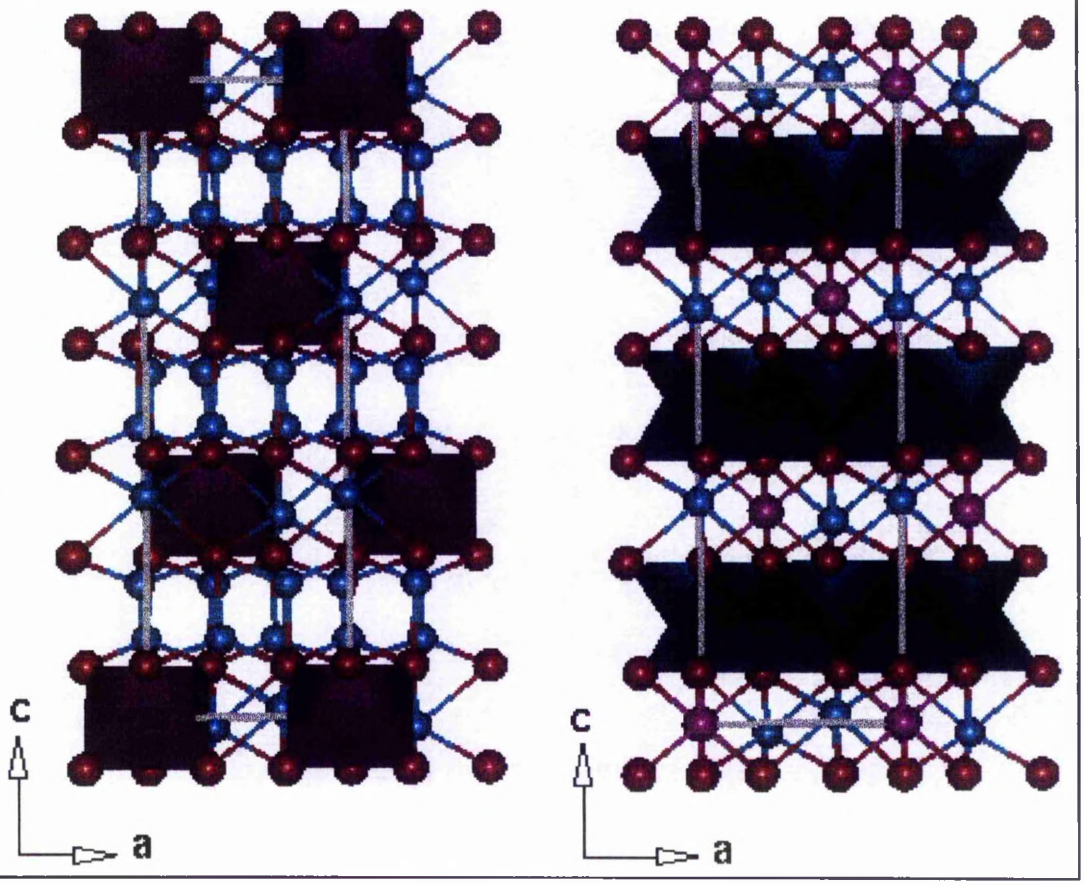

The next layer consists of rows of $Li(1)O_4$ tetrahedra parallel to the crystallographic <110> direction, linked by edge sharing. The tetrahedra lie with one face on the ab plane, but with the orientation of each row alternating along the c direction. Only 1/2 of the tetrahedral sites are filled, with the $Zr(1)$ / $Li(2)O_6$ octahedra situated above the tetahedral vacancies.

The refined atomic parameters and selected bond lengths for the neutron powder diffraction analysis of $Li_{29}Zr_9Nb_3O_{40}$ are given in Tables 6.2.4f and 6.2.4g respectively, and the profile fit is shown in Figure 6.2.4c. The structure is based on a cubic close-packed oxide lattice in which 5 % of the sites are vacant in an ordered manner. The metal atoms adopt a highly novel ordering scheme, occupying all the

available octahedral sites. The structure is best regarded in projection along the short c axis, where a clear view of the ordering of the metals within the octahedral sites may be seen. Equivalent layers, displaced relative to each other by (1/2, 1/2, 0) exist at z = 0 and z = 1/2 (Figure 6.2.4b).

It is clear that the neutron data confirm the basic structure revealed by the X-ray analysis. All sites refined to full occupancy except O(8) and Li(2). The O(8) site has a non-zero occupancy of 0.11(2), and the Li(5) site, which was assigned a nominal occupancy of 0.5 in the X-ray analysis is full, while the Li(2) site was found to have an occupancy of 0.95(5).

The partially occupied O(8) position is adjacent to Li sites only, leading to both square pyramidal and octahedral coordination around Li(4) (depending on whether or not the O(8) site is occupied). The fully occupied Li(5) site will experience square planar coordination if both adjacent O(8) sites are vacant, five coordination if only one O(8) site is occupied and an octahedral environment if both O(8) sites are occupied.

The Li(2) site was also found to be partially filled, with an occupancy of 0.95(5). This is unexpected given the bond valence calculations considered after the X-ray results, but is fully occupied to within one e.s.d. However, any lithium loss on this site may be due to an ordering of the Zr and Nb across the three sites, which is undetectable by either X-ray or Neutron diffraction methods due to the similarity of their scattering factors. If the Zr / Nb(1) site adjacent to Li(2) were to contain only Nb, then the higher charge density in this site may result in repulsion leading to some vacancies on the Li(2) site. The bond valence calculations shown in Table 6.1.3 give a value of 4.969 units for the Zr(1) site (calculated assuming each transition metal site contains only Zr), suggesting that this site may be completely occupied by Nb.

Table 6.2.4f Final refined atomic parameters for $Li_{29}Zr_9Nb_3O_{40}$ from neutron data. Space group *Immm*, a = 9.17409(9), b = 21.30018(21) and c = 4.15302(3)Å.

Atom	Site	x	y	z	B_{iso}/Å^2	Occupancy
Zr/Nb(1)	4g	0	0.20969(11)	0	0.36(2)	0.75/0.25
Zr/Nb(2)	4f	0.3268(2)	0.5	0	0.58(3)	0.75/0.25
Zr/Nb(3)	4g	0	0.36142(10)	0	0.82(3)	0.75/0.25
O(1)	8n	0.1649(3)	0.42847(14)	0	0.64(3)	
O(2)	4e	0.1811(3)	0	0	0.49(4)	
O(3)	8n	0.1488(2)	0.28755(12)	0	0.38(3)	
O(4)	8n	0.1554(3)	0.15024(13)	0	0.75(3)	
O(5)	4h	0.5	0.2838(2)	0	0.89(5)	
O(6)	4h	0.5	0.13430(15)	0	0.42(5)	
O(7)	4h	0.5	0.4364(2)	0	0.63(5)	
O(8)	2b	0.5	0	0	0.5	0.11(2)
Li(1)	8n	0.3174(10)	0.2163(5)	0	1.37(14)	
Li(2)	4g	0	0.0777(7)	0	1.2(3)	0.95(5)
Li(3)	8n	0.3315(13)	0.6461(4)	0	1.25(13)	
Li(4)	8n	0.3071(8)	0.0844(3)	0	1.02(9)	
Li(5)	2d	0	0.5	0	2.8(5)	

This leads to a final composition for the new phase of $Li_{29.79(18)}Zr_9Nb_3O_{40.22(6)}$, to give a total cationic valence of 80.79(18), and a total anionic valence of 80.44(12) per formula unit, assuming the valence on each element is unchanged from that on the reactants (i.e. Li +1, Zr +4, Nb +5, O –2), which charge balances within a 90% confidence interval (i.e. 1.64×e.s.d.).

Table 6.2.4g Selected bond distances from neutron data for $Li_{29}Zr_9Nb_3O_{40}$.

Bond	Length / Å	Bond	Length / Å
Zr(1)-O(3)×2	2.148(5)	Li(1)-O(3) ×2	2.101(14)
Zr(1)-O(4)×2	1.907(8)	Li(1)-O(3)	2.168(14)
Zr(1)-O(5)×2	2.081(5)	Li(1)-O(4)	2.05(2)
Zr(2)-O(1)×2	2.128(6)	Li(1)-O(5)	2.21(2)
Zr(2)-O(2)×2	2.078(4)	Li(1)-O(6)	2.419(14)
Zr(2)-O(7)×2	2.088(5)	Li(2)-O(2)×2	2.35(2)
Zr(3)-O(1)×2	2.080(6)	Li(2)-O(4)×2	2.10(2)
Zr(3)-O(3)×2	2.083(5)	Li(2)-O(7)×2	2.10(2)
Zr(3)-O(6)×2	2.079(6)	Li(3)-O(1)	2.21(2)
		Li(3)-O(3)	2.19(2)
Li(5)-O(1)×4	2.147(4)	Li(3)-O(4)×2	2.082(13)
Li(5)-O(8)×2	2.077	Li(3)-O(5)	2.15(2)
		Li(3)-O(7)	2.34(2)
		Li(4)-O(1)×2	2.110(14)
		Li(4)-O(2)	2.138(12)
		Li(4)-O(4)	1.976(14)
		Li(4)-O(6)	2.064(14)
		Li(4)-O(8)	2.523(13)

In order to investigate further the transition metal ordering in materials with this structure, the tantalum-doped analogue of $Li_{29.79(18)}Zr_9Nb_3O_{40.22(6)}$ was synthesised. Tantalum was chosen because it is chemically similar to niobium (being directly below it in the periodic table), and is of a similar size (the ionic radius is 0.64 Å for Ta^{5+} in a 6 coordinate environment) to niobium (the ionic radius is 0.64 Å for Nb^{5+} in a 6 coordinate environment[15]).

The scattering factors for tantalum and zirconium for neutrons are very similar (Zr = 0.716 and Ta = 0.6910×10^{-12} cm). However, tantalum has a larger relative scattering factor for X-rays than zirconium (73 compared to 40 for $2\theta = 0^{\circ}$ respectively), allowing it to be successfully differentiated in the process of the refinement.

6.3 Determination of the Crystal Structure of $Li_{29}Zr_{9.6}Ta_{2.4}O_{40}$

6.3.1 Introduction

The $Li_6Zr_2O_7$ system was doped with Ta_2O_5 in an attempt to form a new phase of the type $Li_6Zr_{2-x}Ta_xO_{7+x/2}$. The region around x = 0.5 was investigated because a single phase of nominal composition $Li_{29}Zr_9Nb_3O_{40}$ was discovered when $Li_6Zr_2O_7$ was similarly doped with Nb (see section 6.2). A single phase sample was obtained in the Ta system at x = 0.4 and was analysed using a combination of neutron and X-ray powder diffraction techniques.

6.3.2 Experimental Details

The ZrO_2 (Aldrich 99.9 %) [6.7211 g], Ta_2O_5 (Aldrich 99 %) [2.6781 g] and Li_2CO_3 (Aldrich 99.9 %) [7.3890 g] were ground in a 9:1:16.5 stoichiometric ratio (a 10 % molar excess of Li_2CO_3 was used). The mixture was then placed in a gold boat and heated for 12 h at 600°C to decompose the carbonate. The sample was then quenched to room temperature in air, reground and pelletised using a 13 mm die at 4 ton cm^{-2}. The pellets were fired at 900°C for 24 h in a gold boat and air quenched to room temperature to give the desired product.

Data suitable for structure determination were recorded at room temperature in transmission mode on a Stoe STADI/P high-resolution powder diffractometer, using Cu-$K_{\alpha 1}$ radiation. Data were collected over the range $5° < 2\theta < 105°$ in steps of 0.02°, the entire experiment lasting *ca*, 15 h.

Time-of-flight powder neutron diffraction data were collected on the POLARIS diffractometer at ISIS, Rutherford Appleton Laboratory. Approximately 1.5 g of finely ground material was placed in a 6 mm diameter vanadium sample can. Data were collected in the time-of-flight range 0.2 to 19.6 ms at 298 K, with only the

data between 3.5 and 16.0 ms from the backscattering detectors ("C bank" 38 ^{3}He detectors) used in the refinement. The neutron scattering lengths used were Li = −0.190, Zr = 0.716, Ta = 0.6910 and O = 0.5803×10^{-12} cm.

6.3.3 Structural Determination

The X-ray powder pattern was qualitatively very similar to that of the $Li_{29}Zr_9Nb_3O_{40}$ phase (see section 6.2), and the atomic coordinates and lattice parameters from this phase were used as an initial model in the refinement. The neutron data were examined first to obtain accurate site occupancies for Li and O, and then X-ray diffraction was used to probe the Zr / Ta ordering.

A joint X-ray and neutron powder diffraction Rietveld refinement using the GSAS[9] suite of programs was not possible for a structure of this complexity, because the peak shape obtained from the neutron data could not be adequately fitted. The neutron data were therefore analysed using the CCSL[13, 14] package, while the X-ray data were analysed using GSAS.

The Rietveld refinement of the neutron powder diffraction data involved 47 parameters (44 from the main phase and 3 from the vanadium can), using 1374 contributing reflections (1359 from the sample and 15 from the vanadium can) and 3040 data points in the range 3.5-16.0 ms. The Zr:Ta occupancy was fixed at 4:1 according to the synthesis, with equal occupancy of all three sites. Temperature factors for each site of a specific element were constrained to be equivalent. Final agreement factors were R_{wp} = 1.35 %, χ^2 = 3.4729.

6.3.4 Results and Discussion

The neutron powder diffraction data was found to contain reflections from two phases. In addition to those expected, peaks attributable to the vanadium sample can were also observed. Vanadium has a very simple crystal structure, with cubic

symmetry and a lattice parameter of a = 3.028 Å, and was included in the refinement. The refined atomic parameters from the neutron powder diffraction experiment are shown in Table 6.3.4a, the profile fit in Figure 6.3.4a and selected bond distances in Table 6.3.4b.

Table 6.3.4a Final refined atomic parameters for $Li_{29}Zr_{9.6}Ta_{2.4}O_{40}$ from neutron data. Space group *Immm*, a = 9.2067(2), b = 21.3648(6) and c = 4.15372(8)Å.

Atom	**Site**	**x**	**y**	**z**	**B_{iso} / Å^2**	**Occupancy**
Zr/Ta(1)	4g	0	0.2077(3)	0	0.65(4)	0.8/0.2
Zr/Ta(2)	4f	0.3211(7)	0.5	0	0.65(4)	0.8/0.2
Zr/Ta(3)	4g	0	0.3638(3)	0	0.65(4)	0.8/0.2
O(1)	8n	0.1728(7)	0.4257(3)	0	0.71(3)	
O(2)	4e	0.1920(9)	0	0	0.71(3)	
O(3)	8n	0.1502(6)	0.2882(3)	0	0.71(3)	
O(4)	8n	0.1537(8)	0.1481(4)	0	0.71(3)	0.855(22)
O(5)	4h	0.5	0.2939(4)	0	0.71(3)	
O(6)	4h	0.5	0.1375(4)	0	0.71(3)	
O(7)	4h	0.5	0.4364(2)	0	0.71(3)	
O(8)	2b	0.5	0	0	0.71(3)	0.19(5)
Li(1)	8n	0.318(2)	0.2130(10)	0	1.10(8)	
Li(2)	4g	0	0.0783(14)	0	1.10(8)	
Li(3)	8n	0.328(3)	0.6490(9)	0	1.10(8)	
Li(4)	8n	0.299(2)	0.0848(8)	0	1.10(8)	
Li(5)	2d	0	0.5	0	-	0

[Vanadium: Space group $Im\bar{3}m$, a = 3.0278(2) Å, V x = y = z =0, B_{iso} = 1.52(13) Å^2]

Table 6.3.4b Selected bond distances and valences from the neutron refinement of $Li_{29}Zr_{9.6}Ta_{2.4}O_{40}$. (b. v.'s calculated using partially occupied O(4) and O(8) sites).

Bond	Length / Å	Valence	Σ b.v. per atom type
Zr(1)-O(3)x2	2.207(11)	0.9644	
Zr(1)-O(4)x2	1.90(2)	1.8714	
Zr(1)-O(5)x2	2.077(11)	1.3694	4.206
Zr(2)-O(1)x2	2.094(12)	1.3090	
Zr(2)-O(2)x2	2.080(9)	1.3576	
Zr(2)-O(7)x2	2.071(11)	1.3906	4.057
Zr(3)-O(1)x2	2.068(12)	1.4006	
Zr(3)-O(3)x2	2.1260(9)	1.1992	
Zr(3)-O(6)x2	2.077(12)	1.3698	3.970
Li(1)-O(3) x2	2.0979()	0.3626	
Li(1)-O(3)	2.23(3)	0.1277	
Li(1)-O(4)	2.05(3)	0.1760	
Li(1)-O(5)	2.41(3)	0.0783	
Li(1)-O(6)	2.33(3)	0.0975	0.842
Li(2)-O(2)x2	2.43(3)	0.1462	
Li(2)-O(4)x2	2.06(4)	0.3473	
Li(2)-O(7)x2	2.12(3)	0.3432	0.846
Li(3)-O(1)	2.14(3)	0.1603	
Li(3)-O(3)	2.12(3)	0.1717	
Li(3)-O(4)x2	2.08(3)	0.3222	
Li(3)-O(5)	2.00(3)	0.2378	
Li(3)-O(7)	2.49(3)	0.0623	0.954
Li(4)-O(1)x2	2.11(3)	0.3554	
Li(4)-O(2)	2.06(2)	0.2001	
Li(4)-O(4)	1.90(3)	0.2639	
Li(4)-O(6)	2.17(3)	0.1501	
Li(4)-O(8)	2.59(2)	0.0091	0.978

It is clear from the neutron refinement that this structure is very similar to that of the niobium doped analogue discussed in section 4.1, i.e. a cubic close-packed array of oxygen atoms with the metal atoms found in the octahedral sites (Figure 6.3.4b). The O(4) and O(8) sites were found to have partial occupancies, while the Li(5) site at (0, 0.5, 0) was found to be completely empty.

Figure 6.3.4a Profile fit for $Li_{29}Zr_{9.6}Ta_{2.4}O_{40}$ from neutron data.
Experimental data shown as dots, profile fit as a continuous line and difference / e.s.d. at the bottom. Upper set of tick marks are from the main phase, lower from V.

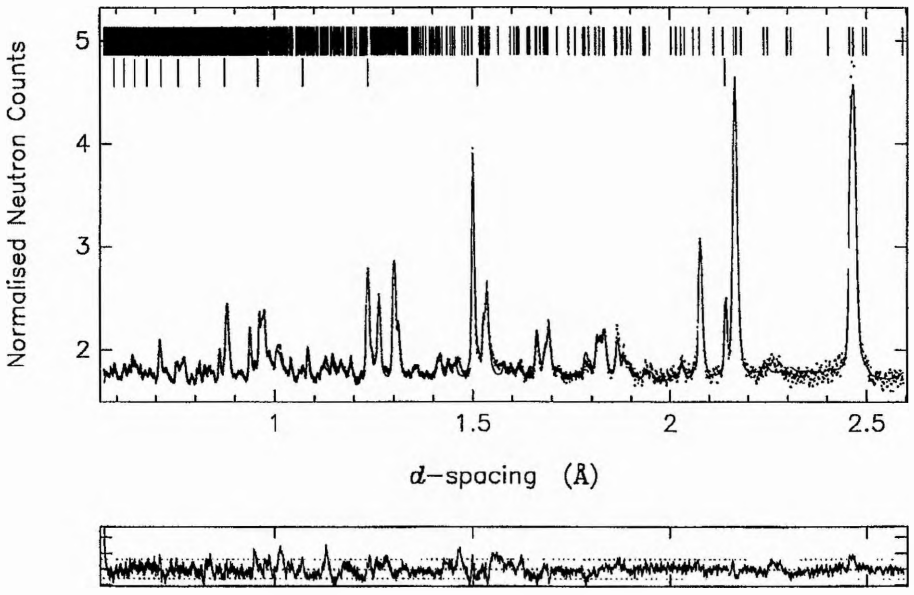

Closer examination of the results show that the Li(2) site, which was fully occupied to within one e.s.d. in the niobium phase is fully occupied in the tantalum doped sample.

The O(8) site has a higher occupancy here than was observed in the niobium analogue- 0.19(5) compared to 0.11(2), but still exhibits significant vacancies. It is these O(8) oxygens which form the apical positions of the octahedral site around

Li(5), which is full in the niobium doped sample, but entirely unoccupied in this tantalum analogue. Oxide ion transport requires the partial occupancy of oxide ion sites and the existence of pathways for migration between sites. Only 20 % of the O(8) sites are filled. In order for migration of the O(8) oxide ion to occur, it must move from its octahedral site and into a neighbouring unoccupied tetrahedral site through the triangular face common to both. From this tetrahedral site, it can return to the original O(8) site or move to the next one along the c axis, providing that it is vacant. If it is occupied, a cooperative mechanism could occur where the next O(8) ion will migrate into a neighbouring tetrahedral site, leaving the its site vacant for the original oxide ion to enter. This process will be made enhanced because all the intervening Li(5) sites between neighbouring O(8) sites along the c axis are vacant. This means that instead of having to hop through a bottleneck of three Li ions forming the face shared between the occupied O(8) site and the vacant tetrahedral site, only two Li ions will form this face. This creates an oxide ion migration route running through the structure parallel to the c axis.

The final partially occupied site is O(4), which coordinates to Zr / Ta(1), as well as Li(1)-Li(4) and has an occupancy of 0.855(22). The Zr / Ta(1) and Li(2) sites coordinate to two O(4) sites on the z = 0 plane, producing a pseudo-tetrahedral environment if both O(4) positions are unoccupied, square pyramidal if only one is occupied, and the expected octahedral coordination if both are occupied. The short bond length between Zr / Ta(1) and O(4) of 1.90(2) Å can then be explained by the transition metal site moving towards the partially filled O(4) positions. The Li(1) site is adjacent to only one O(4), producing a square pyramidal environment if it is vacant, and octahedral if it is occupied. The Li(3) site is coordinated to two apical O(4) sites on the z = 0.5 and z = –0.5 planes. If these are both vacant a square planar environment will be formed, while if one is filled Li(3) will be in a square pyramidal site. Occupancy of both O(4) sites will result in Li(3) lying in an octahedral site. The Li(4) site is coordinated to two partially occupied sites, O(4) and O(8). If both are vacant, a square planar coordination is produced, since the O(4)-Li(4)-O(8) angle is

approximately 180°. If only one of the oxygen sites is occupied, the Li(4) will have a square pyramidal coordination, while if both are occupied it will be in an octahedral site.

Figure 6.3.4b View of $Li_{29}Zr_{9.6}Ta_{2.4}O_{40}$ along c axis, showing the layer at z = 0 only. Zr / Ta octahedra are highlighted in purple. Apical O atoms above and below the layer are not shown. Zr / Ta purple (Zr(1) site dark purple), O red (O(4) site brown, O(8) site yellow), Li light blue spheres.

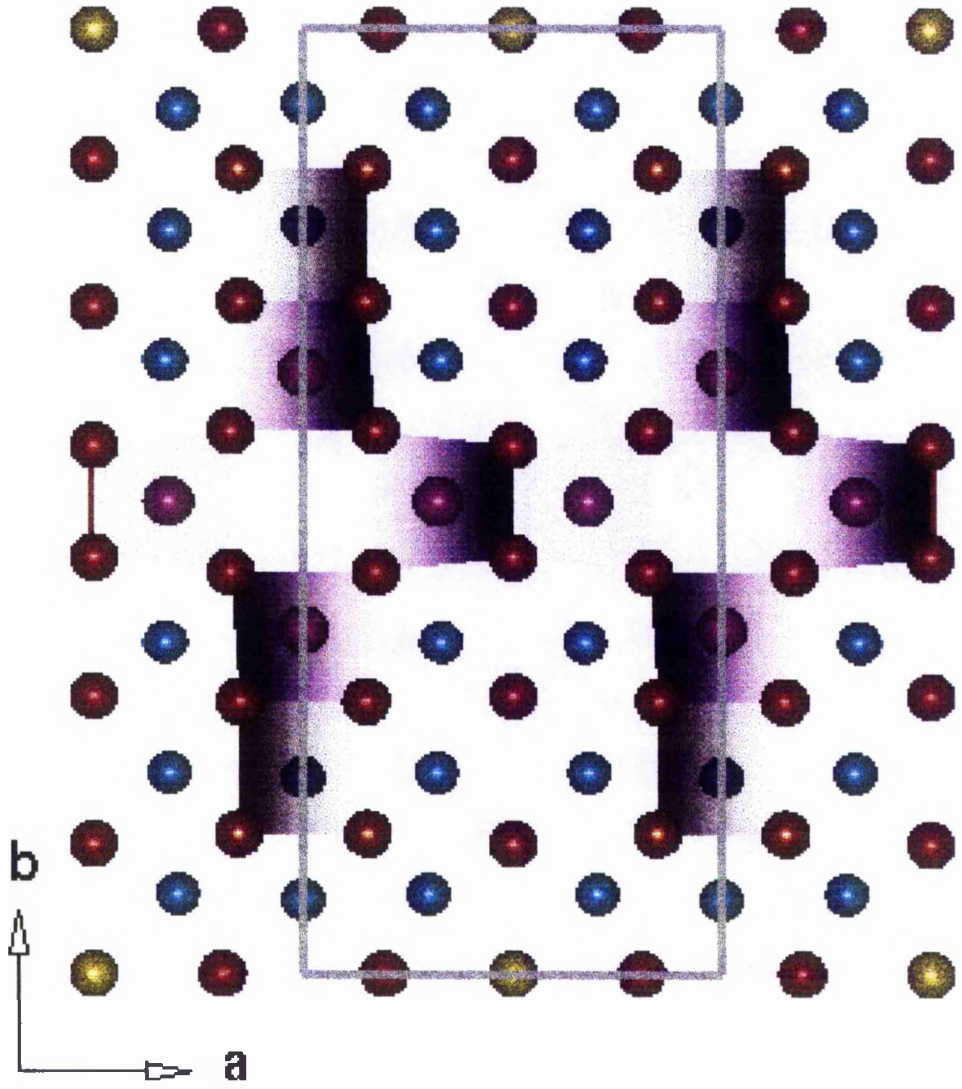

The neutron diffraction experiment cannot be used to differentiate between tantalum and zirconium due to the similar sizes of their scattering factors, however the bond valence calculations shown in Table 6.3.4b suggest a partitioning of the tantalum into the Zr / Ta(1) site. The bond valence sum for this site is 4.206, in contrast to values of 4.057 and 3.970 for the Zr / Ta(2) and Zr / Ta(3) sites respectively, suggesting that the majority of the tantalum is situated on Zr / Ta(1).

Powder X-ray diffraction can be used to differentiate between zirconium and tantalum because of the large difference in their scattering factors (73 for Ta and 40 for Zr at $2\theta = 0°$), making this a complementary technique to neutron diffraction, which allows a more accurate determination of the lithium and oxygen site occupancies.

The final X-ray Rietveld refinement involved 50 parameters using 316 contributing reflections and 4999 data points in the range $5° < 2\theta < 105°$. The data were collected in a 0.2 mm capillary and corrected for sample absorption[16]. Temperature factors for Li were not refined and those for all the O sites were constrained to be equivalent, as were all the Zr / Ta sites. The occupancies of the lithium and oxygen sites were fixed at the values obtained from the neutron refinement, while the total occupancy of each Zr / Ta site was constrained to equal one, but the proportion of each element was allowed to vary. Final agreement factors were $R_{wp} = 5.79$ %. The final refined atomic coordinates for the X-ray experiment are shown in Table 6.3.4c, selected bond distances in Table 6.3.4d and the profile fit in Figure 6.3.4c.

The proportion of metals in both the Zr / Ta(2) and Zr / Ta(3) sites refined to give a full occupancy for zirconium. However, the Zr / Ta(1) site was found to contain all the available tantalum, as indicated by the bond valence calculations, to give a ratio of Zr:Ta of 0.389(10):0.611(10). This produces an overall Zr:Ta ratio of 3.91(1):1.00(1), almost identical to that in the starting materials (4:1).

Table 6.3.4c Final refined atomic parameters for $Li_{29}Zr_{9.6}Ta_{2.4}O_{40}$ from X-ray data. Space group *Immm*, a=9.2052(2), b=21.3629(5) and c=4.15418(9)Å.

Atom	Site	x	y	z	U_{iso} / Å^2	Occupancy
Zr/Ta(1)	4g	0	0.2121(2)	0	0.0094(5)	0.389(10)/0.611(10)
Zr(2)	4f	0.3204(4)	0.5	0	0.0094(5)	
Zr(3)	4g	0	0.3638(2)	0	0.0094(5)	
O(1)	8n	0.173(2)	0.4263(8)	0	0.0033(13)	
O(2)	4e	0.173(3)	0	0	0.0033(13)	
O(3)	8n	0.1438(14)	0.2890(10)	0	0.0033(13)	
O(4)	8n	0.161(3)	0.1488(10)	0	0.0033(13)	0.855
O(5)	4h	0.5	0.289(2)	0	0.0033(13)	
O(6)	4h	0.5	0.1335(13)	0	0.0033(13)	
O(7)	4h	0.5	0.4334(12)	0	0.0033(13)	
O(8)	2b	0.5	0	0	0.0033(13)	0.189
Li(1)	8n	0.302(5)	0.211(3)	0	0.025	
Li(2)	4g	0	0.071(4)	0	0.025	
Li(3)	8n	0.328(7)	0.643(3)	0	0.025	
Li(4)	8n	0.302(6)	0.092(2)	0	0.025	

The final stoichiometry for the phase is then $Li_{28}Zr_{9.56(4)}Ta_{2.44(4)}O_{39.22(27)}$. This gives a total cationic valence of 78.44(27) and a total anionic valence of 78.44(55), which charge balances within one e.s.d. (assuming the valences on each element are unchanged from that of the reactants i.e. Li +1, Zr +4, Ta +5, O –2).

Table 6.3.4d Selected bond distances from X-ray Refinement of $Li_{29}Zr_{9.6}Ta_{2.4}O_{40}$.

Bond	Length/Å	Bond	Length/Å	Bond	Length/Å
Zr(1)-O(3)×2	2.11(2)	Li(1)-O(3) ×2	2.136(11)	Li(3)-O(1)	2.05(7)
Zr(1)-O(4)×2	2.00(3)	Li(1)-O(3)	2.21(5)	Li(3)-O(3)	2.24(7)
Zr(1)-O(5)×2	2.0772(4)	Li(1)-O(4)	1.86(6)	Li(3)-O(4)×2	2.084(6)
Zr(2)-O(1)×2	2.08(2)	Li(1)-O(5)	2.47(6)	Li(3)-O(5)	2.17(7)
Zr(2)-O(2)×2	2.0781(10)	Li(1)-O(6)	2.46(5)	Li(3)-O(7)	2.27(7)
Zr(2)-O(7)×2	2.18(2)	Li(2)-O(2)×2	2.19(6)	Li(4)-O(1)×2	2.127(11)
Zr(3)-O(1)×2	2.08(2)	Li(2)-O(4)×2	2.23(7)	Li(4)-O(2)	2.31(6)
Zr(3)-O(3)×2	2.08(2)	Li(2)-O(7)×2	2.079(4)	Li(4)-O(4)	1.78(6)
Zr(3)-O(6)×2	2.0779(8)			Li(4)-O(6)	2.02(6)
				Li(4)-O(8)	

Figure 6.3.4c Rietveld refinement of $Li_{29}Zr_{9.6}Ta_{2.4}O_{40}$ from X-ray data.

Experimental observations shown as crosses, profile fit as a continuous line, and the difference between the observed data and calculated fit is plotted at the bottom.

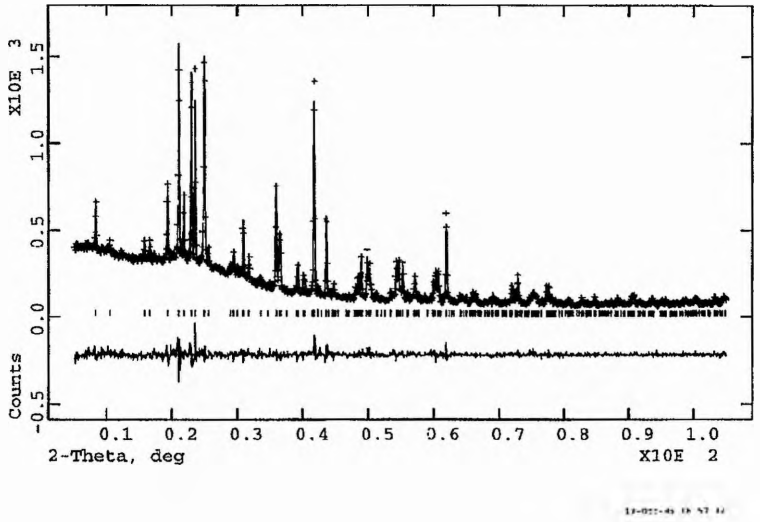

In conclusion, both the niobium and tantalum doped phases seem to possess similar structures, with the specific lithium and oxygen contents dependent upon the transition metal doping ratio. The proportion of the niobium dopant across the three heavy metal sites is still unknown, but if the general structure is identical to that of the tantalum phase then it would seem probable that it is contained in the Zr(1) site.

6.4 A Combined X-ray and Neutron Powder Diffraction Study of Magnesium-doped Lithium Niobate

6.4.1. Introduction

Lithium Niobate, '$LiNbO_3$', is a ferroelectric material with potential applications in a wide range of optical and electronic devices. It is currently used in surface acoustic wave devices and optical waveguides[17, 18], and has potential in optically based storage systems[19], due to the presence of a large photorefractive effect.

In many cases lithium niobate is doped with other cations to improve its performance, and despite the technological and commercial importance of these materials, little is known in detail concerning the nature of their defect structure. The photorefractive performance of lithium niobate is improved by the presence of transition metal cations, because they are responsible for the modification of the optical properties of the matrix. In order to explain fully the optical alterations introduced by the impurities, their lattice location must be elucidated.

Doping congruently melting '$LiNbO_3$' with MgO has been shown to reduce the optical damage due to the photoreflective effect[20]. In order to gain an insight into the effect of dopants on the optical and ferroelectric properties of '$LiNbO_3$', its structure must be analysed in detail.

The crystal structure of '$LiNbO_3$' is related to that of corundum, which has a hexagonal close packed oxide array with Al ions occupying 2/3 of the octahedral sites in an ordered manner. Li^+ and Nb^{5+} have similar ionic radii (0.76 and 0.64 Å respectively, for a six coordinate environment[15]), enabling '$LiNbO_3$' to adopt a corundum-like structure with a hexagonal close-packed oxide array in which 2/3 of the octahedral sites are occupied by the cations in an ordered manner. The nature of the cation ordering within these sites leads to a sequence Li, Nb, vacancy, Li, Nb, vacancy..... for adjacent octahedral sites along the c axis of the rhombohedral unit cell

(Figure 6.4.1a). Both Li^{+} and Nb^{5+} ions are surrounded by distorted octahedra of six oxygen ions.

Figure 6.4.1a Structure of '$LiNbO_3$', showing Li (blue spheres), O (red sheres) and NbO_6 octahedra in purple. Every third octahedral site is vacant.

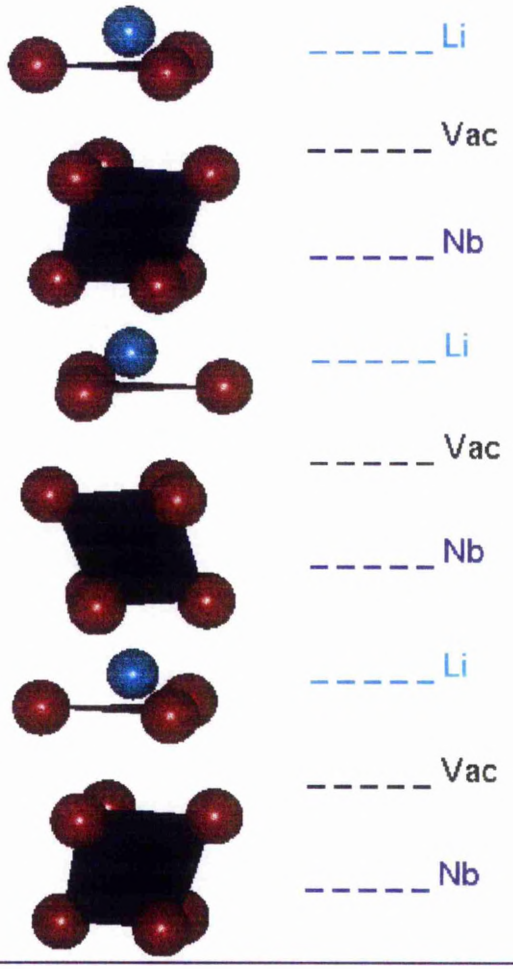

'$LiNbO_3$' has a tendancy to non-stoichiometry with a Li/Nb ratio < 1. A recent study[21] has shown the defect structure of this phase to be of the form $[Li_{1-x}Nb_{x/5}][Nb]O_3$, with a Li/Nb ratio of *ca* 0.95. This suggests that there are no significant vacancies on the niobium or oxygen sites, and only the minimum number of anti-site defects (i.e. Nb on Li site) required to balance the charge. An examination

of congruent lithium niobate (where the ratio of Li/Nb remains fixed) using single crystal X-ray diffraction techniques[28] demonstrated the phase was best formulated as $[Li_{0.94}Nb_{0.059}][Nb_{0.953}]O_3$ i.e. $Li_{0.94}Nb_{1.012}O_3$. With such intrinsic defects, structural flexibility exists which can explain why lithium niobate can tolerate high concentrations of extrinsic defect ions.

Local structural techniques have been used to study the environment of the dopant itself, including EPR[22], optical[23], Mössbauer[24] and, in particular EXAFS[25, 26] and computer modelling methods[26, 27]. The general consensus is that all dopants except Ta^{5+} prefer to substitute at the Li rather than the Nb site. The magnesium doped material was examined in this study since this is technologically important due to its photorefractive properties. In order to achieve the best determination of the defect structure, the complementary scattering characteristics of X-ray and neutron diffraction were exploited.

6.4.2 Experimental Details

Samples of nominal composition '$Li_{1-x}Mg_xNbO_3$' were prepared for x = 0.1, 0.2, and 0.3. The correct stoichiometric mixture of MgO [Aldrich, 99.9 %] and Nb_2O_5 [Aldrich, 99.9 %] was pre-fired with a 10% molar excess of lithium, in the form of Li_2CO_3 [BDH, 99.5 %], at 600°C. The product was then reground, pelletised at 5 ton cm^{-2} and fired at 900°C for 24 h in air to give the desired phase.

Data suitable for structure determination were recorded at room temperature in transmission mode on a Stoe STADI/P high-resolution powder diffractometer, using Cu-$K_{\alpha 1}$ radiation. Data were collected over the range $5° < 2\theta < 85°$ in steps of 0.02°, the entire experiment lasting *ca*, 11 h.

Time-of-flight powder neutron diffraction data were collected on the POLARIS diffractometer at ISIS, Rutherford Appleton Laboratory. Approximately 10 g of finely ground material was placed in an 11 mm diameter vanadium sample can in the neutron beam. Data from the backscattering detectors ("C bank" 38 ^3He

detectors) were collected in the time-of-flight range 0.20 to 19.60 ms at 298K, with only the data between 2.5 and 19.0 ms used in the refinement. The neutron scattering lengths used were Li = –0.203, Mg = 0.5375, Nb = 0.7054 and O = 0.5805×10^{-12} cm.

All the analysis of the diffraction data was carried out using the GSAS[9] suite of programs. This has the facility to refine a model *simultaneously* against several data sets, specifically in this case X-ray and neutron data. This was particularly useful since two independent data sets of differing scattering contrast were needed in order to examine unambiguously the distribution of three cations over two independent sites.

6.4.3 Results and Discussion.

All the refinements were carried out in the space group *R3c* (hexagonal setting) in accord with earlier studies[21, 28], with Li and Nb in 6a (0, 0, z) sites and O in 18b (x, y, z) sites. Each refinement involved the use of both X-ray and neutron data sets, and the refinement of unconstrained individual atomic positional parameters in addition to the usual scale, background, peak-shape and lattice parameters.

There are numerous possible doping mechanisms which may be postulated for the incorporation of Mg^{2+} into '$LiNbO_3$'. Katsumata et al[29] have recently explored this phase diagram in some detail in an X-ray study, examining the four following possibilities:

$$(1\text{-}x)Li_{0.954}Nb_{1.009}O_3 + xMgO \qquad \text{(Eqn. 6.4.3a)}$$

$$(1\text{-}x)LiNbO_3 + xMgO \qquad \text{(Eqn. 6.4.3b)}$$

$$[Li_{1-2x}, Mg_x]_{0.954}Nb_{1.009}O_3 \qquad \text{(Eqn. 6.4.3c)}$$

$$[Li_{1-2x}, Mg_x]NbO_3 \qquad \text{(Eqn. 6.4.3d)}$$

The mechanisms of Eqn. 6.4.3a and Eqn. 6.4.3c are based on the idea that doping would retain the type of non-stoichiometry present in congruently melting '$LiNbO_3$' itself. The types exhibited in Eqn. 6.4.3c and Eqn. 6.4.3d assume that Mg^{2+} replaces Li^+ exclusively in a charge compensating manner. The synthesis used in this study was based upon a simple '1:1' substitution, typified by Eqn. 6.4.3b.

The initial refinements made no assumptions about the nature of the cation doping in these solid solutions except that the oxygen stoichiometry should remain fixed. Hence the occupancies of both Li and Nb on their own sites were allowed to vary freely, and in addition, a variable Mg occupancy was allowed on both sites. The preliminary refinements for all three samples (Table 6.4.3a) clearly showed a marked preference for Mg substitution exclusively on the Li site, and with no deviation of the Nb site occupancy from unity for the x = 0.2 and x = 0.3 samples within a 90 % confidence interval (i.e. 2×e.s.d.). In the x = 0.1 sample, the Nb site occupancy is 1.013(2), a value which is anomalously high, since the scattering factors for Li and Mg are less than that of Nb for both X-rays and neutrons, it is unlikely that either of these elements is present on the Nb site.

Table 6.4.3a Comparison of constrained and unconstrained site occupancies for $Li_{1-x}Mg_{x/2}NbO_3$, x = 0.1, 0.2, 0.3.

	x=0.1		x=0.2		x=0.3	
	unconstrained	constrained[b]	unconstrianed	constrained	unconstrained	constrained
Li	0.71(5)	0.833(3)	0.78(4)	0.779(5)	0.71(6)	0.724(3)
Mg[a]	0.04(2)	0.083(2)	0.12(2)	0.110(2)	0.13(2)	0.138(2)
Nb	1.013(2)	1.013(2)	1.005(3)	1.006(3)	1.004(2)	1.004(2)

[a] Mg occupancy on Li site. [b] constraint of the form (2×Mg + Li) occupancy = 1.

Table 6.4.3b Crystal data for $Li_{1-x}Mg_{x/2}NbO_3$, x = 0.1, 0.2, 0.3.

x = 0.1, space group R3c, a = 5.5148(3), c = 13.8682(8) Å.

Atom	Site	x	y	z	U_{iso} / Å^2	Occupancy
Li	6a	0	0	0.2776(2)	0.0147(6)	0.833(4)
Mg	6a	0	0	0.2776(2)	0.0147(6)	0.083(2)
Nb	6a	0	0	0	0.0036(1)	
O	18b	0.04719(8)	0.34245(13)	0.06413(4)	0.0053(1)	

χ^2 = 5.167, R_{wp} = 0.020 for 3999 X-ray data (28 reflections) and 4057 neutron data (588 reflections).

x = 0.2, space group R3c, a = 5.51605(2), c = 13.8826(6) Å.

Atom	Site	x	y	z	U_{iso} / Å^2	Occupancy
Li	6a	0	0	0.2750(4)	0.0175(11)	0.779(4)
Mg	6a	0	0	0.2750(4)	0.0175(11)	0.110(2)
Nb	6a	0	0	0	0.0053(1)	
O	18b	0.04614(10)	0.34321(15)	0.06465(5)	0.0065(1)	

χ^2 = 20.70, R_{wp} = 0.045 for 3999 X-ray data (28 reflections) and 4057 neutron data (590 reflections).

x = 0.3, space group R3c, a = 5.51623(3), c = 13.8913(8) Å.

Atom	Site	x	y	z	U_{iso} / Å^2	Occupancy
Li	6a	0	0	0.2710(4)	0.0215(9)	0.724(4)
Mg	6a	0	0	0.2710(4)	0.0215(9)	0.138(2)
Nb	6a	0	0	0	0.0052(1)	
O	18b	0.04641(6)	0.3432(10)	0.06486(3)	0.0063(1)	

χ^2 = 8.228, R_{wp} = 0.027 for 3998 X-ray data (28 reflections) and 4057 neutron data (591 reflections).

Figure 6.4.3a Final observed (crosses), calculated (solid line) and difference profiles for the Rietveld refinement of $Li_{1-x}Mg_{x/2}NbO_3$, x = 0.1. The tick marks represent allowed reflections.

a) X-ray Refinement.

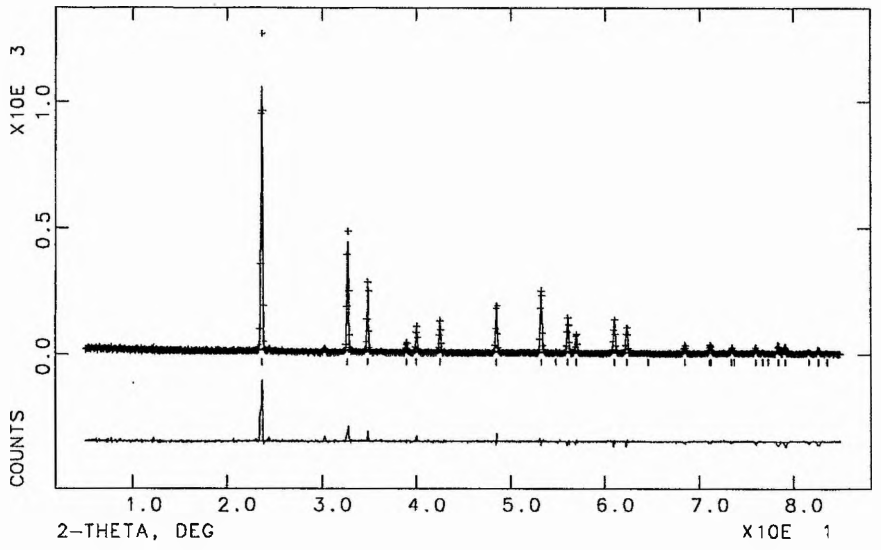

b) Neutron Refinement.

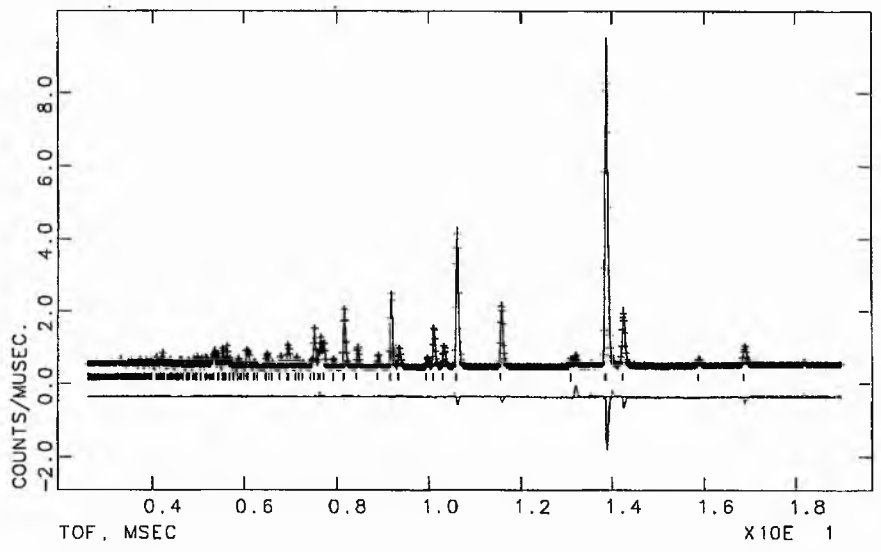

Figure 6.4.3b Final observed (crosses), calculated (solid line) and difference profiles for the Rietveld refinement of $Li_{1-x}Mg_{x/2}NbO_3$, x = 0.2. The tick marks represent allowed reflections.

a) X-ray Refinement.

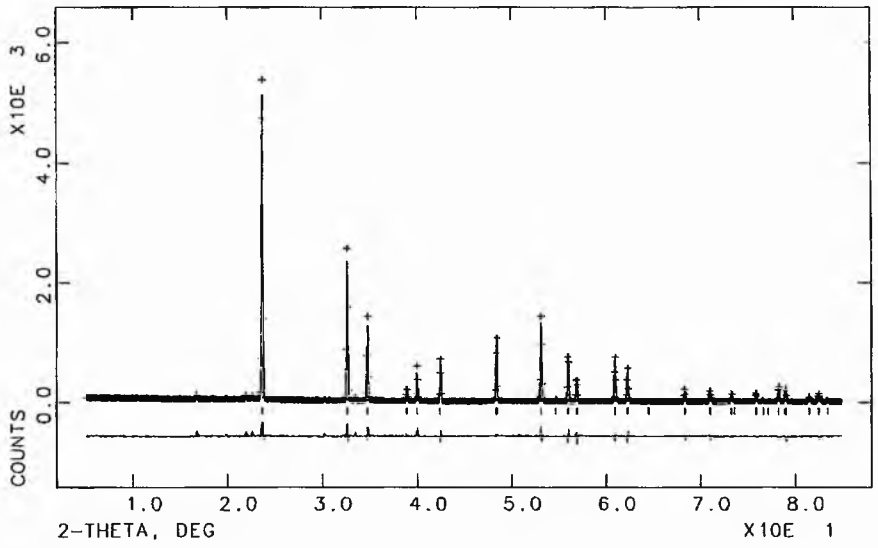

b) Neutron Refinement.

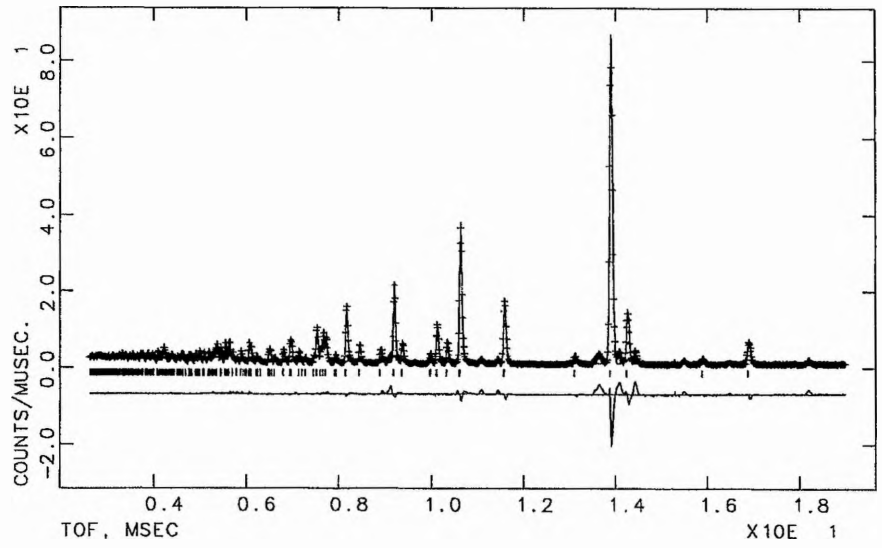

Figure 6.4.3c Final observed (crosses), calculated (solid line) and difference profiles for the Rietveld refinement of $Li_{1-x}Mg_{x/2}NbO_3$, x = 0.3. The tick marks represent allowed reflections.

a) X-ray Refinement.

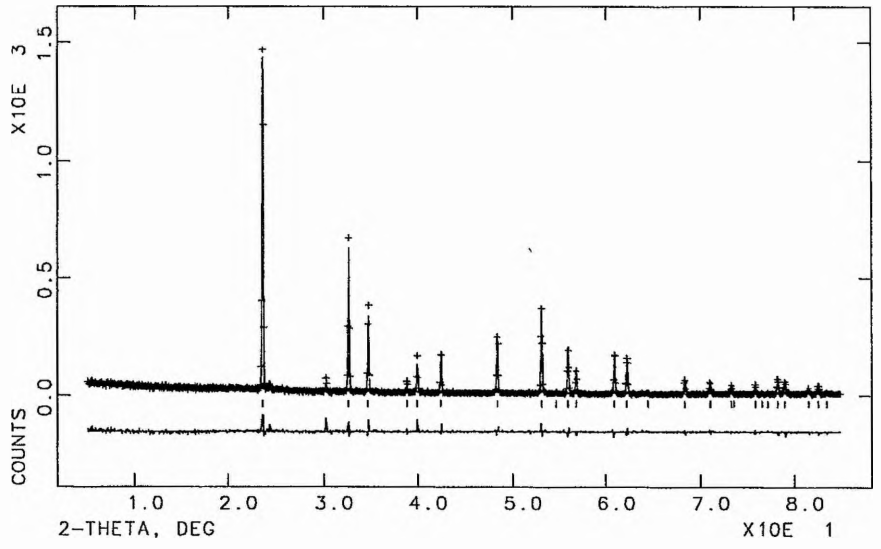

b) Neutron Refinement.

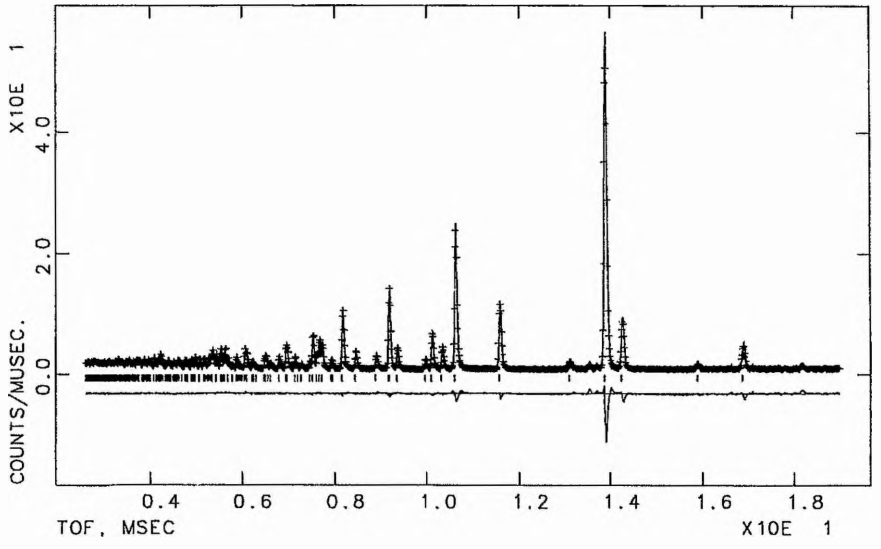

The refined Li site occupancies are in good agreement with the formula '$Li_{1-x}Mg_{x/2}NbO_3$' for x = 0.1, 0.2 and 0.3. The final refinements therefore assumed this doping mechanism (Eqn. 6.4.3d) and the relative Li / Mg occupancies were constrained accordingly. The final refined atomic parameters and occupancies are shown in Table 6.4.3b, with selected bond lengths in Table 6.4.3c.

Table 6.4.3c Selected bond lengths (Å) for $Li_{1-x}Mg_{x/2}NbO_3$, x = 0.1, 0.2, 0.3.

	x = 0.1	x = 0.2	x = 0.3
Li-O×3	2.044(1)	2.026(2)	2.012(2)
Li-O×3	2.295(2)	2.329(2)	2.373(4)
Nb-O×3	1.8806(5)	1.8915(7)	1.8929(4)
Nb-O×3	2.1274(5)	2.1247(7)	2.1235(4)

A number of other possible dopant sites were also considered, the empty octahedral site at [(0, 0, z) z ≅ 0.163], and the tetrahedral sites at (0.335, 0.386, 0.361) and (0.335, 0.382, 0.434). It can be seen from Table 6.4.3d that the occupancies of these sites unambiguously refined to zero within experimental error.

Table 6.4.3d Analysis of occupancies of vacant octahedral and tetrahedral sites in $Li_{1-x}Mg_{x/2}NbO_3$, x = 0.3.

	(0,0,0.163) [O_h]	(0.335,0.386,0.361) [T_d1]	(0.335,0.382,0.434) [T_d2]
Li	-0.009(8)	-0.018(6)	0.001(6)
Mg	0.006(3)	0.009(3)	0.001(2)

(The U_{iso} for each 'vacant' site fixed at 0.0025 $Å^2$).

It can be seen from Table 6.4.3c that as the Mg dopant concentration increases, the Li / Mg cation moves towards the empty octahedral site, presumably due to increased ionic repulsion with the neighbouring Nb site (see Figure 6.4.3d). The final Rietveld plots for the X-ray and neutron data sets are shown in Figures 6.4.3a, b, c. A small amount of unidentified impurity is present in the neutron patterns, but this is not observed in the X-ray data.

Figure 6.4.3d Unit cell of $Li_{1-x}Mg_{x/2}NbO_3$, Li/Mg shown as blue Nb as dark blue and O as red spheres.

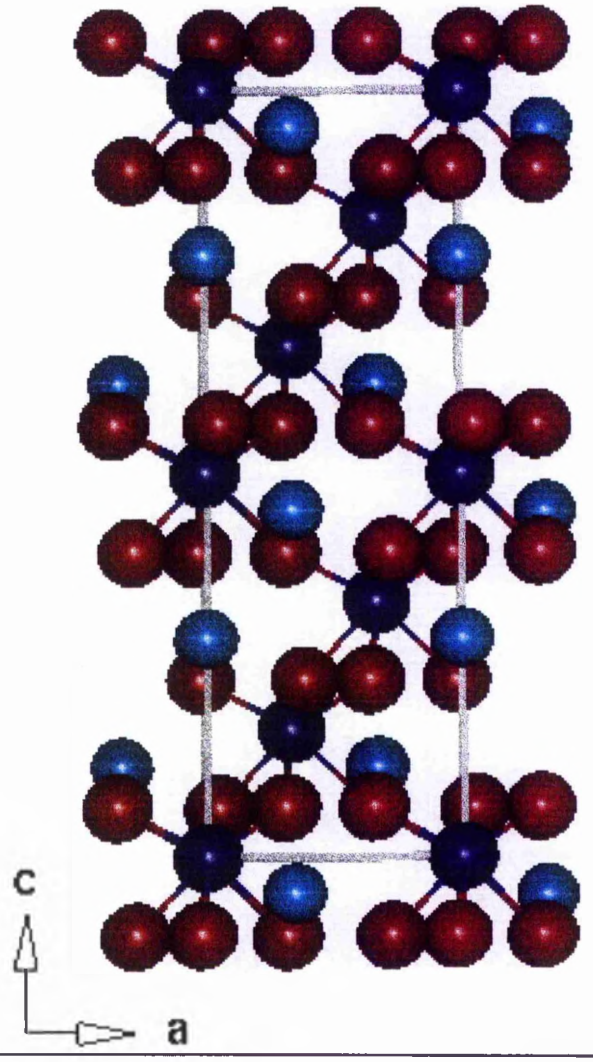

This is the first detailed structural study by diffraction methods of the nature of cation doping in lithium niobate. These results show that at relatively high doping concentrations (5-15 mole % Mg) magnesium exclusively substitutes for lithium according to the formula $Li_{1-x}Mg_{x/2}NbO_3$, x = 0.1, 0.2 and 0.3. Also, there is no evidence for either Nb substitution on the Li site, Mg substitution on the Nb site or deviation of the Nb site occupancy from unity. And finally, there is no evidence for the partial occupation of either the empty octahedral site or the two available tetrahedral sites.

These conclusions are in agreement with models postulated on the basis of lattice parameter/density measurements by Katsumata et al[29], who studied the variation in lattice parameters in samples of nominal composition '$Li_{1-x}Mg_xNbO_3$' for $0 \leq x \leq 0.1$, the same '1:1' synthesis which was used in this study (see Figure 6.4.3e, f).

Figure 6.4.3e A comparison of cell volume in '$Li_{1-x}Mg_xNbO_3$' for $0 \leq x \leq 0.3$. The results $0 \leq x \leq 0.1$ from reference 29 are shown in red. The corresponding results from this work are shown in black.

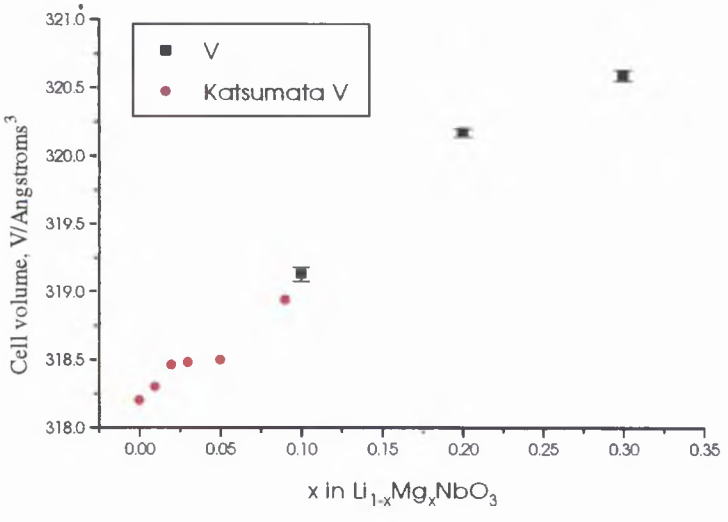

Figure 6.4.3f A comparison of lattice parameters in '$Li_{1-x}Mg_xNbO_3$' for $0 \leq x \leq 0.3$. The results $0 \leq x \leq 0.1$ from reference 29 are shown in red. The corresponding results from this work are shown in black.

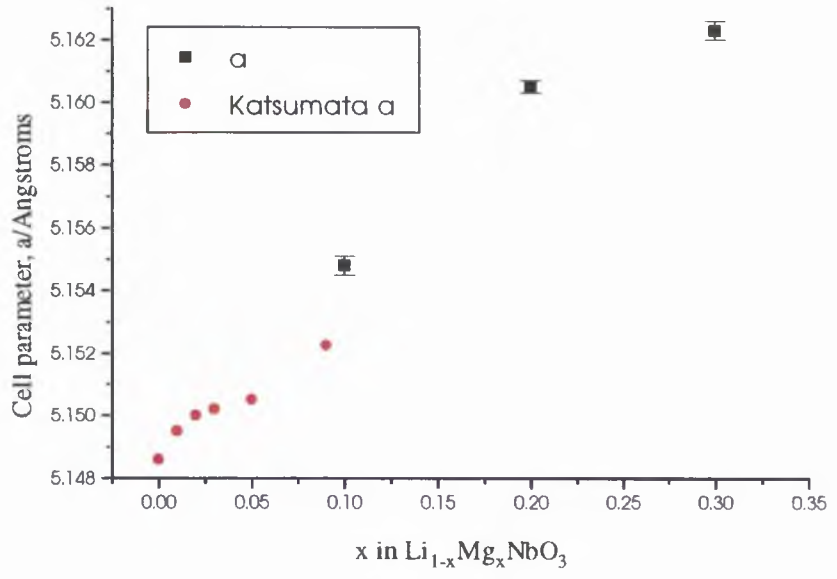

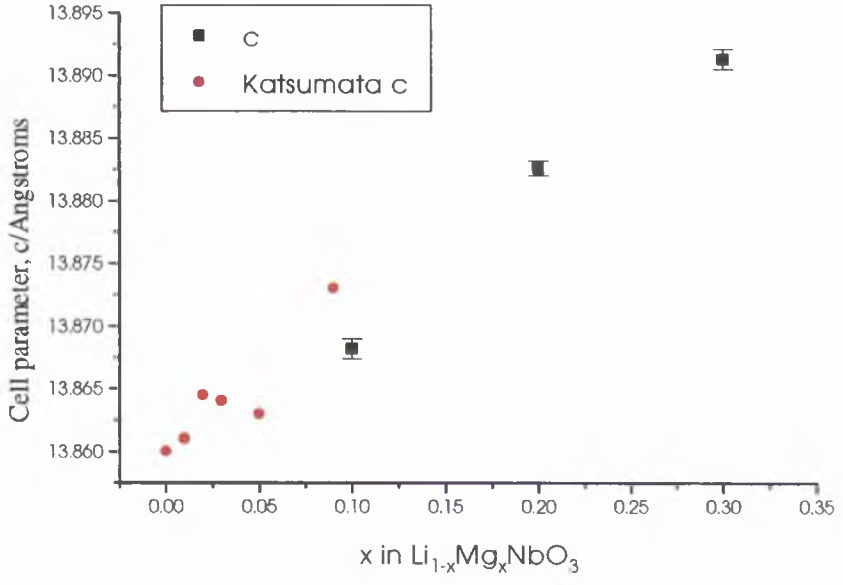

As previously discussed, '$LiNbO_3$' is Nb rich having a formula which can be represented as $Li_{0.94}Nb_{1.012}O_3$. Since the parent material exhibits intrinsic non-stoichiometry, the substitution mechanism of Mg-doped '$LiNbO_3$' is correspondingly complicated. Density measurements performed by Katsumata showed that the densities of sintered specimens are constant from a MgO concentration of 0 to 4 mole %, above which it increased abruptly. These results suggest that the substitution mechanism varies with MgO concentration. Two different defect models have been proposed:

$$[Li_{1-5x}\ Nb_{5x}][Nb_{1-4x},\ V^{Nb}_{4x}]O_3 \qquad \text{(Eqn. 6.4.3e)}$$

$$[Li_{1-5x}\ V^{Li}_{4x},\ Nb_x][Nb]O_3 \qquad \text{(Eqn. 6.4.3f)}$$

where V represents the vacancy. Equations 6.4.3e and 6.4.3f indicate the Nb vacancy and Li vacancy models respectively. Rossner et al[30] reported a doping mechanism based on Eqn. 6.4.3e, the Nb vacancy model, as follows:

$$[Li_{1-5x}\ Nb_{5(x-y)}\ Mg_{5y}][Nb_{1-4x+3y}\ V^{Nb}_{4x-3y}]O_3 \qquad \text{(Eqn. 6.4.3g)}$$

However, this study has found no vacancies on the Nb site. Iyi et al[31] successfully explained the solid solution mechanism using the Li vacancy model. From Eqn. 6.4.3f it is probable that the Mg^{2+} ions occupy the Li sites when the MgO concentration is small. If it is assumed that all the Mg^{2+} ions occupy the Li sites, and reduce the concentration of Nb on the Li sites, at low MgO concentrations, then the following formula is obtained:

$$[Li_{1-5x+3y}\ V^{Li}_{4x-3y}\ Nb_{x-y}\ Mg_y]NbO_3 \qquad \text{(Eqn. 6.4.3h)}$$

This may indicate that the substitution of Nb^{5+} on the Li sites by Mg^{2+} occurs dominantly between 0 and 4 mole % MgO, above which the substitution of Li^{+} on the Li sites by Mg^{2+} occurs. This mechanism is entirely consistant with the results of this study in the 5-15 mole % MgO range.

Combining these results with the studies discussed suggests that there is a strong preference to retain full occupancy of the Nb site, with the non-stoichiometry in general being accounted for by substitution on the Li site. Inherent non-stoichiometry in '$LiNbO_3$' arises from the loss of Li_2O and the subsequent compensation by Nb substitution.

6.5 The Synthesis and Structural Determination of the Oxygen-Deficient Perovskite $Ca_2LaFe_3O_8$

6.5.1 Introduction

The perovskite structure is one of the best known structures in oxide chemistry. It has a general formula ABO_3, where A is usually an alkaline earth or one of the larger lanthanides, and B is usually a transition metal or one of the smaller lanthanides.

As discussed in section 3.1.3, it is possible to have more than one element occupying the A or B sites in a perovskite. Also, elements such as the transition metals in perovskites can all take more than one oxidation state. This leads to the possibility of non-stoichiometry in the oxide sublattice.

Grenier and coworkers have studied a number of $Ca_2Fe_2O_5$-NMO_3[32] systems (N = Y, La, Gd; M = Fe, Ti), where they isolated new phases of the form $Ca_2NFe_3O_8$, corresponding to $A_3B_3O_8$ oxygen deficient perovskites. The magnetic properties of one of these phases, $Ca_2LaFe_3O_8$[33], were subsequently examined, and a model was proposed for the crystal structure from the Mössbauer data. The hypothesised structure was similar to that of $Sr_2LaFe_3O_8$[34], one of a series of orthorhombic perovskite-related phases, where the oxygen vacancies are ordered along the [101] direction of the cubic perovskite cell such that layers of B cations in octahedral and tetrahedral coordination are formed perpendicular to the [010] axis, giving rise to the layer sequence OOTOOT (where O = octahedral and T = tetrahedral B cation coordination).

This structure of $Ca_2LaFe_3O_8$ was examined because it was used as a potential host for oxygen intercalation. A powder neutron diffraction experiment was therefore used to characterise the structure of this phase.

6.5.2 *Experimental Details*

The ferrite $Ca_2LaFe_3O_8$ was prepared from the solid state reaction of the correct stoichiometric mixture of $CaCO_3$ (Aldrich, 99.5%) [1.5560 g], Fe_2O_3 (Aldrich 99%) [1.8619 g] and La_2O_3 (Aldrich 99%) [1.2663 g]. The starting materials were intimately mixed using an agate mortar and pestle and placed in a platinum boat. The mixture was then preheated in air at 1000°C for 12 h to decompose the carbonate and quenched to room temperature, where it was reground. The sample was then fired in air at 1400°C for 48 h, and air quenched to room temperature to produce a cubic perovskite. This material was then reground and heated in a platinum boat for 14 days at 1150°C in air, and then air quenched to room temperature to produce the desired product.

Grenier postulated that the high temperature necessary to produce the initial reaction of the starting materials also favoured the formation of Fe^{4+}, while subsequent annealing at 1150°C favoured some oxygen loss and the formation of Fe^{3+}-

$$2\ Ca_2LaFe_3O_8 + y\ O_2 \underset{1423K}{\overset{1673K}{\rightleftharpoons}} 2\ Ca_2LaFe^{3+}_{3-2y}\ Fe^{4+}_{2y}\ O_{8+y} \qquad \text{(Eqn. 6.5.2a)}$$

Time-of-flight powder neutron diffraction data suitable for structure determination were collected on the POLARIS diffractometer at ISIS, Rutherford Appleton Laboratory. Approximately 3 g of finely ground material was placed in a 6 mm diameter vanadium sample can. Data were collected in the time-of-flight range 0.2 to 19.6 ms at 298K, with only the data between 3.5 and 19.5 from the backscattering detectors ("C bank", 38 ^3He detectors) used in the refinement. The neutron scattering lengths used were La = 0.824, Ca = 0.476, Fe = 0.954 and O = 0.5803×10^{-12} cm.

6.5.3 Structure Determination

The neutron diffraction pattern of the sample of $Ca_2LaFe_3O_8$ could be indexed on an orthorhombic unit cell having a = 5.472(1), b = 11.3119(2) and c = 5.565(1) Å, and space group P*mma*. These unit cell dimensions are similar to those proposed by Battle *et al* for the structure of $Sr_2LaFe_3O_8$[35], and so the atomic coordinates from this material were used as a starting model (Table 6.5.3a).

Table 6.5.3a Atomic parameters for $Sr_2LaFe_3O_8$ at room temperature, space group P*mma*, from Battle *et al*[35].

Atom	Site	x	y	z	Occup.
Sr/La1	2f	0.25	0.5	0.7443	1
Sr/La2	4k	0.25	0.19114	0.7307	1
Fe1	4k	0.25	0.33884	0.2415	1
Fe2	4i	0.2078	0	0.1786	0.5
O1	4g	0	0.3025	0	1
O2	4h	0	0.3406	0.5	1
O3	2f	0.25	0.5	0.2001	1
O4	8l	0.268	0.1420	0.3013	0.5
O5	4i	0.134	0	0.875	0.46

In this cell and space group, the cation arrangement in the expected perovskite-related structure consists of two crystallographically distinct sites for the A cations (initially assumed to be a fully disordered arrangement of Ca and La), one Fe^{3+} site in octahedral coordination (Fe1), and one Fe^{3+} site in tetrahedral coordination (Fe2) to oxygen. The anion sublattice contains three oxide ions which

are arranged only around the six coordinate Fe1 (O1, O2, and O3), one oxide ion which provides the link between the octahedral and tetrahedral layers (O4), and one oxide ion which is coordinated only to the tetrahedral Fe2 site (O5).

The Rietveld refinement of the neutron powder diffraction data involved 41 parameters, using 1096 contributing reflections and 3437 data points. The CCSL suite of programmes[14, 15] were used in the analysis and the final agreement factors were $R_{wp} = 7.38$ %, $\chi^2 = 48.8553$.

6.5.4 Results and Discussion

The atomic coordinates from the $Sr_2LaFe_3O_8$ structure were used as the initial parameters in the analysis of the neutron diffraction data. These data contained additional peaks which could be indexed in a unit cell doubled along y. Since $Ca_2LaFe_3O_8$ is magnetically ordered at room temperature, the neutron data will therefore contain a mixture of nuclear and magnetic scattering. Although the magnetic behaviour of this phase was well studied by Grenier[33], Rietveld refinement code for the magnetic component of the neutron scattering was not available. This work therefore consists only of a characterisation of the nuclear scattering.

The refinement of the positions of the metal atoms provided clear evidence that the four coordinate Fe2 cations are disordered from their ideal 2e (1/4, 0, z) site, in a similar manner to the $Sr_2LaFe_3O_8$. During the initial stages of the refinement, it became clear that there was appreciable disorder in the anion environment around Fe2. In comparison to the Sr anologue, the O5 site was moved off its ideal position of (0, 0, 0), while in contrast to the analogous structure, it did not prove necessary to disorder O4 from the (1/4, y, z) site.

In order to allow for the possible existance of tetrahedral sites with a reversed orientation, an additional anion, O6 was introduced. It is clear that a simple reversal of tetrahedral site orientation would result in the combined occupancies of the O5 and

O6 sites being equal to 0.5, while any excess oxygen in the phase above the stoichiometric value of 8 would lead to an increase in this value.

Although the A site cations were initially assumed to be completely disordered accross the two sites, the refinement showed that they were completely ordered in this structure. The atomic coordinates and selected bond distances for the refinement of $Ca_2LaFe_3O_8$ are shown in Table 6.5.4a and Table 6.5.4b respectively. The profile fit for the refinement is shown in Figure 6.5.4a.

Table 6.5.4a Refined atomic parameters for $Ca_2LaFe_3O_8$, at room temperature in space group *Pmma*, a = 5.46881(5), b = 11.30546(9) and c = 5.55853(5) Å.

Atom	Site	x	y	z	B_{iso} / Å^2	Occup.
La	2f	0.25	0.5	0.7392(15)	0.88(8)	1
Ca	4k	0.25	0.1905(5)	0.7164(14)	0.70(11)	1
Fe1	4k	0.25	0.3295(3)	0.2420(8)	0.37(6)	1
Fe2	4i	0.1926(13)	0.0	0.1886(14)	0.75(13)	0.5
O1	4g	0.0	0.2938(8)	0.0	2.15(13)	1
O2	4h	0.0	0.3427(7)	0.5	1.21(10)	1
O3	2f	0.25	0.5	0.1779(14)	0.06(11)	1
O4	4k	0.25	0.1448(6)	0.3266(11)	1.11(13)	1
O5	4i	0.155(2)	0.0	0.887(2)	2.4(3)	0.5
O6	4i	0.487(7)	0.0	0.561(6)	1.2(7)	0.19(2)

The results presented confirm the structure proposed for $Ca_2LaFe_3O_8$ on the basis of the unit cell size. The structure is shown in Figure 6.5.4b and consists of double layers of $Fe1O_6$ octahedra linked by layers of $Fe2O_4$ tetrahedra. The calcium and lanthanum ions occupy the cavities between the layers in an ordered manner.

Table 6.5.4b Selected bond lengths (Å) and angles (°) for $Ca_2LaFe_3O_8$.

Octahedral Site		**Tetrahedral Site**	
Fe1–O1×2	1.960(9)	Fe2–O4×2	1.835(13)
Fe1–O2×2	1.987(12)	Fe2–O5	1.87(2)
Fe1–O3	1.960(9)	Fe2–O5'	1.95(2)
Fe1–O4	2.141(11)		
O1–Fe1–O1'	88.45	O4–Fe2–O4'	126.28
O1–Fe1–O2×2	91.77	O4–Fe2–O5×2	103.20
O1–Fe1–O2'×2	172.18	O4–Fe2–O5'×2	104.88
O2–Fe1–O2'	86.96	O5–Fe2–O5'	103.99
O2–Fe1–O3×2	93.29		
O2–Fe1–O4	85.11		
O1–Fe1–O3×2	94.49		
O1–Fe1–O4×2	87.09		
O4–Fe1–O3	177.79		

Figure 6.5.4a Profile fit for $Ca_2LaFe_3O_8$ from neutron data.

Experimental data shown as dots, profile fit as a continuous line and difference / e.s.d. at the bottom. Tick marks show nuclear reflections.

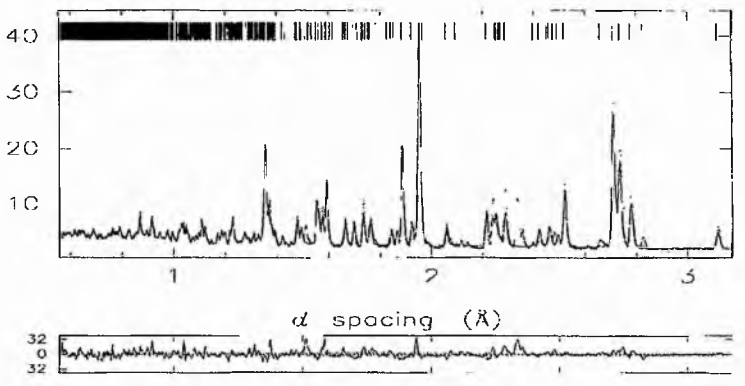

If the packing of sheets of atoms perpendicular to the y axis of the structure is considered, the composition of successive sheets can be represented by the sequence-

$$(Fe1O_2)(LaO)(Fe1O_2)(CaO)(Fe2O)(CaO) \qquad \text{(Eqn. 6.5.4a)}$$

The ($Fe1O_2$) layers lie within the octahedra and contain the atoms Fe1, O1 and O2. The (LaO) layer between the two ($Fe1O_2$) layers contains La and O3. The (CaO) layer between ($Fe1O_2$) and (Fe2O) contains Ca and O4. The A site ordering therefore results in placing the La^{3+} in a perovskite-like site where it is coordinated to 12 oxygens, while the Ca^{2+} is coordinated to 8 oxygens.

Figure 6.5.4b The crystal structure of $Ca_2LaFe_3O_8$.
O shown as red, Fe purple, Ca green, La as blue and O6 yellow spheres. The octahedra are highlighted in purple and tetrahedra in dark green.

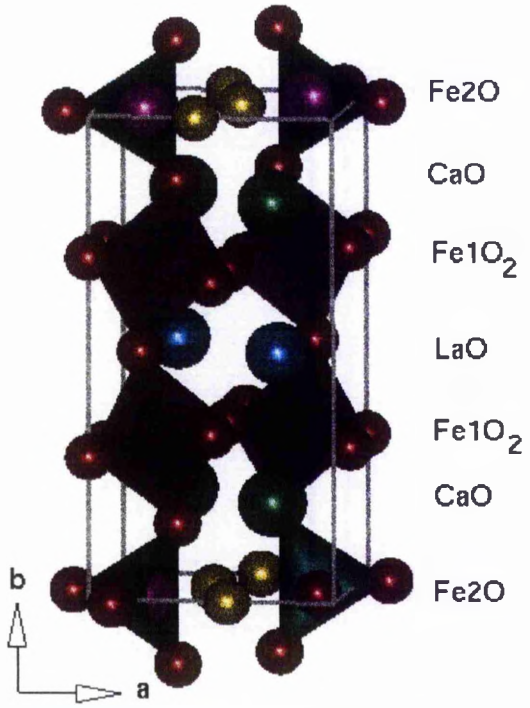

The (Fe2O) layer lies within the tetrahedra and contains Fe2, O5 and O6. The refined value of the O5 occupancy is 0.69(4), more than four e.s.d.'s greater than the expected 0.5. This may be the result of the unfitted intensity due to the magnetic scattering. It is not possible to have this site more than half occupied, and so the occupancy of the O5 site was fixed at 0.5 for the rest of the refinement.

The significant value of the refined occupation number of O6, 0.19(2), suggests that the sample is oxidised. If the occupancies of the O5 and O6 sites had combined to give a total of 0.5, this would have implied that the orientation of the $Fe2O_4$ tetrahedra were disordered. However, since the sum of these two sites is equal to 0.69(2), there is excess oxygen within the structure, resulting in a total stoichiometry of $Ca_2LaFe_3O_{8.38(4)}$. This will also mean that there will be five and six coordinate Fe2 in this layer, caused by the occupancy of the O6 site (see Figure 6.5.4b).

The e.s.d.'s of the atomic coordinates are unusually large for neutron data of this quality. This is likely to be due to the unfitted magnetic scattering intensity interfering with the nuclear refinement where significant peak overlap occurs. This problem will be resolved when the magnetic components of the neutron diffraction pattern are also refined with the data.

6.5 References

1. C. Delmas, A. Maazaz, F. Guillen, C. Fouassier, J. M. Réau and P. Hagenmuller, *Mater. Res. Bull.*, **14**, 619, 1979.

2. E. E. Hellstrom and W. Van Gool, *Solid State Ionics*, **2**, 59, 1981.

3. H. Kwast, E. H. P. Cordfunke and R. Muis in "Fabrication and Properties of Lithium Ceramics III" (I. J. Hastings and G. W. Hollenberg Eds.), Amer. Chem. Soc., Washington, DC (1992).

4. J. L. Hodeau, M. Marzeio, M. Santoro and R. S. Roth, *J. Solid State Chem.*, **45**, 170, 1982.

5. M. Trömel and J. Hauck, *Z. Naturforsch.*, **B23**, 110, 1968.

6. I. Abrahams, P. Lightfoot and P. G. Bruce, *J. Solid State Chem.*, **104**, 397,1993.

7. J. W. Visser, *J. Appl. Crystallogr.*, **2**, 380, 1969.

8. A. LeBail, H. Duroy and L. Fourquet, *Mater. Res. Bull.*, **23**, 447, 1988.

9. A. C. Larson and R. B. Von Dreele, Los Alamos Laboratory Report No. LA-UR-86-748, 1987.

10. G. M. Sheldrick "Crystallographic Computing 3" (O.U.P.), Eds. G. M. Sheldrick.

11. N. E. Brese and M. O'Keeffe, *Acta Crystallogr.*, **B47**, 192, 1991.

12. "Powder Diffraction File", International Centre for Diffraction Data, Pennsylvania, USA, 1993.

13. J. C. Matthewman, P. Thompson and P. J. Brown, *J. Appl. Crystallogr.*, **15**, 167, 1982.

14. P. J. Brown and J. C. Matthewman, Rutherford Appleton Laboratory Report 1987, Ral-87-010.

15. R. D. Shannon, *Acta Crystallogr.*, **A32**, 751, 1976.

16. "International Tables for Crystallography", Vol. C, Ed. A. C. J. Wilson, Klawer Academic Publishers, London, 251, 1995.

17. M. E. Lines and A. M. Glass, "Principles and Applications of Ferroelectrics and Related Materials", Clarendon Press, Oxford, 1977.

18. A. Rauber, in "Current Topics in Materials Science", Ed. E. Kaldis, North-Holland, Amsterdam, **1**, 1, 1978.

19. E. Kratzig and O. F. Schirmer, in "Photorefractive Materials and their Applications I, Springer Topics in Applied Physics" 61, Springer, Berlin, Ch. 5.

20. T. R. Volk and N. M. Rabinina, *Phys. Stat. Sol.*, A108, 437, 1988.

21. A. P. Wilkinson, A. K. Cheetham and R. H. Jarman, *J. Appl. Phys.*, **74**, 3080, 1993.

22. L. E. Halliburton, in "Properties of Lithium Niobate", EMIS Data Reviews Series 5, EMIS, New York, Ch. 6.4.

23. D. M. Pepper, *Opt. Eng.*, **21**, 156, 1982.

24. W. Keune, S. K. Date, U. Gosner and H. Bunzel, *Ferroelectrics*, **13**, 443, 1976.

25. C. Zaldo, C. Prieto, H. Dexpert and P. Fessler, *J. Phys. Condens. Matter*, **3**, 4135, 1991.

26. T. S. Bush, C. R. A. Catlow, A. V. Chadwick, M. Cole, R. M. Geatches, G. N. Greaves and S. M. Tomlinson, *J. Mater. Chem.*, **2**, 309, 1992.

27. H. J. Donnerberg, S. M. Tomlinson and C. R. A. Catlow, *J. Phys. Chem. Solids*, **52**, 201, 1991.

28. S. C. Abrahams and P. Marsh, *Acta Crystallogr.*, **B42**, 61, 1986.

29. T. Katsumata, K. Shibata and H. Imgawa, *Mater. Res. Bull.*, **29**, 559, 1994.

30. W. Rosser, B. C. Grabmaier and W. Wersing, *Ferroelectrics*, **93**, 57, 1989.

31. N. Iyi, K. Kitamura, F. Izumi, J. K. Yamamoto, T. Hayashi, H. Asano and S. Kimura, *J. Solid State Chem.*, **101**, 340, 1992.

32. J-C. Grenier, J. Darriet, M. Pouchard and P. Hagenmuller, *Mat. Res. Bull.*, **11**, 1219, 1976.

33. J-C. Grenier, F. Ménil, M. Pouchard and P. Hagenmuller, *Mat. Res. Bull.*, **12**, 79, 1977.

34. M. Abou Sekina, J-P. Bonnet, J-C. Grenier, M. Pouchard and P. Hagenmuller, *Rev. de Chimie Minérale.*, **17(5)**, 431, 1980.

35. P. D. Battle, T. C. Gibb and P. Lightfoot, *J. Solid State Chem.*, **84**, 237, 1990.

Chapter 7
Structural Studies of Polymer-Salt Complexes

7.1 Introduction

In many technologically important materials, a detailed knowledge of structure provides the foundation on which the understanding of the chemical and physical properties of such compounds must be based.

The polymer-salt complexes provide a prime example of a class of materials whose structures have remained unsolved since their discovery over 20 years ago. These compounds can be prepared as either crystalline or amorphous solids, frequently with the same composition. The crystalline solids melt at a relatively low temperature to form liquids which can be regarded as amorphous solids since they have the bulk mechanical properties of solid materials. The investigation of the crystalline state of matter is generally easier than studying the amorphous state, as detailed and precise information can be obtained from crystal structures. Therefore, in order to understand the structure of polymer-salt complexes, it is necessary to start with the analysis of the crystalline phases, even though it is the amorphous complexes which exhibit appreciable conductivity. Poly (ethylene oxide) [$(CH_2CH_2O)_n$, PEO], forms crystalline complexes with many salts. However, the established techniques based on single crystal X-ray diffraction are not well suited to the investigation of such complexes, as the data is invariably of low quality and difficult to analyse[1].

The recent application of state-of-the-art powder X-ray crystallography to this problem has produced some promising results[2]. It is now possible to prepare samples of polymer-salt complexes which give high quality X-ray powder diffraction data, which have enabled the crystal structures of several important complexes to be determined. Such studies have revealed much structural information. In this chapter the relationships between the crystalline and amorphous, conducting phase of PEO_3:$LiCF_3SO_3$ is examined. This has involved investigating the influence of temperature up to and beyond the melting point, on the powder diffraction patterns.

In addition the crystal structure of PEO_4:RbSCN has been determined. This constitutes the largest cation structure to be solved so far for any polymer electrolyte.

7.2 A Variable Temperature Powder X-ray Diffraction Study of PEO_3:$LiCF_3SO_3$

7.2.1 Introduction

The archetypal polymer-salt complex is $LiCF_3SO_3$ co-ordinated by PEO. This material has been the focus of intensive scientific study, due largely to its use as a lithium ion conducting electrolyte in rechargeable lithium batteries[3].

The most comprehensive phase diagram for the PEO-$LiCF_3SO_3$ system was constructed by Vallée et al[4] (Figure 7.2.1a) from the thermal transitions recorded by DSC upon the first heating of a series of mixtures prepared with the salt.

Figure 7.2.1a The phase diagram of the PEO-$LiCF_3SO_3$ system[4].

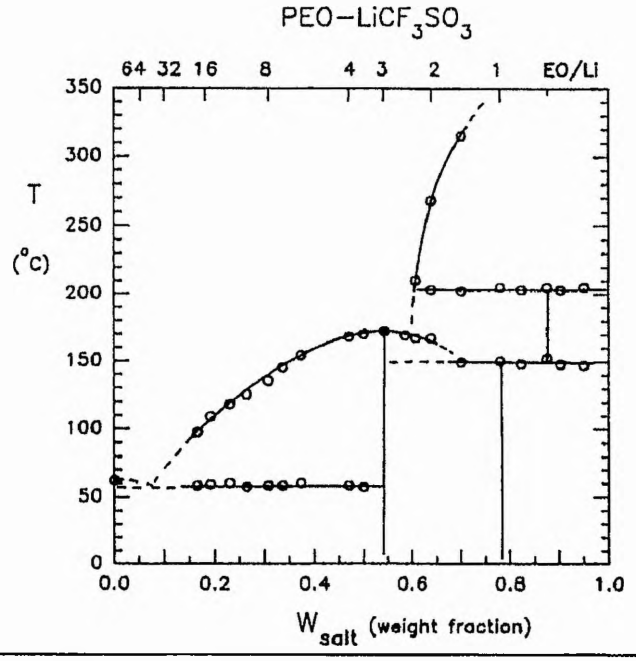

Most of the features of this phase diagram were in agreement with the data previously reported on this system. A number of vertical boundaries exist within this phase diagram characterising the stoichiometry of the intermediate crystalline compounds. The compositions of the 3:1, 1:1 and 0.5:1 crystalline compounds were derived from the calorimetric analysis of the DSC data, and correspond to the compositions at which the heat of fusion (or dissolution) related to each compound exhibits a maximum value.

The crystal structure of the complex formed with a composition of 3 ether oxygens per lithium ion was elucidated by Bruce et al[5] from high resolution powder X-ray diffraction data. The determination of the structure of the PEO-$LiCF_3SO_3$ composition has facilitated the full characterisation of the structure of this material at a variety of temperatures by a variable temperature powder X-ray diffraction study. The complex was examined from room temperature through the melting transition and on up to 250°C.

7.2.2 Experimental Details

The lithium trifluoromethane sulphonate was formed from the reaction shown in equation. 7.2.2a-

$$Li_2CO_3 + 2\ CF_3SO_3H \rightarrow 2\ LiCF_3SO_3 + H_2O + CO_2 \qquad \text{(Eqn. 7.2.2a)}$$

The trifluoromethanesulphonic acid (CF_3SO_3H, Aldrich 99 %) [10 g] was dissolved in 100 ml of distilled water and slowly added to a suspension of lithium carbonate (Li_2CO_3, Aldrich 99.9 %) [2.46 g] in 100ml of distilled water. The solution was stirred for 3 h, filtered through a fine sinter and the majority of the water removed on a rotary evaporator to leave the hydrated salt. The anhydrous salt was obtained after heating the sample under dynamic vacuum for 24 h at 150°C, and was stored in an M Braun Ar filled glove box.

The correct stoichiometric mixture of lithium trifluoromethanesulphonate [0.5902 g] and dry PEO (Aldrich, molecular weight = 4×10^6) [0.5 g] was transferred to a stainless steel tube in the glove box. The tube was one third filled with stainless steel ballbearings and sealed. This container was then removed from the glove box, attached to a mechanical shaker and immersed in liquid nitrogen. The mixture was cryoground for 30 min. Agitating the mixture at low temperatures ensures an intimate mixture is obtained because the PEO becomes very brittle, breaking into small particles and mixing thoroughly with the salt. After allowing the tube to warm to room temperature, it was returned to the glove box where the cryoground mixture was removed and packed into 0.5 mm Lindemann tubes. These capillaries were sealed with Araldite and heated to 190°C for 6 h to ensure dissolution of the salt in the polymer and then annealed at 55°C, just below the melting point for 4 days to produce the crystalline complex.

D.S.C. scans were performed on a Perkin Elmer DSC7 differential scanning calorimeter, equipped with a 3700 data station and a TAC 7/3 instrument controller. A liquid nitrogen cooler was used. A sample of the polymer-salt complex was sealed into an aluminium sample pan inside the glove box. Heating and cooling cycles in the temperature range 25°C to 225°C were applied, using a sealed argon filled pan as a reference.

Data suitable for structural refinement were recorded in the furnace of a Stoe STADI/P high resolution powder diffractometer operating in transmission mode using Cu-$K_{\alpha1}$ radiation. Data were collected over the range $5° < 2\theta < 35°$ in steps of 0.02°, with each experiment lasting approximately 50 min, for the unit cell refinements, and over the range $5° < 2\theta < 35°$ in steps of 0.02°, with each experiment lasting 3 h to produce data suitable for structure refinement.

In order to ensure accuracy in the temperature of the sample a calibration curve was constructed. A 0.2 mm diameter thermocouple was placed within a 0.5 mm Lindemann tube at such a height that the tip of the thermocouple was in the centre of the X-ray beam. The furnace was then ramped from room temperature to 250°C at

10°C intervals with appropriate dwells at each temperature to allow for thermal equilibriation. The calibration curve shown in Figure 7.2.2a was obtained. It can be seen that as the set temperature increases, there is a negative deviation in the sample temperature such that by 200°C, the thermocouple, and therefore the sample, is at a temperature of only 185°C.

Figure 7.2.2a Calibration graph for the furnace on the Stoe diffractometer.

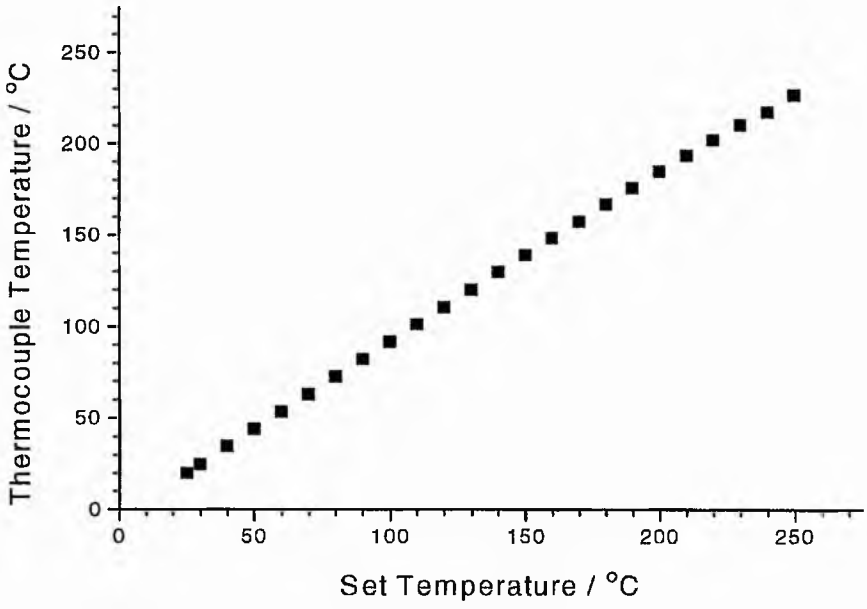

This deviation was checked by examining the variable temperature powder X-ray diffraction patterns of ammonium chloride. This material is well characterised and is known to undergo a "CsCl" to "NaCl" structural transformation[6] at 184.3°C. A D.S.C. analysis of a portion of the sample of NH_4Cl which was used in the diffraction analysis exhibited the onset of a thermal event at 184.3°C. The powder X-ray diffraction pattern of this material was examined in the range $25° < 2\theta < 32°$. The most intense peak of the "CsCl" phase occurs at 26.9°, and that for the "NaCl" phase at 32.05°. On raising the temperature of NH_4Cl in steps of one degree from a set

temperature of 195 to 205°C, the phase change was found to occur at a set temperature of 199.0°C, confirming the calibration graph within this temperature range. It is possible that the disparity between the set temperature and sample temperature may be caused by the design of the furnace itself. Only the base of the sample tube makes physical contact with the heating element, while the top of the capillary is close to the water cooling plate. This construction sets up a temperature gradient within the sample tube which means that the portion in the X-ray beam is at a lower temperature than that which is measured by the furnace thermocouple in contact with the graphite heating element.

All furnace temperatures quoted in the remainder of this chapter refer to the correct temperature of the sample.

7.2.3 Structural Analysis

The structure of the PEO_3:$LiCF_3SO_3$ complex was refined by Bruce and coworkers[5] by using initially low temperature powder X-ray diffraction data and the structure of the PEO_3:NaSCN complex by Chatani[7] as a starting model. At room temperature the lithium complex has a monoclinic space group $P2_1$ / a, with a = 16.768(2), b = 8.613(1), c = 10.070(1) Å and β = 121.02(1)°.

The structure is shown in Figure 7.2.3a. Part a) shows a projection down the b axis of the unit cell which coincides with the fibre axis and is also coincident with the 2_1 screw axis of the helix. Part b) consists of part of one PEO chain with its associated ions. It is evident that the PEO chain in this crystalline complex retains a helical conformation. A lithium ion is located within each turn of the helix, where it is co-ordinated by three ether oxygens from the chain. The co-ordination environment is completed by two further oxygens, one from each of the two triflate anions in approximately a trigonal bipyramidal geometry. The triflate anions can be seen to bridge neighbouring lithium ions along the chain by donating one of their oxygens to

each lithium, with the remaining oxygen being uncoordinated. It is clear that the trifluoromethyl moiety of the triflate anions sits outside the dimensions of the helix.

Figure 7.2.3a The crystal structure of PEO_3:$LiCF_3SO_3$. Li shown as blue, carbon as green, oxygen as red, fluorine as purple and sulphur as yellow spheres.
a) The view down the b (fibre) axis. b) A single PEO chain with associated ions.

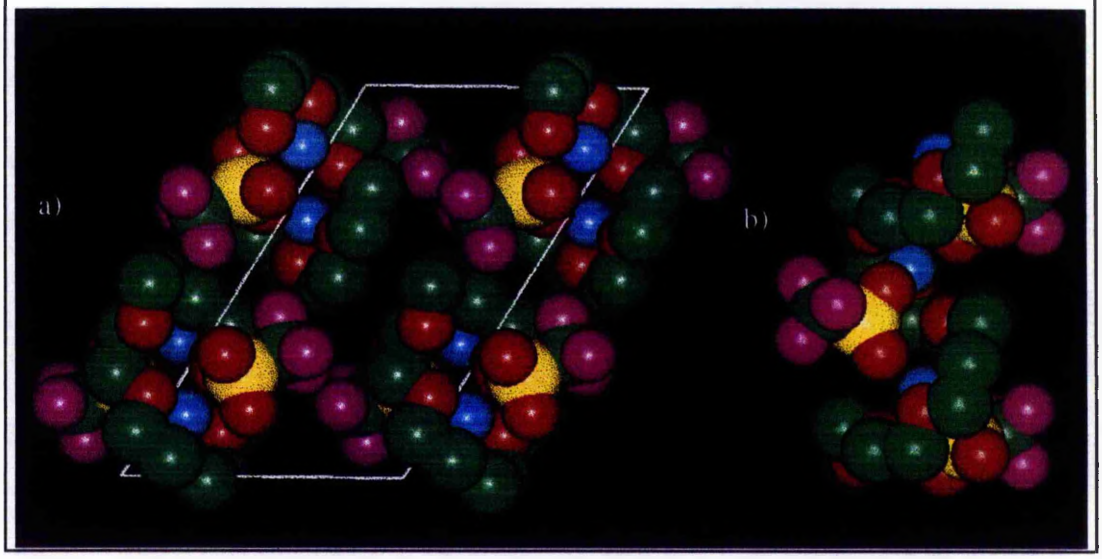

There are a number of consequences of the conformation adopted in this complex. Each chain is associated with a dedicated set of cations and anions which do not bond to any of the other chains, forming isolated, infinitely long one dimensional co-ordination complexes. Interchain interactions will therefore be of a lower order when compared with intrachain interactions. This structure suggests that melting will involve the loss of the weaker interactions between the chains before any dissociation of the ions from their PEO chains. The next section reports one half of a combined crystallographic and spectroscopic study undertaken in collaboration with R. Frech at the University of Oklahoma.

By combining X-ray diffraction and spectroscopy a much deeper insight into the structures in the amorphous state and their relationships to the crystal structure

should be possible. In particular the X-ray data can be used to assign peaks in the infra-red spectrum. Infra-red spectroscopy can be used to probe the vibrational states of the triflate anions in the crystalline and amorphous states. The vibrational frequencies are expected to be different between triflate anions that are free and those that have lithium ions directly co-ordinated to the oxygens of the anion. Frech *et al* found that only one triflate species is observed in the spectrum of the crystalline complex, and from the crystal structure data it is clear that this is a triflate ion which co-ordinates to two lithium ions with each lithium being co-ordinated to one of the triflate oxygens. The temperature of the PEO_3:$LiCF_3SO_3$ complex was then raised up to and beyond the melting point with continuous monitoring of the I.R. spectrum. On melting no other triflate species were detected suggesting that the triflate ions remain attached to two lithium ions simultaneously forming short chains of $-Li^+-CF_3SO_3^-$–Li^+–. Some shifts in the positions of peaks in the infra-red spectra occur on raising the temperature from ambient. Therefore for the hypothesis of local structural invariance on melting to hold it must be proven that the room temperature structure of the crystalline complex is maintained up to the melting point. Variable temperature powder X-ray diffraction is ideal for this structural study.

The GSAS[8] suite of programs was used for the Rietveld refinements of the lattice parameters and structure. The unit cell refinement of the structure involved the minimisation of 9 background terms in a cosine Fourier series, 4 peak shape parameters from a pseudo-Voigt profile function, a zero point and 4 lattice parameters. The full structural refinements included the minimisation of the above parameters with all the atomic co-ordinates, and temperature factors (constrained to be equivalent for each moiety).

7.2.4 Results and Discussion

The variable temperature powder X-ray diffraction patterns of the PEO_3:$LiCF_3SO_3$ phase were examined in three diffraction experiments. All analyses involved polymer complex samples produced from the same batch of starting materials, although the same capillary could not be used in each case because the high crystallinity of the sample was destroyed after heating it above the melting temperature and then cooling.

In order to determine the temperatures at which diffraction patterns should be collected, the thermal behaviour of the complex was examined. The resultant D.S.C. traces are shown in Figure 7.2.4a. The upper heating trace shows one thermal event, the melting of the complex, with an onset temperature of 180.05°C. A D.S.C. analysis of the correct stoichiometric ratio of the starting materials between 20 and 280°C revealed two endotherms on heating. One at 65.3°C, and the other at 178.1°C. The first corresponds to the melting temperature of the PEO[9]. Since this is not observed in the complex sample, any uncomplexed PEO must be entirely absent from this material. On cooling there is only one transition at 152.9°C, caused by the recrystallisation of the complex. The lower cooling trace also shows only one thermal event, the recrystallisation of the complex, with an onset at 149.56°C. Neither of these traces show any other processes occurring, such as the precipitation of a new high temperature phase, or the lithium salt.

Diffraction experiment A therefore examined a number of temperatures from 25°C, through the melting point to 225°C. Lattice parameter refinements were carried out using the structure solution presented by Bruce. The results of experiment A are shown in Table 7.2.4a.

The second variable temperature powder X-ray diffraction analysis, experiment B, examined the region around the melting point of the complex in greater detail i.e. 175 - 185 °C. The results of the lattice refinements are shown in Table 7.2.4b.

Figure 7.2.4a D.S.C. traces for the PEO_3:$LiCF_3SO_3$ complex from 25°C ↔ 275°C. Upper diagram shows the heating behaviour, lower diagram the cooling behaviour.

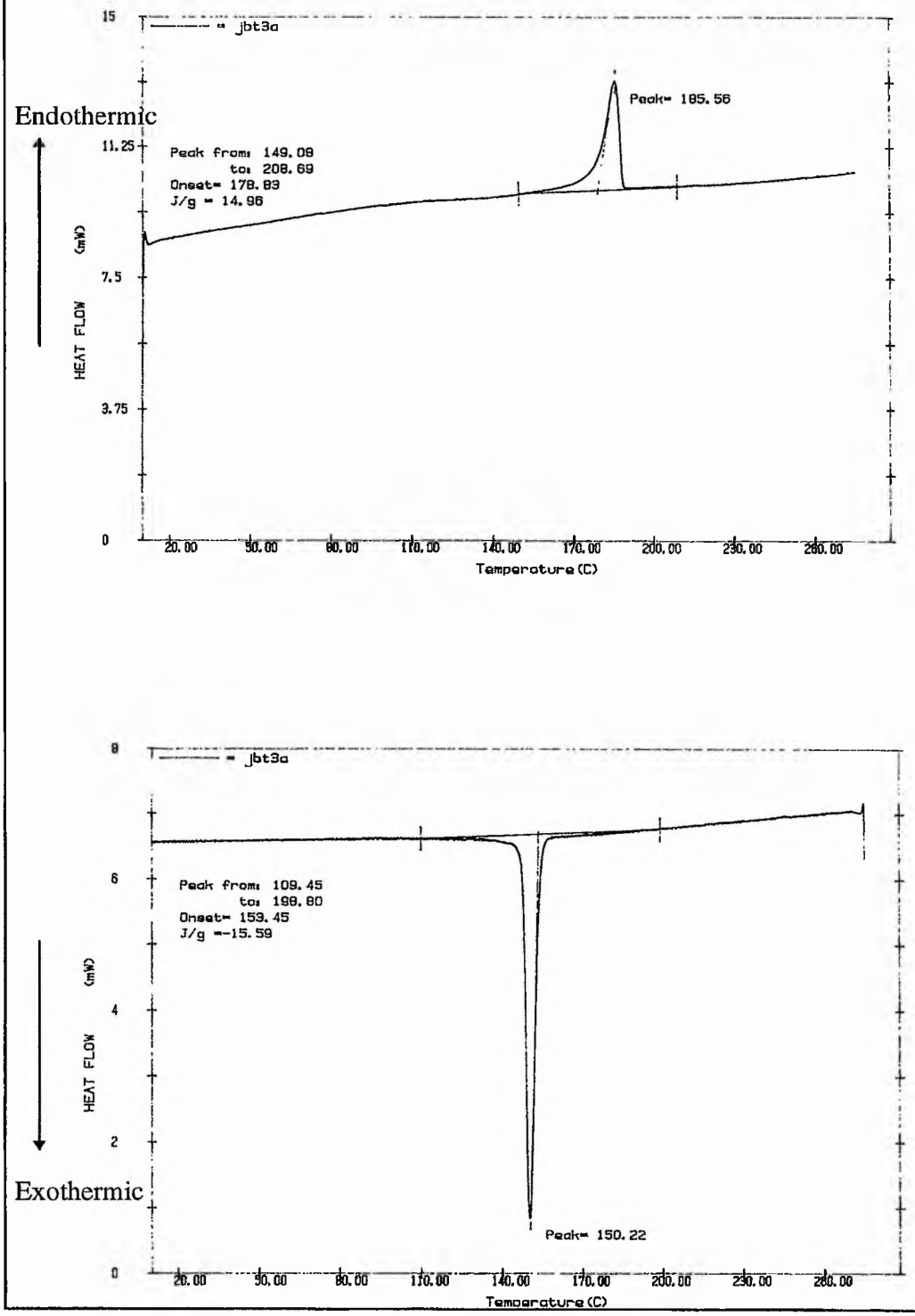

Table 7.2.4a Experiment A lattice refinement of the PEO_3:$LiCF_3SO_3$ complex.

	T / °C	a / Å	b / Å	c / Å	β / °	V / Å^3	R_{wp}
↑	19.8	16.764(4)	8.620(2)	10.082(2)	121.012(9)	1248.7(6)	11.73
|	44.0	16.821(4)	8.6296(14)	10.093(2)	121.016(8)	1255.6(5)	10.83
|	91.8	16.983(3)	8.6528(14)	10.115(2)	121.150(8)	1272.1(5)	11.07
H	139.2	17.199(5)	8.681(2)	10.138(2)	121.493(10)	1290.6(7)	12.50
E	157.5	17.286(6)	8.688(2)	10.141(3)	121.681(11)	1296.0(8)	13.64
A	162.1	17.323(6)	8.693(2)	10.145(3)	121.757(11)	1299.0(8)	13.38
T	164.4	17.329(5)	8.692(2)	10.143(3)	121.729(11)	1299.4(8)	13.37
I	166.7	17.329(5)	8.690(2)	10.138(2)	121.767(11)	1297.9(8)	12.95
N	169.0	17.355(5)	8.694(2)	10.142(2)	121.795(11)	1300.6(7)	12.99
G	171.3	17.368(5)	8.694(2)	10.145(2)	121.828(11)	1301.6(7)	12.75
|	175.8	17.402(5)	8.696(2)	10.148(2)	121.89(10)	1303.9(7)	12.87
↓	185-225	Amorphous, no diffraction peaks observed.					
↑	139.2	17.227(6)	8.685(3)	10.127(3)	121.557(12)	1291.0(9)	15.89
|	132.2	17.192(6)	8.678(2)	10.119(3)	121.508(12)	1287.1(9)	16.06
C	129.9	17.184(6)	8.681(2)	10.122(3)	121.503(11)	1287.4(9)	15.99
O	127.5	17.199(6)	8.683(2)	10.130(3)	121.484(12)	1290.1(9)	16.43
O	125.1	17.170(6)	8.683(2)	10.123(3)	121.505(12)	1286.7(9)	16.63
L	122.6	17.160(5)	8.681(2)	10.124(3)	121.458(11)	1286.4(8)	15.85
I	115.4	17.132(5)	8.676(2)	10.125(3)	121.401(11)	1284.4(8)	16.53
N	91.8	17.006(5)	8.661(2)	10.102(3)	121.266(11)	1271.8(8)	15.98
G	44.0	16.835(5)	8.637(2)	10.078(3)	121.082(11)	1255.0(8)	15.38
↓	19.8	16.759(5)	8.619(2)	10.057(2)	121.100(10)	1243.9(7)	14.59

Crystallinity was observed in the diffraction patterns taken at one degree intervals up to a temperature of 180.4°C. The sample showed no diffraction peaks and was therefore amorphous at 181.3°C, having melted. This temperature is very close to the melting point of the complex at 180.05°C as observed in the D.S.C. trace.

Table 7.2.4b Experiment B lattice refinement of the PEO_3:$LiCF_3SO_3$ complex.

	T / °C	a / Å	b / Å	c / Å	β / °	V / Å^3	R_{wp}
↑	19.8	16.714(10)	8.610(4)	10.064(5)	120.95(2)	1242.1(14)	11.46
H	139.2	17.163(11)	8.665(4)	10.117(6)	121.44(2)	1284(2)	11.66
E	175.8	17.370(11)	8.686(4)	10.131(5)	121.82(2)	1299(2)	11.98
A	178.5	17.378(12)	8.687(4)	10.130(5)	121.84(2)	1299(2)	11.50
T	179.4	17.391(13)	8.685(5)	10.136(6)	121.88(3)	1300(2)	11.37
	180.4	17.38(2)	8.685(8)	10.132(9)	121.94(4)	1298(3)	11.60
↓	181.3-250	Amorphous, no diffraction peaks observed.					
C	152.9	17.265(12)	8.685(5)	10.118(6)	121.71(2)	1291(2)	13.88
O	148.3	17.245(11)	8.679(4)	10.115(5)	121.64(2)	1289(2)	13.52
O	143.8	17.227(11)	8.682(5)	10.120(5)	121.59(2)	1289(2)	13.76
L	139.2	17.192(10)	8.681(4)	10.114(5)	121.56(2)	1286(2)	13.56
↓	19.8	16.758(9)	8.617(4)	10.058(4)	121.07(2)	1244.0(13)	11.98

Beyond the melting point of the complex, no other crystalline phases were observed up to a temperature of 250°C. This implies that after melting, lithium triflate does not precipitate out from the amorphous mixture.

If experiments A and B are examined together, then the influence of temperature on various unit cell parameters can be investigated. Figure 7.2.4b shows the variation of the lattice parameter **a**, with temperature.

Figure 7.2.4b Plot of refined lattice parameter, a, versus temperature during heating and cooling in experiments A and B.

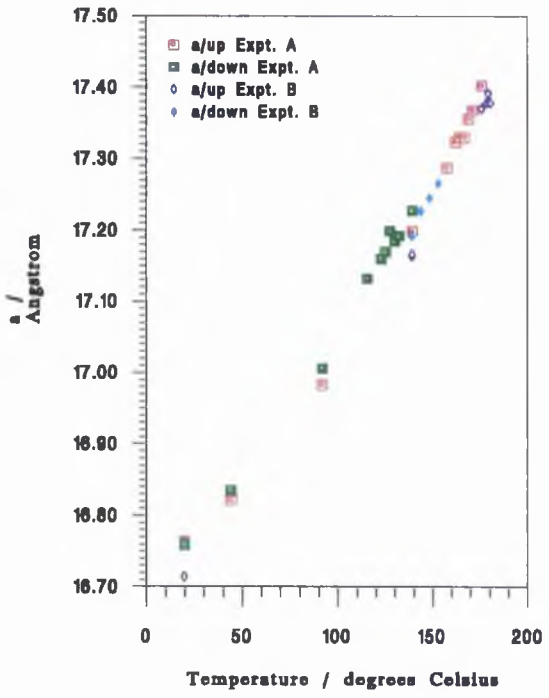

The plot above shows a smooth, but not linear variation of lattice parameter with temperature, with no discontinuities evident. All peaks found in the powder patterns could be attributed to the model generated from the proposed structure. This implies that the structure of the complex at room temperature is very similar to that which is

adopted as the melting point is approached, with the main change being the expected expansion of the lattice parameter.

Similar results are observed in Figure 7.2.4c, which shows the variation of the b lattice parameter with temperature. Again, an increase in the lattice parameter with temperature is seen. Although this is much smaller in the latter and compared with Figure 7.2.4b the increase appears to be smooth. It is interesting to note that in both Experiments A and B, the lattice parameter measured at a given temperature is significantly greater upon cooling than that measured on heating. This may be due to slow kinetics. Rapid cooling may result in a less densely packed structure and smaller crystallites, both of which lead to larger lattice parameters.

Figure 7.2.4c Plot of refined lattice parameter, b, versus temperature during heating and cooling in experiments A and B.

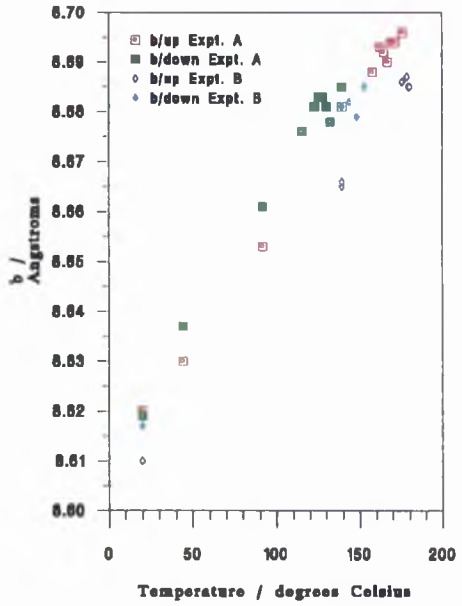

Figure 7.2.4d. shows the smooth variation of the refined lattice parameter c with temperature. The errors in the lattice parameter from the Rietveld refinement are too small to be displayed on any of the plots examined. However, the spread of values at similar temperatures (e.g. Experiment A, cooling between 140 and 115°C) can be used to gauge the degree of uncertainty in the experiment, which seems to be greater than the expected standard deviations obtained from the Rietveld analysis. The discussed spread of values is therefore not a function of uncertainty in the experiment but is again an effect of the influence of sample history on the unit cell dimensions.

Figure 7.2.4d Plot of refined lattice parameter, c, versus temperature during heating and cooling in experiments A and B.

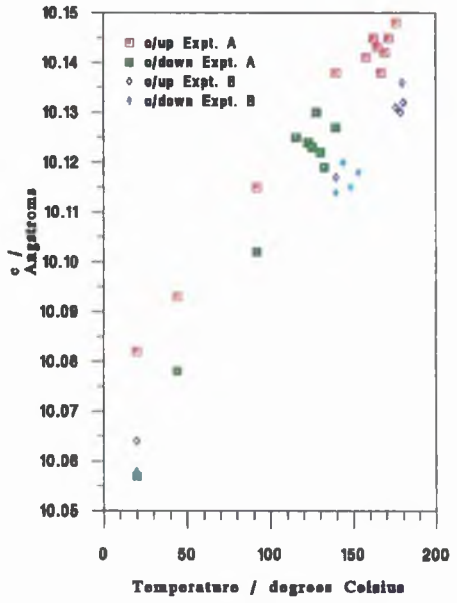

The variation of the unit cell angle β with temperature is plotted in Figure 7.2.4e. As the temperature increases, the rate of increase in β can be seen to continue

until it reaches a maximum value of 121.94(4)°, one degree below the melting point. However, there are no abrupt changes in the angle suggesting again that no discontinuous structural reorganisations occur in the temperature range studied.

Figure 7.2.4e Plot of refined unit cell angle, β, versus temperature during heating and cooling in experiments A and B.

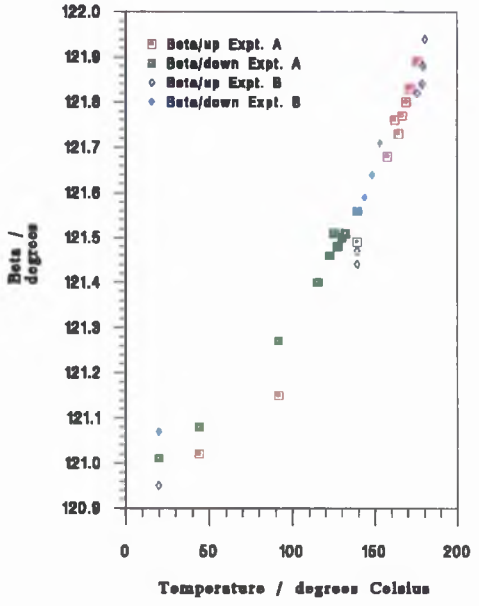

Finally, the variation of V with temperature is shown in Figure 7.2.4f. Again, there is a smooth variation of cell volume with temperature, with no obvious discontinuities in the temperature range studied.

Together these results suggest that the PEO_3:$LiCF_3SO_3$ complex does not undergo a first order structural phase transition up to its melting point. In order to confirm this, full profile refinement was carried out using the Rietveld method at room temperature, 139 and 171°C. In order to refine the structure at these

temperatures it was necessary to limit the bond distances and angles to those expected for the polyethylene oxide and triflate moieties.

Figure 7.2.4f Plot of refined lattice volume, V, versus temperature during heating and cooling in experiments A and B.

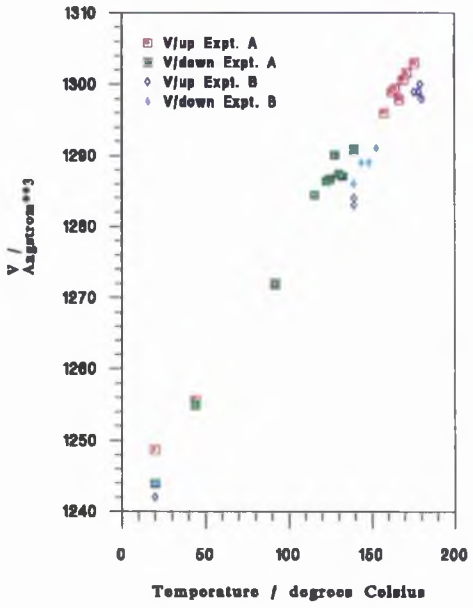

This is achieved by inserting a number of soft constraints into the refinement to stabilise the geometry of the various groups. The soft constraints effectively act as additional observations, which were necessary to improve the data-to-parameter ratio. The various constraints are shown in Figure 7.2.4g. It is not possible to constrain a bond angle directly within the GSAS suite of programmes, and so optimal atomic distances were used.

Figure 7.2.4g Representation of the triflate group (top) and PEO chain (bottom) showing the soft constraints (Å).

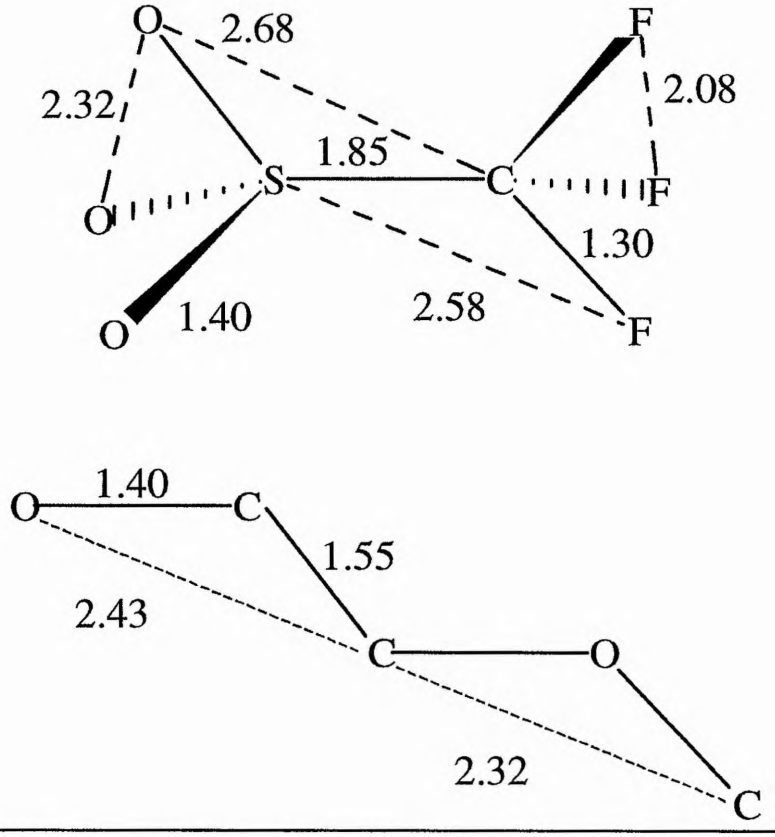

For example, the F-C-F angle at the carbon in the triflate group was constrained by minimising the S–F distances to 2.58 Å and the F–F distances to 2.08 Å. Each constraint has an associated variation of 0.2 Å, which enables the various moieties to distort so they may relax to the lowest possible local minimum during the refinement. No constraints were placed on the dihedral angles of the PEO chain or triflate moieties, so that the chain could adopt *trans* or *gauche* conformations, and the triflate group could be staggered or eclipsed.

The isotropic temperature factors were refined for all atoms except Li and H, which were set at 0.05 $Å^2$. The U_{iso} values were constrained according to atom type, so that all non-hydrogen atoms in the PEO chain were constrained to be equivalent

(C1-C6 and O1-O3), as were the various groups within the triflate moiety (S1 and C7; F1-F3 and O4-O6). All atoms were in 4e sites (general position).

The refined atomic co-ordinates for the room temperature analysis are shown in Table 7.2.4c, with selected bond distances and angles in Table 7.2.4d and the profile fit in Figure 7.2.4h.

Figure 7.2.4h Profile fit of Rietveld refinement of PEO_3:$LiCF_3SO_3$ at 19.8°C. Experimental data shown as crosses, profile fit as a continuous line and the difference between observed data and calculated fit at the bottom.

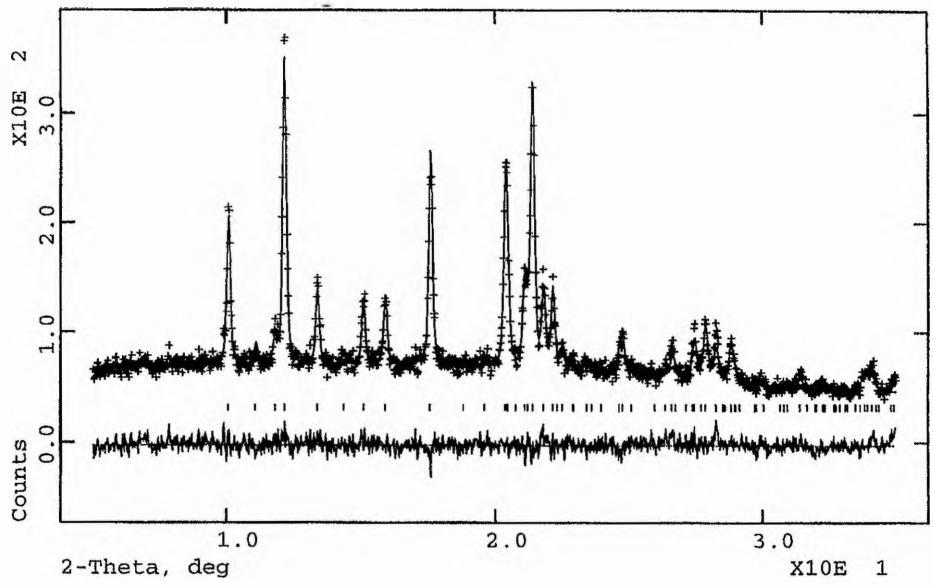

The structure obtained from the refinements is extremely close to the one proposed by Bruce *et al.* Similarly large values of U_{iso} for the atoms of the triflate moiety were observed, and it was concluded that this phenomenon was associated with thermal and not static disorder due to the smooth increase of these thermal parameters with temperature. They found relatively large displacements (0.10 Å) for F even at low temperature and attributed this to the very weak co-ordination of this part of the complex due to the projection of the fluorines into the interchain space.

Table 7.2.4c Refined atomic parameters for $PEO_3:LiCF_3SO_3$ at 19.8°C.

Space group $P2_1$ / a, a = 16.713(4), b = 8.5973(14), c = 10.054(2) Å and β = 120.980(8)°. Hydrogen atoms were included in the refinement but are not reported.

Atom	x	y	z	$*U_{iso}$ / Å^2	Occup.
O1	0.196(3)	0.094(3)	1.070(5)	0.112(12)	1
C1	0.246(5)	0.080(3)	1.235(5)	0.112(12)	1
C2	0.353(4)	0.078(3)	0.296(3)	0.112(12)	1
O2	0.377(2)	0.220(4)	0.251(3)	0.112(12)	1
C3	0.476(2)	0.234(7)	0.335(2)	0.112(12)	1
C4	0.5031(11)	0.405(7)	0.326(4)	0.112(12)	1
O3	0.4637(14)	0.447(5)	0.168(5)	0.112(12)	1
C5	0.460(3)	0.613(5)	0.155(7)	0.112(12)	1
C6	0.394(4)	0.658(3)	0.982(7)	0.112(12)	1
S1	0.2262(8)	0.119(2)	0.806(2)	0.19(3)	1
C7	0.3273(10)	0.079(2)	0.700(2)	0.19(3)	1
O4	0.280(3)	–0.008(4)	0.906(4)	0.12(2)	1
O5	0.302(3)	0.257(4)	0.894(5)	0.12(2)	1
O6	0.1693(9)	0.137(6)	0.697(2)	0.12(2)	1
F1	0.328(3)	0.203(3)	0.628(4)	0.27(2)	1
F2	0.285(3)	–0.030(4)	0.599(4)	0.27(2)	1
F3	0.4125(13)	0.040(6)	0.797(3)	0.27(2)	1
Li1	0.183(10)	0.88(2)	0.91(2)	0.05	1

* values constrained according to moiety. Li not refined. R_{wp} = 7.04.

Table 7.2.4d Selected bond lengths and angles for PEO_3:$LiCF_3SO_3$ at 19.8°C.

Bond	Distance / Å	Angle	Angle / °
O1–C1	1.424(6)	C6–O1–C1	109.7(6)
C1–C2	1.555(5)	O1–C1–C2	109.1(5)
C2–O2	1.429(5)	C1–C2–O2	108.4(5)
O2–C3	1.428(5)	C2–O2–C3	108.1(6)
C3–C4	1.555(5)	O2–C3–C4	109.2(5)
C4–O3	1.421(5)	C3–C4–O3	109.1(5)
O3–C5	1.426(5)	C4–O3–C5	109.3(6)
C5–C6	1.555(5)	O3–C5–C6	108.7(5)
C6–O1	1.424(6)	C5–C6–O1	108.9(5)
S1–O4	1.419(6)	O1–Li1–O2	159(7)
S1–O5	1.418(6)	O1–Li1–O3	75(4)
S1–O6	1.422(6)	O1–Li1–O4	81(7)
S1–C7	1.839(5)	O1–Li1–O5	82(6)
C7–F1	1.293(6)	O2–Li1–O3	84(5)
C7–F2	1.292(6)	O2–Li1–O4	113(9)
C7–F3	1.289(6)	O2–Li1–O5	101(8)
Li1–O1	2.37(16)	O3–Li1–O4	130(8)
Li1–O2	1.97(16)	O3–Li1–O5	93(7)
Li1–O3	2.23(13)	O4–Li1–O5	126(8)
Li1–O4	1.92(18)		
Li1–O5	2.10(16)		

The results of the Rietveld refinement of the complex at 139°C are presented below. Figure 7.2.4i shows the profile fit while the atomic co-ordinates are shown in Table 7.2.4e and selected bond distances and angles in Table 7.2.4f.

In order to check that the complex had attained thermal equilibrium at this temperature, the powder X-ray diffraction pattern was obtained before the long run required for a full refinement to check the lattice parameters. The refined lattice parameters from the short run were found to be, a = 17.163(11), b = 8.665(4), c = 10.117(6) Å and β = 121.44(2)°. These are within one e.s.d. of the values obtained in the full refinement suggesting that thermal equilibrium of the complex at this temperature had been attained.

Figure 7.2.4i Profile fit of Rietveld refinement of PEO_3:$LiCF_3SO_3$ at 139.2°C. Experimental data shown as crosses, profile fit as a continuous line and the difference between observed data and calculated fit at the bottom.

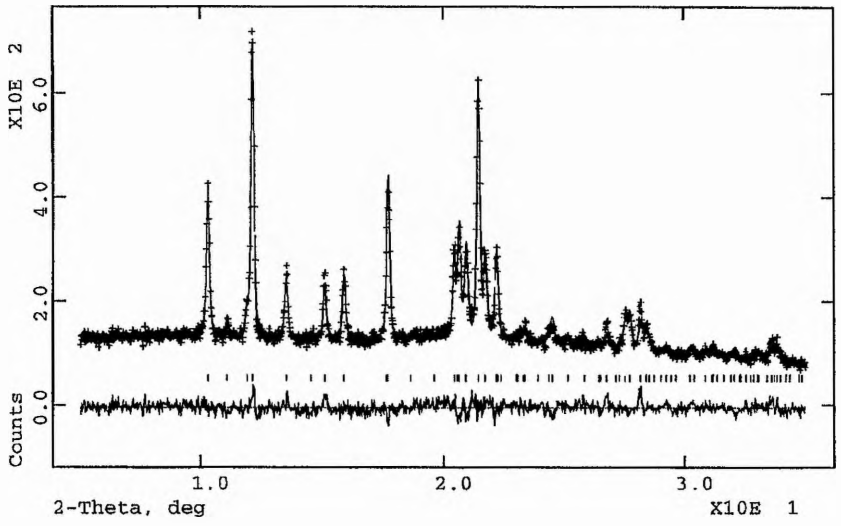

The structure is very similar to that of the complex at room temperature.

Table 7.2.4e Refined atomic parameters for $PEO_3:LiCF_3SO_3$ at 139.2°C.

Space group $P2_1$ / a, a = 17.162(3), b = 8.6646(10), c = 10.1152(15) Å and β = 121.461(6)°. Hydrogen atoms were included in the refinement but are not reported.

Atom	x	y	z	*U_{iso} / Å^2	Occup.
O1	0.205(2)	0.105(3)	1.080(4)	0.118(9)	1
C1	0.259(3)	0.094(3)	1.245(3)	0.118(9)	1
C2	0.362(3)	0.094(3)	0.300(3)	0.118(9)	1
O2	0.382(2)	0.232(3)	0.248(3)	0.118(9)	1
C3	0.4785(15)	0.248(5)	0.324(2)	0.118(9)	1
C4	0.5031(10)	0.417(5)	0.309(3)	0.118(9)	1
O3	0.4560(12)	0.460(3)	0.150(3)	0.118(9)	1
C5	0.450(2)	0.624(3)	0.137(5)	0.118(9)	1
C6	0.382(3)	0.667(3)	0.965(5)	0.118(9)	1
S1	0.2655(8)	0.125(2)	0.8062(14)	0.15(2)	1
C7	0.3255(10)	0.086(2)	0.7027(14)	0.15(2)	1
O4	0.285(2)	0.008(3)	0.916(4)	0.26(2)	1
O5	0.294(3)	0.269(3)	0.883(4)	0.26(2)	1
O6	0.1700(8)	0.130(6)	0.696(2)	0.26(2)	1
F1	0.322(3)	0.209(3)	0.626(5)	0.36(3)	1
F2	0.285(3)	–0.023(4)	0.603(4)	0.36(3)	1
F3	0.4095(13)	0.054(6)	0.801(2)	0.36(3)	1
Li1	0.172(7)	0.862(15)	0.901(13)	0.05	1

* values constrained according to moiety. Li not refined. R_{wp} = 6.68.

The Li co-ordination environment has not changed significantly. If the isotropic temperature factors for the PEO chain and S1 and C4 of the triflate group are

considered, then they have not changed from the values adopted at room temperature to within one e.s.d.

Table 7.2.4f Selected bond lengths and angles for PEO_3:$LiCF_3SO_3$ at 139.2°C.

Bond	Distance / Å	Angle	Angle / °
O1–C1	1.426(6)	C6–O1–C1	109.1(6)
C1–C2	1.554(5)	O1–C1–C2	109.4(5)
C2–O2	1.424(6)	C1–C2–O2	108.5(5)
O2–C3	1.426(6)	C2–O2–C3	108.6(6)
C3–C4	1.554(5)	O2–C3–C4	109.5(5)
C4–O3	1.423(6)	C3–C4–O3	109.5(5)
O3–C5	1.427(6)	C4–O3–C5	109.3(6)
C5–C6	1.553(5)	O3–C5–C6	108.3(5)
C6–O1	1.426(6)	C5–C6–O1	108.8(5)
S1–O4	1.413(6)	O1–Li1–O2	162(7)
S1–O5	1.418(6)	O1–Li1–O3	71(4)
S1–O6	1.423(6)	O1–Li1–O4	69(7)
S1–C7	1.842(6)	O1–Li1–O5	75(6)
C7–F1	1.295(6)	O2–Li1–O3	92(5)
C7–F2	1.294(6)	O2–Li1–O4	118(7)
C7–F3	1.286(6)	O2–Li1–O5	113(8)
Li1–O1	2.63(12)	O3–Li1–O4	122(6)
Li1–O2	1.72(12)	O3–Li1–O5	95(5)
Li1–O3	2.15(10)	O4–Li1–O5	113(5)
Li1–O4	2.25(13)		
Li1–O5	2.10(10)		

However, the isotropic temperature factors of the O and F on the triflate group have increased significantly, reflecting the increasing thermal disorder as the temperature rises.

At 171°C, the complex is within 10°C of its melting point. The refined lattice parameters from the short run to check that thermal equilibrium had been obtained were a = 17.34(2), b = 8.682(7), c = 10.121(9) Å and β = 121.74(4)°. These parameters were within one e.s.d. of the lattice parameters obtained from the full refinement, showing equilibrium had been achieved.

The atomic positions obtained from a full refinement at this temperature are given in Table 7.2.4g, selected bond distances and angles in Table 7.2.4h and the profile plot in Figure 7.2.4j.

Figure 7.2.4j Profile fit of Rietveld refinement of PEO_3:$LiCF_3SO_3$ at 171.3°C. Experimental data shown as crosses, profile fit as a continuous line and the difference between observed data and calculated fit at the bottom.

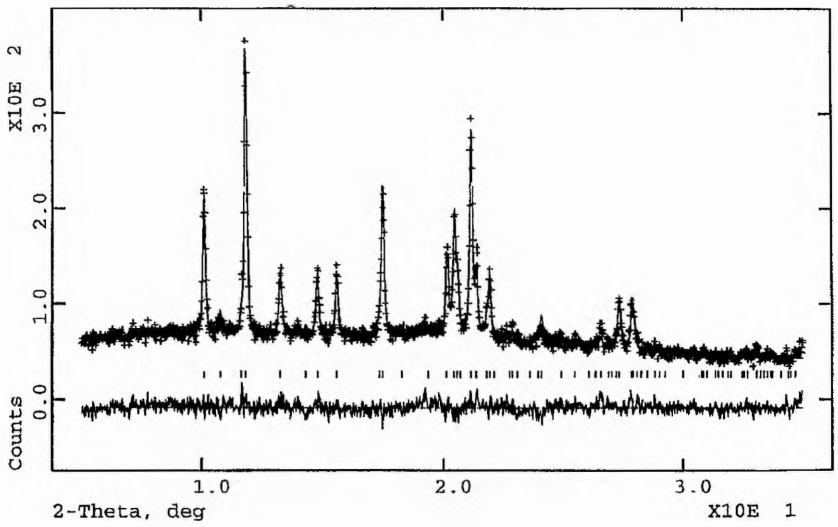

At this temperature the structure is again very similar to that adopted by the complex at room temperature, with an expansion of the lattice parameter.

Table 7.2.4g Refined atomic parameters for PEO_3:$LiCF_3SO_3$ at 171.3°C. Space group $P2_1$ / a, a = 17.331(4), b = 8.6748(13), c = 10.119(2) Å and β = 121.821(8)°. Hydrogen atoms were included in the refinement but are not reported.

Atom	x	y	z	*U_{iso} / Å^2	Occup.
O1	0.206(3)	0.092(3)	1.085(5)	0.26(2)	1
C1	0.260(5)	0.089(4)	1.251(5)	0.26(2)	1
C2	0.362(5)	0.088(3)	0.308(3)	0.26(2)	1
O2	0.381(3)	0.223(5)	0.249(3)	0.26(2)	1
C3	0.477(2)	0.238(8)	0.325(3)	0.26(2)	1
C4	0.5008(11)	0.408(8)	0.309(5)	0.26(2)	1
O3	0.454(2)	0.450(6)	0.149(5)	0.26(2)	1
C5	0.447(3)	0.614(5)	0.138(8)	0.26(2)	1
C6	0.380(4)	0.658(4)	0.965(8)	0.26(2)	1
S1	0.2625(13)	0.126(3)	0.796(2)	0.4	1
C7	0.3341(11)	0.087(3)	0.716(2)	0.4	1
O4	0.276(3)	0.009(4)	0.905(4)	0.20(3)	1
O5	0.286(4)	0.270(3)	0.873(6)	0.20(3)	1
O6	0.1698(11)	0.127(8)	0.673(3)	0.20(3)	1
F1	0.337(4)	0.209(3)	0.644(7)	0.4	1
F2	0.300(4)	–0.023(6)	0.615(7)	0.4	1
F3	0.416(2)	0.055(10)	0.827(4)	0.4	1
Li1	0.203(9)	0.83(2)	0.88(2)	0.05	1

* values constrained according to moiety. Li not refined. R_{wp} = 7.47.

Table 7.2.4h Selected bond lengths and angles for PEO_3:$LiCF_3SO_3$ at 171.3°C.

Bond	Distance / Å	Angle	Angle / °
O1–C1	1.426(6)	C6–O1–C1	109.0(6)
C1–C2	1.555(5)	O1–C1–C2	109.5(5)
C2–O2	1.427(6)	C1–C2–O2	108.3(5)
O2–C3	1.423(5)	C2–O2–C3	108.7(6)
C3–C4	1.556(5)	O2–C3–C4	109.5(5)
C4–O3	1.423(6)	C3–C4–O3	109.5(5)
O3–C5	1.430(6)	C4–O3–C5	108.7(6)
C5–C6	1.550(5)	O3–C5–C6	108.6(5)
C6–O1	1.429(6)	C5–C6–O1	108.6(5)
S1–O4	1.419(6)	O1–Li1–O2	82(7)
S1–O5	1.420(6)	O1–Li1–O3	145(4)
S1–O6	1.420(6)	O1–Li1–O4	109(7)
S1–C7	1.839(5)	O1–Li1–O5	87(6)
C7–F1	1.294(6)	O2–Li1–O3	74(5)
C7–F2	1.292(6)	O2–Li1–O4	146(11)
C7–F3	1.290(6)	O2–Li1–O5	103(8)
Li1–O1	2.51(17)	O3–Li1–O4	105(11)
Li1–O2	1.64(16)	O3–Li1–O5	74(5)
Li1–O3	2.79(14)	O4–Li1–O5	109(5)
Li1–O4	1.91(19)		
Li1–O5	2.50(17)		

The isotropic temperature factors for the S1, C4 and F1-3 of the triflate group just below the melting point of the complex refined to the maximum value allowed by the GSAS programme, 0.4. Difference Fourier plots showed no evidence of alternative sites for those atoms, instead the scattering density appeared to be smoothed out. Therefore these thermal parameters were fixed at this value.

As the temperature increases, the isotropic temperature factor on the F of the triflate group increases (20°C, 0.27(2) $Å^2$; 139°C, 0.36(3) $Å^2$ and 171°C, 0.4 $Å^2$), and those of the S1 and C1 rise sharply from 0.15(2) $Å^2$ at 139°C to 0.4 $Å^2$ at 171°C. Since diffraction techniques define the structure both spatially and temporally it is difficult to decouple static from dynamic disorder. The continuous increase in thermal parameters for F suggests that this at least may be dynamic disorder. Studies by, for example, ^{19}F NMR could resolve this issue.

However, this work has shown that the structure of the complex, even at 10°C below its melting point, is very similar to the structure at room temperature. The Li is still co-ordinated to five oxygens, three from the PEO and two from the triflate groups. The bond distance calculations shown in Table 7.2.4h show that the Li is co-ordinated more strongly to one of the ether oxygens (Li–O2, 1.64(16) Å) than the other two, which have co-ordination lengths of 2.51(17) (Li–O1) and 2.79(14) Å (Li–O3). The Li still maintains a strong co-ordination one of the triflate oxygens (Li–O4, 1.91(19) Å) while the bond length to the other triflate oxygen is 2.50(17) Å for Li–O5. The infra-red results show that this $Li^+ - O_3SCF_3^-$ co-ordination is maintained on melting.

7.3 4:1 PEO:Alkali metal salt complexes

7.3.1 Introduction

The crystalline polymers have been the focus of much research in this laboratory because of the detailed information which can in principle be obtained by applying X-ray crystallography to such systems. The difficulties in solving the structures of these materials were discussed in the introduction to this chapter. However, by applying state-of-the-art powder X-ray crystallographic techniques, including in some instances methods which permit the determination of complete crystal structures from powder X-ray data ab initio i.e. without any prior knowledge of the structure[10], the structures of several important polymer electrolytes have been elucidated. These include PEO_3:$LiCF_3SO_3$[5], PEO_3:$NaClO_4$[11], PEO_4:KSCN and PEO_4:NH_4SCN[12] and most recently PEO_3:$Li(CF_3SO_2)_2N$.

The crystal structure of the PEO_4:RbSCN complex contains the largest cation to be studied by crystallographic techniques to date and thus extends the range over which the parameters that control the structures of polymer electrolytes have been varied. The solution of this structure allows a comparison with the structures which have been previously investigated and thus enables the development of some of the basic principles that determine the structure of polymer electrolytes.

7.3.2 Experimental Details

RbSCN was prepared by dissolving Rb_2CO_3 (Aldrich, 99.8 %) [2.0111 g] in 100 ml of distilled water along with the correct stoichiometric ratio of NH_4SCN (Aldrich, 97.5 %) [1.3257 g]. This was then stirred for 2 h and the water and ammonium

carbonate removed on a rotary evaporator (> 58°). The crystalline product was subsequently dried for 48 h at 120°C.

The PEO_4:RbSCN sample was prepared by mixing appropriate molar ratios of dry PEO (Aldrich, molecular weight = 5 x 10^6) [0.5 g] and RbSCN [0.4073 g] in a M Braun argon filled glove box from which the O_2 and H_2O were continuously removed. The mixture was then sealed in a stainless steel tube, removed from the glove box and ground at liquid nitrogen temperature for approximately 20 minutes. After the mixture was returned to room temperature it was transferred back to the glove box and sealed in a 0.5 mm Lindemann tube. This was heated at 170°C for 4 h to allow dissolution of the salt in the polymer, followed by annealing at 55°C for 14 days to promote crystallinity.

X-ray powder diffraction data were collected on a Stoe STADI/P diffractometer operating in transmission mode and utilising $CuK_{\alpha 1}$ radiation. Data were collected at room temperature in the range $5° < 2\theta < 60°$ in 0.02° steps, the entire run lasting 15 hours. Rietveld refinement of the X-ray powder data was carried out using the GSAS suite of programs[8] and structures were represented using Insight II, (Biosym Corporation)[13].

7.3.3 Structural Determination

Preliminary examination of the data suggested a resemblance to the powder X-ray diffraction pattern for PEO_4:KSCN solved previously[12], hence indexing of the pattern was carried out on this basis. The data could be indexed in the monoclinic system, space group C2 / c with approximate cell dimensions a = 25.75, b = 8.23, c = 16.05 Å, β = 126°. Due to the anticipated structural similarity between this phase and the previously characterised 4:1 phases, the structural model obtained for the PEO_4:KSCN complex was used as the basis for Rietveld refinement. In the model, the

PEO chain forms a helix with a conformation which is represented as ttgttgtt $\bar{g}$ tt $\bar{g}$, ie. all C-O bonds *trans*, but C-C bonds adopting *gauche* or *gauche minus* orientation.

As previously mentioned, Rietveld refinements of such complex structures (~ 100 refinable structural parameters) with limited data are not reliable unless extra information is available in the form of soft "chemical" constraints. Hence, all bond lengths and angles within the PEO chain together with the S-C and C-N bond lengths of the anion were constrained within typical values throughout the refinement. Values for the PEO chain are shown in Figure 7.2.4g. while the constraints for the thiocyanate were S-C 1.64(2) Å and C-N 1.14(2) Å. The torsion angles of the PEO chain were not restrained, and refined to chemically reasonable values corresponding to the expected chain conformation. Thermal parameters were refined within three groups - i.e. Rb and SCN together, polymer C and O together and H's together. Combining the above with the usual profile parameters, the final refinement thus consisted of 126 variables refined against 2732 observations, leading to final agreement factors of $R_{wp} = 4.3\%$.

7.3.4 Results and Discussion

The final refined atomic parameters for the PEO_4:RbSCN complex are given in Table 7.3.4a and selected bond lengths in Table 7.3.4b. The structure of PEO_4:RbSCN is presented in Figure 7.3.4a. The structure corresponds to that of PEO_4:KSCN and PEO_4:NH_4SCN.

The profile fit of the Rietveld refinement of the PEO_4:RbSCN complex is shown in Figure 7.3.4c.

Table 7.3.4a Refined atomic parameters for PEO_4:RbSCN at room temperature. Space group C2 / c, a = 25.754(2), b = 8.2265(6), c = 16.0455(11) Å and β = 125.946(3)°. Hydrogen atoms were included in the refinement but are not shown.

Atom	x	y	z	U_{iso} / Å^2
Rb1	0.2986(3)	0.3526(7)	0.3355(4)	0.097(3)
S1	0.4198(6)	0.167(2)	0.2743(9)	0.097(3)
C1	0.3447(12)	0.119(8)	0.231(4)	0.097(3)
N1	0.2918(9)	0.081(5)	0.198(3)	0.097(3)
O1	0.3331(10)	0.112(2)	0.505(2)	0.096(6)
C2	0.2951(12)	–0.031(2)	0.468(2)	0.096(6)
C3	0.2229(11)	0.017(3)	0.404(2)	0.096(6)
O2	0.2039(10)	0.101(4)	0.313(2)	0.096(6)
C4	0.1436(10)	0.178(4)	0.267(2)	0.096(6)
C5	0.1176(14)	0.242(2)	0.158(2)	0.096(6)
O3	0.1003(14)	0.104(2)	0.093(2)	0.096(6)
C6	0.0784(12)	0.153(3)	–0.007(2)	0.096(6)
C7	0.0449(10)	0.003(3)	–0.090(2)	0.096(6)
O4	0.0880(10)	–0.131(3)	0.961(2)	0.096(6)
C8	0.4393(10)	0.229(3)	0.6022(13)	0.096(6)
C9	0.3969(11)	0.079(3)	0.541(2)	0.096(6)

Focusing first on Figure 7.3.4a-(b) which illustrates part of just one chain from the crystal structure, the helical conformation adopted by the PEO chain is evident with a rubidium ion located inside each turn of the helix. Each rubidium ion is co-ordinated by five ether oxygens from the chain, three of which are dedicated to just one rubidium while the remaining two each bridge between neighbouring rubidium ions.

Figure 7.3.4a (a) View of the structure of the PEO_4:RbSCN complex down the fibre axis. Rb shown as purple, C as green, O as red, N as blue and S as yellow spheres. (b) Shows a portion of a single PEO chain with associated ions.

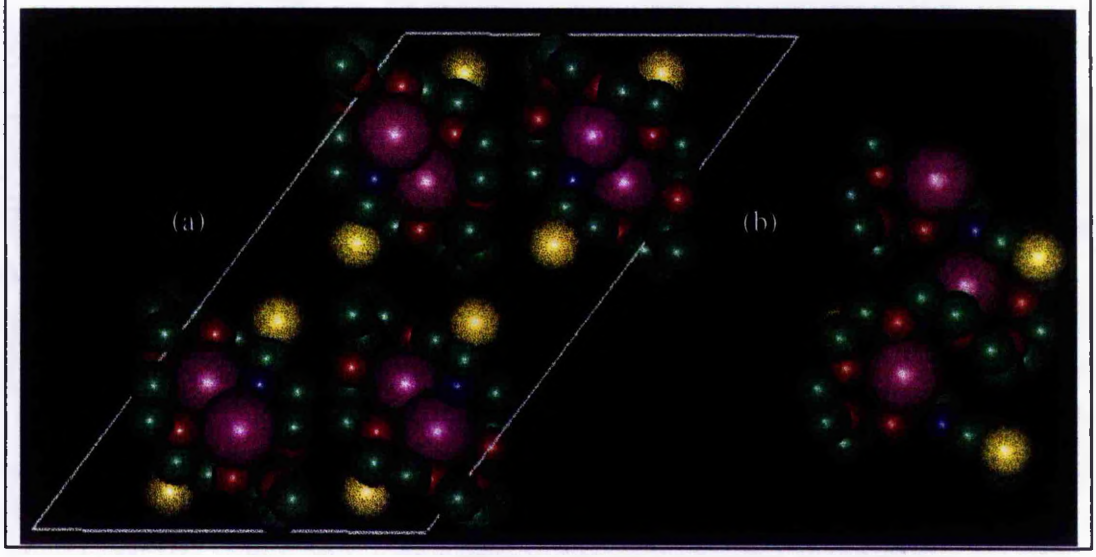

The thiocyanate ions are located with their nitrogen atoms pointing towards the rubidium, two thiocyanate ions are co-ordinated to each rubidium with the nitrogen atoms in each case bridging two neighbouring rubidium ions.

The rubidium ions are therefore co-ordinated by seven atoms, Figure 7.3.4b.

Figure 7.3.4b Local co-ordination around Rb1.

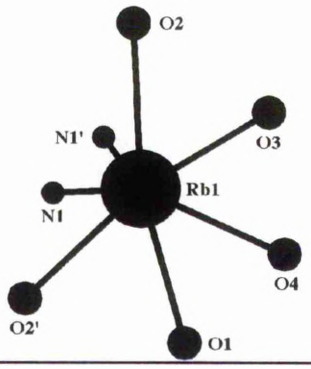

Figure 7.3.4a-(a) illustrates a view down the fibre axis i.e. down the axis of the helical chains. It is clear from this picture that the chains are essentially isolated from each other, each PEO chain is tightly bound to a dedicated set of cations and anions.

Table 7.3.4b Selected bond distances for PEO_4:RbSCN at room temperature.

Bond	Distance / Å	Bond	Distance / Å
Rb1–O1	3.05(2)	Rb1–O4	2.83(2)
Rb1–O2	3.05(3)	Rb1–N1	3.07(4)
Rb1–O2'	3.11(3)	Rb1–N1'	2.79(2)
Rb1–O3	2.98(3)		

Figure 7.3.4c Profile fit for the Rietveld refinement of PEO_4:RbSCN at room temperature. Experimental data shown as crosses, profile fit as a continuous line, allowed reflections shown as tick marks and difference plot shown at the bottom.

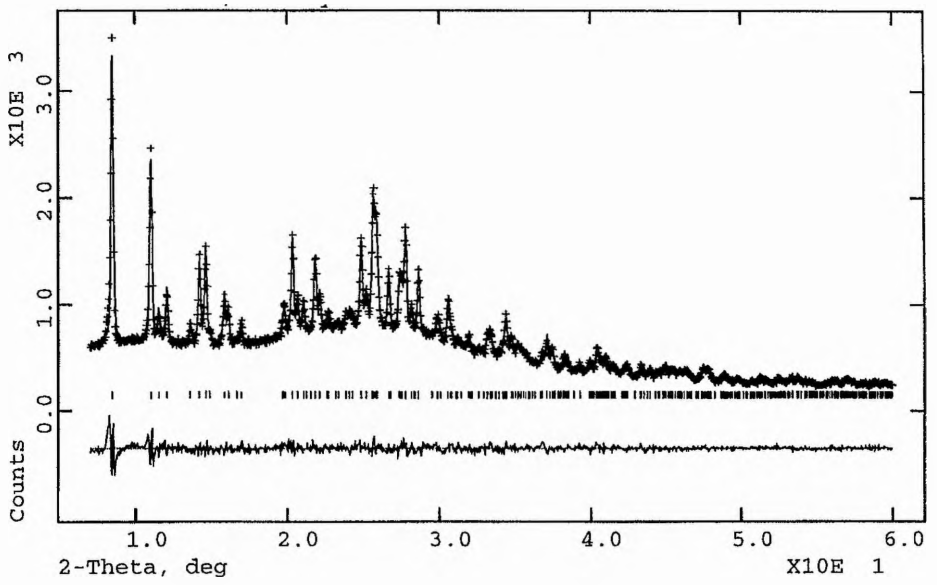

7.3.5 Structural Principles

The crystal structures of several polymer electrolytes containing alkali metal cations ranging in size from Li^+ (ionic radius 0.76 Å) to Rb^+ (ionic radius 1.52 Å) have now been solved. It is therefore possible to examine the influence of cation radius on the structures of polymer electrolytes and to begin to develop an understanding of the general principles which control the structures that form when polymers and salts combine in the solid state. This discussion is based on the crystal structures of the following polymer electrolytes: PEO_3:$LiCF_3SO_3$, PEO_3:$NaClO_4$, PEO_4:KSCN and PEO_4:RbSCN; it is apposite first to summarise the structures of these. The crystal structure of PEO_3:$LiCF_3SO_3$ is shown in Figure 7.2.3a and was discussed in section 7.2.3. In summary, the PEO chain forms a helix, where the C–O bonds are in all cases *trans* but the C–C bonds can adopt a *gauche* or a *gauche minus* orientation. This produces an overall conformation of ttgttgtt$\bar{g}$. Each turn of the helix accommodates one Li^+ ion which is co-ordinated by three ether oxygens that do not co-ordinate to any other cations. The co-ordination around the lithium ions is completed by one oxygen from each of two triflate anions. In total the co-ordination number around the lithium ion is five and the geometry is approximately trigonal bipyramidal. The structure of PEO_3:$NaClO_4$ is similar to that of PEO_3:$LiCF_3SO_3$. The PEO chains adopt the same conformation with a cation again located in each turn of the helix although in this case the cation co-ordination involves four ether oxygens from the chain. Two of the oxygens from the perchlorate group directly replace the two co-ordinating oxygens from the $–SO_3$ of the triflate anion, so that the total co-ordination around Na^+ is six. The structure of PEO_4:KSCN is very similar to that of PEO_4:RbSCN and may be derived by replacing the rubidium cation by potassium although of course the dimensions (in particular the cation–oxygen and cation–nitrogen bond lengths) are different.

The general structural features of the polymer electrolyte systems ranging in cation size from Li^+ to Rb^+ are summarised in Table 7.3.5a.

Table 7.3.5a Basic structural details of some polymer-salt complexes.
Ionic radii are taken from work by Shannon[14] and are based on a 6 co-ordinate oxygen environment.

Complex	PEO	PEO conformation	Ionic radius of cation / Å	No of ether O	No of anions	Total C. N.
$PEO_3:LiCF_3SO_3$[5]	helix	ttgttgtt$\bar{g}$	0.76	3	2	5
$PEO_3:NaClO_4$[11]	helix	ttgttgtt$\bar{g}$	1.02	4	2	6
$PEO_4:KSCN$[12]	helix	ttgttgtt$\bar{g}$ tt$\bar{g}$	1.38	5	2	7
$PEO_4:NH_4SCN$[12]	helix	ttgttgtt$\bar{g}$ tt$\bar{g}$	1.61*	5	2	7
PEO_4:RbSCN	helix	ttgttgtt$\bar{g}$ tt$\bar{g}$	1.52	5	2	7

*There is considerable debate concerning the effective ionic radius of NH_4^+; it can vary substantially from solid to solid. The lattice parameter measurements place it between K^+ and Rb^+ in polyethers.

In all cases the PEO chains adopts a helical conformation with cations located inside the helix despite a doubling in the cation radius from Li^+ to Rb^+. This demonstrates the remarkable ability of PEO to wrap around cations of widely varying size, albeit with a change of chain conformation in going from Na^+ (ionic radius 1.02 Å) to K^+ (ionic radius 1.38 Å) in order to produce a larger pocket for the cations (Figure 7.3.5a). This is an important result which overturns a long held view in the field that cations larger than sodium could not be accommodated within the helix but must be located in the interchain space.

An important consequence of the crystallographic studies is that they indicate strong interactions between each chain and its dedicated ions but only weak interactions between the chains. It is a well established phenomenon that as the amorphous salt concentration of a polymer electrolyte increases, the conductivity decreases. This was assumed to be due to an increase in interionic crosslinking arising

from the increasing salt content pining the polymer chains and therefore reducing ion mobility. However, this structural study suggests that the well established decrease in conductivity with increasing salt concentration in amorphous polymer electrolytes may be due to intrachain crosslinking rather than the widely accepted view which has attributed it to interchain crosslinking.

Figure 7.3.5a A comparison of the PEO chain conformation in the PEO_3:$LiCF_3SO_3$ complex (left) and PEO_4:RbSCN complex (right).

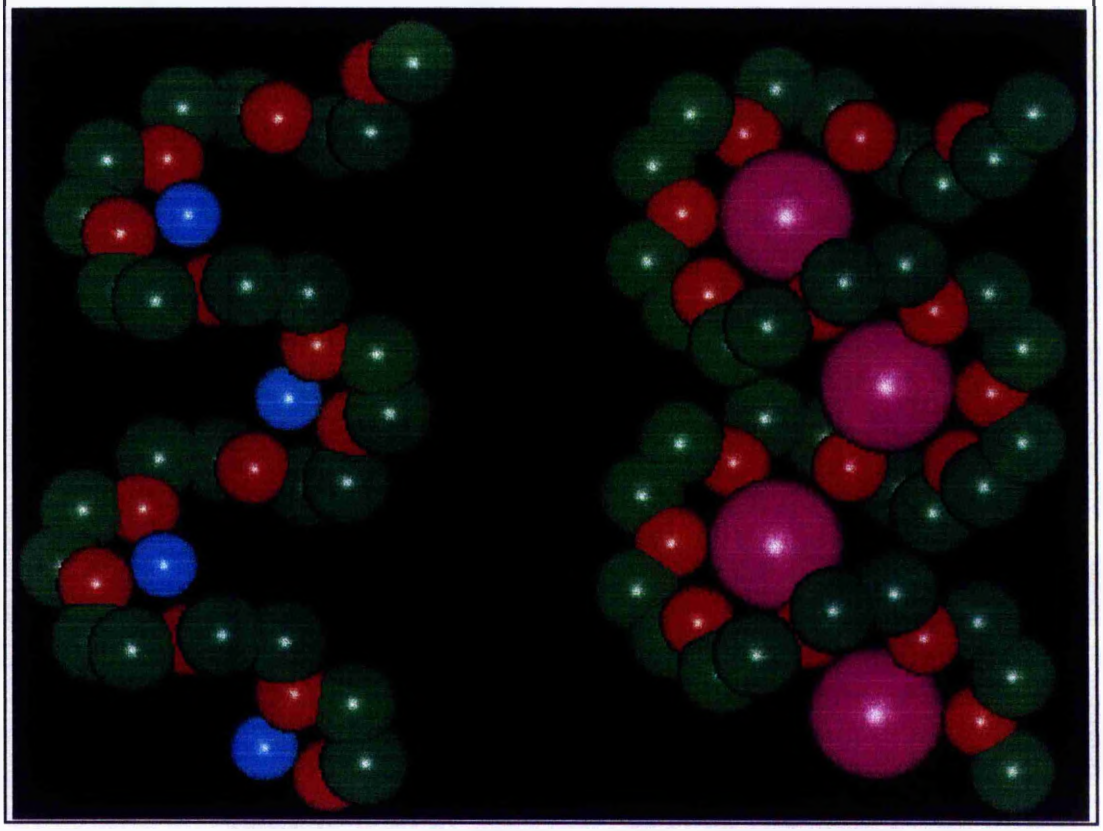

These results allow the comparison of the local co-ordination around the cations in polymer electrolytes with those in the simple crown ethers. In the sodium complexes, the Na^+ achieves the highest stability in 18–crown–6 in which the cation exhibits a co-ordination number of 6 involving complexation by the six oxygens of the

crown[15]. On the other hand, in the polyether, Na^+ is co-ordinated by only four ether oxygens, the preferred co-ordination of 6 being completed by two anions. PEO can provide a pocket with more than 4 ether oxygens in the co-ordination sphere as demonstrated by the PEO_4:Rb(K)SCN complex, but in that case the cation to ether oxygen distance would be too large for Na^+, hence the adoption of the 4 + 2 configuration for sodium. It is evident that the structures of the polymer-salt complexes are governed by the desire to adopt a helical conformation for PEO as well as the need to achieve a preferred cation to ether oxygen bond length, with the anions making up the desired co-ordination number. Potassium ions are stable in 18–crown–6 but in addition the anions occupy the apical positions[15]. In the case of ligation by PEO, the structure is similar but with only 5 ether oxygens in the "ring".

This study proves that the crystal structures themselves provide a great insight into the structural chemistry of crystalline polymer-salt complexes and permits the development of general principles for the interaction between co-ordinating polymers and salts. There is also little doubt that a knowledge of the crystal structures when combined with spectroscopic studies of the analogous amorphous phases will prove far more illuminating than isolated spectroscopic studies of the amorphous phases on their own.

7.4 References

1. Y. Chatani and S. Okamura, *Polymer*, **28**, 1815, 1987.

2. P. Lightfoot, C. Glidewell and P.G. Bruce, *J. Mater. Chem.*, **2**, 361, 1992.

3. C. D. Robitaille and D. Fauteux, *J. Electrochem. Soc.*, **133**, 315, 1986.

4. A. Vallée, S. Besner and J. Prud'homme, *Electrochimica Acta*, **37**(9), 1579, 1992.

5. P. Lightfoot, M. A. Mehta and P. G. Bruce, *Science*, **262**, 883, 1993.

6. V. Srinivasa and S. Banerjee, *Indian J. Phys.*, **50**, 108, 1976.

7. Y. Chatani, Y. Fujii, T. Takayanagi and A. Honma, *Polymer*, **31**, 2238, 1990.

8. A. C. Larson, R. B. Von Dreele, Los Alamos Laboratory Report No. LA-UR-86-748, 1987.

9. F. W. Stone and J. J. Stratta, *Encycloped. Polym. Sci. Technol.*, **6**, 103, 1967.

10. M. Tremayne, P. Lightfoot, M. A. Mehta, P. G. Bruce, K. D. M. Harris, K. Shankland, C. J. Gilmore and G. Bricogne, *J. Solid State Chem.*, **100**, 191, 1992.

K. D. M Harris, M. Tremayne, P. Lightfoot and P. G. Bruce, *J. Am. Chem. Soc.*, **116**, 3543, 1994.

11. P. Lightfoot, M. A. Mehta and P. G. Bruce, *J. Mater. Chem.*, **2**(4), 379, 1992.

12. P. Lightfoot, J. L. Nowinski and P. G. Bruce, *J. Am. Chem. Soc.*, **116**, 7469, 1994.

13. InsightII User Guide, Biosym Technologies, San Diego, 1993.

14. R. D. Shannon, *Acta Crystallogr.*, **A32**, 751, 1976.

15. G. Gokel, "Crown Ethers and Cryptands", Royal Society of Chemistry, 1991.

Chapter 8
Concluding Remarks

8 Concluding Remarks

The importance of powder X-ray and neutron diffraction to structural characterisation in the field of solid state chemistry has been shown by the series of structural studies of new inorganic oxides and polymer electrolytes presented in this work. In particular, the complementary nature of these two diffraction techniques has allowed the elucidation of the structures of complex metal oxides which could not have been achieved by a single technique.

As the structures of these materials have been obtained, still more questions have been raised. Future work into these topics could involve further investigation into the $Ce_2Zr_2O_{7+x}$ system. Diffuse scattering or oxygen NMR could be used to investigate the heterogeneity of oxygen intercalation on the nm scale, while conductivity studies could be used to determine the oxide ion conductivity in this structure. Conductivity studies could also reveal if $Li_{29}Zr_9Nb_3O_{40}$ and $Li_{29}Zr_{9.6}Ta_{2.4}O_{40}$ exhibit the ionic conductivity expected as a consequence of their partial Li and O site occupancies. The kinetics of oxygen intercalation using the hypobromite system could be further investigated by an analysis of the rates of oxygen insertion into $Sr_2M_2O_5$ (M = Co, Fe) and La_2TO_4 (T = Cu, Ni). The magnetic structure of the oxygen deficient perovskite $Ca_2LaFe_3O_8$ still remains to be extracted from the powder neutron diffraction data. This could be facilitated by further neutron diffraction experiments. Finally, ^{19}F NMR could be used to resolve the issue of static / dynamic disorder encountered in the triflate groups of the PEO_3:$LiCF_3SO_3$ polymer-salt complex on heating.

In conclusion, this work has shown the usefulness of diffraction techniques in the investigation of new materials, however it is clear that in order to achieve the complete characterisation of a system, it is necessary to call upon a number of the analytical techniques which are at the disposal of a solid state chemist today.

Appendix 1
Abbreviations and Constants

Appendix 1: Abbreviations

Abbreviation	*Meaning*
Å	angstrom i.e. 10^{-10}m
atm	atmosphere
AES	Auger electron spectroscopy
b.v.	bond valence
c.c.p.	cubic close packed
cm	10^{-2}m
dm	10^{-1}m
°C	degrees Centigrade
DSC	differential scanning calorimmetry
DTA	differential thermal analysis
EELS	electron energy loss spectroscopy
ESR	electron spin resonance
eV	electron-volt
EXAFS	extended X-ray absorption fine structure
g	grammes
G	guest
h	hour
H	host
HREM	high resolution electron microscopy
HRNMR	high resolution nuclear magnetic resonance
IR	infra red
K	degrees Kelvin
LEED	low energy electron diffraction
m	meter
μm	10^{-6}m
mm	10^{-3}m

Abbreviation	*Meaning*
mol	mole
nm	10^{-9}m
NMR	nuclear magnetic resonance
PEO	polyethylene oxide
PDF	powder data file
PXRD	powder X-ray diffraction
s	second
S	Siemen
SCE	standard calomel electrode
SEM	scanning electron microscopy
STEM	scanning transmission electron microscopy
TEM	transmission electron microscopy
TGA	thermogravimetric analysis
UV	ultra violet
XANES	X-ray absorption near edge structure
XPS	X-ray photoelectron spectroscopy

Appendix 1: Constants

Constant	*Value*
b, neutron coherent scattering length	Li = –0.190, O = 0.5803, Mg = 0.5375, V = –0.3824, Fe = 0.954, Co = 0.278, Ni = 1.03, Cu = 0.7718, Sr = 0.702, Zr = 0.716, Nb = 0.7054, La = 0.824, Ce = 0.484 and Ta = 0.691×10^{-12} cm*
c, speed of light	2.99792458×10^{8} ms^{-1}
e, elementary charge	1.602177×10^{-19} C
F, Faraday constant	9.6485×10^{4} $Cmol^{-1}$
h, Planck constant	6.62608×10^{-34} Js
m_e, electron mass	9.910939×10^{-31} kg
m_n, neutron mass	1.77493×10^{-27} kg
R, gas constant	8.31451 $JK^{-1}mol^{-1}$

* V. F. Sears, "Neutron Scattering Lengths and Cross Sections", AECL Research, Chalk River Laboratories, Canada, 1991.

Appendix 2
Structural Refinements from Oxygen Intercalation Studies

Table 1 Crystallographic data from the neutron refinement of La_2CuO_4.

Space group *Cmca*, 3693 observations, a = 5.35342(3), b = 13.14159(6), c = 5.39984(3) Å, V = 379.892(6) $Å^3$, R_{wp} = 1.72.

Atom	Site	x	y	z	$B_{11}/Å^2$	$B_{22}/Å^2$	$B_{33}/Å^2$	$B_{23}/Å^2$
La	8f	0	0.36172(3)	0.00679(15)	0.419(14)	0.210(12)	0.47(2)	0.21(2)
Cu	4a	0	0	0	0.18(2)	0.65(2)	0.17(2)	0.20(3)
O(1)	8e	0.25	–0.00721(8)	–0.25	0.35(2)	0.86(3)	0.37(2)	
O(2)	8f	0	0.18313(7)	–0.03395(13)	1.45(3)	0.47(2)	1.02(3)	0.07(3)

O(1) B_{13} = 0.229(11) $Å^2$, occupancy = 0.990(3); O(2) occupancy = 0.998(3).

Figure 1 Profile fit from the neutron refinement of La_2CuO_4.

Experimental data shown as dots, profile fit as a continuous line, and difference / e.s.d. is shown at the bottom. Tick marks represent allowed reflections.

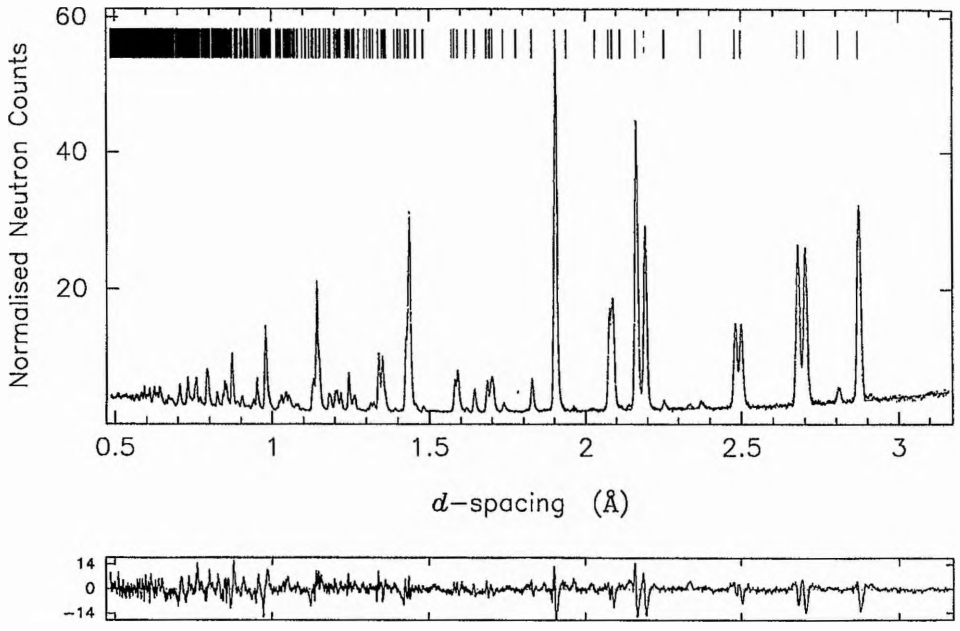

Table 2 Crystallographic data from the neutron refinement of La_2CuO_4 oxidised for 20 h in NaOBr (aq).

Phase 1

Space group *Cmca*, 2787 observations, a = 5.35866(10), b = 13.1782(2), c = 5.39007(10)Å, R_{wp} = 3.25, phase fraction = 0.524(12).

Atom	**Site**	**x**	**y**	**z**	**B_{iso}/Å^2**
La	8f	0	0.36122(2)	0.0034(9)	0.60(2)
Cu	4a	0	0	0	0.61(2)
O(1)	8e	0.25	–0.00712(4)	–0.25	0.71(3)
O(2)	8f	0	0.1824(4)	–0.0217(11)	1.57(8)

Phase 2

Space group *Fmmm*, a = 5.34243(10), b = 5.40883(11), c = 13.2144(2) Å, V = 381.85(2) Å^3, refined formula $La_2CuO_{4.03(6)}$.

Atom	**Site**	**x**	**y**	**z**	**B_{iso}/Å^2**	**Occup.**
La	8i	0	0	0.3607(2)	0.60(2)	
Cu	4a	0	0	0	0.61(2)	
O(1)	8e	0.25	0.25	0	0.71(3)	
O(2)	8i	0	0	0.1798(6)	0.13(8)	
O(3)	32p	–0.0393(14)	–0.082(2)	0.1836(9)	0.13(8)	0.104(3)
O(4)	8f	0.25	0.25	0.25	0.5	0.016(6)

Constraints: 2×Occupancy O(2) + 8×Occupancy O(3) = 2; B_{iso} O(2) = B_{iso} O(3).

Figure 2 Profile fit from the neutron refinement of La_2CuO_4 oxidised for 20 h in NaOBr (aq).

Experimental data shown as dots, profile fit as a continuous line, and difference / e.s.d. is shown at the bottom. Upper set of tick marks are associated with phase 1, lower with phase 2.

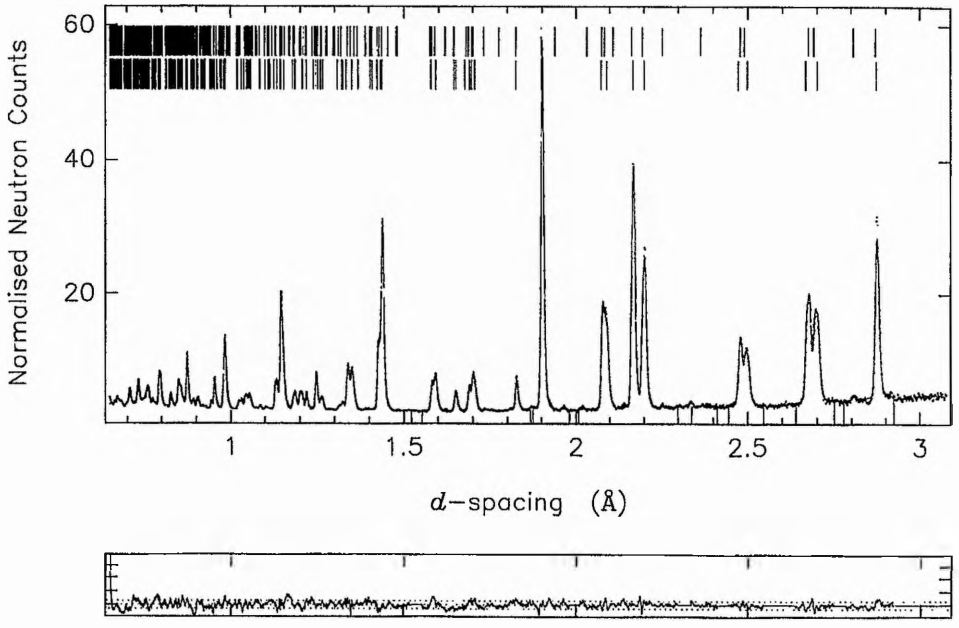

Table 3 Crystallographic data from the neutron refinement of La_2NiO_4.

Space group *Cmca*, 3693 observations, a = 5.48068(4), b = 12.58362(6), c = 5.49858(4) Å, R_{wp} = 2.95.

Atom	Site	x	y	z	Site	B_{iso}/Å^2
La	8f	0	0.36343(6)	0.0065(3)		0.458(11)
Ni	4a	0	0	0		0.424(12)
O(1)	8e	0.25	–0.00863(12)	–0.25		0.62(2)
O(2)	8f	0	0.17735(14)	–0.0319(3)	0.979(6)	0.07(3)

Figure 3 Profile fit from the neutron refinement of La_2NiO_4.

Experimental data shown as dots, profile fit as a continuous line, and difference / e.s.d. is shown at the bottom. Tick marks represent allowed reflections.

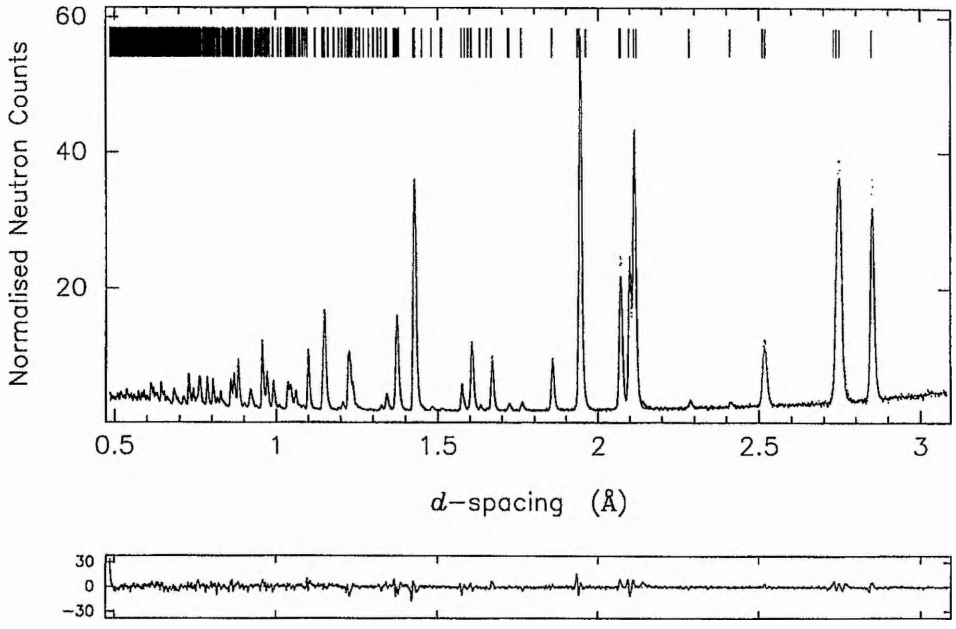

Table 4 Crystallographic data from the neutron refinement of La_2NiO_4 oxidised for 20 h in NaOBr (aq).

Space group *Fmmm*, 3693 observations, R_{wp} = 3.20, a = 5.46266(8), b = 5.46829(8), c = 12.69286(5) Å, formula $La_2NiO_{4.14(7)}$.

Atom	**Site**	**x**	**y**	**z**	**B_{iso}/Å**	**Occup.**
La	8i	0	0	0.36089(6)	0.443(11)	
Ni	4a	0	0	0	0.525(15)	
O(1)	8e	0.25	0.25	0	0.86(2)	
O(2)	8i	0	0	0.1746(2)	0.81(6)	
O(3)	32p	–0.061(4)	–0.065(4)	0.1710(5)	1.10(11)	0.095(4)
O(4)	8f	0.25	0.25	0.25	0.5	0.070(3)

Constraint: 2×Occupancy O(2) + 8×Occupancy O(3) = 2.

Figure 4 Profile fit from the neutron refinement of La_2NiO_4 oxidised for 20 h in NaOBr (aq).

Experimental data shown as dots, profile fit as a continuous line, and difference / e.s.d. is shown at the bottom. Tick marks represent allowed reflections.

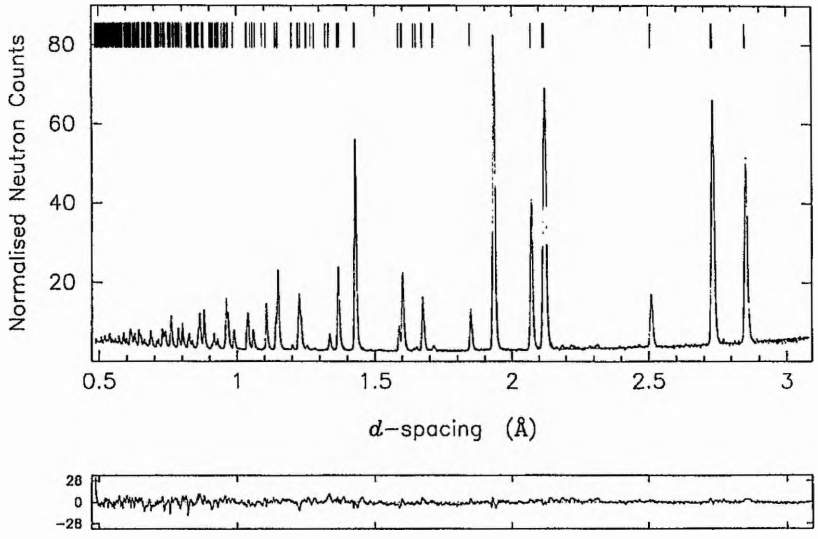

Table 5 Crystallographic data from the neutron refinement of $Sr_2Fe_2O_5$.

Space group I*cmm* 2671 observations, $R_{wp} = 4.20$, a = 5.66340(4), b = 15.58597(10), c = 5.52141(4) Å, formula $Sr_2Fe_2O_{2.485(11)}$.

Atom	Site	x	y	z	Occup.	B_{iso}/Å^2	m.m./μ_B
Fe(1)	4a	0	0	0		0.73(3)	3.98(10)
Fe(2)	8i	0.5679(3)	0.25	0.4573(4)	0.500(5)	0.03(6)	3.35(12)
Sr	8h	0.5133(3)	0.60956(7)	0		0.50(3)	
O(1)	8g	0.25	0.99205(13)	0.25		0.27(3)	
O(2)	8h	0.0478(3)	0.14123(11)	0		0.92(4)	
O(3)	8i	0.6409(7)	0.25	0.1241(7)	0.485(11)	0.14(11)	

Code for magnetic refinement supplied by Dr J. Bruce Forsyth, Rutherford Appleton Laboratory.

Figure 5 Profile fit from the neutron refinement of $Sr_2Fe_2O_5$.

Experimental data shown as dots, profile fit as a continuous line, and difference / e.s.d. is shown at the bottom. Tick marks represent allowed reflections.

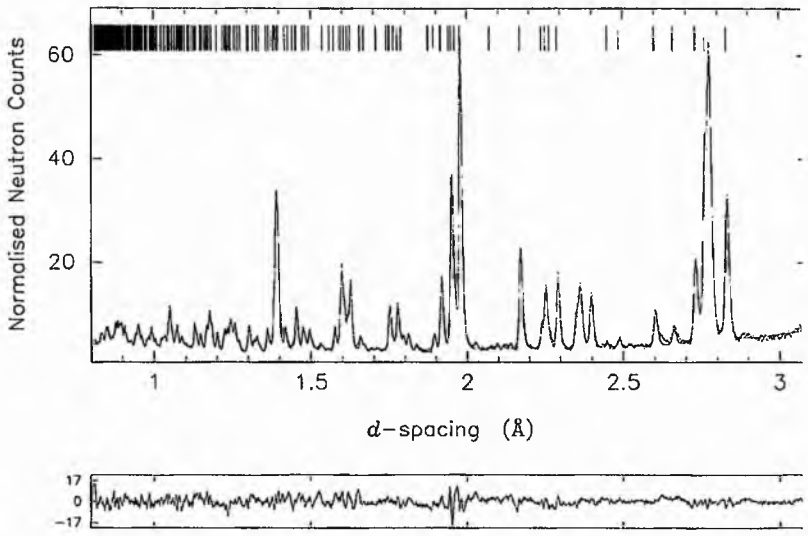

Table 6 Crystallographic data from the neutron refinement of $Sr_2Fe_2O_5$ oxidised for 20 h in NaOBr (aq).

Space group $Pm\bar{3}m$ 4503 observations, R_{wp} = 2.84, a = 3.85794(1) Å, formula $SrFeO_{2.795(12)}$.

Atom	Site	x	y	z	B_{iso}/Å^2	B_{11}/Å^2	B_{22}/Å^2	B_{33}/Å^2
Sr	1b	0.5	0.5	0.5	0.495(10)			
Fe	1a	0	0	0	0.216(8)			
O	3d	0	0.5	0		0.89(2)	−0.23(2)	0.89(2)

Occupancy O = 0.932(4)

Figure 6 Profile fit from the neutron refinement of $Sr_2Fe_2O_5$ oxidised for 20 h in NaOBr (aq).

Experimental data shown as dots, profile fit as a continuous line, and difference / e.s.d. is shown at the bottom. Tick marks represent allowed reflections.

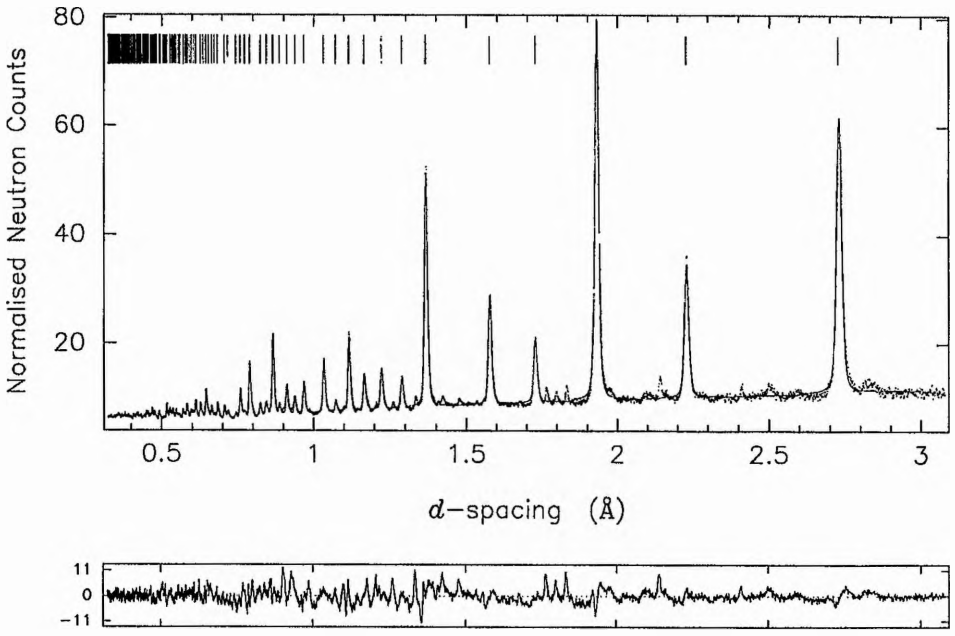

Table 7 Crystallographic data from the neutron refinement of $Sr_2Co_2O_5$.

Space group I*cmm* 2671 observations, R_{wp} = 3.68, a = 5.56382(9), b = 15.8126(2), c = 5.47281(8) Å, formula $Sr_2Co_2O_{2.5}$.

Atom	Site	x	y	z	Occup.	B_{iso}/Å^2	m.m./μ_B
Co(1)	4a	0	0	0		1.24(11)	3.06(14)
Co(2)	8i	0.540(2)	0.25	0.470(3)	0.5	1.2(2)	1.70(15)
Sr	8h	0.5060(5)	0.61308(11)	0		0.60(3)	
O(1)	8g	0.25	0.9947(3)	0.25		1.51(4)	
O(2)	8h	0.0391(5)	0.1409(2)	0		1.17(6)	
O(3)	8i	0.6471(12)	0.25	0.1397(12)	0.5	2.12(10)	

Code for magnetic refinement supplied by Dr J. Bruce Forsyth, Rutherford Appleton Laboratory.

Figure 7 Profile fit from the neutron refinement of $Sr_2Co_2O_5$.

Experimental data shown as dots, profile fit as a continuous line, and difference / e.s.d. is shown at the bottom. Tick marks represent allowed reflections.

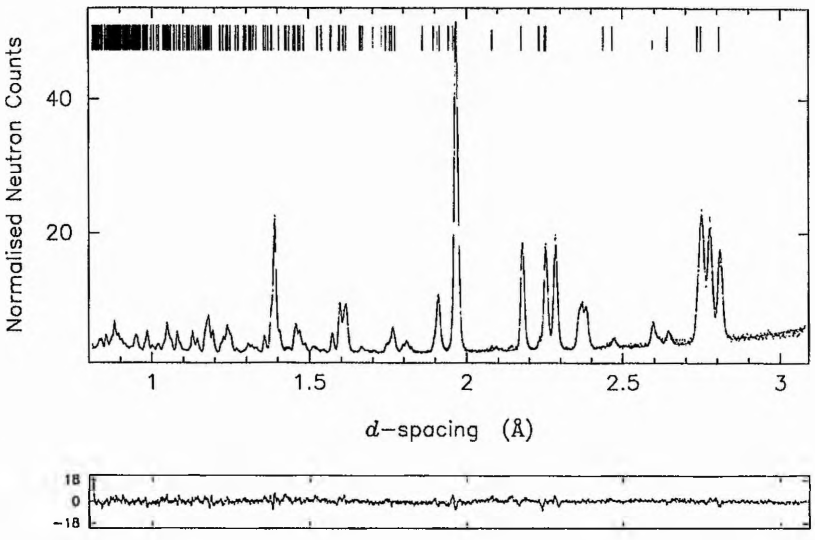

Table 8 Crystallographic data from the neutron refinement of $Sr_2Co_2O_5$ oxidised for 1 h in NaOBr (aq).

Space group $Pm\bar{3}m$ 4503 observations, R_{wp} = 2.47, a = 3.83412(1) Å, formula $SrCoO_{2.936(12)}$.

Atom	Site	x	y	z	B_{iso}/Å^2	B_{11}/Å^2	B_{22}/Å^2	B_{33}/Å^2
Sr	1b	0.5	0.5	0.5	0.493(11)			
Fe	1a	0	0	0	0.279(13)			
O	3d	0	0.5	0		1.144(12)	0.38(2)	1.144(12)

Occupancy O = 0.979(4)

Figure 8 Profile fit from the neutron refinement of $Sr_2Co_2O_5$ oxidised for 1 h in NaOBr (aq).

Experimental data shown as dots, profile fit as a continuous line, and difference / e.s.d. is shown at the bottom. Tick marks represent allowed reflections.

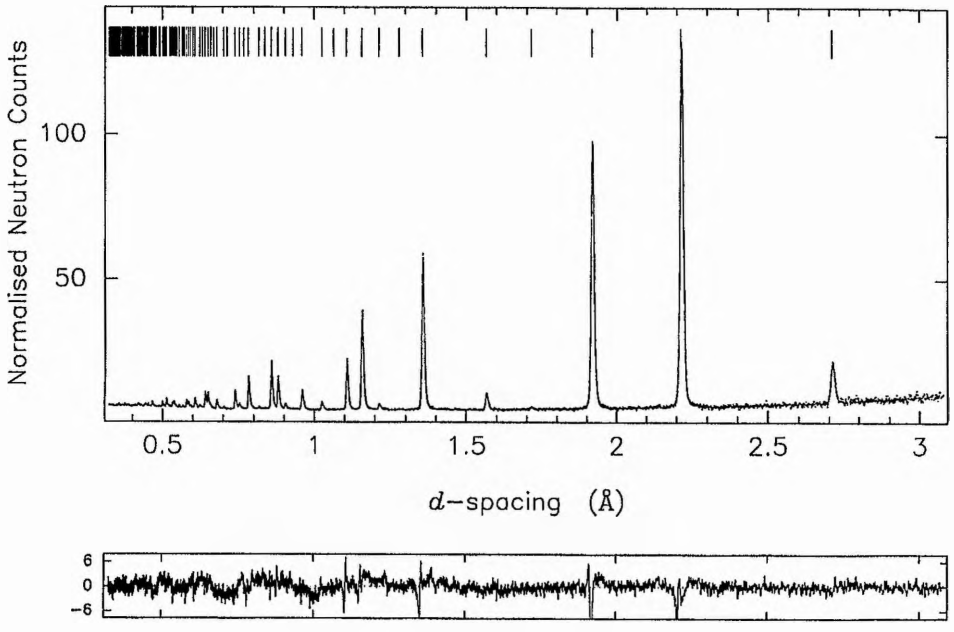

Table 9 Crystallographic data from the neutron refinement of Sr_2CoFeO_5.

Space group I*cmm* 2671 observations, R_{wp} = 3.68, a = 5.6163(9), b = 15.6834(2), c = 5.50142(7) Å, formula $Sr_2CoFeO_{2.463(10)}$.

Atom	Site	x	y	z	Occup.	B_{iso}/Å^2	m.m./μ_B
Fe(1)/ Co(1)	4a	0	0	0		0.86(4)	3.43(8)
Fe(2)/ Co(2)	8i	0.5658(4)	0.25	0.4596(5)	0.5	10.27(7)	2.70(9)
Sr	8h	0.5105(3)	0.61026(6)	0		0.55(2)	
O(1)	8g	0.25	0.99361(13)	0.25		0.66(2)	
O(2)	8h	0.0435(3)	0.14082(9)	0		1.12(3)	
O(3)	8i	0.6353(6)	0.25	0.1285(6)	0.5	0.52(11)	

Code for magnetic refinement supplied by Dr J. Bruce Forsyth, Rutherford Appleton Laboratory. Constraints: Occupany Fe(1) + Occupancy Co(1) = 1; B_{iso} Fe(1) = B_{iso} Co(1); magnetic moment Fe(1) = magnetic moment Co(1); Occupany Fe(2) + Occupancy Co(2) = 0.5; Occupancy Fe(1) = 2×Occupancy Fe(2) = 1; Occupancy Co(2) = 2×Occupancy Co(2) = 1; B_{iso} Fe(2) = B_{iso} Co(2); magnetic moment Fe(2) = magnetic moment Co(2); x Fe(2) = x Co(2); z Fe(2) = z Co(2). Occupancy Fe(1) = 0.628(7), occupancy Co(1) = 0.372(7); occupancy Fe(2) = 0.186(4), occupancy Co(2) = 0.314(4).

Figure 9 Profile fit from the neutron refinement of Sr_2CoFeO_5.

Experimental data shown as dots, profile fit as a continuous line, and difference / e.s.d. is shown at the bottom. Tick marks represent allowed reflections.

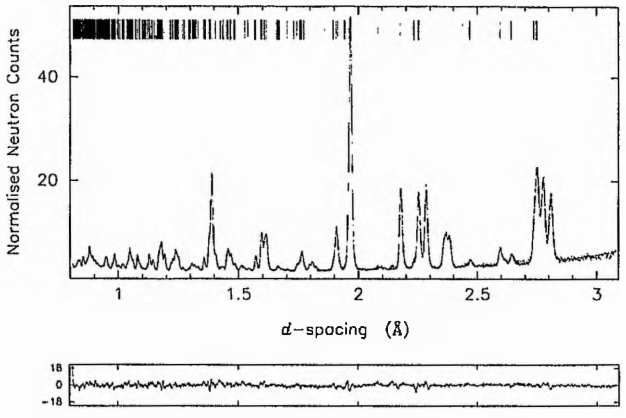

Table 10 Crystallographic data from the neutron refinement of Sr_2CoFeO_5 oxidised for 1 h in NaOBr (aq).

Space group $Pm\bar{3}m$ 4503 observations, R_{wp} = 2.28, a = 3.83310(1) Å, formula $SrCo_{0.5}Fe_{0.5}O_{2.992(8)}$.

Atom	Site	x	y	z	B_{iso}/Å^2	B_{11}/Å^2	B_{22}/Å^2	B_{33}/Å^2
Sr	1b	0.5	0.5	0.5	0.427(5)			
Fe/Co	1a	0	0	0	0.241(5)			
O	3d	0	0.5	0		0.792(6)	0.345(9)	0.792(6)

Constraints: Occupancy Fe + Occupancy Co = 1, B_{iso} Fe = B_{iso} Co.

Occupancy O = 0.997(3), occupancy Fe = 0.513(3), occupancy Co = 0.487(3).

Figure 10 Profile fit from the neutron refinement of $Sr_2Co_{0.5}Fe_{0.5}O_5$ oxidised for 1 h in NaOBr (aq).

Experimental data shown as dots, profile fit as a continuous line, and difference / e.s.d. is shown at the bottom. Tick marks represent allowed reflections.

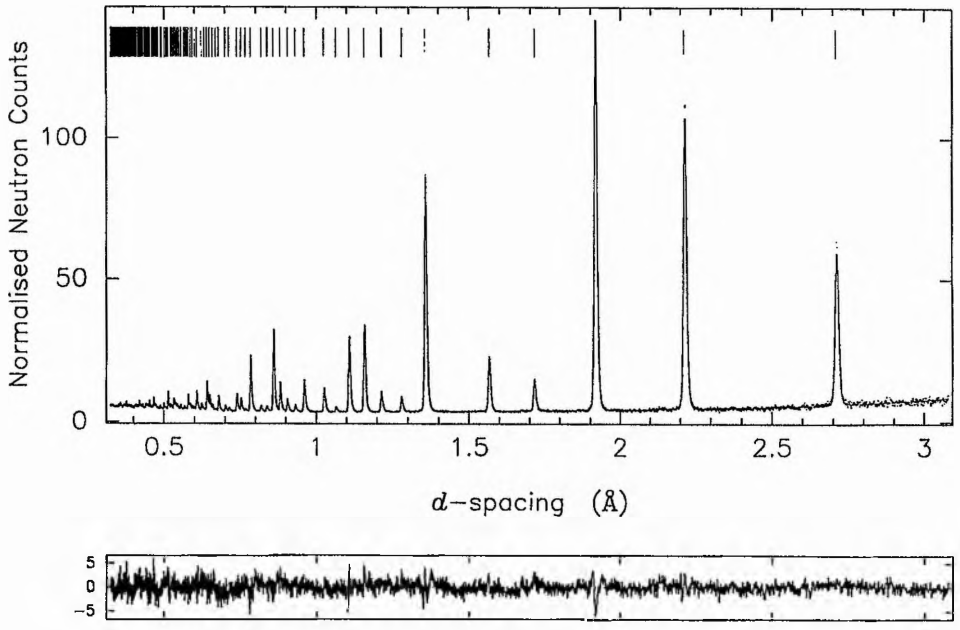

Table 11 Crystallographic data from the neutron refinement of $YBa_2Cu_3O_{6.20}$.

Space group P4/*mmm*, 3693 observations, R_{wp} = 1.89, a = 3.86460(1), c = 11.80219(7) Å, refined formula $YBa_2Cu_3O_{6.20(6)}$.

Atom	Site	x	y	z	B_{iso}/Å^2	B_{11}/Å^2	B_{22}/Å^2	B_{33}/Å^2
Y	1d	0.5	0.5	0.5		0.36(2)	0.36(2)	0.68(4)
Ba	2h	0.5	0.5	0.19422(7)		0.41(2)	0.41(2)	0.76(3)
Cu(1)	1a	0	0	0		1.18(2)	1.18(2)	0.80(3)
Cu(2)	2g	0	0	0.36111(6)		0.170(11)	0.170(11)	0.97(3)
O(1)	4i	0	0.5	0.37849(5)		0.495(15)	0.200(14)	1.06(2)
O(2)	2g	0	0	0.15299(10)		1.44(2)	1.44(2)	1.14(4)
O(3)	2f	0.5	0	0	1.0			

Occupancy O(3) = 0.099(3). Minor CuO impurity, included in the refinement. a = 4.69170, b = 3.41793, c = 5.13323, β = 99.56°;Cu (0.25, 0.25, 0), Cu B_{iso} = 0.65(7) Å^2; O (0, 0.4107(15), 0.25), O B_{iso} = 0.81(9) Å^2.

Figure 11 Profile fit from the neutron refinement of $YBa_2Cu_3O_{6.20}$.

Experimental data shown as dots, profile fit as a continuous line, and difference / e.s.d. is shown at the bottom. Upper set of tick marks are associated with main phase, lower with CuO.

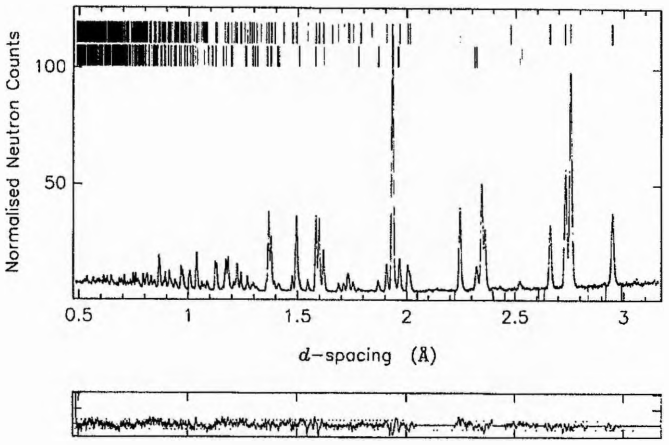

Table 12 Crystallographic data from the neutron refinement of $YBa_2Cu_3O_{6.20}$, 72 h tetrabutylammonium periodate in dioxane.

Space group P4/*mmm*, 3693 observations, R_{wp} = 1.84, a = 3.86424(1), c = 11.79967(7) Å, refined formula $YBa_2Cu_3O_{6.201(6)}$.

Atom	Site	x	y	z	B_{iso}/Å^2	B_{11}/Å^2	B_{22}/Å^2	B_{33}/Å^2
Y	1d	0.5	0.5	0.5		0.37(2)	0.37(2)	0.64(3)
Ba	2h	0.5	0.5	0.19418(8)		0.40(2)	0.40(2)	0.74(3)
Cu(1)	1a	0	0	0		1.20(2)	1.20(2)	0.73(3)
Cu(2)	2g	0	0	0.36110(6)		0.180(11)	0.180(11)	0.89(3)
O(1)	4i	0	0.5	0.37850(5)		0.487(15)	0.205(14)	1.04(2)
O(2)	2g	0	0	0.15298(10)		1.44(2)	1.44(2)	1.06(4)
O(3)	2f	0.5	0	0	1.0			

Occupancy O(3) = 0.101(3). Minor CuO impurity, included in the refinement. a = 4.69052, b = 3.41819, c = 5.13325, β = 99.59°;Cu (0.25, 0.25, 0), Cu B_{iso} = 0.77(8) Å^2; O (0, 0.4118(2), 0.25), O B_{iso} = 0.72(10) Å^2.

Figure 12 Profile fit from the neutron refinement of $YBa_2Cu_3O_{6.20}$, 72 h tetrabutylammonium periodate in dioxane. Experimental data shown as dots, profile fit as a continuous line, and difference / e.s.d. is shown at the bottom. Upper set of tick marks are associated with main phase, lower with CuO.

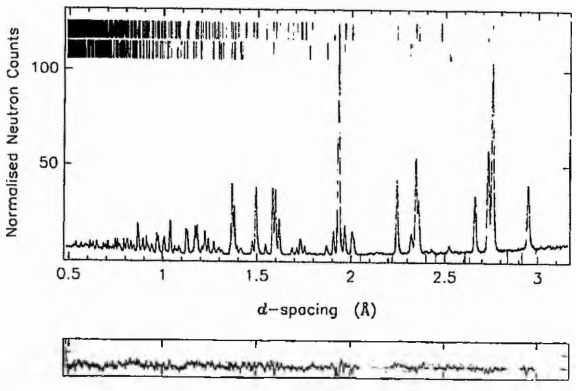

Table 13 Lattice refinement of La_2CuO_4 before and after 48 h in $NaIO_4$ (aq).

Parameter	**Initial**	**Final**
a	5.3628(13) Å	5.354(2) Å
b	13.153(5) Å	13.133(2) Å
c	5.4075 (15) Å	5.405(2)Å
V	381.4(3) $Å^3$	380.0(4) $Å^3$
Zero point	0.028(11)°	0.02(16)
Figure of merit	58.0	13.9

Space group C*mca*.

Acknowledgements

I'd like to thank everyone in Lab 238 for keeping me (in)sane enough to last the distance over the past 3½ years. Special thanks must go to our resident computer whizzes, Ali and RobRab, who achieved the impossible, and made my PC go; to Phil for starting me off on the right crystallographic *footing* and for all his help in the "early days"; to MiJiT and Ian for their friendship; to Lynn for all the juicy gossip; and to Sooz and Andy for being there.

Thanks must also go to the unsung heroes of the School, Marjorie, Sylvia and Bobby, who always found the time to help.

I must also thank Peter, my supervisor for all his help and guidance over the course of my research, and EPSRC for providing the *generous* funding for my project. Last but by no means least, serious amounts of thanks to two people without whom this would have been a very different story, Cap'n Bob and Big John - thank you very much indeed - the whisky is on its way!